znadasdy_144_23

Patterns of the brain

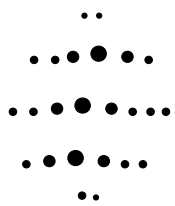

Az agy mintázatai

Akadémiai Doktori Értekezés

Nádasdy Zoltán Ph.D.

2023

Table of Content

Papers:

[Paper 1] **Nadasdy, Z.,** Hirase, H., Czurko, A., Csicsvari, J., & Buzsaki, G. (1999). Replay and time compression of recurring spike sequences in the hippocampus. *J Neurosci*, *19*(21), 9497–9507. http://www.ncbi.nlm.nih.gov/entrez/query.fcgi?cmd=Retrieve&db=PubMed&dopt=Citation&list_uids=10531452

[Paper 2] Wagenaar, D. A., **Nadasdy, Z**., & Potter, S. M. (2006). Persistent dynamic attractors in activity patterns of cultured neuronal networks. Phys Rev E Stat Nonlin Soft Matter Phys, 73(5 Pt 1), 51907. http://www.ncbi.nlm.nih.gov/entrez/query.fcgi?cmd=Retrieve&db=PubMed&dopt=Citation&list_uids=16802967

[Paper 3] **Nadasdy, Z.** (2009). Information encoding and reconstruction from the phase of action potentials. *Front Syst Neurosci*, *3*, 6. https://doi.org/10.3389/neuro.06.006.2009

[Paper 4] **Nadasdy, Z.** (2010). Binding by asynchrony: the neuronal phase code. Front Neurosci, 4. https://doi.org/10.3389/fnins.2010.00051

[Paper 5] **Nadasdy, Z.**, Nguyen, T. P., Török, Á., Shen, J. Y., Briggs, D. E., Modur, P. N., & Buchanan, R. J. (2017a). Context-dependent spatially periodic activity in the human entorhinal cortex. *Proceedings of the National Academy of Sciences*, *114*(17), E3516–E3525. https://doi.org/10.1073/pnas.1701352114

[Paper 6] **Nadasdy, Z.**, Howell, D. H. P., Török, Á., Nguyen, T. P., Shen, J. Y., Briggs, D. E., Modur, P. N., & Buchanan, R. J. (2022). Phase coding of spatial representations in the human entorhinal cortex. *Science Advances*, *8*(18), eabm6081. https://doi.org/10.1126/sciadv.abm6081

Acknowledgment

My background in psychology helped me focus on questions that neuroscientists ignore or avoid. Such as, can memory manifest as dynamic patterns in the brain? How do we define neuronal representations? What is self-awareness? Before I became a student at ELTE, Donald Hebb's book "The Organization of Behavior: A neuropsychological theory" (Hebb, 1995, 2005) was recommended for the admission exam. It was a wise choice by the faculty of Psychology because, unlike a textbook offering explicit knowledge, it provided an overarching approach with many conjectures and vague definitions, inspiring to think it further. Full of insights about the mind-brain, and structure-function relationships, many of them enduring the trial of time. Hebb inspired us to think about the neuronal underpinning of learning and memory as a network that accounts for the enormous flexibility of the human mind. Hebb's foundational concepts of reverberation circuits and cell assemblies were easy to consolidate with Hopfield and neural networks, plasticity, synaptic modulation by long-term potentiation (LTP), and spike-time-dependent-plasticity (STDP) with it later. As a student of the ELTE Dept. of Psychology, I cannot be more grateful to the faculty of Psychology at ELTE, especially to Csaba Pléh and his ongoing intellectual support. Among the few people who took me under their wings at ELTE was Anikó Kónya, who showed me that my unorthodox ideas about memory were not as far-fetched as I thought. Later, excellent teachers like László Mérő and János Geier fostered my love of math and expanded my interdisciplinary horizon with concepts borrowed from the works of Dawkins, Hofstadter, Dennett, Tversky, and Kahneman.

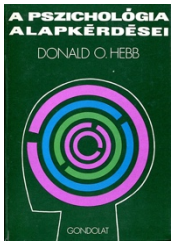

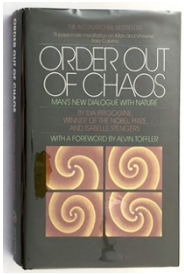

My other constant source of inspiration was the work of János Szentagothai, even before I started my undergraduate studies at ELTE. I read everything I could find published by him, including his research papers and more philosophical essays. Those introduced me to the work of Ilya Prigogine and the field of nonlinear dynamics. I consumed Haken's foundational book on Synergetics, which introduced "dissipative systems," a concept readily applicable to neural systems. With this background, when György Buzsáki introduced the work of Walter Freeman to me, all those pieces fell in place at the level of mesoscopic brain dynamics. The third source of inspiration was the concept of cellular automatons introduced by Von Neumann and the idea that simple transfer functions can implement complex pattern-generating algorithms by iteration. It also made me realize the enormous power of simulations and numerical models over thought experiments. It turned out that all these readings prepared me for the embracement of the new wave in cognitive science: connectionism. When the double volume of Parallel Distributed Processing (edited by Rumelhart and McClelland) got published, it took cognitive

psychology by storm. ‘Connectionism’ was the beginning of brain-inspired Neural Networks before engineers converted them to thousands of “smart applications” on your smartphone. That was also the seed of the development of Generative Pre-trained Transformers, the heart of ChatGTP, and the new generation of AI that is truly reshaping our society.

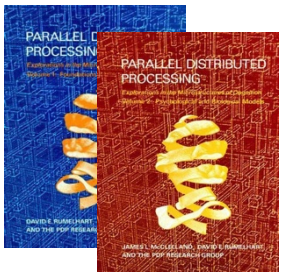

While this exciting paradigm shift of neural networks and parallel processing was happening, I also developed an adherence to working with empirical data, especially EEG, the only noninvasive data available to me at that time. That motivation naturally gravitated me to the Institute of Psychology of the Hungarian Academy of Science to work under Magda Marton’s supervision together with an outstanding team of József Szirtes, Péter Breuer, Nándor Donnauer, and our ‘extended family,’ including György Karmos, Márk Molnár, István Winkler, István Czigler, and Valéria Csépe, just to name a few. I was thrilled as an aspiring young scientist to be able to record signals from the human brain during action, the feeling so intoxicating that it never seizes to exist. In addition to the intellectually stimulating environment at MTA, my ongoing curiosity for cognitive development yielded enduring friendships with György Gergely, Gergely Csibra, Ilona Kovács, and József Fiser, with whom we all consider ourselves as Csaba Pléh’s students. In addition, I am grateful for the ongoing support and illuminating conversations with my colleagues over the last 10 years at the Institute for Psychology at ELTE, Ildikó Király, Attila Krajcsi, Dezső Németh, and Anett Ragó. Finally, I am indebted to express my gratitude to my mentors, György Buzsáki at Rutgers and NYU, Richard Andersen and Shinsuke Shimojo at Caltech, and Moshe Abeles at the Hebrew University, all of whom guided me through my graduate school and postdoc training. Among the most enduring collaborations, I owe special thanks to László Záborszky (Rutgers) who taught me neuroanatomy and with whom we developed a few state-of-the-art quantitative neuroanatomy methods to decipher the structural and functional relationship between the basal forebrain cholinergic system and its cortical associations.

In this dissertation, I build my arguments around the following core concepts (in chronological order): reverberatory activity (Hebb, 1949), self-organizing networks (Haken, 1983; Kauffman & Kauffman, 1993), Hopfield network (Hopfield, 1982), recurrent network (Rajan et al., 2016; Rumelhart et al., 1986) dynamic reconfiguration of synaptic weights, functional connectivity, engrams, neuronal representation, spike sequences (Nadasdy, Hirase, Czurkó, et al., 1999), replay (Skaggs & McNaughton, 1996), balanced inhibition-excitation (Softky & Koch, 1993; van Vreeswijk & Sompolinsky, 1996), circuitry, mesoscopic brain dynamics (Freeman, 2000), oscillatory network, attractor dynamics (Amit, 1989), dimensionality reduction (Pang et al., 2016) and manifolds (Mitchell-Heggs et al., 2023). The above list is also the core vocabulary of current computational neuroscience

and the indispensable cheat sheet for anyone trying to navigate the early 21st-century cognitive neuroscience zeitgeist.

Figure numbering:

Figures referenced as “Fig. D1, D2,…, D6” refer to graphical illustrations in the dissertation. In contrast, “Fig. 1, Fig. 2, … Fig. 8” refer to figures of the related papers.

Disclaimer:

All graphical illustrations and figures in the rest of the dissertation are my original figures and have not been published elsewhere.

Introduction

"Until not many years ago, the "existence" of a mind or soul would have been passionately denied by most physical scientists. ... There are [however] several reasons for the return, on the part of most physical scientists, to the Spirit of Descartes' "Cogito ergo sum" .... When the province of physical theory was extended to encompass microscopic phenomena, through the creation of quantum mechanics, the concept of consciousness came to the fore again: it was not possible to formulate the laws of quantum mechanics in a consistent way without reference to consciousness."

(Eugene Wigner, 1961)

Nothing was further from Wigner's science philosophy than panpsychism. It's rather the opposite. He proposed that physical measurements involve the "conscious perception" of a human observer. He did not use the term information, but when "measurement" becomes data and data becomes information, that information does not exist outside the brain. It must be born in the brain. How information is created in the brain is the subject of this dissertation.

Our brain is specialized for information processing, but there is no consensus among neuro- or cognitive scientists on the main driving force of the evolution of the nervous system. Many may think of "adaptation to the environment." However, adaptation to the same environment produced different phenotypes, each equally fitting. Others think of the efficacy of information processing or the reduction of free energy (Friston, 2010). But information processing is just as efficient in the nervous system of jellyfish as in the human brain. Could it be a "more precise representation of the world"? Donald Hoffman argues with examples that evolution has nothing to do with improving the physical precision of our senses or the accuracy of neuronal representations of our environment (Hoffman, 2019). What about "predicting the future"? Humans championed that, and predictive coding is one cornerstone of Friston's free-energy principle (Friston, 2010; Rao & Ballard, 1999). To predict the future, the nervous system, as an agent[1], must discriminate between the environment's constant and variable features.

The variable parts often exhibit specific rules. The agent with the nervous system must also be able to separate its behavioral impact from the state of the environment to capture the constant invariable aspects of it. Let's call this the detection of *invariances*. We argue that the nervous system evolved partly under the pressure of *extracting invariances* because those invariances

[1] Agent means the organism is able to interact with the environment through the motor system by locomotion or by using actuators, limbs, tentacles, or antennae.

are keys for building stable neuronal representations of the surrounding space. In psychology, we group those invariances as "*constancies*," such as color constancy and size constancy, all are crucial parts of object permanence. These examples illustrate that the physical feature may change with the context (illumination, viewing angle, appearance), but the biologically relevant features of objects (identity, material, spatial position) remain constant. The invariances that our brain can capture among the astronomical number of descriptive feature combinations must be reflected by consistent patterns of neuronal activity in the brain, called "sequences." There seems to be no alternative to that principle. Hence, we naturally arrive at the question. Whether ***the observable invariant activity patterns "inside" are the*** *mere* ***imprints of permanent features "outside" or those apparent permanent features "outside" are projections of the recurring, hence invariant, activity patterns "inside?"*** Although this question is beyond the scope of this dissertation, it will reverberate through the chapters, and by the end, the reader may correctly guess my ambiguous answer of "***both***."

The quest for understanding the neuronal underpinning of thoughts, concepts, representations, intentions, emotions, and behavior is a daunting challenge, which requires an interdisciplinary approach including psychology, neuroscience, cognitive science, medicine, computer science, medicine, linguistics, various subfields of physics, mathematics, molecular biology, evolutionary biology, and genetics. My research was a continuous strive to resolve the fundamental dilemma of modern-day dualism (Eccles, 1994), seeking key neuronal mechanisms underlying the formation of mental representations. The task has been to define the most basic meaningful entity above the level of neurons. More specifically, determine the patterns that embody *information* and enable the separation of it from the biological medium by unlocking the mechanism to generate memories, concepts, emotions, imagery, symbols, intentions, feeling of agency, and predictions of the future states of the world around, fundamental constituents of consciousness. In this dissertation, I review the pursuit of the enigma of "*engrams"* through my research, motivated by the idea that stable representations can be created by the collective dynamics of neuronal activity above the level of individual neurons, the hallmark of *synergy* (Haken, 1983). I will cover this in 5 chapters and three steps.

(1) First, we hypothesize that *multi-neuronal firing patterns* serve as the first meaningful level of cognition in the hierarchy of patterns, representations, concepts, narratives, and theorems that comprise the "language" of cognition (Fig. D1).

(2) Second, based on empirical evidence, we will argue that this level does not depend on the invariable contribution of individual neurons (Chapters 1-4).

(3) Finally, we prove the above hypothesis (1) by demonstrating that exists a metric of neuronal activity that can more accurately predict the behavior of the agent than the firing rate. We show that applying Bayesian decoding on spike phases can recover the allocentric position. This metric (the phase of spiking activity) can localize oneself in space, regardless of whether the brain uses it (Chapter 5).

In this dissertation, I summarize my endeavor of finding the meaning of these patterns in neuronal communication and the mechanism that generates them.

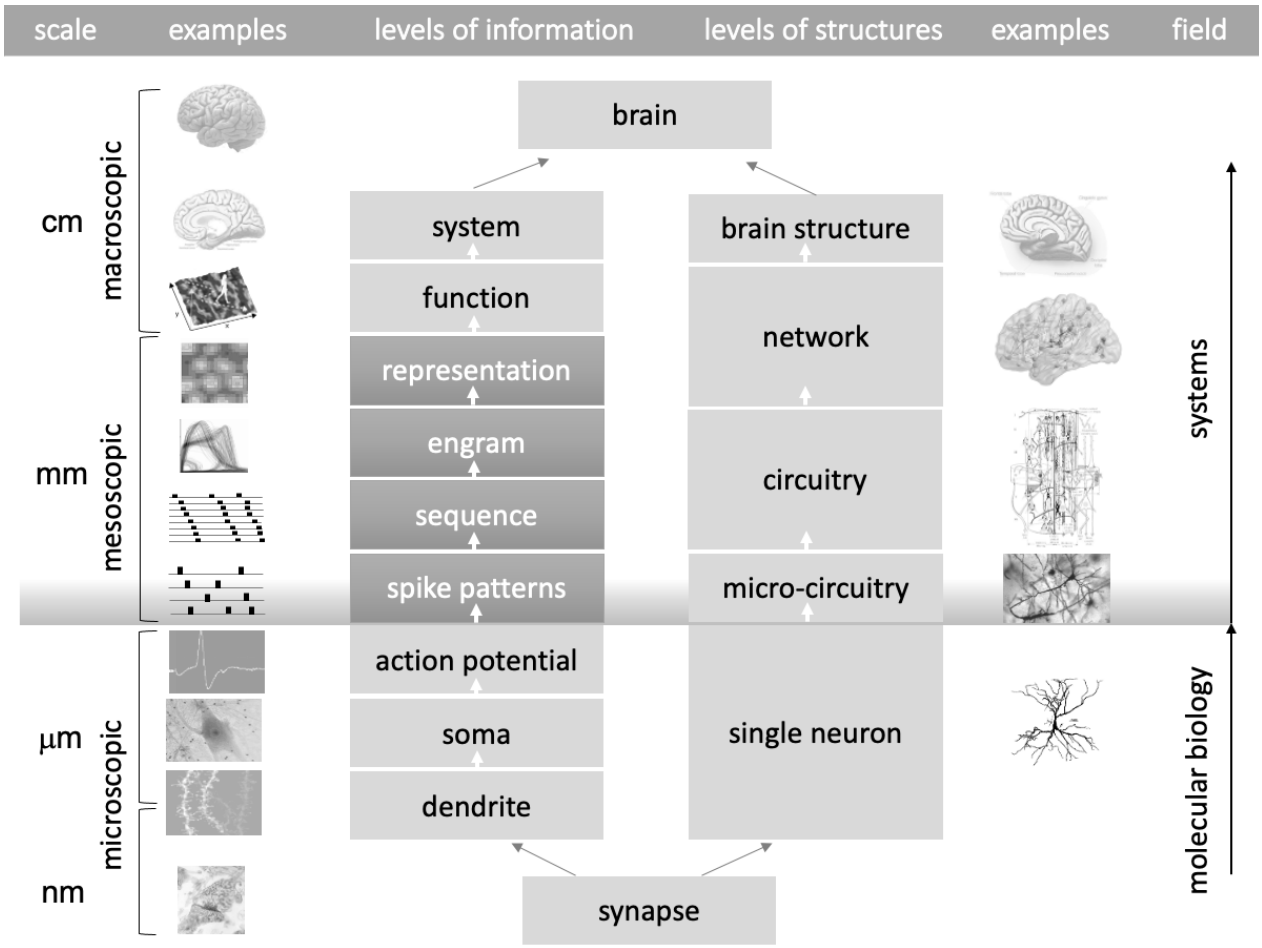

Figure D1. The levels of information generation in the brain. The two middle panel represent the levels of signal (on the left) and levels of structural (on the right) complexity. We posit that at the level between the single neuron and micro-circuitry where action potentials self-organize themselves into spike patterns and sequences is where information separates from the biological medium and fundamentally different laws take control. The laws of computation and mathematics.

Chapter 1

6. Sequences of spikes: what makes them, and what do they do?

> *"I can now return to the digital character of this mechanism. The nervous pulses can clearly be viewed as (two-valued) markers, in the sense discussed previously: the absence of a pulse then represents one value (say, the binary digit 0), and the presence of one represents the other (say, the binary digit 1). This must, of course, be interpreted as an occurrence on a specific axon (or, rather, on all the axons of a specific neuron), and possibly in a specific time relation to other events. It is, then, to be interpreted as a marker (a binary digit 0 or 1) in a specific, logical role."*
>
> *Furthermore, "... This is clearly the description of the functioning of an organ in a digital machine, and of the way in which the role and function of a digital organ has to be characterized. It therefore justifies the original assertion, that the nervous system has a prima facie digital character."*
>
> *(Von Neumann, 1958)*

In his unfinished book *"The Computer and the Brain,"* John von Neumann drew a parallel between computers and the nervous system (Von Neumann, 1958). He capitalized on brains' advantages in energy dissipation, size, and parallel computation and disadvantages in speed, while also pointing out the similarities, among which was the digital nature of computation.

Neumann emphasized "prima facie," as it was mounting evidence suggesting the digital nature, and he was right. One of the fundamental features of neural computation is the binary nature of action potentials, acknowledged since Sherrington (Sherrington, 1906) and predominates all models of the nervous system. However, a Polish physiologist, Adolf Beck, revealed another aspect of neuronal activity in 1890 (Coenen et al., 2014), followed by Hans Berger and his invention, the electroencephalograph or EEG (Berger, 1929). The EEG unraveled the importance of continuous oscillations in the brain. The most prominent oscillations, classified as delta, theta, alpha, beta, and gamma, appeared to correlate with behavioral states from sleep, dream, drowsiness, and active awake and attentive state, respectively. While these oscillations were evident from the scalp electrodes of EEG, the same oscillation frequencies were also discernible in vivo in animal preparations by recording almost anywhere inside the brain. The oscillations that we can discriminate from surface EEG were also recognized in the local field potentials (LFP) recorded from inside the neuronal tissue extracellularly as well as intracellularly as subthreshold membrane oscillations. It is reasonable to assume that the sources of oscillations observed in the scalp EEG are, at least partly, associated with the sum of cellular-level subthreshold oscillations expressed at a macroscopic scale due to population-

wide synchrony. Alternatively, the most widely shared assumption relates LFP to the synaptic input or the phasic modulation of postsynaptic potentials (Logothetis, 2003; Mitzdorf, 1987). We must add the two hypotheses, the subthreshold potential origin and the synaptic origin, are not mutually exclusive.

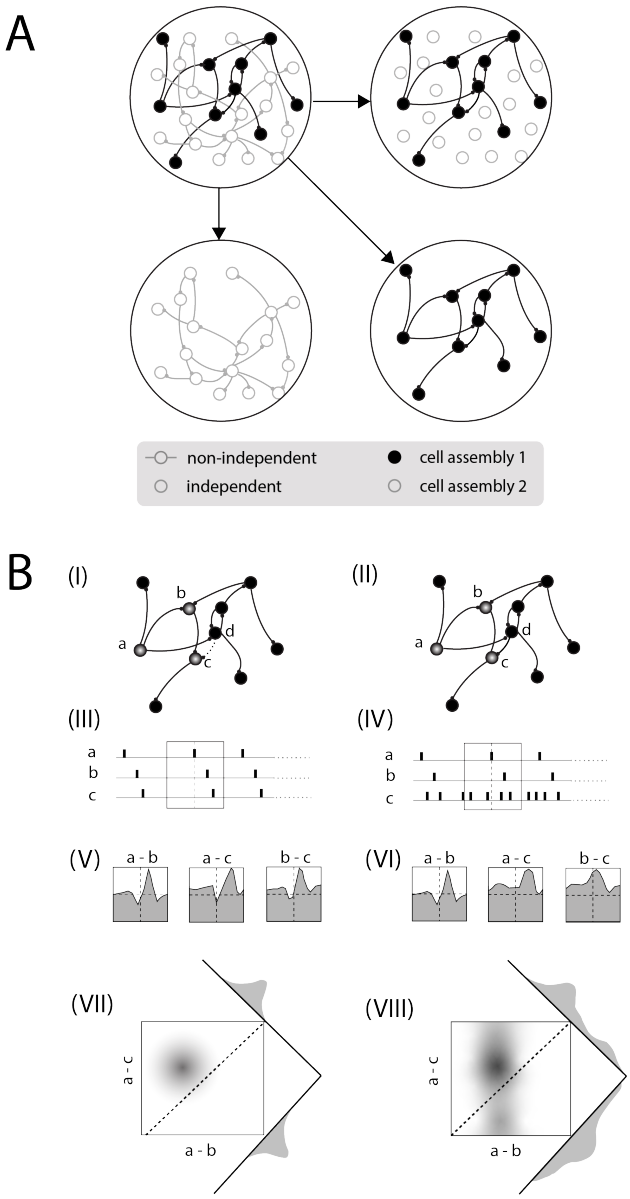

Figure D2: Functional connectivity inferred from the independence vs. non-independence of neurons. (A) Two functional cell-assemblies superimposed (filled and open circles). Both contain cells that are connected and mutually dependent, but the two assemblies are independent from one another (no connections between them). The task is to separate the two cell-assemblies based on their activities (bottom). Small buttons represent synaptic connections. (B) Network dynamics depends on the functional connectivity: (I) A subnetwork of neurons *a* → *b* → *c* generates a recurring "*a-b-c"* spike sequence (III) with a constant delay between spikes. (II) Changing a connection by adding d→c opens *c* for influences outside of the *a* → *b* → *c* circuitry. (IV) As a result, *c* will be active independently from *a* and *b* neurons. The connectivity change affects spike pattern as well as the cross-correlations in a subtle fashion by adding an extra bump to a-c and b-c cross-correlograms (V-VI). In contrast, the three-fold joint-peri-stimulus-time histogram (JPSTH) reveals the impact of the new connection on the dynamics in an explicit fashion (VII-VIII).

Action potentials and subthreshold membrane oscillations represent a combination of digital and analog modes of operation in the brain, respectively. Both are essential for information processing in the brain. If we experimentally abolish action potentials by a Na+ channel blocker, such as tetrodotoxin (TTX), the neuron stops relaying messages to the postsynaptic neurons (Narahashi, 2008). On the other hand, if we reduce the oscillations by

tetraethylammonium (TEA), the timing of action potentials becomes seriously affected (Desmaisons et al., 1999; Engel et al., 2008; C. J. Wilson et al., 2018). The information transfer depends on the interaction between the spikes and the resonant membrane properties expressed as the fluctuation of subthreshold membrane potential, and we will unravel how through a list of articles.

My earliest paper addressing the temporal organization of action potentials was focused on spike sequences (Nadasdy et al., 1999; Z Nadasdy et al., 1998). We defined spike sequences as the temporal pattern of a small number of action potentials ($2 < n < 20$) generated by more than two neurons repeating the order of firing $m > 1$ times. To understand the underlying neural computation, we need to outline a group of cells in which the neurons are non-independent of one another and separate it from another group of cells in which the neurons are independent of one another (Fig. D2 A), or they may be dependent of each other within the group but independent of the former group (Fig. D2 B). This classification is consistent with Hebb's concept of "*cell assembly*," defined as a temporary coalition of neurons engaged in a synchronized or "reverberating" activity (Hebb, 2005). Hebb was intentionally vague about what a coalition represents. Was it the neurons, groups, or areas? The dependency of the neuronal states (firing, not firing) on other neurons within the assembly might distinguish an assembly from other networks. Therefore, the first method developed to identify this type of dependency was the cross-correlation method introduced by Moore et al. (Moore et al., 1970; Perkel et al., 1967a, 1967b). However, the cross-correlation method had many limitations, most notably the failure to detect higher-order dependency between more than two neurons. Regardless of how one breaks all pairwise cross-correlations down into a large (n * (n-1) / 2) matrix of pairwise cross-correlations, the higher-order correlations remain obscured (Fig. D2 B) unless we use joint-peristimulus-time-histograms (JPSTH) for visualization of second order cross-correlations. Looking at the multi-neuronal activity through the aperture of pairwise cross-correlations is like listening to Bach's Toccata and Fugue in D minor after silencing all but two organ pipes. Would that be the same musical experience as with all the organ pipes sounding? Probably not. Obviously, we are interested in "listening to the whole melody" of multiple neurons as it unfolds and repeats like the verse and the refrain as signatures of a cell assembly.

Despite its limitations, the cross-correlation method made a big splash in the field when Wilson and McNaughton demonstrated the reactivation of ensemble activity during sleep following

exploratory behavior in rats (M. A. Wilson & McNaughton, 1994). Cross-correlation also played a key role in the subsequent paper by Skaggs and McNaughton that defined firing sequences (Skaggs & McNaughton, 1996), even if calling two spikes a 'sequence' is arguably a bit of stretch.

At the same time, when those two high-impact papers were published, I was working on generalizing the cross-correlation method to higher-order correlations under György Buzsáki's supervision at Rutgers University. We collected the same type of datasets from multiple single-cell rat electrophysiology as the above studies, except we did not map the spatial activity of the neurons. Our experiment consisted of three parts: (1) first sleep, (2) a subsequent active awake behavior (running in the wheel), followed by (3) a second sleep (Nadasdy, Hirase, Czurkó, et al., 1999). Let's call this the S1-R-S2 paradigm. After establishing three conditions: (i) using silicon multiprobes, (ii) reliable spike sorting, (iii) and robust behavioral paradigm with stereotypical behavior (S1-R-S2), we were able to analyze the simultaneous activity of the same neuronal ensemble of 3-8 neurons under different behavioral conditions. For spike sorting, I introduced a multielectrode projection method, and I applied mean-field to resolve the neuronal sources relative to the geometry of the Michigan probes (Nadasdy et al., 1998). In addition, I developed a pattern-searching algorithm based on template matching that was defined by the combination of neurons co-firing within a 200 ms time window. The algorithm exhaustively matched the template with all the neuronal activity patterns within the critical time window. The method effectively extracted a rich collection of patterns that finally met the definition of "sequences" because they represented higher than first- or second-order correlations. The extracted sequences often captured patterns generated by 4-8 neurons (Nadasdy, 2000). Detecting sequences was the easy part. The more laborious part was to prove that these sequences were not a result of a by-chance process. To do that, I applied two methods: One to validate the higher order cross-correlations (a-b-c-d) by a three-fold cross-correlation of the (a-b-c) triplets. Here, I introduced a template-based pattern-searching algorithm for the task in many respects similar to the problem of gene sequencing (Nadasdy, Hirase, Czurkó, et al., 1999). Found only later that the method was similar to the one published earlier by Legéndy and Salcman (Legéndy & Salcman, 1985). The other method was to generate surrogate datasets by shuffling the inter-spike-intervals (ISI), the cellular identity, or theta field coherence. These manipulations altered different aspects of the original spike train leaving other features intact. (For instance, ISI shuffling leaves the firing rate unchanged but alters spike times.) After generating thousands of surrogate datasets, I ran the shuffling tests

day and night for two weeks per session on supercomputers. In the paper, I show through examples (Fig. 5 E, 6) and statistics that such sequences are improbable to be the results of a by-chance process (Nadasdy, Hirase, Czurkó, et al., 1999). Instead, they reflect the coordinated activity of a group of neurons, supporting Hebb's definition of a cell assembly. These simulations with surrogate spike trains served as indispensable steps in validating the neuronal sequences. Still, they should not steal the spotlight from the four main findings we outlined in that paper:

1. Recurring spike sequences involving four and more neurons in the rat hippocampus were detected.
2. They emerged during active exploratory behavior and were replayed during subsequent sleep.
3. The spike patterns recurred with 4-5 x compression during sharp wave activity.
4. Sequences aligned with theta during the awake state while aligned with ripples during slow-wave sleep.

The paper was the first rigorous demonstration that, beyond the level of single action potentials, exists a deterministic process that generates precisely coordinated spatiotemporal constellations of spikes. I capitalize on "deterministic" because all point-process models describing spike process before these studies postulated that neuronal firing is a stochastic process where only the probability of firing can be determined and neither the timing nor the order of spikes followed a deterministic rule (Shadlen & Newsome, 1994) (Georgopoulos et al., 1986). The dogma of stochastic firing has predominated the literature on neural coding for 40 years as a legacy of Adrian (Adrian, 1954), even though Adrian has never argued that the control of firing rate is a stochastic process. The alternative idea, the precise coordination of action potentials across neurons, areas, and time intervals, was proposed by George Gerstein and colleagues (Perkel et al., 1967a, 1967b), all of them recording cortical neurons in rats and primates (Abeles & Gat, 2001; Diesmann et al., 1999; Shmiel et al., 2006). It was unexpected that the most substantial supporting evidence base for higher-order correlations and cell assemblies derived from the hippocampus (Harris et al., 2003; Nadasdy, Hirase, Czurko, et al., 1999; Skaggs & McNaughton, 1996; M. A. Wilson & McNaughton, 1994), which forced to revise the statistical approach of cortical dynamics. The resistance to embracing the idea of precise temporal patterns beyond the firing rate statistics is still relatively strong. Statistical

models of modulated Poisson spike processes and Gaussian or cosine tuning curves are still dominating the field, and they are taken as evidence for stochastic processes, despite neither Poisson nor Gaussian or cosine tuning curves implying random underlying processes.

The take-home message of the paper on “sequences” were as follows:

1. Recurring spike sequences involving four and more neurons were found: Regardless of shifting the viewpoint on spike processes, a new model of memory encoding and the neuronal underpinning of the concept of “engrams” emerged. The new model was consistent with Hebb’s prediction of cell assembly, which postulated that coalitions of neurons can be formed dynamically under functional or task constraints. These coalitions can emerge and dissolve, and new coalitions self-organize from the same pool of neurons to contribute to different functions by synchronizing other groups of neurons. This mechanism would unlock the capacity of the network of neurons beyond what was thought earlier because it enables information to be superimposed and multiplexed over the same network, a principle that enhances memory storage, reduces disruptive interference, and improves retrieval efficacy.
2. Sequences emerge during active exploratory behavior and are replayed during subsequent sleep: Sleep has long been considered a process of memory consolidation (Buzsaki, 1989; Fosse et al., 2003; Wamsley & Stickgold, 2011). The paradigm of recording neuronal ensemble activity during three successive stages (S1-R-S2) has become a standard design. While many studies focused only on the awake-to-sleep comparison, the correct comparison is S1-to-awake and S2-to-awake because we only expect spike pattern replay from awake to S2 and not from awake to S1 (backward causation). In other words, the awake exploratory experience cannot be accounted for patterns already present in the first sleep.
3. The spike patterns recur with 4-5 x compression during sharp wave activity: The compression of spike patterns is necessary to associate the spike patterns expressed during theta with the spike patterns observed during sharp wave ripples (SWR) as the time scales of the two types of events are quite different. The duration of one theta cycle is typically 140-250 ms, while a single SPW ripple is rectified within 50 ms. The other factor is the firing rate. During exploratory behavior, the average firing rate of pyramidal cells is less than 10 spike/s in contrast with the 40-100 spike/s rate during the short period of SWRs. The fraction of spike patterns recurring with the highest rate

spans over 1 or 2 theta cycles and aligns with the gamma oscillation phases (1-15 gamma cycles). If we rescale these gamma cycles to match the scale of SWR, the gamma bouts with spikes in them will co-register with the ripple time slots. Hence the spike patterns during theta are reflected by the spike sequences observed during SWRs. The scaling factor is about 4-5 x, meaning that the predominant spike patterns observed during theta are replayed in a compressed fashion during SPW within a 4-5 times shorter time window. The 4-5 x is the same as the time scale difference between a theta cycle and a sharp wave event and the scaling factor between the gamma rhythm and the high-frequency ripples. The precise phase-locking between gamma oscillations and spikes was demonstrated more than 20 years later in my 2022 article (Nadasdy et al., 2022).

4. Sequences tend to align with theta during the awake state, while they align with the ripples of sharp waves during slow-wave sleep: This is a key point of the paper and has far-reaching implications. Together with other papers, it fertilized a whole new lineage of research investigating the conspicuous relationship between theta-embedded spikes and sequences of spikes replayed during sharp waves, including forward and reverse replays (Diba & Buzsáki, 2007; Nadasdy, Hirase, Czurkó, et al., 1999).

This paper consolidated spike-field coherence in theta phase precession (O'Keefe & Recce, 1993) with the sequence replay (Skaggs & McNaughton, 1996; M. A. Wilson & McNaughton, 1994) as the mechanism for memory consolidation and facilitated the conceptual shift of integrating binary spike processes with continuous local field potentials (Nadasdy, Hirase, Czurkó, et al., 1999). While this conceptual shift was evident in hippocampal electrophysiology by the late '90s, it remained unorthodox in the primate cortical and sensory electrophysiology until 2010.

The Journal of Neuroscience, November 1, 1999, *19*(21):9497–9507

Replay and Time Compression of Recurring Spike Sequences in the Hippocampus

Zoltán Nádasdy, Hajime Hirase, András Czurkó, Jozsef Csicsvari, and György Buzsáki

Center for Molecular and Behavioral Neuroscience, Rutgers, The State University of New Jersey, Newark, New Jersey 07102

Information in neuronal networks may be represented by the spatiotemporal patterns of spikes. Here we examined the temporal coordination of pyramidal cell spikes in the rat hippocampus during slow-wave sleep. In addition, rats were trained to run in a defined position in space (running wheel) to activate a selected group of pyramidal cells. A template-matching method and a joint probability map method were used for sequence search. Repeating spike sequences in excess of chance occurrence were examined by comparing the number of repeating sequences in the original spike trains and in surrogate trains after Monte Carlo shuffling of the spikes. Four different shuffling procedures were used to control for the population dynamics of hippocampal neurons. Repeating spike sequences in the recorded cell assemblies were present in both the awake and sleeping animal in excess of what might be predicted by random variations. Spike sequences observed during wheel running were "replayed" at a faster timescale during single sharp-wave bursts of slow-wave sleep. We hypothesize that the endogenously expressed spike sequences during sleep reflect reactivation of the circuitry modified by previous experience. Reactivation of acquired sequences may serve to consolidate information.

Key words: sharp waves; θ; memory; coding; decoding; retrieval; network; sleep

Although it is a widely accepted notion that information is distributed in cell assemblies rather than encoded by single cells, the nature of coding in cell assembly has remained a major challenge for neuroscience research. Several explanations have been proposed on theoretical grounds, including frequency coding (Sherrington, 1906; Eccles, 1957; Barlow, 1972; Georgopoulos et al., 1982), temporal coincidence coding (von der Malsburg and Bienenstock, 1986; Singer, 1993), temporal delay of spikes (O'Keefe and Recce, 1993; Buzsáki and Chrobak, 1995; Hopfield, 1995; Lisman and Idiart, 1995; Skaggs et al., 1996), and spatiotemporal spike sequence coding (Buzsáki, 1989; Abeles, 1991). If spatiotemporal patterns of neural activities serve to code and/or decode information, one could look for evidence in the temporal structure of activity within neuronal ensembles. Temporal coordination of spike sequences, in relation to stimulus presentation, has been described in various invertebrate (Dayhoff and Gerstein, 1983; Laurent et al., 1996; Marder and Calabrese, 1996) and vertebrate (Strehler and Lestienne, 1986; Ts'o et al., 1986; Vaadia and Abeles, 1987; Eckhorn et al., 1988; Gray and Singer, 1989; Frostig et al., 1990b; Aertsen et al., 1991; Abeles et al., 1993; Riehle et al., 1997) brains.

Because hippocampal pyramidal neurons discharge selectively at certain spatial locations ["place" cells (O'Keefe and Nadel, 1978)], it is expected that they are activated sequentially while the animal moves about in a structured environment (Wilson and McNaughton, 1994; Skaggs and McNaughton, 1996; Brown et al., 1998; Zhang et al., 1998). During sleep, on the other hand, there is no external perceptual reference or motor behavior to drive hippocampal cells. Therefore, if recurring spike sequences are present during sleep, they are likely to be internally generated. In a previous study, Pavlides and Winson (1989) examined pairs of putative pyramidal cells recorded by the same single wire. When one of the neurons in the pair was activated by confining the rat to the spatial field of the unit, the firing rate of the neuron during the subsequent sleep epoch increased relative to that of its pair. A more recent study, however, failed to confirm the relationship between firing rates in the awake and sleeping rat (Wilson and McNaughton, 1994). On the other hand, neuron pairs, which represented similar parts of the environment in the awake rat and therefore fired together during exploration, showed an increased correlation in their firing during the subsequent slow-wave sleep episode compared with the preceding sleep episode (Wilson and McNaughton, 1994; Skaggs and McNaughton, 1996). Pairwise cross-correlograms, however, are not sufficient to analyze the exact temporal structure of more than two cells (Hampson et al., 1996; McNaughton et al., 1996; Moore et al., 1996; Quirk and Wilson, 1998).

Here we examined the spatiotemporal firing patterns of hippocampal CA1 principal neurons in awake and sleeping rats. Spatiotemporal sequences of spike patterns were detected either by a template-matching method or by the joint probability mapping of spikes. The results indicate that repeating spike sequences are present in both the awake and sleeping animal in excess of what is predicted by random coincidences. Furthermore, the spike sequences observed in the behaving rat were "replayed" at a faster timescale during sharp-wave bursts of slow-wave sleep.

Parts of this paper have been published previously (Nadasdy et al., 1996, 1997, 1998).

Received May 24, 1999; revised Aug. 13, 1999; accepted Aug. 16, 1999.

This work was supported by National Institutes of Health Grants NS34994 and MH54671 and by the Human Science Frontier Program. We thank Moshe Abeles, Michale Fee, Stuart Geman, Stephen Hanson, Darrell Henze, Günther Palm, Michael Recce, and Matthew Wilson for their suggestions with data analysis and comments on this manuscript.

Correspondence should be addressed to Dr. György Buzsáki, Center for Molecular and Behavioral Neuroscience, Rutgers University, 197 University Avenue, Newark, NJ 07102. E-mail: buzsaki@axon.rutgers.edu.

Dr. Nádasdy's present address: Department of Physiology, The Hebrew University of Jerusalem, Jerusalem, 91120 Israel.

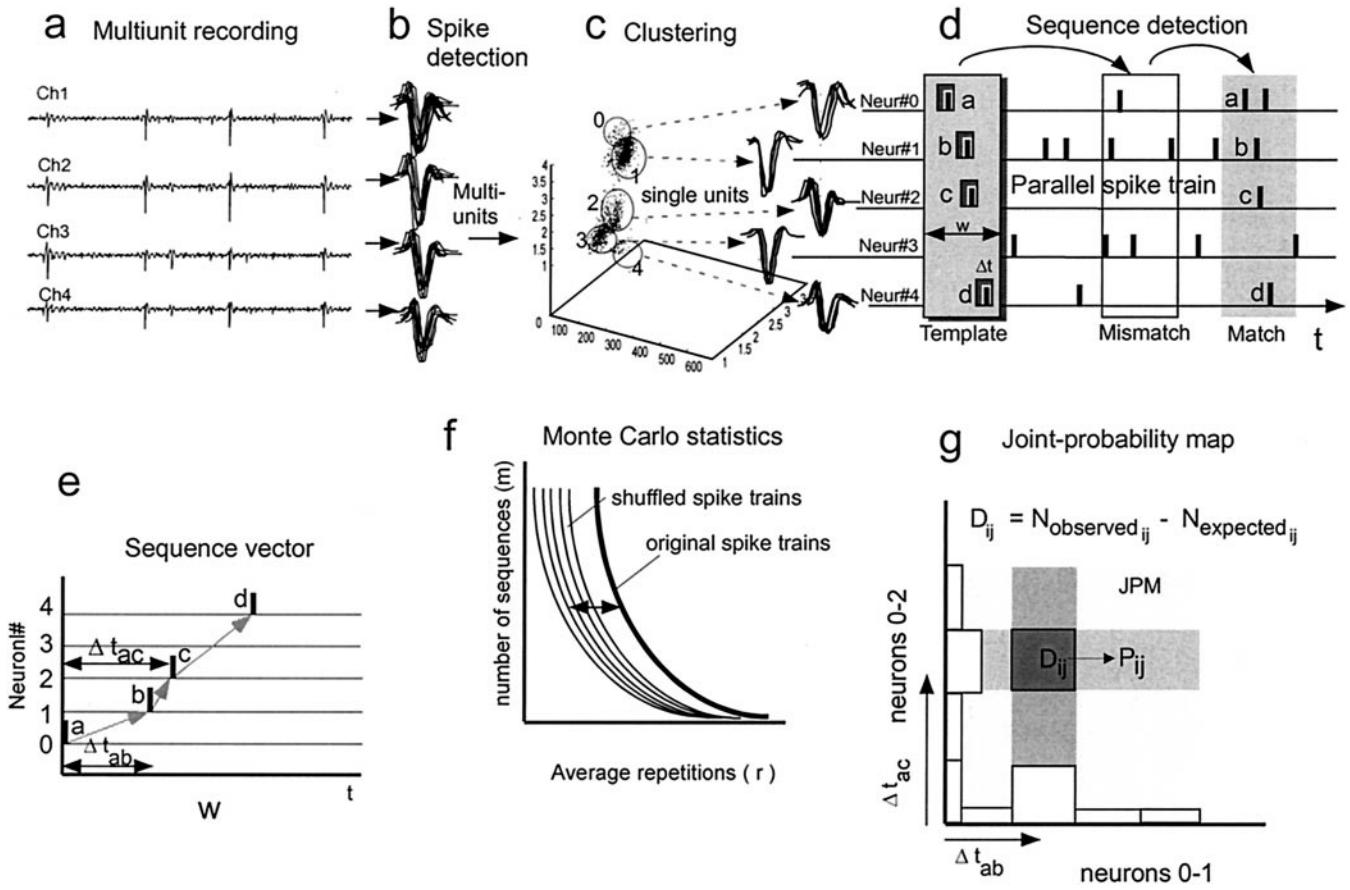

Figure 1. Spike sequence extraction methods. *Panel a,* Unit activity was recorded simultaneously from multiple tetrodes. Filtered recordings from a single tetrode are shown (*Ch1–Ch4*). *Panel c*, Spike sorting resulted in 4–8 neurons/tetrode. *Panel b*, Superimposed waveforms of a single cell are shown. *Panel d,* The parallel spike train (*vertical tics*; cells 0–4) was analyzed by a sequence-search algorithm for repeating spike sequences. All possible sequences were considered as a template. The duration of the template window (*w*) was typically 200 msec. The tolerance of spike match (spike window; d*t*) was 10 or 20 msec. *Neur*, Neuron. *Panel e*, Spike sequences of neurons *a–d* are represented as spatiotemporal vectors. For graphical illustrations, repeating sequences are superimposed in subsequent figures. *Panel f*, The significance of sequence repetition was tested by Monte Carlo statistics. *Panel g*, Spike triplets were also detected by the JPM method. The distribution of spike triplets (*a*, *b*, *c*; Δt_{ab}, Δt_{ac}) within the *w* time window was investigated by constructing a joint peri-event time histogram. A difference map (D_{ij}) was created by subtracting chance combinations, as predicted by the corresponding spike doublets, from the joint peri-event time histogram. The pixels of the difference map (JPM) represent the probability of observing a given triplet.

MATERIALS AND METHODS

The surgical procedures, electrode implantation, and spike sorting have been described in detail previously (Csicsvari et al., 1999). Briefly, wire tetrodes or silicon electrode arrays were implanted in the CA1 pyramidal layer of 18 Sprague Dawley rats. Electrical activity was recorded while the rat was in its home cage followed by exploration. Six rats were trained to run in a wheel for a water reward (Czurko et al., 1999). The apparatus was a 30 × 40 × 35 cm box with a glass front wall. The running wheel (10 cm wide; 29.5 cm in diameter) was attached to the side of the box. A drinking tube protruded from the back wall of the box 5 cm above the floor. Five to 20 turns of the wheel triggered an acoustic "go" signal, which indicated the availability of the water reward (Czurko et al., 1999). After the task is learned, the behavior is stereotypic: running in the wheel, approaching the waterspout, drinking, and returning to the wheel. In the trained rats, electrical activity was recorded during sleep in the home cage (session 1), followed by wheel running in an identical wheel-running apparatus but in a different spatial location of the room (session 2) and a second recording session during sleep (session 3). Units were separated on the basis of their spike amplitude and waveform using principal component analysis and spatial clustering (Wilson and McNaughton, 1994; Nádasdy et al., 1998; Csicsvari et al., 1999). Only pyramidal cells with clear cluster boundaries and >2 msec refractory periods were included in the analyses (Fig. 1). For the extraction of sharp-wave (SPW) ripple events during sleep, the wide-band recorded data were bandpass filtered digitally (150–250 Hz). The power (root mean square) of the filtered signal was calculated, and the beginning, peak, and end of individual ripple episodes were determined. The threshold for ripple detection was set to 7 SDs above the background mean power (Csicsvari et al., 1999). θ epochs were detected by calculating the ratio of the θ (5–10 Hz) and δ (2–4 Hz) frequency bands in 2.0 sec windows. A Hamming window was used during the power spectra calculations.

Neuronal spike times of simultaneously recorded neurons are referred to as the "parallel spike train." For the detection of invariant temporal structures of spikes from parallel spike trains, two different methods were used: (1) the template-matching method and (2) the joint probability map method. Complex-spike bursts [<6 msec interspike intervals (Ranck, 1973)] were regarded as single events, represented by the time of the first spike.

The template-matching method

The template-matching method was a modified version of the "sliding-sweeps" algorithm introduced by Gerstein and colleagues (Dayhoff and Gerstein, 1983; Abeles and Gerstein, 1988; Frostig et al., 1990a). The search for repeating spike sequences was performed within a specific time window, denoted as the template window *w* (Fig. 1*d*). The 0 point of a *w* time window was assigned to a spike of the selected reference neuron. The temporal positions of *c* spikes, detected from the spike train, within the *w* time window were considered as a template. The *T* template was represented by a temporal vector of *p* neurons and *t* spike positions relative to the $t_{(0)}$ reference spike and the $c - 1$ co-occurring spikes from

the other spike trains: $T = (p_i; t_j)$. Here $p$denotes the different cells as $p = (p_i, \ldots, p_n)$, where n is the number of parallel-recorded cells, and $t = (\Delta t_j, \ldots, \Delta t_{c-1})$ denotes the corresponding intervals between the initial spike and subsequent spikes where $\Delta t_{c-1} \leq w$. Next, the template was shifted to successive spikes of the reference neuron throughout the recording session, and recurrences of the T template were counted. During the search, each spike sequence was considered as an exemplar and compared with the T template sequence. A match between the template and the exemplar was counted when spikes occurred within a predetermined time window dT (or spike jitter; Fig. 1*d*). The spike time window (dT) was set at 10 or 20 msec in most searches because in preliminary experiments the best separation between the real spike train and shuffled spike trains was observed using 10–20 msec spike windows (dT was varied between 2.5 and 20 msec; $n = 2$ rats). In each search, the template window (w) and the spike window (dT) were set by the experimenter. The template window was typically set to 200 msec (Fig. 1*d*). The dependent variables of the search were the number of spikes in a given template (sequence complexity), the number of different sequences (m), and the number of repetitions of a given sequence (r). During the search, every spike was considered as a part of a template sequence of c complexity, each template occurred at least once, and the entire spike train was searched exhaustively by templates. The sequences were visualized as temporal vectors (Fig. 1*e*).

The statistical significance of the observed repetition of spike sequences was assessed by comparing the repetition of the original sequences (r_{orig}) with the repetition of the pseudorandom sequences (r_{rnd}) generated by spike shuffling. The null hypothesis was that the statistical distribution of r_{orig} is equal to that of r_{rnd}. We reasoned that if r_{rnd} of every possible sequence in 100 simulated spike trains is smaller than the r_{orig}, the null hypothesis can be rejected with $p < 0.01$ probability (Fig. 1*f*). In these comparisons, we assumed that in a shuffled parallel spike train with the same first-order statistics (firing rate and population covariance) as the original spike train, the number of repeating spike sequences should reflect chance occurrences. Spike shuffling thus served to eliminate the temporal correlation generated by an assumed biological mechanism. Four randomization procedures were applied.

Within-spike-train random shuffling. Interspike intervals, derived from the original spike trains, were exchanged between two pseudorandomly selected positions from the first to the last interspike interval, and this procedure was iterated (Fig. 2*b*). Within-spike-train shuffling preserves the average firing rates of individual cells. However, it can eliminate population synchrony among the simultaneously recorded spike trains, present during θ and sharp-wave patterns.

Temporal displacement of spikes. This procedure is similar, in principle, to the within-spike-train shuffling. However, in this procedure spikes were displaced temporally by adding a pseudorandom interval from 0 to 50 msec. This range was used because this temporal displacement was small enough to preserve population synchrony during both θ and sharp waves (Fig. 2*c*).

Across-spike-train shuffling. Each spike of the spike trains was assigned to a pseudorandomly selected cell (Fig. 2*d*). As a result, the population level modulation of the firing rate in the surrogate spike trains remained the same as in the original spike train. A caveat of this procedure is that the differences in discharge frequencies of individual spike trains, which may be present in the original spike trains, are reduced as a result of spike shuffling across trains.

θ phase-invariant shuffling. This procedure preserved the periodic modulation of discharge frequency both within and across the spike trains (see Fig. 5*a*). First, the peaks of the field θ waves were identified. Second, the spike times were converted to phases of the θ cycle (Csicsvari et al., 1999). Third, the phase-encoded spikes within a given θ cycle were exchanged with other pseudorandomly selected cycles within the same spike train.

Joint probability map method

Repeating spike triplets were detected by the joint peri-event time histogram method (JPTH) (Aertsen et al., 1989). The construction of a joint peri-event time histogram was restricted to spike triplets co-occurring within a w time window. The histogram displayed the repetition of the same triplet at all interspike intervals. First, all possible $n!/(n-3)!$ variations of temporal orders of triplets were determined, where n is the number of parallel spike trains. All triplets $T = (p_1, p_2, p_3; \Delta t_1, \Delta t_2)$ with $\Delta t_1 < \Delta t_2$ and $w \geq \Delta t_2$ were registered and represented as pixels in a two-dimensional coordinate system at Δt_1 and Δt_2 as x and y coordinates, respectively. For the estimation of the spurious occurrence

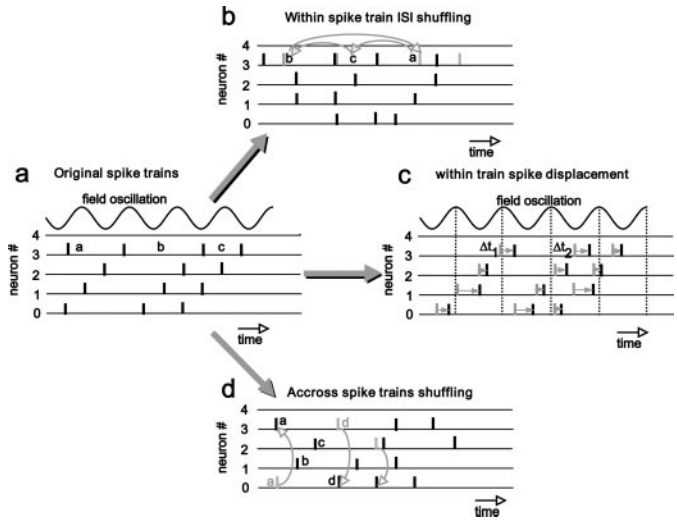

Figure 2. Spike-shuffling methods. *Panel a,* Original parallel spike train. Three repetitions of the same spike sequence (0, 1, 2, 3) are shown. *Panel b,* Elimination of temporal correlation between the spikes by shuffling the interspike intervals (*ISI*) within each spike train. *Gray tics* indicate the original spikes. *Panel c,* Spike displacement. Spikes of the original spike train (*gray tics*) are randomly shifted in time by 0–50 msec (Δt; *black tics*). Although the interspike intervals may change somewhat by this method, the field modulation of the neurons is better preserved. *Panel d,* Shuffling of spikes across spike trains. This method preserves population modulation of spike timing but may reduce firing-rate differences between the original spike trains. A fourth method (phase-invariant spike shuffling) is illustrated below (see Fig. 5).

of triplets, the cross products of the (neuron$_1$ neuron$_2$), (neuron$_1$ neuron$_3$), and the (neuron$_2$ neuron$_3$) cross-correlograms were constructed and normalized by the total number of observed triplets (Fig. 1*g*). The histogram of expected triplets was subtracted from the histogram of observed triplets, resulting in a histogram of unexpected triplets [difference map or joint probability map (JPM)]. Each pixel of the JPM was tested with the Fisher's exact probability test (Frostig et al., 1990a,b). To reduce the error inherent in repeated comparisons, the exact probability was multiplied by the number of pixels of the JPTH. The difference map is referred to as the JPM. Similar JPMs were constructed also from all shuffled surrogate trains. In the next step, the incidences of significant pixels in the JPM of the original and shuffled trains were compared statistically. Again, we assumed that if the number of significant triplets in 100 simulated spike trains is smaller than the observed number of triplets in the original spike train, the null hypothesis can be rejected with $p < 0.01$ probability. Because of the behavior-dependent time compression of spike sequences (see Results), the temporal information between spikes was discarded for this analysis.

Clustering artifacts

The reliable identification of spikes with individual neurons is a prerequisite for sequence detection. False clustering can cause the dispersion of single-unit activity to different clusters, and the spike train will be erroneously decomposed to different spike trains. A potential source of false clustering is the amplitude variation of extracellular units (Quirk and Wilson, 1998). As a consequence, temporal regularities of action potentials of a single neuron would lead to spuriously recurring multiple-unit spike sequences in parallel spike trains. The potential contribution of such an artifactual cause of the repeating spike sequences was tested by dividing the original clusters into small-amplitude and large-amplitude subclusters. As a result, the firing rate was reduced by 50% in each of the newly created trains. According to the formula of Abeles and Gerstein (1988), the number of spurious spike sequences should decrease exponentially as a function of spike count. In contrast, we found that the number of different sequences and the number of recurring sequences decreased only slightly less than one-half, indicating that spike amplitude variation cannot account for the repeating spike sequences. It is important to emphasize that only well-identified spike clusters with clear boundaries and refractory periods (Csicsvari et al., 1999) were included

in this study. In another approach, spikes that were part of the detected spikes sequences were highlighted in the original unit clusters. The rationale of this approach was that if spike sequences result as a consequence of poor clustering, spikes of the detected sequences should either reside near the cluster borders or coincide with small-amplitude spikes. This backprojection method, however, clearly revealed that spikes that were part of sequences were evenly distributed in the cluster clouds of spikes.

Computation

The sequence search, spike train shuffling, and the Monte Carlo statistics were run on an IBM SP2 scalable parallel computer with six nodes of RS/6000, 120 MHz P2SC processors (IBM, White Plains, NY), on a Silicon Graphics Onix2 with a 120 MHz MIPS R10000 processor (Silicon Graphics, Mountain View, CA), and on a Sun Enterprise with two UltraSPARC processors (Sun Microsystems, Palo Alto, CA). Identification of repeating spike sequences in a 10-min-long file, containing five parallel spike trains, typically required 175 min (Onix2) or 12.5 hr (SP2) of central processing unit time. The complete hypothesis testing of a single data set, including the generation of 100 surrogates and the sequence search, required 175 × 101 = 17,675 min (294.6 hr or ~12 d) on the Onix2.

RESULTS

The most prominent slow-wave sleep pattern in the hippocampus is an irregularly occurring population burst of pyramidal cells, associated with an SPW in the stratum radiatum and fast (150–200 Hz) field oscillation in the pyramidal layer of the CA1 region. Population activity of pyramidal cells between SPW events is relatively quiescent (Csicsvari et al., 1999). The long-term firing rates of pyramidal cells were similar during θ (1.4 × 0.10 Hz) and non-θ (1.4 × 0.09 Hz) behaviors. However, during SPW events, the firing rates of pyramidal cells increased by sevenfold (Csicsvari et al., 1999).

First, we examined whether participation of pyramidal neurons in SPW bursts is stochastic. On average, a pyramidal cell participated in 15% of successive SPWs. The probability of participation of individual neurons, however, varied extensively (2–40%; Fig. 3*A*). In other words, some pyramidal cells discharged consistently more reliably during SPW bursts than did others. The participation probability of a pyramidal neuron during SPW could be predicted from the firing rate of the cell during θ activity in rapid-eye-movement (REM) sleep ($r = 0.59$; $p < 0.0001$; Fig. 3*B*). These findings indicated that participation of pyramidal cells in the SPW event is not random and that the probability of their discharge in SPW correlates with the discharge frequency during θ behaviors.

Spike sequences in the awake and sleeping animal

The database for spike sequence analysis consisted of 10 sets of parallel-recorded spike trains of physiologically identified pyramidal neurons (n = 4–13 cells) from six rats. Repetition of spike sequences was observed in every animal investigated (Fig. 4). Sequences were detected from neurons recorded from both a single tetrode and neighboring tetrodes. Spike trains of larger numbers of simultaneously recorded cells yielded more sequences, but spike sequences could be identified reliably in records containing as few as four neurons. As expected, a large number of repeating spike patterns were observed in the wheel-running behavioral task, especially when two or more of the recorded pyramidal cells were selectively activated in the wheel (Czurko et al., 1999) (Fig. 4*b*). Importantly, repeating spike sequences were also present during sleep, when no external reference or motor behavior was available to generate repeating discharge sequences (Fig. 4*a*). The fraction of repeating spike sequences ($r \geq 2$) and single (nonrepeating) patterns varied from

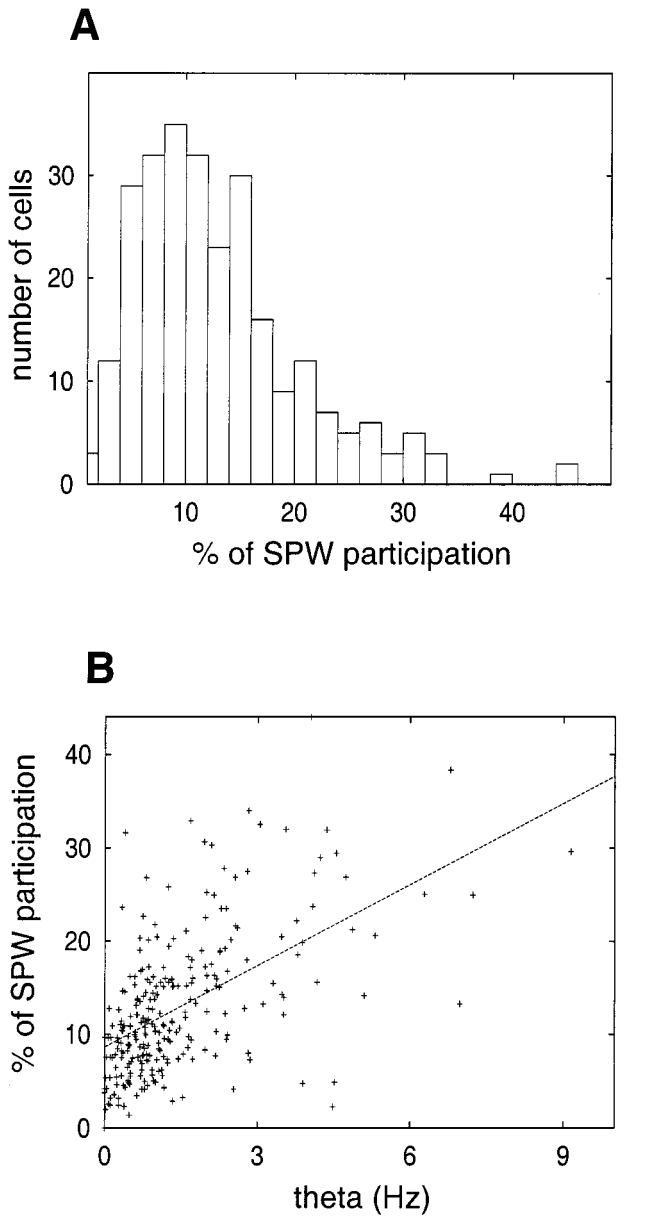

Figure 3. Relationship between the firing rate during θ behavior and the probability of spike participation in SPW. *A*, Probability of discharge of single pyramidal neurons in SPW events. Note that the majority of pyramidal neurons discharge <15% of all recorded SPWs. *B*, Relationship between the firing rate during θ and the probability of discharge during SPW events. Note that increased discharge rate during θ predicts a higher incidence of participation in SPWs.

8 to 56%. The exact percentage depended on the choice of sequence-search parameters (time window and spike jitter).

The number of repeating spike sequences detected also depended on the reference (sequence "initiator") neuron (Fig. 4). The inequality of the number of repeating sequences for different initiator neurons indicated that the sequences may reflect biological mechanisms because, in a random parallel spike train, spikes of a given neuron are expected to precede and follow spikes of other neurons with equal probability regardless of the firing rates. To examine further whether the repeating spike sequences reflected cellular interactions or simply Poisson coincidences of random events (Abeles and Gerstein, 1988), we compared the original spike trains with their shuffled surrogates.

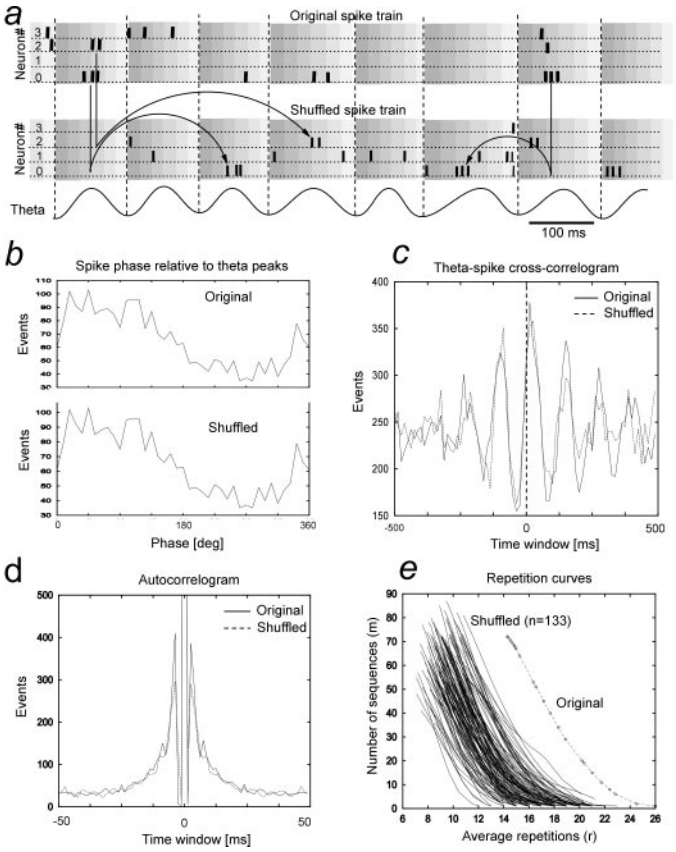

Figure 5. Comparison of repeating spike sequences in a parallel spike train, recorded during wheel running, with its shuffled surrogates. *a,* Peaks of θ oscillation were taken as a reference point, and the spike timing was converted to phase values within the θ cycle. During shuffling, sets of spikes within a given θ cycle were transposed randomly (*arrows*). *b*, Phase-normalized spike density histograms during the θ cycle are shown. *c*, Cross-correlogram between the negative peaks of local θ and unit discharges is shown. *d*, Spike autocorrelograms of units are shown. Note the similar spike dynamics in the original and shuffled spike trains. *e*, Repetition curves of spike sequences in the original spike train and in its shuffled surrogates are shown.

Figure 4. Examples of the spike sequences during sleep (*a*) and running (*b*) sessions, detected by the template-matching method. Only spike sequences of neurons, recorded by a single tetrode, are shown. The sleep session preceded the run session. The sequence initiator neuron is indicated by *arrows*. Recordings during sleep and running sessions were obtained from a single rat. The spike window (d*t*) was set to 10 msec in these searches. Different *colors* indicate different patterns. The *gray lines* in *b, top,* indicate all nonrepeating (single) sequences for comparison. *Cell numbers* refer to the same cells within the same behavioral category. *m*, Number of different sequences; *r*, number of repetitions of a given sequence. Also see: FTP://speedy2.md.huji.ac.il/pub/neuron.mid.

The incidence of repeating spike sequences during wheel running was compared with surrogate trains obtained by each of the four shuffling methods ($n = 1$ rat). The number of repeating sequences extracted from the original spike train exceeded the number of repeating sequences present in each of the 100 surrogate trains. Comparison between the original spike train and its θ phase-corrected shuffled surrogates (see θ phase-invariant shuffling in Materials and Methods) is illustrated in Figure 5. The θ phase-corrected shuffling procedure preserved the phase relationship between θ and the individual spikes, therefore reproducing the population dynamics of the parallel spike train as revealed by the identical θ phase-locked modulation and the similar cross-correlograms of both original and shuffled spikes (Fig. 5*b,c*). This procedure also preserved the within-spike-train dynamics of single neurons, as indicated by the similar autocorrelograms of the original and shuffled spike trains (Fig. 5*d*). Comparison of repeating spike sequences indicated that the number of repeating spike sequences (*r*) was less for all sequences (*m*) in any of the 133 shuffled surrogates compared with the original spike train (Fig. 5*e*). Of the various shuffling methods, across-spike-train shuffling resulted in the most spike sequence repetitions; therefore it may be regarded as the most rigorous test. Figure 6 illustrates the difference between repeating spike sequences obtained from the original parallel spike trains recorded from five rats and the Monte Carlo surrogates of those recordings (100 shuffled trains in each case). Shuffling was performed across spike trains for these tests because the spike trains contained both θ and non-θ epochs (see Across-spike-train shuffling; Fig. 2). For a given spike sequence (*c*), the number of spike sequences (*m*) that recurred at least r_{min} number of times was determined, and the average of the actual repetitions (r_1, r_2, r_3, . . . , r_n) was calculated. In all five cases, the number of repeating spike sequences in the surrogates was less than that in the original parallel spike trains ($p < 0.01$) in the entire range of *ms–s*.

A second method used for the evaluation of repeating spike sequences was the JPM. In contrast to the template-matching method, the complexity of the spike sequence was limited to three in this analysis. On the other hand, the JPM detected all se-

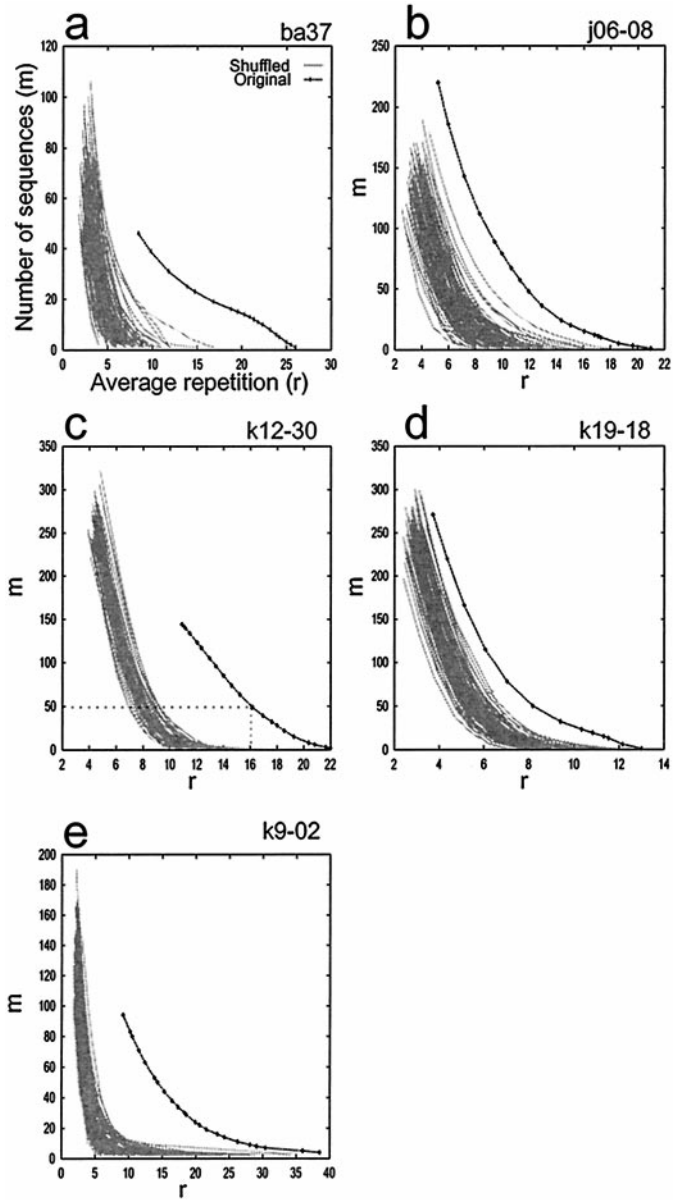

Figure 6. Comparison of repeating spike sequences in real spike trains (original) and their shuffled surrogates. *a–e*, Data from five different rats. The *y*-axis indicates the number of different sequences (*m*), and the *x*-axis indicates the average number of repeating sequences (*r*); e.g, 50 different sequences were repeated 16 times on average in rat k12-30 (*panel c*). Note that the repetition rate in the original spike train is higher than that in any of the 100 shuffled surrogates ($p < = 0.01$). In these comparisons, shuffling was done across spike trains. Rats are identified in each *top right corner*.

quences of spike triplets within a predefined time window (*w*), regardless of the specific temporal position of spikes (Fig. 1*g*). The distribution of repeating spike triplets was visualized as cumulative values in the bins of a joint peri-event histogram (Fig. 7*a*). Cross-correlation histograms for spike doublets were also calculated (Fig. 7*b*), and the expected co-occurrences of the corresponding spike doublets (i.e., random triplets) were subtracted from the observed distribution of triplets, resulting in a histogram of unexpected triplets (JPM, Fig. 7*c*; see Materials and Methods). The statistical significance of the difference between the observed and expected spike triplets was calculated by the Fisher's exact probability test. In the example shown in Figure 7*a–d*, a high incidence of triplets occurred at the temporal positions between *x* values of 50 and 80 msec and *y* values of 150 and 190 msec (e.g., 3, 2, 0; 50, 180 msec). The Fisher's exact probability test indicated three significant ($p < 0.02$) triplet positions in the corresponding pixels [(3, 2, 0; 50, 182 msec), (3, 2, 0; 64, 173 msec), and (3, 2, 0; 72, 154 msec)]. Importantly, these time patterns were similar to the repeating spike sequences detected independently by the template-matching method from the same data set (Fig. 7*d*).

To examine the null hypothesis that significant spike triplets are generated by random coincidences, 100 JPMs were created from the shuffled surrogates and compared with the original data sets shown in Figure 6. In these shuffling tests, the temporal-displacement-of-spikes procedure was used to ensure that shuffled spike trains have the same average firing rates and the same joint probability as the original data. Spikes were displaced in time by adding random intervals from 0 to 50 msec (see Temporal displacement of spikes; Fig. 2). For each of the original and the corresponding surrogate trains (total of 505 data sets), three separate JPMs were created, using 5, 6.7, and 10 msec bins. The number of repeating spike triplets in the original data sets was significantly larger than that in the shuffled correlates in every rat at the 6.7 and 10 msec bins (Fig. 7*e*). At 5 msec, more spike triplets were detected from the shuffled spike trains in two animals than in the original spike trains (j0-08 and k9-02). However, the differences were not significant for either of the two animals.

Behavioral modification of spike sequences

Next, we addressed the issue whether behaviorally imposed sequences can modify the probability of occurrence of those same sequences during subsequent slow-wave sleep. In two rats, stable recordings from the same neurons were obtained during Sleep1, Run, and Sleep2 sessions (Fig. 8). The similarity of spike sequence structure between any two states was tested in two steps. First, the significant triplets at all possible temporal positions were identified by the JPM method in each state. Second, the number of shared repeating spike sequences in different states was calculated, regardless of the exact temporal position of the spikes. For example, if the sequence 2;1;4 had significant pixels at any interspike intervals during the Run but not during the Sleep1 session, then it was not a common triplet between Run and Sleep1. However, if the triplet 2;1;4 was significant at 3 and 15 different temporal positions (pixels) during Run and Sleep2 sessions, respectively, then it was a common triplet. In the first rat, 13 pyramidal cells were recorded (Fig. 8). Only 87 of the 1716 possible triplets (5%) were common to both Sleep1 and Run sessions (Fig. 8*a*). In contrast, 160 triplets (9%) were observed in both Run and Sleep2 sessions (Fig. 8*b*; $\chi^2 = 21.58$; $p < 0.01$). In addition, the number of significant pixels of common triplets correlated significantly between Run and Sleep2 sessions (Pearson $r = 0.737$; $p < 0.001$). In contrast, during the Run session, triplet incidences during Sleep1 were independent from those in Run and Sleep2 sessions (Pearson $r = 0.393$; $r = 0.326$; $p > 0.05$). In the second rat four pyramidal cells were recorded in all three sessions. In this animal, statistically significant spike triplets common to two testing conditions were detected only between Run and Sleep2 sessions (Pearson $r = 0.679$; $p < 0.001$).

Both the template-matching and the JPM methods indicated that the majority of spike sequences were either <50 or >100 msec. In general, short sequences dominated in slow-wave sleep, whereas the longer sequences occurred in the awake animal or REM sleep (e.g., Fig. 4*a,b*). To quantify this observation, we

Figure 7. Spike triplets detected by the JPM method. *a,* The JPTH of a spike triplet (3, 2, 0). Summed pixels in the *x*- and *y*-axes are also shown. *b,* "Expected" JPTH, constructed on the assumption that triplets are random coincidences of spike doublets (see Materials and Methods). *c,* The excess number of triplets expressed as the difference between the observed and expected JPTHs. Significant pixels (Fisher's exact probability test) are *framed* in *boxes*. *d,* Vector representation of 3, 2, 0 sequences extracted by the template-matching method. Note that the latencies of the triplets match the significant pixels in the JPM. *e,* JPM maps constructed using three different pixel sizes (5, 6.7, and 10 msec) from the original and 100 shuffled surrogates (same original data sets shown in Fig. 6). The number of significant pixels in the surrogate JPMs is expressed as a percentage of the significant pixels in the original JPM. *Color bars,* Number of events.

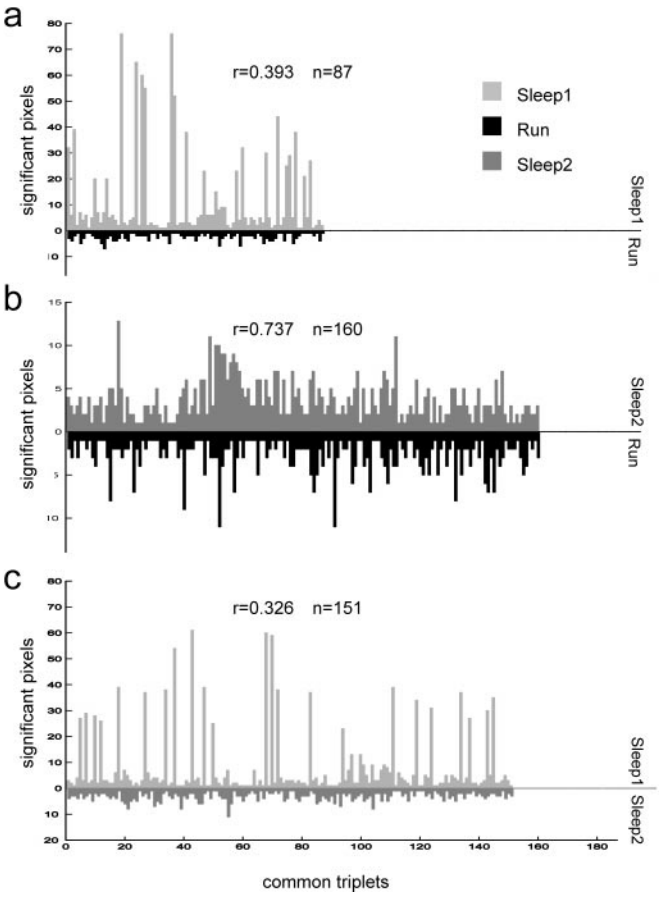

Figure 8. Spike sequences during sleep are influenced by previous wheel-running behavior. Histograms of significant triplets common to Sleep1 and Run sessions (*a*), to Run and Sleep2 sessions (*b*), and to Sleep1 and Sleep2 sessions (*c*). A sequence was considered to be "common" if it was significant by the JPM method (Fig. 7) in both behavior sessions regardless of the interspike intervals (e.g., 4-1-2 at 50 and 80 msec and at 5 and 8 msec). Individual triplets are listed on the *x*-axis. The *upward* and *downward bars* at any given location on the *x*-axis indicate the number of significant pixels of the JPM of a common triplet in the two sessions, respectively. Note that there were almost twice as many triplets common to Run and Sleep2 sessions than to Sleep1 and Run sessions. The *r* values (Pearson's product moment correlation coefficient) indicate the correlation of the number of common triplets between the respective two sessions.

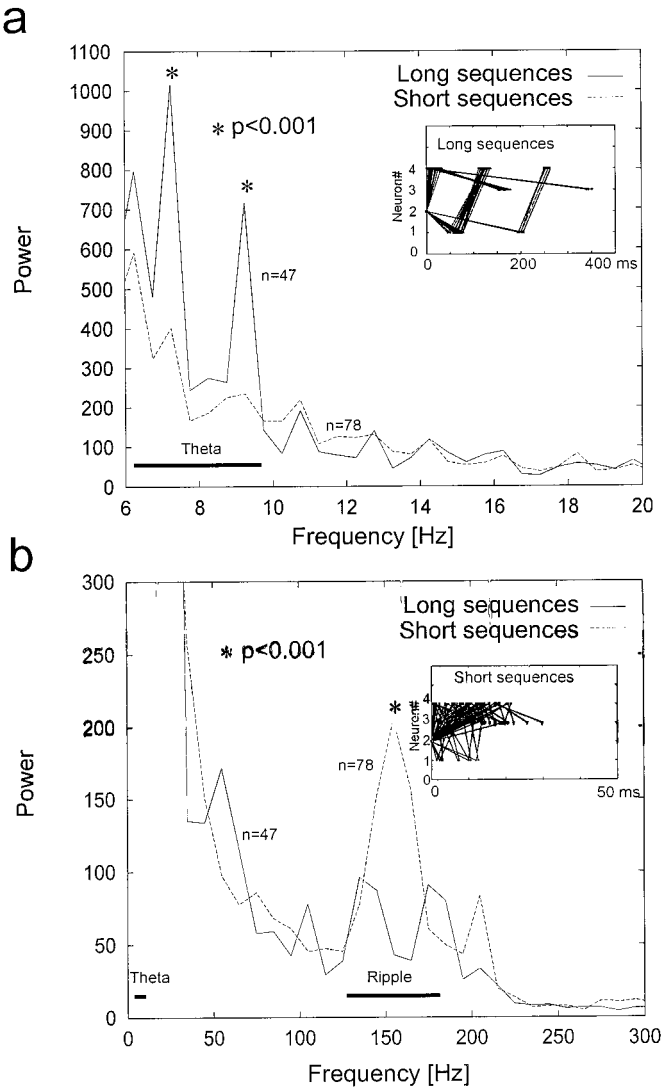

Figure 9. Long and short repeating spike sequences are associated with θ and ripple field activity, respectively. The power spectra of background field activity, associated with short and long sequences, were compared. The first spike of the same long (termination $>$ 100 msec; $n = 47$) or short (termination $<$ 50 msec; $n = 78$) spike sequences was regarded as the reference event for extracting field EEG information. *a,* EEG power in the low-frequency band surrounding long (*solid line*) and short (*interrupted line*) repeating spike sequences. Note the increased θ power during long sequences. *b,* EEG power in the ripple frequency band (100–200 Hz) surrounding long and short repeating spike sequences. Note the large power peak at 160 Hz during short sequences. *Insets,* Long (in *a*) and short (in *b*) sequences of the same neurons. Note the difference in timescale; short sequences are shown at an enhanced timescale.

examined the EEG correlates of repeating spike sequences. The independent variable in these tests was the length of the spike sequences, irrespective of the behavioral state of the rat. Spike sequences of the same pyramidal cells and temporal order were selected and subdivided into two groups, one with sequence termination <50 msec and one with termination >100 msec, and the power spectra of their associated background field activity were compared. Two different epochs were extracted from the EEG. The shorter epochs (204.8 msec before the first spike of the sequence) provided a more precise estimate of the exact EEG state, whereas the longer ones (−819.2 to 2457.6 msec) were used to assess the EEG power at lower frequencies. For these comparisons, spike sequences common to θ and SPW states were used. Power spectra, calculated from the short and long EEG epochs (0–300 and 0–20 Hz, respectively), revealed that short spike sequences were associated with a significant peak at 140–200 Hz (Fig. 9*b*), corresponding to field "ripples" in the EEG (Buzsβki et al., 1992). Conversely, the long spike sequences were associated with increased power at θ frequency (Fig. 9*a*). These findings suggested that sequences associated with θ behavior were replayed during SPW-associated ripples in a time-compressed manner.

DISCUSSION

Quantification of repeating spike sequences

The template method and the JPM detected similar spike sequences. Nevertheless, a critical issue that must be addressed is whether the repeating spike sequences were generated by biological mechanisms or emerged simply as a result of random coincidences of spike trains. The reliability of the Monte Carlo test

depends critically on the choice of the proper shuffling method. The ideal shuffling protocol should maintain the discharge frequency of individual spike trains and should not alter the population dynamics of the parallel-recorded neurons. Because none of the known shuffling methods are universally applicable in all situations, we used four different shuffling protocols.

If the dynamics of cortical neurons could be described by a Poisson process (Bair and Koch, 1996; Shadlen and Newsome, 1998), then within-spike-train randomization of spike occurrences would be appropriate because this procedure does not alter the average firing rate of the individual neurons. Unfortunately, random shuffling within the same spike train (see Within-spike-train random shuffling) may alter the population dynamics of the parallel spike trains. This issue is very important, because population synchrony of hippocampal pyramidal cells varies with behavior and their dynamics do not follow simple Poisson statistics (Csicsvari et al., 1999). Random shuffling across spike trains (see Across-spike-train shuffling) preserved the population dynamics. However, this method tends to equalize the firing-rate differences of individual neurons relative to the original spike trains. This may be important because the number of repeating spike sequences in random spike trains varies with discharge frequency (Abeles and Gerstein, 1988). To retain both population behavior and firing-rate changes, two additional shuffling protocols were used. The temporal displacement method (see Temporal displacement of spikes) shifted spikes randomly within a 50 msec time window with the goal of retaining the population synchrony across spike trains during both θ waves and SPWs. The phase-invariant shuffling method (see θ phase-invariant shuffling) preserved spike dynamics both within and across spike trains. Regardless of the shuffling method used, excessively repeating spike sequences were found in each of the parallel-recorded spike trains. Furthermore, the number of different sequences, the number of repeating spike sequences, and the number of spikes within a given sequence (complexity) varied even within the same data set depending on the neuron that served as a sequence initiator. Finally, the discharge probability of pyramidal cells in SPW varied substantially from cell to cell. Together, these observations indicate that the observed spike sequences cannot be accounted for fully by random coincidences of neuronal discharges of hippocampal cells.

Externally controlled and internally generated recurring spike sequences

Spike sequences were observed in both the awake and sleeping animal. The spatially distributed pattern of temporally precise single pyramidal neuron spikes during sleep could be a consequence of some hard wiring (Hampson et al., 1996) or may reflect synaptic changes as a result of learning in the awake animal (Wilson and McNaughton, 1994; Mehta et al., 1997). We hypothesized previously that the behavior-dependent electrical changes in the hippocampal formation (θ- and SPW-associated states) might subserve a two-stage process of information storage (Buzsáki, 1989). Mnemonic information is assumed to be encoded in the recurrent and Schaffer collateral synapses of CA3 pyramidal cells during θ-associated learning behavior. When the network state of the CA3 matrix switches to SPW bursts during consummatory behaviors and slow-wave sleep, synaptic connections that were active during the learning state are spontaneously reactivated. Rapid reinstatement of the spatiotemporal patterns of pyramidal cell activity in the CA3–CA1 regions and deep layers of the entorhinal cortex (Chrobak and Buzsaki, 1994, 1996) is hypothesized to transfer the stored representations in the hippocampus to neocortical networks (Buzsáki, 1989; Wilson and McNaughton, 1994; McClelland et al., 1995; Siapas and Wilson, 1998). Consistent with this speculation, the probability of SPW-associated discharge of pyramidal neurons correlated with the discharge frequency of these neurons during θ behavior. In addition, spike sequences that were observed in the wheel-running task were observed in the subsequent slow-wave sleep episode at a higher probability than during sleep before the wheel-running session. These findings support and extend observations by Wilson and McNaughton (1994) and Skaggs and McNaughton (1996) [but see also Hampson et al. (1996); McNaughton et al. (1996); Moore et al. (1996)], who found that cell pairs with overlapping place fields had an increased correlation during subsequent sleep. Our findings also demonstrate that sleep-associated replay of the sequences observed during θ behavior are mainly confined to SPW bursts. It was demonstrated previously that the correlation between cell pairs is significantly increased during SPW (Wilson and McNaughton, 1994). However, such increased correlation may be a spurious consequence of an increased firing rate during SPW (Csicsvari et al., 1999). In the present study, the SPW-associated time compression of spike sequences was demonstrated by the correlation between the occurrence of short sequences and increased power at the ripple frequency. The effect of increased discharge rate on the probability of sequences during SPW was reduced or eliminated by shuffling across spike trains. These observations support the suggestion that time-compressed neuronal patterns during SPW bursts are generated within the hippocampus and are a consequence of firing patterns in the wake brain (Buzsáki, 1989; Chrobak and Buzsaki, 1994; Bibbig et al., 1995; Hinton et al., 1995; McClelland et al., 1995; Skaggs and McNaughton, 1996; Wallenstein and Hasselmo, 1997; Menschik and Finkel, 1998; August and Levy, 1999). It may be argued that both the slow and fast sequences were imposed onto the hippocampal circuitry by the entorhinal input; thus the hippocampus does not play an active role in generating endogenous repeating spike sequences. This possibility is not likely because during sleep SPW bursts are initiated in the CA3 region of the hippocampus (Buzsáki, 1989). In fact, the incidence of SPWs increases dramatically after entorhinal cortex lesion (Bragin et al., 1995).

Physiological role of spike sequence replay

What is the physiological importance of the recurring spike sequences (Lisman, 1998)? In a weaker formulation of the replay hypothesis, the exact sequence of neuronal firing is not critical. What is important is that neurons, which discharge in a temporally discontiguous manner during θ behavior and possibly encode different representations, are brought together during SPW on the timescale of the time constant of NMDA receptors. From this perspective, the function played by the time-compressed replay of the active neurons in the awake animal is to ensure Hebbian modification among pyramidal cells, which did not discharge together within the critical time window of synaptic plasticity during learning but nevertheless carry related information. For example, during spatial behavior, various place cells are activated as the animal explores its environment (O'Keefe and Nadel, 1978). Because the same spatial position can be approached from various directions, hence associated by the activation of different neuronal sequences, most neurons do not discharge together in time. During SPW bursts, these same neuron sets may be endogenously reactivated within the time constant of the NMDA receptors, providing an opportunity for Hebbian

synaptic modification of the recurrent and Schaffer synapses of the CA3 pyramidal cells.

Alternatively, one can argue that the replay of spike sequences is critical for the activation of relevant target neurons downstream from the hippocampus (Chrobak and Buzsáki, 1996; Siapas and Wilson, 1998). This model assumes the existence of neuronal mechanisms for decoding spike sequences with ripple frequency (5 msec) resolution both within the hippocampus and in its targets. Recent works on individual pyramidal neurons and their network interactions suggest that pyramidal cells are equipped with intrinsic oscillatory properties (Llinás, 1988; Leung and Yim, 1991; Kamondi et al., 1998) and are embedded in an oscillatory network of interneurons (Buzsáki and Chrobak, 1995; Whittington et al., 1995). Within these oscillatory patterns, the ratio of excitation and inhibition can vary substantially (Rudell et al., 1980; Buzsáki et al., 1981; Csicsvari et al., 1999). We hypothesize that the oscillatory network of neuronal assemblies may provide "temporal windows of opportunity" to ignore or enhance selectively the effectiveness of presynaptic activity. As a result, individual spikes of a given spike sequence, as shown here, could exert a differential impact on their postsynaptic targets, depending on the relationship between the spike and network activity.

Finally, it should be emphasized that the time-compression effect is caused by the population dynamics of the hippocampal network and that its mechanism is orthogonal to the formation of spike sequences. During SPW bursts, the discharge probability of pyramidal neurons increases several-fold (Csicsvari et al., 1999), independent of whether a neuron is part of an observed spatiotemporal spike sequence or not. Nevertheless, temporal coactivation of neurons, brought about by SPW bursts, is expected to strengthen their synaptic weights. Direct demonstration of SPW-induced synaptic changes, however, remains a future challenge.

Note added in proof. While this manuscript was under review, a paper with relevant content has been published [Barnes CA, McNaughton BL (1999) Reactivation of hippocampal cell assemblies: effects of behavioral state, experience, and EEG dynamics. J Neurosci 19:4090–4101].

REFERENCES

Abeles M (1991) Corticonics: neural circuits of the cerebral cortex. Cambridge, U.K.: Cambridge UP.

Abeles M, Gerstein GL (1988) Detecting spatiotemporal firing patterns among simultaneously recorded single neurons. J Neurophysiol 60:909–924.

Abeles M, Bergman H, Margalit E, Vaadia E (1993) Spatiotemporal firing patterns in the frontal cortex of behaving monkeys. J Neurophysiol 70:1629–1638.

Aertsen AM, Gerstein GL, Habib MK, Palm G (1989) Dynamics of neuronal firing correlation: modulation of "effective connectivity." J Neurophysiol 61:900–917.

Aertsen A, Vaadia E, Abeles M, Ahissar E, Bergman H, Karmon B, Lavner Y, Margalit E, Nelken I, Rotter S (1991) Neural interactions in the frontal cortex of a behaving monkey: signs of dependence on stimulus context and behavioral state. J Hirnforsch 32:735–743.

August DA, Levy WB (1999) Temporal sequence compression by an integrate-and-fire model of hippocampal area CA3. J Comput Neurosci 6:71–90.

Bair W, Koch C (1996) Temporal precision of spike trains in extrastriate cortex of the behaving macaque monkey. Neural Comput 8:1185–1202.

Barlow HB (1972) Single units and sensation: a neuron doctrine for perceptual psychology? Perception 1:371–394.

Bibbig A, Wennekers T, Palm G (1995) A neural network model of the cortico-hippocampal interplay and the representation of contexts. Behav Brain Res 66:169–175.

Bragin A, Jando G, Nadasdy Z, van Landeghem M, Buzsáki G (1995) Dentate EEG spikes and associated population bursts in the hippocampal hilar region of the rat. J Neurophysiol 73:1691–1705.

Brown EN, Frank LM, Tang D, Quirk MC, Wilson MA (1998) A statistical paradigm for neural spike train decoding applied to position prediction from ensemble firing patterns of rat hippocampal place cells. J Neurosci 18:7411–7425.

Buzsáki G (1989) Two-stage model of memory trace formation: a role for "noisy" brain states. Neuroscience 31:551–570.

Buzsáki G, Chrobak JJ (1995) Temporal structure in spatially organized neuronal ensembles: a role for interneuronal networks. Curr Opin Neurobiol 5:504–510.

Buzsáki G, Grastyán E, Czopf J, Kellenyi L, Prohaska O (1981) Changes in neuronal transmission in the rat hippocampus during behavior. Brain Res 225:234–247.

Buzsáki G, Horvath Z, Urioste R, Hetke J, Wise K (1992) High-frequency network oscillation in the hippocampus. Science 256:1025–1027.

Chrobak JJ, Buzsáki G (1994) Selective activation of deep layer (V–VI) retrohippocampal cortical neurons during hippocampal sharp waves in the behaving rat. J Neurosci 14:6160–6170.

Chrobak JJ, Buzsáki G (1996) High-frequency oscillations in the output networks of the hippocampal-entorhinal axis of the freely moving rat. J Neurosci 16:3056–3066.

Csicsvari J, Hirase H, Czurko A, Mamiya A, Buzsáki G (1999) Oscilatory coupling of hippocampal pyramidal cells and interneurons in the behaving rat. J Neurosci 19:274–287.

Czurko A, Hirase H, Csicsvari J, Buzsáki G (1999) Sustained activation of hippocampal pyramidal cells by "space clamping" in a running wheel. Eur J Neurosci 1:344–352.

Dayhoff JE, Gerstein GL (1983) Favored patterns in spike trains. I. Detection. J Neurophysiol 49:1334–1348.

Eccles JC (1957) The physiology of nerve cells. Baltimore: Johns Hopkins.

Eckhorn R, Bauer R, Jordan W, Brosch M, Kruse W, Munk M, Reitboeck HJ (1988) Coherent oscillations: a mechanism of feature linking in the visual cortex? Multiple electrode and correlation analyses in the cat. Biol Cybern 60:121–130.

Frostig RD, Frostig Z, Harper RM (1990a) Recurring discharge patterns in multiple spike trains. I. Detection. Biol Cybern 62:487–493.

Frostig RD, Frysinger RC, Harper RM (1990b) Recurring discharge patterns in multiple spike trains. II. Application in forebrain areas related to cardiac and respiratory control during different sleep-waking states. Biol Cybern 62:495–502.

Georgopoulos AP, Kalaska JF, Caminiti R, Massey JT (1982) On the relation between the two-dimensional arm movements and cell discharge in primate motor cortex. J Neurosci 2:1527–1537.

Gray CM, Singer W (1989) Stimulus-specific neuronal oscillations in orientation columns of cat visual cortex. Proc Natl Acad Sci USA 86:1698–1702.

Hampson RE, Byrd DR, Konstantopoulos JK, Bunn T, Deadwyler SA (1996) Hippocampal place fields: relationship between degree of field overlap and cross-correlations within ensembles of hippocampal neurons. Hippocampus 6:281–293.

Hinton GE, Dayan P, Frey BJ, Neal RM (1995) The "wake-sleep" algorithm for unsupervised neural networks. Science 268:1158–1161.

Hopfield JJ (1995) Pattern recognition computation using action potential timing for stimulus representation. Nature 376:33–36.

Kamondi A, Acsády L, Wang X-J, Buzsáki G (1998) Theta oscillations in somata and dendrites of hippocampal pyramidal cells in vivo: activity dependent phase-precession of action potentials. Hippocampus 8:244–261.

Laurent G, Wehr M, Davidowitz H (1996) Temporal representations of odors in an olfactory network. J Neurosci 16:3837–3847.

Leung LS, Yim CY (1991) Intrinsic membrane potential oscillations in hippocampal neurons in vitro. Brain Res 553:261–274.

Lisman JE (1998) What makes the brain's tickers tock. Nature 394:132–133.

Lisman JE, Idiart MA (1995) Storage of 7 ± 2 short-term memories in oscillatory subcycles. Science 267:1512–1515.

Llinás RR (1988) The intrinsic electrophysiological properties of mammalian neurons: insights into central nervous system function. Science 242:1654–1664.

Marder E, Calabrese RL (1996) Principles of rhythmic motor pattern generation. Physiol Rev 76:687–717.

McClelland JL, McNaughton BL, O'Reilly RC (1995) Why there are

complementary learning systems in the hippocampus and neocortex: insights from the successes and failures of connectionist models of learning and memory. Psychol Rev 102:419–457.

McNaughton BL, Barnes CA, Gerrard JL, Gothard K, Jung MW, Knierim JJ, Kudrimoti H, Qin Y, Skaggs WE, Suster M, Weaver KL (1996) Deciphering the hippocampal polyglot: the hippocampus as a path integration system. J Exp Biol 199:173–185.

Mehta MR, Barnes CA, McNaughton BL (1997) Experience-dependent, asymmetric expansion of hippocampal place fields. Proc Natl Acad Sci USA 94:8918–8921.

Menschik ED, Finkel LH (1998) Neuromodulatory control of hippocampal function: towards a model of Alzheimer's disease. Artif Intell Med 13:99–121.

Moore GP, Rosenberg JR, Hary D, Breeze P, Skaggs WE, McNaughton BL (1996) "Replay" of hippocampal "memories." Science 274: 216–1217.

Nadasdy Z, Bragin A, Buzsáki G (1996) Repeating spatio-temporal patterns of neuronal activity in the hippocampus during sleep. Soc Neurosci Abstr 22:445.11.

Nadasdy Z, Bragin A, Csicsvari J, Hirase H, Moore K, Buzsáki G (1997) Relationship between recurring spatio-temporal spike patterns and local field oscillations in the hippocampus. Soc Neurosci Abstr 23:188.5.

Nadasdy Z, Csicsvari J, Hirase H, Czurko A, Buzsáki G (1998) Persistence, compression and behavioral induction of spike sequences in the hippocampus. Soc Neurosci Abstr 24:362.18.

Nádasdy Z, Csicsvari J, Penttonen M, Hetke J, Wise K, Buzsáki G (1998) Extracellular recording and analysis of neuronal activity: from single cells to ensembles. In: Neuronal ensembles: strategies for recording and encoding (Eichenbaum H, Davis J, eds), pp 17–55. New York: Wiley.

O'Keefe J, Nadel L (1978) The hippocampus as a cognitive map. Oxford: Clarendon.

O'Keefe J, Recce ML (1993) Phase relationship between hippocampal place units and the EEG theta rhythm. Hippocampus 3:317–330.

Pavlides C, Winson J (1989) Influences of hippocampal place cell firing in the awake state on the activity of these cells during subsequent sleep episodes. J Neurosci 9:2907–2918.

Quirk MC, Wilson MA (1998) Temporal changes in the firing properties of CA1 pyramidal cells in the freely behaving rat. Soc Neurosci Abstr 24:758.13.

Ranck JB (1973) Studies on single neurons in dorsal hippocampal formation and septum in unrestrained rats. I. Behavioral correlates and firing repertoires. Exp Neurol 42:461–531.

Riehle A, Grün S, Diesmann M, Aertsen A (1997) Spike synchronization and rate modulation differentially involved in motor cortical function. Science 278:1950–1953.

Rudell AP, Fox SE, Ranck JB (1980) Hippocampal excitability phase-locked to the theta rhythm in walking rats. Exp Neurol 68:87–96.

Shadlen MN, Newsome WT (1998) The variable discharge of cortical neurons: implications for connectivity, computation and information coding. J Neurosci 18:3870–3896.

Sherrington CS (1906) Integrative action of the nervous system. New Haven, CT: Yale UP.

Siapas AG, Wilson MA (1998) Coordinated interactions between hippocampal ripples and cortical spindles during slow-wave sleep. Neuron 21:1123–1128.

Singer W (1993) Synchronization of cortical activity and its putative role in information processing and learning. Annu Rev Physiol 55:349–374.

Skaggs WE, McNaughton BL (1996) Replay of neuronal firing sequences in rat hippocampus during sleep following spatial experience. Science 271:1870–1873.

Skaggs WE, McNaughton BL, Wilson MA, Barnes CA (1996) Theta phase precession in hippocampal neuronal populations and the compression of temporal sequences. Hippocampus 6:149–172.

Strehler BL, Lestienne R (1986) Evidence of precise time-coded symbols and memory patterns in monkey cortical spike trains. Proc Natl Acad Sci USA 83:9812–9816.

Ts'o DJ, Gilbert CD, Wiesel TN (1986) Relationship between horizontal interactions and functional architecture in cat striate cortex as revealed by cross-correlation analysis. J Neurosci 6:1160–1170.

Vaadia E, Abeles M (1987) Temporal firing patterns of single units, pairs and triplets of units in the auditory cortex. Isr J Med Sci 23:75–83.

von der Malsburg C, Bienenstock E (1986) A neural network for the retrieval of superimposed connection patterns. Neurosci Lett 3:1243–1249.

Wallenstein GV, Hasselmo ME (1997) GABAergic modulation of hippocampal population activity: sequence learning, place field development, and the phase precession effect. J Neurophysiol 78:1393–1408.

Whittington MA, Traub RD, Jefferys JG (1995) Synchronized oscillations in interneuron networks driven by metabotropic glutamate receptor. Nature 373:612–615.

Wilson MA, McNaughton BL (1994) Reactivation of hippocampal ensemble memories during sleep. Science 265:676–679.

Yuste R, Denk W (1995) Dendritic spines as basic functional units of neuronal integration. Nature 375:682–684.

Zhang K, Ginzburg I, McNaughton BL, Sejnowski TJ (1998) Interpreting neuronal population activity by reconstruction: unified framework with application to hippocampal place cells. J Neurophysiol 79:1017–1044.

Chapter 2

7. Sequences in dissociated tissue cultures

> *"The existence of a neuron chain, in any piece (column) of the cortex, routing the input through the local neuron network towards an output, is an obvious necessity and was implicit - from the very beginning - in all diagrams that tried to visualize the possible function of the cortex as a processor of information."*
>
> *(János Szentágothai, 1978)*

While the concepts of spike sequences and replay were rapidly gaining traction in memory research, I took the opportunity to engage in collaboration with two outstanding colleagues from the late Jerry Pine's lab at Caltech between 2003-2006. Their team just implemented a new protocol to record the multi-unit activity of dissociated tissue by multielectrode arrays (MEAs), unraveling a collection of stereotypical activity patterns these cultures spontaneously exhibit. They managed embryotic cortical neurons to grow on a thin layer of agarose gel for a few weeks, and having the neurons established a dense connectivity network, they turned the amplifiers on and recorded the entire tissue culture by a grid of 64 electrodes (Potter, 2001). Because tissue cultures develop dense recurrent connectivity and given that they are closed systems, we expected that spike sequences would evolve spontaneously. Owing to the method to keep the cultures alive and the recent advancement in the MEA technique made it possible for the first time to monitor the aggregate activity of thousands of neurons (Potter, 2001). I capitalize on "aggregate" because the MEA grid did not allow for the isolation of single-unit activity, but it was adequate for quantifying the mesoscopic-scale multi-unit activity. This project was funded by S.M.P.'s NIH grant, and D.A.W. did the experiments and data processing, while the data analysis and computational method development were done by D.A.W. and Z.N., the author of this dissertation (Wagenaar et al., 2006).

Because the outcomes of this study are highly relevant to the narrative of my dissertation, I summarize them as follows:

1. Dissociated neuronal tissue exhibits stereotypical activity patterns at a specific age of the culture, which are common across cultures.
2. These stereotypical patterns consist of a two-level hierarchical pattern of bursts and superbursts (composed of 6-7 bursts). Superbursts spontaneously recur without any external trigger.

3. Superbursts are periodic, just like the individual bursts within the superburst.
4. Individual bursts display specific propagation dynamics where the 1st burst differs from the 2nd and 3rd, and so on. On the other hand, the 1st bursts of every superburst are alike, and all the 2nd, 3rd, 4th, 5th, and 6th bursts are likewise. If we assign letters to the burst sequence from the first to the sixth, we can describe this sequence composition as {A-B-C-D-E-F-G}, …, {A-B-C-D-E-F-G}, where each letter denotes different propagation dynamics.
5. The burst pattern generates a sequence of trajectories as the activity propagates through stereotypical paths like a cascade that reproduces itself. This activity pattern is persistent over days and weeks.
6. Superbursts are all-or-none kind: once a super-burst is triggered, it will complete all 7 bursts.
7. Bursts are also all-or-none kinds: once a burst is triggered, it will proceed with propagation dynamics characteristic to the burst order in the sequence.
8. Neurons are *interchangeable*: The contribution of individual neurons to the burst pattern varies but the population dynamics do not change. The population dynamic is *invariant* to the change of neurons.
9. While these bursts are unlike any neuronal activity observed *in vivo* in the brain, they express the self-organizing nature of the neurons. The exact pattern is constrained by the 3D connectivity of the tissue culture, which can be very different from the organic, slice, or organotypic tissue cultures.

An obvious question inspired by these results was whether these patterns are modifiable by external input such as micro-stimulation. If they do, that would be the signature of adaptative attractor dynamics, supporting the notion of dynamic engrams. The answer is not as simple as the question.

The spontaneous emergence of these in vitro burst patterns is relevant because it proves the potential for cortical neurons to self-organize into circuitries that generate recurring spatiotemporal activity without any external trigger. Unless there is a mechanism to prevent that specifically, this should also happen in vivo. The recurrence of activity patterns is an embodiment of Hebb's reverberatory circuitry that provides a sequential firing of an ensemble of neurons that Hebb also defined as "cell assembly." Beyond the reverberatory activity, the temporal hierarchy of burst-superburst patterns and the distinct trajectories of A, B, C,.., and

G sub-bursts suggest that these are not just simple neuronal short circuits. Instead, these are complex trajectories that display the attributes of limit cycle behavior like strange attractors

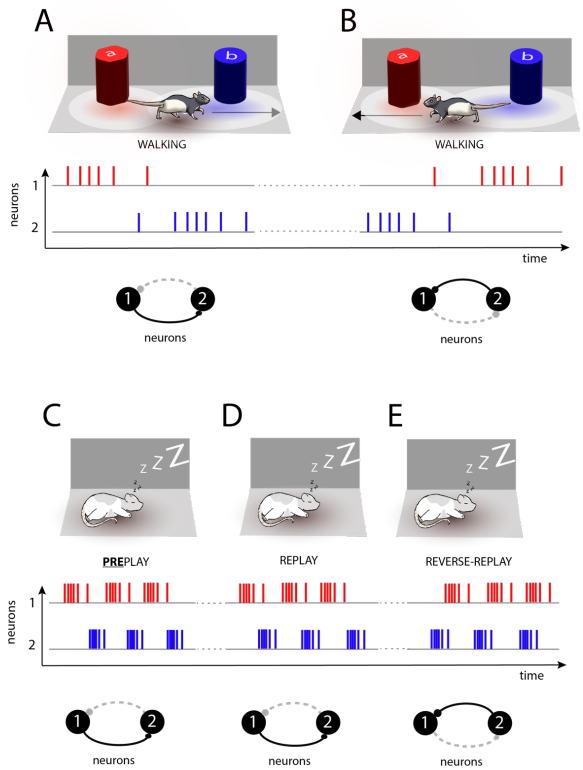

Figure D3: The two hypotheses of sequence replay: (A-B) According to the 'engram' hypothesis, external cues or objects elicit packets of spikes along the path of the animal as it encounters them. (**A**) When the animal runs in one direction, the rat encounters object "a" first and object "b" second, which elicits a train of action potential in place cell 1 and place cell 2, respectively. The repeated coactivation of the two place cells instantiate an associative link between the locations and generates an engram of the route from (a) to (b). (**B**) The sequence of events as well as the sequential activation of neurons 1 and 2 are reversed when the rat is running in the opposite (b) to (a) direction. During free exploration, the rat may run in both directions, hence reinforcing both types of activation sequences between neuron 1 and 2 (redrawn from Nadasdy, 2000). **(C-E**) The alternative model suggests that new sequences are spontaneously generated during sleep ("preplay") and the most likely sequence will predetermine the order of firing of these neurons during a run. When the animal explores a new environment, it is not the sequential order of sensory input that determines the firing sequence. Instead, the firing sequence is determined by a preexisting attractor. This attractor will serve as a string of placeholders for experience specific objects to fill and it will also facilitate to replay and reverse-replay of these sequences (D and E) appearing the same as in (A and B).

(Anishchenko & Strelkova, 1997), such as the Lorenz attractor. Whether we use Hebb's terminology or not, these pattern formations provide a substrate to form dynamic attractors; as such, they can represent and maintain information. The three key features making attractor dynamics work are the *renewal process*, *invariance,* and *multi-stability*. All three are necessary to generate patterns that are self-triggered in the absence of external input (*renewal process*). They go through similar state transitions (*invariance*), stable over time but can switch states upon perturbation (*multi-stability*) (Dias et al., 2021). As a result of these properties combined, it can store and maintain information. Hence, these patterns adhere to the definition of engrams or memories.

Regarding spike patterns as products of a *renewal* process generating *invariant, multi-stable* sequences of neuronal activity, there is a broad consensus that they follow attractor dynamics as a candidate mechanism to implement information storage in neuronal circuitries as

memories. However, we can distinguish between two approaches pursuing two different classes of models. First is the *'engram sequence'* hypothesis, which considers the dynamic patterns of spike sequences as fingerprints of engrams. Accordingly, engrams encode and maintain information by the synaptic weights as imprints. This model assumes that sequences of action potentials evoked by precisely timed input can induce conservative synaptic remodeling. Synaptic remodeling is a well-understood second-messenger-mediated process involving mRNAs translation and protein synthesis necessary for stabilizing or growing new synaptic connections to accommodate memory by connectivity (Alberini & Kandel, 2015). The rewired network can recognize other inputs based on a partial or global overlap with the original input pattern that created the engram in the first place. This model was outlined in my paper in 2000 (Nadasdy, 2000), where I proposed that when a rat passes location (a) and location (b) en route to a goal, then place-cell-1 and place-cell-2 must fire at location (a) and (b), respectively, in a sequence, assuming that those two locations have overlapping place fields (Fig. D3 A-B). The activity of (a) and (b) neurons will drive a correlation between spikes at $a(t_1)$ and $b(t_2)$. After transiting through these locations several times, the coupling between $a(t_1)$ and $b(t_2)$ stabilizes and will be replayed during the subsequent slow wave sleep by sharp wave activity. This is also called the "forward replay." While this working hypothesis was widely shared and consistent with experimental results (Dragoi & Buzsáki, 2006), it had two serious problems: It was too slow to enable rapid exploration and integration of new information. Second, the brain does not have a "clean slate" (tabula rasa) state in which the new input would impose itself like a fingerprint on a white paper. Instead, those neurons are active, exhibiting spontaneous patterns, far from random activity (see the tissue culture findings above.) At the same time, disconcerting results started to surface, indicating that many of the sequences detected during the first run and repeated over time, were already preexisting during sharp-wave ripples in the preceding slow-wave sleep episodes. This model is called the "pre-play" hypothesis, which forces us to revise and update our mechanistic model.

Now consider the following alternative explanation. What if spike sequences are continuously generated as spontaneous activity of the network of neurons? This spontaneous activity naturally unfolds sequentially due to the delays in the circuitry, pretty much how Hebb envisioned "reverberatory activity." If such a reverberatory activity exists, it must prevail in a closed-loop neuronal architecture system such as dissociated cortical tissue culture. Then stimulation of the network (which may represent itself as pre-processed sensory input in vivo, cortico-cortical input projection, direct microsimulation, or optogenetic stimulation) will

perturb the sequential order of activity or the timing of activity in the network. By using dynamic system terminology, the input perturbation would shift the attractor of the network. As a result, the network will adhere to a slightly different setpoint or limit cycle, which accommodates the new sequence (Fig. D4). For instance, a network of neurons spontaneously generates the recurring A-B-C-D sequence without any external input. Then we repeatedly apply a stimulation that will force the sequence to take the **A-B-*E-F*** route. Depending on the flexibility of the attractors in that culture, if the **A-B-*E-F*** sequence is part of the repertoire supported by the network (i.e., consistent with one of the attractors), then it will replay as a new branch of the *"persistent renewal"* dynamics. If the A-B-C-D is a strongly wired attractor in the network, it may replay with a partial modification of A-B-C-D-***F*** or A-B-C-***E-F*** fashion. Empirical data from dissociated cortical tissue culture support the perturbation hypothesis for these attractor states (Madhavan et al., 2007; Pasquale et al., 2017).

The first model has driven much ongoing research as a working hypothesis, such as the molecular, synaptic tagging during long-term potentiation and most synaptic engram models (Frey & Morris, 1997; Josselyn & Tonegawa, 2020; Tonegawa et al., 2015). Nevertheless, mounting evidence supports the second model (Dragoi & Tonegawa, 2011, 2013; Farooq et al., 2019; Grosmark & Buzsáki, 2016). Note that the two are not mutually exclusive. Accordingly, neurons generate deterministic pseudo-periodic sequences due to their intrinsic recurrent circuitry. These precursor sequences are relatively rigid and associated with the activity of fast-firing neurons in contrast with the sparse-spiking neurons that are flexible and generate trainable action potentials (Grosmark & Buzsáki, 2016). We can consider these sequences as placeholders for the experience-dependent information to plug in. Let me illustrate this concept with the metaphor of a Christmas tree. The preformed sequences are the branches of the Christmas tree, and the experience would decorate them with ornaments. Although the branches limit the positions where ornaments can be placed, a virtually infinite number of ornament arrangements are possible. The heavier the ornament is, the more it bends the branch, hence more lighter ones can be placed on the same branch than heavier ones without bending it. The "bending metaphor" depicts the flexibility of these precursor sequences. Some branches can only hold lighter, and other branches can hold heavier ornaments. Likewise, some precursor sequences can be altered by weaker external input, some others can be altered only by a stronger input. Assuming an intrinsic renewal process, millions of those activity patterns, only different at a cellular level, can spontaneously be generated. Nevertheless, they derive from a few types of attractor-generating algorithms. Most importantly, individual neurons'

roles in reproducing those attractors are interchangeable within the network. This concept has recently reemerged as "*representational drift*" (Pinotsis & Miller, 2022). The intrinsic flexibility of cell assemblies, which allows the reproduction of attractors without re-instantiating the same neuronal sequence, makes the neuronal representation much more robust (Katlowitz et al., 2018). It is redundant but improves stability and reproducibility, and we get noise tolerance out of it for free. In addition, by the spontaneous generation of attractors, the nervous system creates variations not unlike to how Darwinian evolution generates genetic variations and lets natural selection make the fittest survive. In our example, attractor variations that best reproduce external inputs will be pertinent, and other attractors vanish, a concept perfectly aligned with the premise of Darwinian neurodynamics (Szilagyi et al., 2017).

A fundamental feature of spontaneous (self-initiated) attractor generation is the pattern-generating mechanism that generates a variety of sequences without purpose. However, these purposeless sequences will be utilized by the external input (the arrangement of objects, fields, landmarks, visual and proprioceptive inputs, etc.) and modulate the attractor basins that will be transferred between different brain areas for consolidation (for instance, from the hippocampus to the entorhinal and other cortical areas). Instead of a physical transfer, the attractor will trigger copies of the same attractor by impinging on neurons in the target areas, which enables the target area to decode the information (like an engram) mapped to the attractor. With this mechanism, the neuronal networks can generate many different attractor states to transfer together with the stimulus-modulated signal, where the attractor states can act metaphorically as keys to unlock the code of sensory information. This principle foreshadows *phase coding* (chapter 3), where the idea of generating a reference wave for information reconstruction by oscillations will be further exploited.

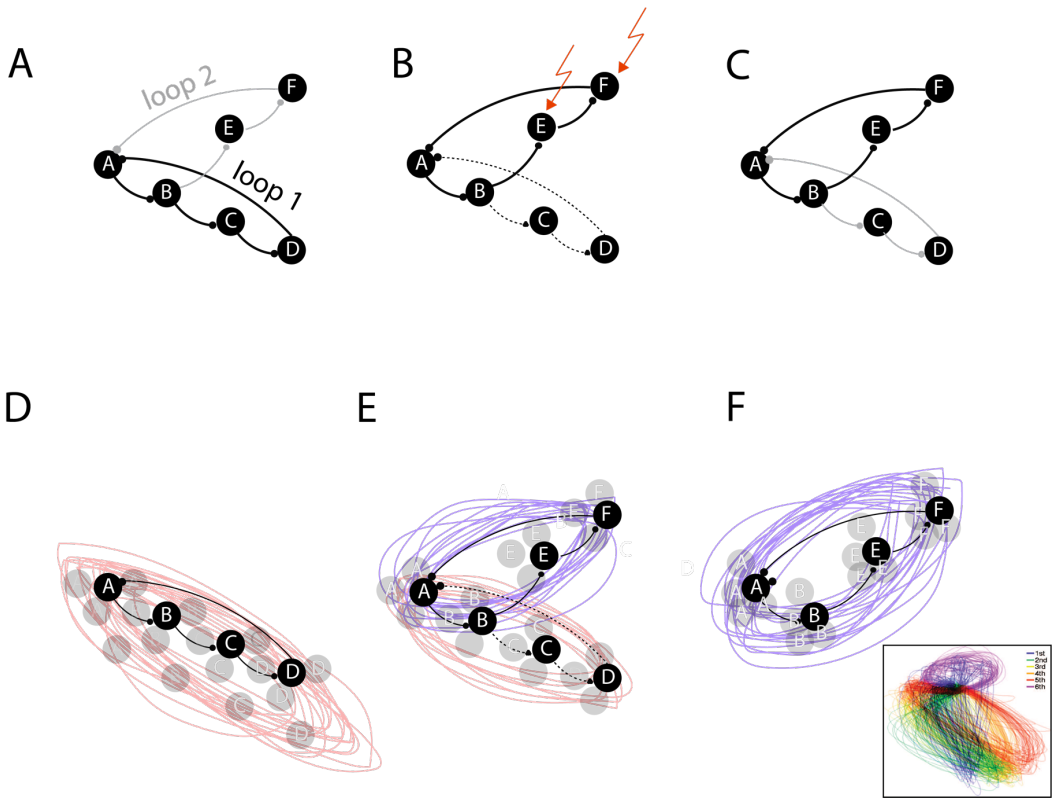

Figure D4: Scheme of switching attractors in a balanced inhibitory-excitatory network. (A) Consider a network of 6 excitatory neurons (A-F) with their active (black) and latent connections (grey). For the sake of simplicity, we omitted inhibitory neurons from the figure. The state space of the network can accommodate two loops. One loop connects neuron A→B→C→D and another loop connects A→B→E→F. Since loop 1 connections are stronger, loop 1 attractor predominates the limit cycle for neuronal activity (red traces in D). (B and E) Stimulation of E and F can switch the attractor from loop 1 to loop 2, which can alter the limit cycle of activity-flow to a new route (purple traces). In the absence of stimulation, the new route (loop 2) may stabilize as a co-existing attractor state C and F). Please note, that each loop of a given limit cycle (same color) may engage different sets of neurons to fire at a specific time without significantly changing the trajectory within the boundaries set by the limit cycle. Inset in (F) represent an empirical data as example of the limit cycle behavior of the neuronal activity in a tissue culture, an excerpt from Figure 5 of Wagenaar, Nadasdy and Potter (2006). (Small circles represent synapses, pink and purple lines are limit cycles representing attractor 1 and attractor 2).

PHYSICAL REVIEW E **73**, 051907 (2006)

Persistent dynamic attractors in activity patterns of cultured neuronal networks

Daniel A. Wagenaar*
Department of Physics, California Institute of Technology, Pasadena, California 91125, USA

Zoltan Nadasdy
Division of Biology, California Institute of Technology, Pasadena, California 91125, USA

Steve M. Potter†
Laboratory of Neuroengineering, Coulter Department of Biomedical Engineering, Georgia Institute of Technology and Emory University, Atlanta, Georgia 30332, USA

(Received 31 January 2006; published 11 May 2006)

Three remarkable features of the nervous system—complex spatiotemporal patterns, oscillations, and persistent activity—are fundamental to such diverse functions as stereotypical motor behavior, working memory, and awareness. Here we report that cultured cortical networks spontaneously generate a hierarchical structure of periodic activity with a strongly stereotyped population-wide spatiotemporal structure demonstrating all three fundamental properties in a recurring pattern. During these "superbursts," the firing sequence of the culture periodically converges to a dynamic attractor orbit. Precursors of oscillations and persistent activity have previously been reported as intrinsic properties of the neurons. However, complex spatiotemporal patterns that are coordinated in a large population of neurons and persist over several hours—and thus are capable of representing and preserving information—cannot be explained by known oscillatory properties of isolated neurons. Instead, the complexity of the observed spatiotemporal patterns implies large-scale self-organization of neurons interacting in a precise temporal order even *in vitro*, in cultures usually considered to have random connectivity.

DOI: 10.1103/PhysRevE.73.051907 PACS number(s): 87.18.−h, 87.19.La

I. INTRODUCTION

In models of neural networks, attractor dynamics displaying complex reverberations emerge naturally if there are sufficient feedback connections [1–3]. Donald Hebb proposed that such reverberations may be used to encode and maintain information in the nervous system [4]. Recurring short spatiotemporal patterns of action potentials recovered from simultaneous recordings of multiple neurons *in vivo*, variously called "sequences" [5,6], or "synfire chains" [7], may be subsamples of such dynamics. Recurring spatiotemporally complex activity patterns has been observed in sensory systems [8], where they have been described in terms of attractor dynamics [9], as well as in motor systems [10]. There is increasing evidence that even *in vitro*, excised brain slices can repeatedly express patterns of activity that are conserved for minutes or hours [11–14].

To test whether specific cortical microstructure is required for the emergence of precise spatiotemporal activity, we studied the activity of cortical neurons in dissociated culture. Neurons in dissociated culture retain many basic physiological properties, but do not develop the typical layered columnar organization of cortical tissue *in vivo*. The electric activity of such cultures is dominated by culture-wide bursts of high-frequency action potential firing, separated by periods of low firing rates [15–19]. Bursting in culture is reminiscent of bursting observed *in vivo* in the developing cortex [20] and elsewhere in the developing nervous system [21], as well as of sleep spindles in the thalamic reticular nuclei [22] and subthalamic nucleus during slow wave activity [23]. Here we report how at certain stages of development burst patterns have a precisely defined spatiotemporal structure that recurs with great fidelity over an interval of many hours. This shows that dissociated cortical networks in culture are capable of generating complex stereotypical behaviors that were previously believed to require specific network architecture.

II. METHODS

A. Cell culture

Dense cultures of rat cortex were prepared on multielectrode arrays (MEAs) as described before [19,24]. Briefly, cortices from E18 rat embryos were dissected and dissociated using papain and trituration. Cells—neurons and glia—were plated at a density of 2500/mm^2, on MEAs coated with poly-ethylene-imine (PEI) and laminin. Cultures were maintained in a serum-containing DMEM-based medium. We recorded daily from 30 cultures from day 3 to day 35 *in vitro*. Five cultures were followed for 2 to 3 days continuously.

*Present address: Division of Biological Science, University of California at San Diego, La Jolla, CA.
†Corresponding author. Email address: steve.potter@ece.gatech.edu

B. Data analysis

1. Spike detection and sorting

Electrical signals from 59 electrodes were sampled at 25 kHz. Putative spikes were detected by thresholding the electrode traces at 4.5× estimated RMS noise. Double detection of multiphasic spikes was prevented by discarding candidate spikes in a ±0.5 ms window around spikes of larger amplitude.

Most subsequent analysis was performed using multi-unit activity, obtained from 59 electrodes in a square grid with 200 μm spacing. In two cultures, we analyzed single-unit activity, obtained by using an unsupervised spike sorting method [25] with cross- and autocorrelation verification. Only the largest four spike clusters per electrode (i.e., four neurons with highest firing rates) were included in the data analysis. To ensure stability of clusters over time, the sorting was done in data segments of 400 with 40 s overlaps. The redundant clustering on the overlaps allowed us to match spike clusters consistently across segments. Spike clusters were tested for refractoriness. In both cultures the sorting resulted in 236 putative neurons (59 electrodes × 4 clusters).

Cross-correlation analysis revealed that inter-electrode spacing was such that cells did not evoke potentials on more than one electrode. This also implied that using multi-unit data does not compromise the spatial resolution of the analysis.

2. Burst identification

Bursts were detected by means of the SIMMUX algorithm [26]. Briefly, each electrode trace was searched for *burstlets*: sequences of at least four spikes with all interspike intervals less than a threshold (set to 1/4 of that electrode's inverse average spike detection rate, or to 100 ms, whichever was less). Any group of burstlets across several electrodes that overlapped in time was considered a *burst*.

3. Similarity indices

A superburst similarity index S_{super} was computed based on the (multi-unit) firing rate summed over all electrodes. For each superburst n, we computed this firing rate, $f_n(t)$, in 50 ms Gaussian sliding windows (sampled at 500 Hz). $f_n(t)$ was set to zero for $t<0$ or $t>$ (the duration of superburst n). The similarity index $S_{\text{super}}(n,m)$ between two superbursts n and m was then defined as the correlation coefficient between the functions f_n and f_m, optimally time-shifted:

$$S_{\text{super}}(n,m) = \max_{\tau}\left(\frac{\int (f_n(t)-\overline{f_n})(f_m(t+\tau)-\overline{f_m})dt}{\sqrt{\int (f_n(t)-\overline{f_n})^2 dt}\sqrt{\int (f_m(t)-\overline{f_m})^2 dt}} \right),$$

where $\overline{f_n}$ is the average of $f_n(t)$ over the duration of the superburst.

A subburst similarity index S_{sub} was based on the times at which individual electrodes started to record bursts. The onset time $t^c_{\text{on}}(n,k)$ of electrode c in the kth subburst of the nth superburst was defined as the moment when the baseline-substracted firing rate first increased to 25% of its peak during that subburst. [This use of relative thresholds ensured that differences in firing rates between electrodes did not cause a systematic bias in onset time estimation. We tested the independence of onset time estimates and firing rates by calculating the Pearson correlation coefficient, and found it was negligible ($r=-0.05$, $p=0.13$; $N=845$).] The similarity index $S_{\text{sub}}(n_1,k_1;n_2,k_2)$ between two subbursts (n_1,k_1) and (n_2,k_2) was then defined as the correlation coefficient between onset times across electrodes:

$$S_{\text{sub}}(n_1,k_1;n_2,k_2) = \frac{\sum_c (t^c_{\text{on}}(n_1,k_1)-\overline{t_{\text{on}}}(n_1,k_1))(t^c_{\text{on}}(n_2,k_2)-\overline{t_{\text{on}}}(n_2,k_2))}{\sqrt{\sum_c (t^c_{\text{on}}(n_1,k_1)-\overline{t_{\text{on}}}(n_1,k_1))^2}\sqrt{\sum_c (t^c_{\text{on}}(n_2,k_2)-\overline{t_{\text{on}}}(n_2,k_2))^2}},$$

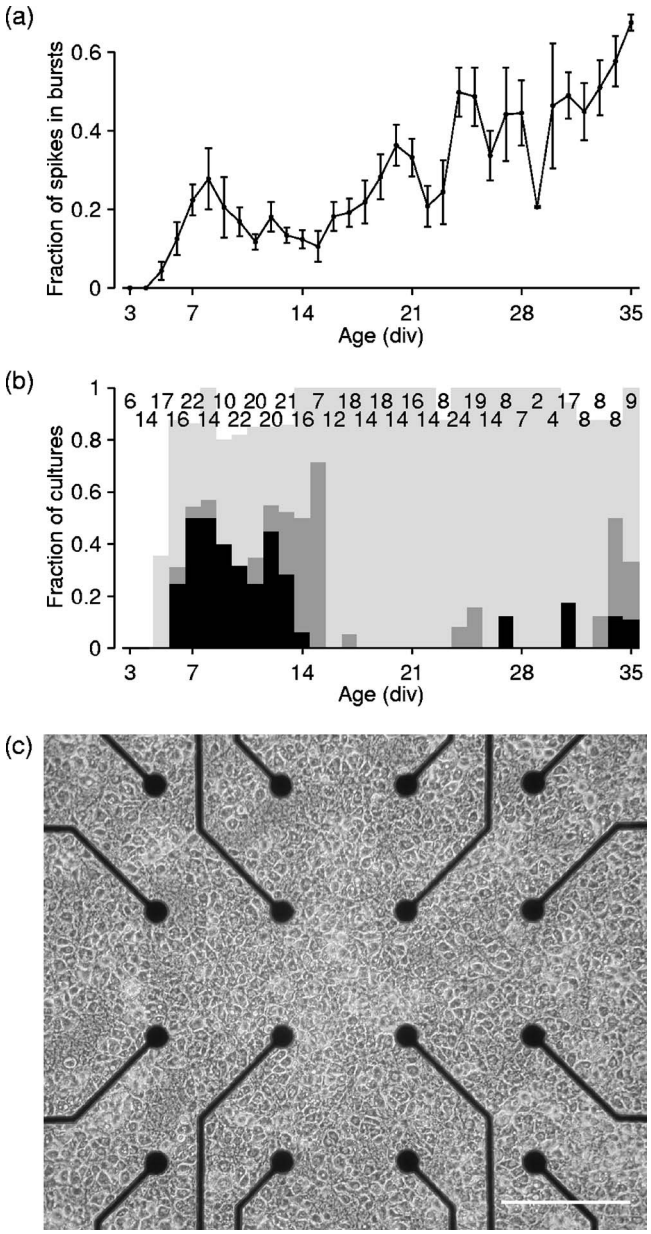

FIG. 1. Development of bursting. (a) The fraction of spikes that occur in large bursts (rather than during tonic dispersed firing) grows with culture age [measured in days *in vitro* (div)]. Here, "large" means at least 5 participating sites with a total of at least 50 spikes. (b) Fraction of cultures that fire superbursts exclusively (black) or superbursts mixed with other bursts (dark gray). Light gray indicates fraction of cultures that exhibits any kind of bursts. Numbers on top indicate number of cultures studied at each age. (c) Phase contrast micrograph of a superbursting culture at 9 div. Scale bar: 200 μm.

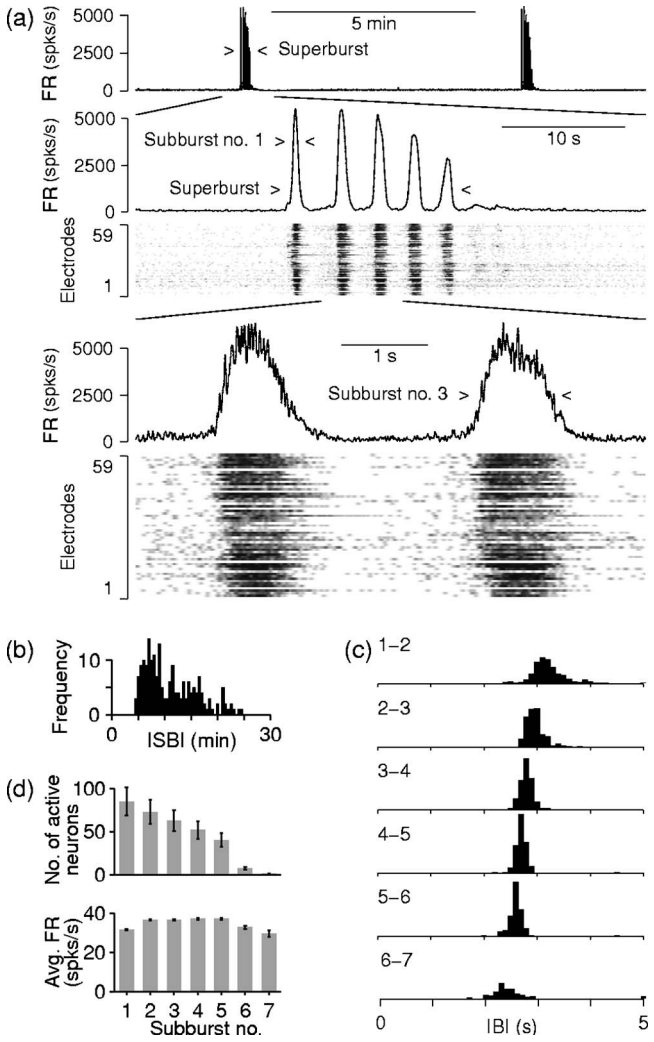

FIG. 2. (a) An example of a 10 min data segment illustrates the typical two-level temporal organization of population activity in superbursts. Firing rates (FR) are culture-wide aggregates. Simultaneous raster plots from 59 electrodes reveal that nearly all electrodes record from neurons participating in this structure. Note that the beginning of each burst occurs at slightly different times at different electrodes, defining a characteristic onset-time profile. This is further explored in Figs. 3(d) and 3(e). (b) The distribution of intervals between 195 superbursts recorded over a 35 h period (inter-superburst intervals; ISBI). (c) The distributions of the intervals between subbursts within superbursts (inter-burst intervals; IBI). Histograms show all subburst intervals at a fixed ordinal position (indicated on top-left) in their superbursts. (d) Number of active neurons (top) and average firing rate per active neuron (bottom), per subburst. Spike sorting was performed using superparamagnetic clustering [25].

where $\overline{t_{\mathrm{on}}}(n_i,k_i)$ is the mean onset time of the k_ith subburst of the n_ith superburst across electrodes. Only electrodes with peak firing rates of at least 75 spikes per second were used in this calculation (typically: 40 electrodes).

4. Return plots

We performed return plot analysis on the onset latencies of individual electrodes in successive bursts, defined as $\lambda^c_{n,k} \equiv t^c_{\mathrm{on}}(n,k) - \overline{t_{\mathrm{on}}}(n,k)$. After spike sorting, we repeated this analysis at the level of single neurons. Return plots elucidate higher order temporal relationship between successive events, by recursively plotting the latency of the nth event against the latency of the $n+1$st. The appearance of clusters in return plots indicates a conserved temporal pattern in successive events, and the spread of clusters reflects the precision of conservation. When comparing return plot correlation coefficients at electrode level with those at single cell level,

TABLE I. Compendium of parameters for all five extended recordings.

	CultureNo.1	No.2	No.3	No.4	No.5
Age (div)	10	19	9	8	12
Duration of superbursting (h)	63	11[a]	41	49	3[a]
Number of superbursts	292	49	94	154	24
Average number of subbursts	7	12	3	7	5
Superburst similarity index S_{super} (see text)	0.89	0.81	0.73	0.76	0.81

[a]These cultures were still superbursting when the recording was terminated.

we balanced the sample size by randomly sub-sampling the population spikes. Thus we obtained an unbiased estimate of reproduction fidelity.

III. RESULTS

Bursting in dissociated cultures commenced after 5–8 days *in vitro* (Fig. 1), and persisted throughout a culture's lifetime (over one year [24]). During most of a culture's life, burst patterns were relatively unstructured. Burst frequencies ranged from 1 to 30 per minute, and appeared to be generated by a Poisson-like process modulated by a refractory period of 1–5 s. However, a majority of cultures (18 out of 30 cultures followed) passed through a developmental period lasting 3–5 days during the second week *in vitro*, during which burst patterns acquired a large degree of structure. During such epochs, bursts occurred in sequences of 5–12, with inter-burst intervals of 2–4 s (Fig. 2(a) and Movie 1 [45]). These sequences, which we call "superbursts," were separated by 1–10 min with a steady low firing rate (<0.2 spikes/electrode/second). In contrast, the firing rate of the cells increased almost 100-fold when transitioning from nonbursting to bursting mode, implying that population-wide interactions of neurons were only enabled during the bursting phases. The intervals between superbursts were consistent with a Poisson process modulated by refractoriness [Fig. 2(b)]. In contrast, the intervals between the constituent bursts ("subbursts") within superbursts were highly stereotyped [Fig. 2(c)]. The number of bursts per superburst was likewise strongly conserved over long periods of time, though it varied considerably from culture to culture. As for the constituent bursts themselves, the first burst in a superburst typically contained the largest number of spikes, followed by a gradual decline, due to a reduction in the number of participating neurons. Remarkably, single-neuron firing rates remained nearly constant during most of the superburst [Fig. 2(d)]. In Fig. 2 as well as in the following, we concentrate on results obtained from the longest recorded superburst epoch (63 h). Results from all extended recordings are summarized in Table I.

The overall structure of superbursts in any given culture persisted for hours, and any changes were usually discontinuous. To quantify this observation, we measured the array-wide aggregate of the firing rate in 50 ms sliding windows. This yielded a firing rate profile for each superburst [Fig. 3(a)]. We defined a "superburst similarity index," S_{super}, between a pair of superbursts as the correlation coefficient between their firing rate profiles (aligned to maximize S_{super}, but not time-warped; see *Methods*). The similarity index between consecutive superbursts was very high (>90% on average), and remained high (>80%) between pairs of superbursts separated by dozens of other superbursts [Fig. 3(c)]. The matrix form of S_{super} of our longest recording is characterized by a block-diagonal structure, indicating that changes in the temporal structure of population firing during superbursts occurred in discrete steps of varying size [Fig. 3(b)].

Like the global activity profile, the spatiotemporal dynamics of the activity spreading across the culture were also preserved within and across superbursts. We quantified this by the relative times at which individual electrodes started to record each subburst, and combining those into a (59-dimensional) vector, which constitutes an "onset-time profile" for the subburst. We defined a "subburst similarity index," S_{sub}, as the correlation coefficient between pairs of such vectors (see *Methods*). This revealed considerable similarity between subbursts within a superburst, particularly between the second and fifth subbursts [Fig. 3(d)]. Moreover, homologous (like-numbered) subbursts had very similar onset profiles between consecutive superbursts [Fig. 3(e)]. Between the second and fifth subbursts, this "inter-superburst" S_{sub} exceeded the "intra-superburst" S_{sub}. Comparing pairs of superbursts with more time between them, the S_{sub} index between the first subbursts was much reduced, indicating a gradual change of the state of the network. In striking contrast, the S_{sub} index between the second and fifth subbursts remained high, indicating that, despite this gradual change, the superburst attractor is conserved, and that the attractor trajectory can be reached from many different initial conditions.

For another view of the dynamics of burst onset, we constructed return plots of the onset latencies of individual electrodes both between consecutive subbursts within a superburst, and between homologous subbursts of successive superbursts. After spike sorting, analogous plots were constructed at the single-cell level, to help determine whether the activity of specific neurons was crucial to the structure of superbursts. If individual neurons play conserved roles in different bursts, their relative burst onset latencies should be conserved from burst to burst, causing the latencies to line up along the diagonal of the return plot. Moreover, the latencies of an individual cell should cluster in a confined region along the diagonal. Both effects are indeed evident in Fig. 4. The relative latencies of different elec-

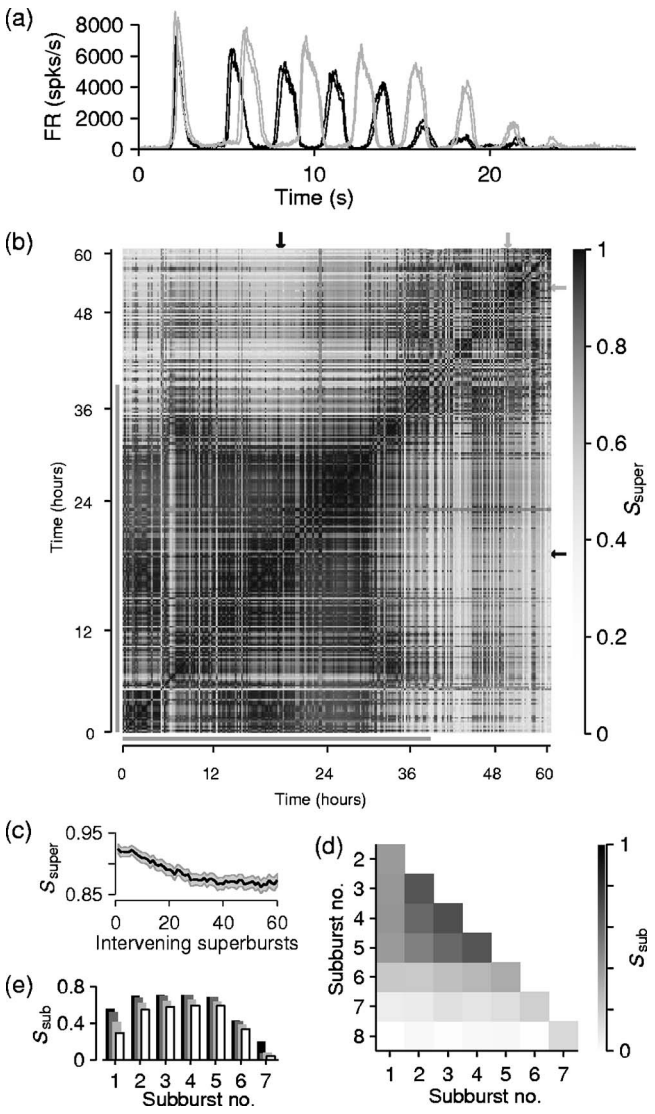

FIG. 3. Conservation of firing rates and activity propagation between superbursts. (a) Aggregate firing rates of two pairs (one pair black, one pair gray) of consecutive superbursts separated by 30 h comprising 150 superbursts (not shown here). While consecutive superbursts are seen to be almost indistinguishable in shape the difference after 30 h is apparent. (b) A matrix of the global similarity index (S_{super}; see text) between superbursts recorded over a 63 h period. Two main blocks of strongly conserved similarity can be distinguished. Black and gray arrows mark examples shown in (a). Gray bars mark portion of data used in (c)–(e). (c) Even with dozens of intervening superbursts, the S_{super} index between superbursts separated by many hours remains very high. (Mean ± SEM for 170 superbursts.) (d) Subburst similarity index (S_{sub}; see text) between bursts within a superburst, averaged over 170 superbursts. A conserved structure is observed between subbursts 2 and 5. (e) S_{sub} index between homologous subbursts across superbursts. Between consecutive superbursts (black), the second through fifth subbursts are more conserved than the first subburst. Between superbursts 30–60 min apart (dark gray), 1 to 2 h apart (light gray) or 6–24 h apart (white), this effect is even more pronounced.

trodes were consistent across successive component bursts [$r=0.55$; $p<0.01$; Fig. 4(a)]. Individual neurons engage in the successive bursts with similarly precise latency relative to other neurons [$r=0.58$; $p<0.01$; Fig. 4(b)]. A neuron that started bursting earlier than the population would always be earlier than a neuron that started bursting later [Fig. 4(c)]. The gross conservation of latencies was complemented by a systematic drift in the onset latencies for a given neuron across successive component bursts [Fig. 4(d)]. Relative onset latencies of different neurons were also strongly preserved between homologous components of consecutive superbursts [$r=0.57$; $p<0.01$; Fig. 4(e)]. The observation that the latency profile is consistent across subbursts and superbursts implies that the transition from tonic to burst-firing propagates across the culture following a similar path each time. Since the burst onset order at cellular level was slightly more consistent than at electrode level ($r=0.58$ verus $r=0.55$), we concluded that this path must be dependent on the transmission between individual neurons. Given that this difference was small, however, we mostly used electrode-level dynamics for the subsequent analysis, since that level allowed for higher precision (due to larger spike counts).

After burst onset, the subsequent firing rate dynamics were also conserved. We visualized the temporal evolution of superburst dynamics with a phase plot of the aggregate firing rate (in 100 ms sliding windows) during superbursts [Fig. 5(a)]. The discrete bands formed by the orbits of homologous subbursts are signatures of the distinctive propagation dynamics that consistently recur with each superburst. The systematic variation of subburst trajectories suggests that the generation of superbursts is determined by a higher order attractor that unfolds in different well-defined propagation patterns for each subburst. The reproduction of the same dynamics in each subsequent superburst cannot be explained by intrinsic oscillatory features of individual neurons. Instead, the reproduction depends on the state of the whole network, which imposes on each neuron a precise input configuration that regenerates via recurrent connections. The bands formed by the second through fifth subbursts were much closer together than the band of the first subbursts, re-affirming that the initial stages of the superbursts were variable, while subsequent bursts self-organized into a precise temporal pattern—a dynamic attractor—that was stable for hours or days.

All measures discussed so far focus on the temporal structure of the observed recurring activity patterns, and do not speak directly to their spatial structure. For a simple metric of the spatial aspects of superburst dynamics, we defined the horizontal differential firing rate of a culture as the aggregate firing rate in the right half of the array minus the aggregate firing rate in the left half of the array (in 200 ms sliding windows). A vertical differential firing rate was analogously defined. The orbits of superbursts in the state space of differential firing rates show that the preservation of burst shape increases from the first to fifth subbursts [Fig. 5(b)]. The sixth subbursts, which mark the end of the superburst structure for this culture, have orbits of distinctly different shapes than the earlier subbursts.

FIG. 4. (Color) Return plots [explained in (f) and (g)], representing the temporal structure of burst propagation by recursively plotting the latencies at which a cell or electrode starts to participate in one burst against its latency in the next (or next homologous) burst. (a) Electrode-level return plot of burst onset latency from the fourth to the fifth subburst in successive superbursts. The diagonal represents exact latency preservation. Electrodes are color-coded according to the inset. (b) The same return plot as in (a), but instead of combining all spikes from a given electrode, we isolated the most active single unit from each electrode. Color code as in (a). Note how closely the single-unit activity matches the multi-unit activity. (c) The burst onset latency return plot for two neurons, extracted from (b). One neuron (blue) was selected that tended to burst early, and one (red) that tended to burst late. Inset shows the locations of the two neurons. (d) Single-neuron return plots of burst latency across different subbursts, for the blue neuron in (c). Interval number is color-coded. (e) Single–neuron level return between the fifth component-bursts across successive superbursts. (f) and (g) Explanation of return plots: (f) In (a)–(d), features of successive subbursts within a superbursts are compared; (g) In (e), features of homologous subbursts of successive superbursts are compared.

IV. DISCUSSION

The locations and connectivity of neurons in culture, at least at the outset, is random. This is a consequence of the method of dissociation and seeding onto the substrate; we made no efforts to create defined structure in the networks, e.g., by using patterned or micromachined substrates as others have [27–30]. The assumption has been that activity in such 'random' networks will likewise be without coherent structure. Nevertheless, self-organization of activity patterns into a two-level structure of subbursts and superbursts was consistently observed (Table I). While superbursts appeared at irregular intervals, their internal structure was highly regular and strongly conserved for hours or days: Once a superburst had been initiated, it generated a constant number of subbursts that each had its own well-preserved geometry of propagation and temporal dynamics. This preservation was found to be precise at the single-neuron level. The spontaneous occurrence of superbursts shows that neurons and glia retain an ability to self-organize into multicellular ensembles with nontrivial functional structure, even when taken out of their physiological context.

Bursting has been described in dissociated cortical culture (e.g., [17,19,31–38]), but previously described bursts did not exhibit the two-level structure of superbursts. In MEA recordings from dissociated cultures of neonatal rat cortex, Segev *et al.* [37] found bursts that clustered into several distinct types based on their spatiotemporal substructures, and that these substructures were reproduced with high fidelity over several hours. We similarly find conservation of the spatiotemporal substructure of bursts, but in addition find conservation of sequence: Figure 5 shows that the substructures of all subbursts at a given ordinal position in

FIG. 5. (Color) Spatiotemporal structure of superbursts. (a) Phase plots of the aggregate firing rate for 50 consecutive superbursts. The delay, 500 ms, is short enough to not mix subbursts. The sequential order of trajectories is indicated by different colors. (b) *X-Y* plot of differential firing rate (see text) for the same 50 superbursts.

their superbursts are similar to each other, and distinct from those at different positions. Interestingly, in cortical slices, a different kind of bursts has been observed, at a shorter time scale, governed by a critical branching process reminiscent of avalanches [12]. These bursts consisted of precisely defined firing patterns lasting tens of milliseconds. A given slice could exhibit several different patterns, each of which was conserved for multiple hours [13]. Given the disparity of time scales, both kinds of bursts could in principle co-exist in the activity patterns of a neuronal ensemble, although we have no evidence of preserved firing sequences on a millisecond scale in our cultures.

In vivo, short conserved patterns of activity have been described in several preparations, in terms of action potentials [5,6], or intracellular calcium increases [11,14], and fixed-point attractors have been observed in the form of up/down state transitions [39]. Superbursts constitute much longer and more detailed patterns, and are among the longest conserved activity patterns observed in any neural system to date. In *in vivo* experiments, such patterns may have remained hidden because only a small fraction of the neurons from a large ensemble were monitored, or because recordings were too short. By contrast, the use of dissociated cultures permitted us to monitor and evenly sample an entire intact network for weeks.

The coordination of cellular dynamics at the superburst level indicates that information is maintained by a global dynamic process which persists orders of magnitude longer than the time constants of synaptic processing. This allows the information to be protected from the interference of local processing: Individual neurons can engage in multiple functions without disrupting the recurring motif reverberating in the larger-scale circuitry of the culture. Such globally organized and tightly orchestrated activity is of critical importance for any neuronal tissue that generates highly stereotyped sequential behaviors, from locomotion to language. The same mechanism may also support a sensory persistence and memory that does not require synaptic plasticity. *In vitro* systems are ideal for studying in detail the conditions that allow such activity patterns to emerge, and for testing mathematical models of neuronal pattern generation at a population level with cellular precision. Moreover, the robustness of the complex pattern generation behavior can open avenues for computation and artificial intelligence applications such as controlling hybrid neural-robotic systems [40–42]. We are currently experimenting with triggering superbursts with electrical stimulation [43], and initial results look promising. A critical issue for future study is whether an electrical stimulation paradigm can be used to modify the attractors in a controlled manner, as required for learning [44].

ACKNOWLEDGMENTS

We thank Jerry Pine for useful discussions, and Sheri McKinney for technical assistance with cell culture. This work was partially supported by Grants Nos. NS38628 and NS44134 from NINDS, and EB00786 from NIBIB, and by the Whitaker Foundation and the NSF Center for Behavioral Neuroscience.

[1] H. R. Wilson and J. D. Cowan, Kybernetik **13**, 55 (1973).

[2] D. J. Amit, *Modeling Brain Function: The World of Attractor Neural Networks* (Cambridge University Press, Cambridge, 1989).

[3] X. J. Wang, Trends Neurosci. **24**, 455 (2001).

[4] D. O. Hebb, *The Organization of Behavior: A Neuropsychological Theory* (Wiley, New York, 1949).

[5] Y. Prut, E. Vaadia, H. Bergman, I. Haalman, H. Slovin, and M.

Abeles, J. Neurophysiol. **79**, 2857 (1998).
[6] Z. Nádasdy, H. Hirase, A. Czurkó, J. Csicsvari, and G. Buzsáki, J. Neurosci. **19**, 9497 (1999).
[7] M. Abeles, *Corticonics: Neural Circuits of the Cerebral Cortex* (Cambridge University Press, Cambridge, 1989).
[8] M. Stopfer, V. Jayaraman, and G. Laurent, Neuron **39**, 991 (2003).
[9] M. Rabinovich, A. Volkovskii, P. Lecanda, R. Huerta, H. D. I. Abarbanel, and G. Laurent, Phys. Rev. Lett. **87**, 068102 (2001).
[10] A. Leonardo and M. S. Fee, J. Neurosci. **25**, 652 (2005).
[11] Y. Ikegaya, G. Aaron, R. Cossart, D. Aronov, I. Lampl, D. Ferster, and R. Yuste, Science **304**, 559 (2004).
[12] J. M. Beggs and D. Plenz, J. Neurosci. **23**, 11167 (2003).
[13] J. M. Beggs and D. Plenz, J. Neurosci. **24**, 5216 (2004).
[14] J. N. MacLean, B. O. Watson, G. B. Aaron, and R. Yuste, Neuron **48**, 811 (2005).
[15] H. Kamioka, E. Maeda, Y. Jimbo, H. P. C. Robinson, and A. Kawana, Neurosci. Lett. **206**, 109 (1996).
[16] R. Segev, M. Benveniste, E. Hulata, N. Cohen, A. Palevski, E. Kapon, Y. Shapira, and E. Ben-Jacob, Phys. Rev. Lett. **88**, 118102 (2002).
[17] J. van Pelt, M. A. Corner, P. S. Wolters, W. L. C. Rutten, and G. J. A. Ramakers, Neurosci. Lett. **361**, 86 (2004).
[18] M. H. Droge, G. W. Gross, M. H. Hightower, and L. E. Czisny, J. Neurosci. **6**, 1583 (1986).
[19] D. A. Wagenaar, J. Pine, and S. M. Potter, BMC Neurosci. **7**, 11 (2006).
[20] C. Y. Chiu and M. Weliky, J. Neurosci. **21**, 8906 (2001).
[21] M. J. O'Donovan, Curr. Opin. Neurobiol. **9**, 94 (1999).
[22] D. Contreras, A. Destexhe, T. J. Sejnowski, and M. Steriade, J. Neurosci. **17**, 1179 (1997).
[23] P. J. Magill, A. Sharott, J. P. Bolam, and P. Brown, J. Neurophysiol. **92**, 2122 (2004).
[24] S. M. Potter and T. B. DeMarse, J. Neurosci. Methods **110**, 17 (2001).
[25] R. Q. Quiroga, Z. Nadasdy, and Y. Ben-Shaul, Neural Comput. **16**, 1661 (2004).
[26] D. A. Wagenaar, T. B. DeMarse, and S. M. Potter, in *Proc. 2nd Intl. IEEE EMBS Conf. on Neural Eng.* (2005), pp. 518–521.
[27] P. Clark, P. Connolly, A. S. Curtis, J. A. Dow, and C. D. Wilkinson, Development **99**, 439 (1987).
[28] D. Kleinfeld, K. H. Kahler, and P. E. Hockberger, J. Neurosci. **8**, 4098 (1988).
[29] D. W. Branch, J. M. Corey, J. A. Weyhenmeyer, G. J. Brewer, and B. C. Wheeler, Med. Biol. Eng. Comput. **36**, 135 (1998).
[30] D. A. Stenger, J. J. Hickman, K. E. Bateman, M. S. Ravenscroft, W. Ma, J. J. Pancrazio, K. Shaffer, A. E. Schaffner, D. H. Cribbs, and C. W. Cotman, J. Neurosci. Methods **82**, 167 (1998).
[31] Y. Jimbo, H. P. C. Robinson, and A. Kawana, IEEE Trans. Biomed. Eng. **40**, 804 (1993).
[32] P. E. Latham, B. J. Richmond, S. Nirenberg, and P. G. Nelson, J. Neurophysiol. **83**, 828 (2000).
[33] R. Segev, Y. Shapira, M. Benveniste, and E. Ben-Jacob, Phys. Rev. E **64**, 011920 (2001).
[34] T. Opitz, A. D. De Lima, and T. Voigt, J. Neurophysiol. **88**, 2196 (2002).
[35] T. Tateno, A. Kawana, and Y. Jimbo, Phys. Rev. E **65**, 051924 (2002).
[36] D. A. Wagenaar, R. Madhavan, J. Pine, and S. M. Potter, J. Neurosci. **25**, 680 (2005).
[37] R. Segev, I. Baruchi, E. Hulata, and E. Ben-Jacob, Phys. Rev. Lett. **92**, 118102 (2004).
[38] E. Hulata, I. Baruchi, R. Segev, Y. Shapira, and E. Ben-Jacob, Phys. Rev. Lett. **92**, 198105 (2004).
[39] R. Cossart, D. Aronov, and R. Yuste, Nature (London) **423**, 283 (2003).
[40] D. J. Bakkum, A. C. Shkolnik, G. Ben-Ary, P. Gamblen, T. B. DeMarse, and S. M. Potter, in *Embodied Artificial Intelligence*, edited by F. Iida, L. Steels, and R. Pfeifer (Springer-Verlag, 2004), pp. 130–145.
[41] Z. C. Chao, D. J. Bakkum, D. A. Wagenaar, and S. M. Potter, Neuroinformatics **3**, 263 (2005).
[42] T. B. DeMarse, D. A. Wagenaar, A. W. Blau, and S. M. Potter, Auton. Rob. **11**, 305 (2001).
[43] D. A. Wagenaar, J. Pine, and S. M. Potter, J. Neurosci. Methods **138**, 27 (2004).
[44] G. Shahaf and S. Marom, J. Neurosci. **21**, 8782 (2001).
[45] See EPAPS Document No. E-PLEEE8-73-109605 for a movie showing an example of a superburst in real time. For more information on EPAPS, see http://www.aip.org/pubservs/epaps.html.

Chapter 3

8. Can phase be the code?

> *"But where is the information in this chaos? It can be shown that it (the hologram) is not as irregular as it appears. It is not as if grains of sand had been scattered over the plate at random. It is rather a complicated figure, the diffraction pattern of the object, which is repeated at random intervals, but always in the same size and same orientation."*
>
> *(Dennis Gabor: Holography, 1948-1971, Nobel Lecture, December 11, 1971)*

I can hardly think of an idea more compelling than the notion that everything from subatomic particles through biological systems to the galaxies and beyond, including the history of the universe from one Big Bang to the next one, oscillates. The states of neurons in our brains are no exception. However, the adoption of the concept that oscillations constitute an integral part of neural computation took a long time. While in physics, the dual nature of particles is a well-established fact (for instance in the dual-slit experiment, photons behave as continuous waves under one detection condition and as particles in another), a similar duality has long been denied in neuroscience for a long been. Many prominent neuroscientists are still skeptical about the role of oscillations in the brain and consider them as epiphenomena or byproducts of neuronal activity, but rhythms themselves are not causally related to the computational role of neurons. One of the biggest conceptual barriers in neuroscience today is the integration of oscillations with the discrete nature of neural computation. In this regard, phase coding may bridge the conceptual gap between continuous rhythms and the quantal nature of action potentials.

The idea that the phase of action potentials encode information has surfaced in different contexts at different times in the last 50 years but was never fully integrated into a coherent theoretical framework. Likewise, it represents a methodologically diverse domain in the map of neural coding. My 2009 and 2010 papers were overt attempts to make a case for an integrated general theory of phase coding (Nadasdy, 2009, Nadasdy 2010). The theoretical foundation laid on four different models:

I. Binding by synchrony
II. Theta phase precession
III. Latency coding
IV. Synfire chains

I. In chronological order, McCullough and Pitts proposed first that neurons may represent logical operators such as “AND” gates, “X OR” gates, and “NOT” gates, and the combination of those can implement any computation (McCulloch & Pitts, 1943). This was inspired by the transistor technology in digital computers from early on. Even before McCullough and Pitts, Alen Turing defined how simple writing and reading of a tape can implement the algorithm of computability (Turing, 1937). The common problem that all these approaches had to solve was segmentation of messages. The computer needs to know when a message starts and ends, and it needs to know whether the next number on the tape (or register) is an instruction or a piece of data. This was not an issue for Adrian who posited that sensory input in a peripheral nerve was decoded by spinal-cord neurons using a firing-rate code (Adrian, 1954) because everything those neurons relayed was data that spinal sensory neurons integrate over time continuously. However, it becomes an issue when sensory information enters the circuitries of the cerebral cortex. In cortical circuitries, there is neither time nor dedicated storage capacity to buffer the input of neurons to count spikes over time before deciding whether the average spike rate exceeds a threshold or not. Cortical neurons integrate the excitatory postsynaptic potentials over the entire dendritic space within a small time window (~15-20 ms) (Eyal et al., 2018). There is an obvious trade-off between the time window of obtaining a firing-rate estimate from a distribution of spikes and the precision of that estimate. The longer the time window is the more precise the firing rate estimate becomes. Therefore, we can assume that peripheral and sympathetic nerves integrate over a longer period and smaller dendritic space, while cortical neurons integrate over a shorter period and larger dendritic space.

Amongst the first few researchers who recognized the insufficiency of firing-rate models in cortical information processing was Moshe Abeles who wrote a seminal paper about cortical pyramidal neurons as coincidence-detectors (Abeles, 1982). This resonated strongly with the McCulloch-Pitts neuron model (McCulloch & Pitts, 1943) by placing the AND gate inside the neurons. With this mechanism, neurons are able to select the relevant information from the bombardment of input in real-time based on the temporal association of two or more inputs. This concept

was borrowed by von der Malsburg (Bienenstock & Malsburg, 1987) under a new cover name of "*binding-by-synchrony*" (BbS). The empirical evidence was provided by the experiments of Wolf Singer and Charles Gray (Gray & Singer, 1989). They recorded V1 neurons in the lightly anesthetized cat and observed an increased gamma-band modulation evident from the autocorrelation of the LFP with a concomitant phase locking of unit-activity in response to coherently moving edges in the visual display. The result was concordant with the BbS framework, which predicted that invariant features of objects (contours, shapes, colors) can be captured by a subset of simultaneously activate neurons that are tuned to those features. The combination of simultaneously active neurons represents a combination of features invariant of our movement, or our eyes' movements, or the object's movement, rotation or other transformation. Hence, the role of gamma rhythm is to define the time window within which this simultaneity manifests. If neurons at next level receiving input from the feature detector cells act like coincidence detectors, they can keep track of the synchronized subset of neurons. Hence, those neurons that coactive in a gamma cycle "binds" a dissociated set of features into a "gestalt" shape, where the gestalt becomes the precursor of objects. This is how neurons embedded in a gamma rhythm can segment the visual input according to objects, foregrounds and backgrounds, shapes, planes and surfaces efficiently within a very short time by conjunctive combinations of features that move together (von der Malsburg, 1999).

Synchronized gamma oscillations shared across neurons driven by iso-oriented drifting gratings provided the missing link, the time frame of coincidences, within which neurons downstream can read the output of coincidence detectors and extract correlating features. The surface texture of a moving object will elicit simultaneous activity in many neurons within V2 and that synchrony can be detected by downstream coincidence-detector neurons at each gamma cycle. This mechanism was able to explain any associative binding between stimuli that made up the concept of objects. Even multisensory inputs such as sound, touch, and visual cues can be combined in a flexible way by BbS. Pieces of this puzzle suddenly fell into place and the concept of BbS went viral in the early 90s. Wolf Singer devoted his research carrier to rigorously proving the idea that gamma-synchrony provides the fundamental organizing principle for neuronal coalition formation. The principle of

BbS is thrilling because it also explained multiplexing, the idea that synchronization between one subset of neurons can functionally link those neurons together for a period, while the same neurons can be part of other coalitions at another time. In addition, multiplexing of neuronal activity over neurons during different tasks, as we have seen in the previous chapter, was one of the unsolved issues.

The concept that neurons form coalitions by synchrony fits nicely with Hebb's concept of cell-assembly (Hebb, 2005). In addition, learning by adapting to that synchrony can be implemented by Hebb's rule, which postulates that coincidence between synaptic input to a neuron enhances the efficacy of signal transmission through that synapse, i.e., amplify the impact of input conveyed by that connection, or, in simulations, strengthens the weight of that synapse: "neurons that fire together also wire together". While all puzzle pieces seemed to fall in place, the BbS did not fulfill the promise of explaining all functions, and the empirical support for gamma synchrony was partial (Shadlen & Movshon, 1999; Tan et al., 2014). Gamma, in vivo in the mammalian brain is much more volatile than predicted by the models. It also forms propagating waves that destabilize standing waves, the necessary condition for a BbS (Bahramisharif et al., 2013). Propagating gamma waves make synchrony break down over a distance as opposite phases cancel when integrating gamma oscillations over a larger area. Therefore, the model of BbS fell short of fulfilling the premise of providing an all-encompassing model for neural computation. I argue that this was due to the limitation that BbS only considered standing waves, a notion that was never explicitly stated, but the traveling wave alternative was not considered. According to BbS, neurons either synchronize with gamma or desynchronize, but phase coherence, which allows for coupling between oscillators that are not synchronous was outside of the scope. This new direction motivated my paper in 2010 "Binding by Asynchrony" where I argued that instead of synchrony, the subtle asynchrony of phases may represent information, an idea we will unpack later in this chapter.

II. During this academic debate between the temporal-coding models (BbS was one of them) and rate-coding models, mostly behind the back of the primate and cat electrophysiologists, a paradigm shift started. But instead of the context of sensory or motor systems, it started in the field of hippocampal electrophysiology tanks to

the rapidly advancing electrode and amplifier technology capable of recording stable multiple single-units and LFP on freely moving rodents during natural behavior relatively artifact-free. In rodents, the most prominent oscillation that correlates with the active exploratory behavior in the awake animal (but also during REM sleep) is theta. Theta derives from the medial septum cholinergic neurons and entraining rhythmic activity of hippocampal, parahippocampal, and entorhinal neurons. Theta has a major influence on pyramidal cell firing. By rhythmic depolarization and hyperpolarization of pyramidal cells in the dentate, CA1, CA2, and CA3 area, theta modulates the firing likelihood of these neurons. It defines the bouts of pyramidal cell activity. Theta phase locks to the whisking cycles (Grion et al., 2016), as well as provides temporal modulation for place cells firing with an initial phase-coupling, precession and decoupling stages (Souza & Tort, 2017).

The most surprising discovery in context to theta rhythm was made by John O'Keefe and Michael Recce in 1993 (O'Keefe & Recce, 1993) when looking at correlations between place cell firing and ongoing theta rhythm recorded from the same electrode. This was not the first attempt to correlate neuronal firing with LFPs, as that was introduced 10 years earlier by a human neurosurgery team (Wyler et al., 1982), but the first overt attempt to correlate them during precisely-defined behavioral events, such as place cell activity. It turned out that place cells fired at a specific phase of the theta cycle at a specific location of the apparatus. Conspicuously, the phase of the unit activity progressively advanced relative to the theta as the animal was advancing toward the center of the place field and continued advancing while the animal exited from the place field closing a full double-pi cycle of rotation until the activity declined to baseline. This was reproduced over repeated trials. The phenomenon is called "*phase precession*". Although theta phase precession was mostly reported as phase advancement, progressive phase lagging has also recently been documented as "theta phase rolling" (Sloin et al., 2022). Whether phase precession is an epiphenomenon, i.e., a corollary effect of the interplay between local theta rhythm and the neuronal excitability, or it reflects the coordinated act of neurons to encode the precise location (within a few centimeters) beyond the granularity of place fields (20-60 cm), is still an open question (O'Keefe & Recce, 1993). Nevertheless, phase precession represents an explicit well-reproducible example of phase coding, even though not a single study demonstrated

that perturbation of phase precession would interfere with the animal's ability to localize itself or would entail any spatial navigation deficit. The journey of phase precession had two important updates: (1) A study by Chris Harvey and David Tank showed that intracellularly recorded action potentials do not exhibit phase-precession with intracellular subthreshold theta oscillations (Harvey et al., 2009). This means that phase precession only exists relative to extracellularly measure theta oscillation field. If precession is evident only from extracellular theta, then precession cannot be considered a product of the spiking neuron but the product of the LFP field around it. Then, the logical assumption is that theta precession is caused by the drifting phase of theta, which is only possible if theta propagates. The proposal that theta propagates is not new since Lubenov et al. have shown by using multielectrode arrays implanted longitudinally in the hippocampus that theta forms recurring traveling waves along the long axis (Chiang & Durand, 2023; Lubenov & Siapas, 2008; Patel et al., 2012). (2) At the same time, several papers reported phase precession in other areas than the hippocampus such as visual and prefrontal cortices (Fournier et al., 2020; Jones & Wilson, 2005). As a result of the increasing number of reports documenting phase precession in different brain areas with diversely different functions, the premise that phase precession plays a critical role in neuronal information processing is getting inflated.

I remark that the literature on phase precession shows a sign of denial. Numerous reports on theta phase precession included figures of progressive phase delay besides phase advancement, yet no published report was devoted to the subject until 2022. Notably, the model of phase-coding in 2009 explicitly predicted the existence of progressive phase-lagging (Z Nadasdy, 2009) until the phenomenon was compellingly demonstrated by Eran Stark's group (Sloin et al., 2022).

III. At about the same time, in 1995, no other than John Hopfield published a relatively underrated theoretical article in the pages of Nature (Hopfield, 1995). With very little math Hopfield proposed the following model: subthreshold oscillations affect not only the likelihood of membrane potential reaching the threshold but also the latency when it crosses the threshold. Hence, continues Hopfield, when different intensity input depolarizes the same neuron at different levels, it will elicit an action potential with a latency proportional to the intensity (Zoltan Nadasdy, 2010a).

Therefore, a neuron downstream reading the input of the latency encoder neuron can recover the input intensity from the latency. Suppose that we have not one, but an array of neurons receiving simultaneously different intensity signals, like a distribution of light intensities over a photoreceptor array. Then, the temporal pattern of action potentials generated by the latency encoder neurons could encode the intensity and that code can be recovered with high precision. Fast-forward 13 years and Tim Gollish and Markus Meister reported, using the flattened sheet of salamander retina over an MUA illuminated with a projection of an image, that they could recover the image from the latency pattern of spikes fired by the retinal ganglions (Gollisch & Meister, 2008) confirming Hopfield's hypothesis. Hopfield and Meister were just one step away to generalize latency to phase, a metric much more suitable to the oscillatory landscape of neurons.

IV. Another answer for the binding-problem was proposed by Moshe Abeles (Moshe Abeles, 1991), the synfire-chain model (SFC). In contrast with BbS, the SFC model disregarded oscillations and instead focused on evidence for the precise timing of multi-neuronal spikes in feed-forward neuronal network architectures. Abeles' idea was similar to Hebb's cell-assembly idea in the sense that he predicted precise sequences of action potentials recurring in correlation with behavior. Abeles proved with numerical simulations that such precisely synchronized spike volleys necessarily emerge in feed-forward networks sequences triggered by a random input (Aviel et al., 2004; Litvak et al., 2003). Because empirically we can sample a very small subset of these neurons, we may only capture a few spikes likely originating from different neurons following one another with a constant delay as a signature of synfire chains. The question was of course how to define "precise timing". Abeles hypothesized a +/- 1 ms precision of cortical information processing. To prove that the detected recurring patterns are consistent with the hypothesis, Abeles used a jittering method suggested by Bienenstock and Geman (Hatsopoulos et al., 2003). With this method, one can determine the minimum temporal jitter of spikes (in ms) necessary to scramble the pattern such that the number of detected repeats is no different from by chance. He found spike triplets repeating with 2 ms precision in motor cortical single-unit recordings spike trains during motor tasks in monkeys, that were significantly unlikely to occur by chance.

I was honored to work with Abeles as a postdoc on these recordings of single unit activity from multiple electrodes and multiple sites including the motor- and somatosensory cortices while Abeles ran a triplet-searching algorithm on our spike train datasets. It was a "finding the needle in the haystack" type of problem, but the algorithm detected a few examples repeating at 1 ms precision, a few more with 2 ms precision, and the number of triplets increased as the precision condition was relaxed. Then by applying a jittering analysis (Abeles & Gat, 2001; Hatsopoulos et al., 2003), Abeles showed that the likelihood of such 2 ms precise triplets to occur by chance is extremely low. Hence the time base of cortical computation is close to 2 ms (Abeles & Gat, 2001; Shmiel et al., 2005). I have seen the data, and I ran my own pattern search and statistical analysis I have developed for the hippocampal recordings and found that the number of repeating triples increased nonlinearly and reached a plateau at 15-20 ms precision. We may see isolated examples of a few triplets repeating with 1-2 ms precision but the majority showed a larger jitter of 15-20 ms consistent with the time window of the period duration of a gamma oscillation. Since then, I have growing confidence that the precision we are seeking as evidence for discrete-timescale cortical processing is ~20 ms, equivalent to one gamma cycle. However, in contrast with the standing-wave model of gamma that Singer and Gray proposed in their BbS model, I suggested considering propagating gamma waves that depolarize ensembles of neurons in sequential order and elicit firing sequences that can be reproduced by the same propagating gamma oscillation. This idea was further exploited by the phase coding model I proposed in 2009 and 2010.

Between 2007 and 2009 I submitted a manuscript to a few journals that reported phase coding relative to gamma LFP recorded from primary visual cortical neurons in the awake primate brain during a visual discrimination task (Nadasdy & Andersen, 2007, 2009). The manuscript was rejected because the phase differences that discriminated different stimulus features seemed "too small" according to the reviewers, nevertheless highly significant. One year later, Nikos Logothetis and Stefano Panzeri published a paper on phase-of-firing coding (phase-coding in short) in the visual cortex of anesthetized monkeys, which left a significant footprint in the field (Besserve, Lowe, Logothetis, Schölkopf, & Panzeri, 2015; Montemurro, Rasch, Murayama, Logothetis, & Panzeri, 2008). That was followed by another publication where the

same team applied the same approach to auditory cortical data and divided the 4-8 Hz LFP (Kayser et al., 2009) and a few years later in awake monkeys and gamma oscillations during a visual task but this time on awake primate and using a continuous phase of Hilbert transform on the 50-80 Hz gamma oscillations (Besserve et al., 2015).

Let's take a closer look at the Logothetis' electrophysiology data analyzed by Panzeri (Besserve et al., 2015; Montemurro et al., 2008). The data consisted of continuous wide-band data with spikes. The monkeys in their experiment were watching movies, a continuous stimulus providing continuous LFP and single-unit data. They focused their approach on low-frequency fluctuations (delta: 1-4 Hz) because that captured the episodic segmentation of the movies the best. Instead of computing the Hilbert transform to obtain instantaneous phases, they divided the delta cycles into 4 phase quadrants and relabeled each spike by the phase quadrant they appeared in. They found that by comparing the Shannon information computed from the firing rate about the movie with the information available from the phase of firing, the latter conveyed 54% additional information.

For the phase to encode information requires a reference wave. The frequency of this oscillation has not been identified. We have discussed three candidates, gamma, theta, and delta, but there could be more. This reference wave must be present in both the sender neuron and the receiving neuron to support phase encoding and decoding. Suppose a neuron is receiving an input at time t_0. This input, to be decoded as f_0, has to be expressed relative to a wave with a starting and ending period. This starting and ending period of the reference wave must be shared between the sender and receiver neurons. Now consider the synaptic and conductive delay between the two neurons. This delay, even if only a few milliseconds, is not negligible and it will add to the phase at the receiver side. If the information sent was f_0 , then by reception, it will be $f_0 + Dt$. To compensate for the delay, the reference wave must be updated and adjusted by the Dt delay factor. The natural condition to compensate for the delay is the propagation of oscillation itself. We assume that the wave travels with a speed comparable to the speed of conductivity through synaptic transmission. Hence, the reference wave that decodes the information from the phase will remain aligned with the message to provide a correct phase readout. The search for the oscillation that would fulfill the role of fundamental common reference wave boils down to reliability and universality. There is only one oscillation ubiquitous and prevalent from insects to primates, ongoing during wakefulness, and does not reset upon external input, which is *gamma*. It is one of the highest-frequency oscillations in the brain, only ripples have a higher

frequency. We can discriminate between slow gamma (25-50 Hz) and fast gamma (50-80 Hz), which may play different roles in memory encoding and retrieval (Colgin et al., 2009).

For the above reasons, I built my phase-coding model on gamma as a reference oscillation. Gamma is predominant in the retinal ganglia, and it is triggered by micro-saccades. It is also prevalent in the LGN and in V1. Gamma oscillations in retinal ganglions phase-lock to gamma in the LGN (Koepsell et al., 2009) and LGN gamma phase locks to gamma in V1 (Saleem et al., 2017; Schneider et al., 2021), hence V1 sporadically phase locks to V1. I remark again that phase locking does not mean synchrony. It means coherence that permits a constant phase offset between two oscillations. It turns out that gamma cooccurs with theta in the hippocampus in all mammalian species. The only qualifying difference is that theta is more segmented in chiropterans and primates (including humans) relative to rodents. This is because processing sensory information is fundamentally different between rodents and chiropterans or primates (this topic will be discussed in the last chapter.)

The propagation of gamma waves unlocks a wide array of computations (Z Nadasdy, 2009; Zoltan Nadasdy, 2010b, 2015). For instance, it does not matter what the exact phase of the subthreshold oscillation is at a given neuron at a given time because that phase is continuously changing by the wave spreading through a layer of neurons. However, if the whole layer receives the same input, there will be a few neurons that receive the input at the peak depolarization phase, therefore it will relay the input to the next layer of neurons. The topography of propagating gamma waves makes it necessary that neighbors of neurons will reach a peak depolarization phase with the same delay as the neighbor neurons in the sensory surface. Hence, the neurons in the best position to decode the phase-encoded sensory information are the ones that have the same topographical relationship to the propagating gamma waves as the sensory neurons have in the sensory organ. A retinotopic activation of two adjacent ganglia at *t0* and *t1* will map on two closely situated neurons in V1 (given that V1 is retinotopically organized). Therefore, it does not matter which phase the input was encoded at, the decoding is possible based on the relative spatial phase distribution as long as the phase gradient of the oscillation is the same for the decoding layer as for the encoding layer.

The generalization of this principle was outlined in my papers from 2009 and 2010 and a book chapter (Z Nadasdy, 2009; Zoltan Nadasdy, 2010b, 2015). The propagating gamma waves also explained why “gamma synchrony” received very limited empirical support to play a critical

role in feature binding. It turns out, instead of synchrony, *coherence* is what matters because coherence can be maintained between any asynchronous oscillators. The coherence of gamma can define cell assemblies by activating a synergistic group of neurons while separating other cell assemblies by decoherence. Synergy does not mean synchrony. Synergy means that the components interlock in smooth phase transitions. Those phase transitions are not synchronous, but they display subtle asynchrony. Hence the playful title of my second paper “Binding by asynchrony”.

frontiers in
SYSTEMS NEUROSCIENCE

ORIGINAL RESEARCH ARTICLE
published: 28 July 2009
doi: 10.3389/neuro.06.006.2009

Information encoding and reconstruction from the phase of action potentials

Zoltan Nadasdy*

California Institute of Technology, Pasadena, CA, USA

Edited by:
Michael E. Hasselmo, Boston University, USA

Reviewed by:
Paul Miller, Brandeis University, USA
Neil Burgess, University College London, UK

****Correspondence:***
Zoltan Nadasdy, Scott & White Memorial Hospital, Texas A&M Health Science Center, Neuroscience Institute, 2401 South 31st Street, Suite 652, Temple, Texas 76508, USA.
e-mail: zoltan@vis.caltech.edu

Fundamental questions in neural coding are how neurons encode, transfer, and reconstruct information from the pattern of action potentials (APs) exchanged between different brain structures. We propose a general model of neural coding where neurons encode information by the phase of their APs relative to their subthreshold membrane oscillations. We demonstrate by means of simulations that AP phase retains the spatial and temporal content of the input under the assumption that the membrane potential oscillations are coherent across neurons and between structures and have a constant spatial phase gradient. The model explains many unresolved physiological observations and makes a number of concrete, testable predictions about the relationship between APs, local field potentials, and subthreshold membrane oscillations, and provides an estimate of the spatio-temporal precision of neuronal information processing.

Keywords: neural coding, action potential, local field potential, subthreshold membrane potential oscillations, gamma

INTRODUCTION

Whatever code neurons use for encoding, transferring, and decoding sensory information in the central nervous system (CNS) must be robust to a number of compromising factors. The integrity of the information transferred in massively parallel pathways of the brain is highly sensitive to distortions from different conduction delays (Rockland et al., 1997) and from intrinsic correlations due to the divergence and convergence of axonal projections (de la Rocha et al., 2007). Nevertheless, neuronal responses are increasingly specific to objects and progressively invariant with respect to incidental physical features, the times of occurrences, and the spatial locations of stimuli as we follow the activation from the sensory neurons through the primary sensory and ultimately to associational cortical areas. The high specificity of neuronal representations in higher cortical and associational areas relies on an unknown mechanism that enables the generation of action potentials (APs) in the same neuron consistently and independent of its neighbors ("sparse coding") (Quiroga et al., 2005). This requires precise coincidences of membrane depolarization with the arrival of excitatory postsynaptic potentials (EPSPs) at the level of individual neurons (Abeles, 1982). I investigated through numerical simulations whether the phase of APs relative to the intrinsic subthreshold membrane potential oscillations (SMOs) could encode and retain information with high spatial and temporal selectivity. Our model relied on two basic assumptions: first, that the timing of AP initiation is dependent on the phase of the SMO (Llinas et al., 1991); and second, that SMO is nearly synchronized with a phase gradient across a local population of neurons (Benucci et al., 2007; Bringuier et al., 1999; Grinvald et al., 1994; Prechtl et al., 2000). To relate the second assumption to empirical data, we further assumed that the SMO correlates with local field potentials (LFP, Buzsáki et al., 2003; Lagier et al., 2004; Leung and Yim, 1986). The results derived from the model are consistent with empirical data, and they provide a unified framework to answer a diverse set of daunting problems (see Table 1 in Supplementary Material).

The indirect evidence for the tight relationship between AP timing and SMO derives from observations of high correlation between extracellular APs and LFP. High coherency between APs and LFP oscillations is predominant at the gamma and theta frequency bands in the awake brain (Bragin et al., 1995; Chrobak and Buzsaki, 1998; Kamondi et al., 1998; Womelsdorf et al., 2007), and phase lock between APs and high frequency LFP occurs during slow wave sleep (Buzsaki et al., 1992; Chrobak and Buzsaki, 1996; Cisse et al., 2007). Gamma and theta oscillations also phase lock in the hippocampus and in the entorhinal cortex during active exploration of the environment and processing of sensory input (Chrobak and Buzsaki, 1998; Robbe et al., 2006). At the same time, APs phase lock with gamma oscillations (Chrobak and Buzsaki, 1998). Moreover, gamma band LFP and AP coherence has been found to be sensitive to motor task (Mehring et al., 2003) and preparatory activity during working memory (Pesaran et al., 2002) and related to selective visual attention (Fries et al., 2008). The autocorrelogram of multiunit activity in visual cortical areas of the cat is strongly modulated at 40–60 Hz and correlates with the gamma LFP, suggesting a functional link between AP generation and gamma oscillations (Gray and Singer, 1989). The multiunit–multiunit and the multiunit–LFP coherences are both increased during visual stimulation in the gamma (Womelsdorf et al., 2007) and during decision making in the beta frequency bands (Pesaran et al., 2008). Although AP-LFP phase coherency has been observed within the low-frequency LFP bands in the primary visual cortex of anesthetized primates (Montemurro et al., 2008), the feature-dependence of AP-LFP coherency in primary sensory areas is yet to be investigated. Notably, APs phase lock to 20–40 Hz LFP in the primate somatosensory cortex (Murthy and Fetz, 1996). The majority of pyramidal cells fire at the trough of the theta cycle and align to

the gamma (Bragin et al., 1995), and specific types of interneurons also phase lock to gamma (Tukker et al., 2007). Moreover, pyramidal cell firing in the hippocampus and entorhinal cortex of rodents also express a progressive theta phase precession consistent with the animal's position relative to the place field (O'Keefe and Recce, 1993) leading to the proposal that the AP phase relative to theta may encode the precise location of the animal (O'Keefe and Burgess, 2005; O'Keefe and Recce, 1993; Skaggs et al., 1996). All previous models of hippocampal phase coding assumed that phase precession is generated inside of the hippocampus as a result of interaction between two slightly different frequency theta oscillations (Blair et al., 2008; Lengyel et al., 2003; O'Keefe and Burgess, 2005); phase precession originating from the phase-coded sensory input and imposed on the hippocampus by the entorhinal cortex has not yet been proposed. Likewise, oscillatory interference models, relying on multiple oscillators, were proposed to explain grid cell behavior in the entorhinal cortex (Burgess, 2008; Burgess et al., 2007). However, as we show, coincidences of phase-modulated sensory input with a single propagating oscillation field are able to generate grid topography without further assumptions.

The mechanism by which local SMOs synchronize and generate coherent LFP relies on inhibitory interneurons (Lagier et al., 2004; Soltesz and Deschenes, 1993; Traub et al., 1996). To simplify terminology, we refer to LFP as the extracellular indicator of SMO; however, the performance of the model does not depend on the equivalence of LFP and SMO.

The aim of this study is twofold. First, we present a model that explains how feature-dependent phase coding may be employed in sensory information processing. Second, we investigate potential benefits of phase coding through examples, including generalization of 1-D phase coding to 2-D fields, information compression, selective reconstruction from combined representations, retaining stimulus invariants, and spatio-temporal transformations.

MATERIALS AND METHODS

COMPUTATIONAL MODEL

The core computational model consists of three layers, an input layer, a transformation layer, and an output layer. Each layer contains n neurons arranged in a 1-D array or a 2-D grid structure. The sensory input (1-D or 2-D) maps to the first layer. The first two layers are connected through n one-to-one unidirectional connections. In contrast, the second and third layers are connected through a single channel. Thus, the complete architecture is an n-to-n to one-to-n feed-forward network. For the sake of simplicity, we first consider a 1-D array of neurons to introduce the basic operations, and then we demonstrate that these operations are applicable to a 2-D grid as well.

I modeled neurons as deterministic state machines with binary AP or non-AP states and a real-valued baseline function $\varphi(t)$ representing the voltage of the SMO. The state of each neuron is defined by the combination of these two parameters. Although time is a continuous variable in the model, for numerical simulations we applied a discrete timescale ~0.2 ms ($T_\gamma = 0.01$).

We denote $\varphi_i(t)$ as a wave function with frequency γ and period $T = 1/\gamma$ corresponding to each neuron's SMO. We assume that $\varphi_i(t)$ is coherent among the neurons of a given layer with a constant phase offset $d_i\Delta\Phi$ proportional to the distance of the neurons from the origin of the oscillation (d_i), like a propagating wave

$$\varphi_i(t) = \varphi_0(t + d_i\Delta\Phi), \tag{1}$$

where $\Delta\Phi$ has units of time/distance. For an n-dimensional grid of neurons ($n = 1, 2, 3$), this phase gradient causes the neurons to express a coherent but phase-shifted n-dimensional oscillation field, where the phase difference between grid points is proportional to the difference between their distances from the center of oscillation (**Figure 2E**). At grid points where the phase difference reaches 2π, neurons have a zero phase-lag difference. The phase gradient starts to increase from homogeneously distributed centers and attenuates at the edges where spreading oscillations derived from adjacent centers meet (Benucci et al., 2007; Rubino et al., 2006).

The sequence of events from encoding to decoding are as follows:

(1) Encoding phase (layer 1): First we generate a 1-D input pattern **S**, a stimulus vector of length n representing the intensity of the stimulus acting on each of the respective n neurons (**Figure 1** stage 1). We now define **A** as the pattern of APs induced by **S**. **A** is an $n \times n$ binary matrix with elements $\mathbf{a}_{i,t}$, representing the time t at which each neuron i receives an input, that is computed by converting the intensity vector **S** to a latency vector such that a higher intensity input induces a shorter latency AP (**Figure 1** stage 2) (Hopfield, 1995).

$$\mathbf{a}_{i,t} = f(\mathbf{s}_i) \tag{2}$$

The function f assigns each input value $\mathbf{s}_i$ to a time $\mathbf{t}_i$, where

$$\mathbf{t}_i = \frac{n}{\gamma \cdot \mathbf{s}_i} \tag{3}$$

and γ is the frequency of SMO. The role of n is to scale the AP times to encompass multiple SMO periods. Importantly, the exact function in Eq. 2 does not matter as long as the latency is a monotonic function of the $\boldsymbol{s}_i$ input. Moreover, it does not matter whether the input is sensory or it was derived from another brain region; the model is only concerned with the pattern of APs that is induced by **S**.

(2) Transformation phase (layer 2): Now, we define **A′** as the gamma-aligned pattern of APs in **A**. More precisely, **A** is transformed into **A′** by delaying each AP until the neuron reaches the local maximum of its SMO. As a result, each i-th neuron generates an AP at a peak of $\varphi_i(t)$. We implement this delay by aligning each binary AP event to the peak of the respective neuron's intrinsic oscillation $\varphi_i(t)$ (Eqs. 4 and 5).

$$\mathbf{a}'_{i,\tau_i} = \mathbf{a}_{i,t} \tag{4}$$

where

$$\tau_i = \varphi_i^{-1}\left(\max\left[\varphi_i(t)\right]\right) \tag{5}$$

and *max* is defined as the next local maximum of $\varphi_i(t)$ after the time of the received input $\mathbf{a}_{i,t}$. Here $\mathbf{a}'_{i,\tau_i}$ are the elements of **A′**, a matrix with binary elements, where columns correspond to 0.1 ms time bins and rows correspond to specific neurons.

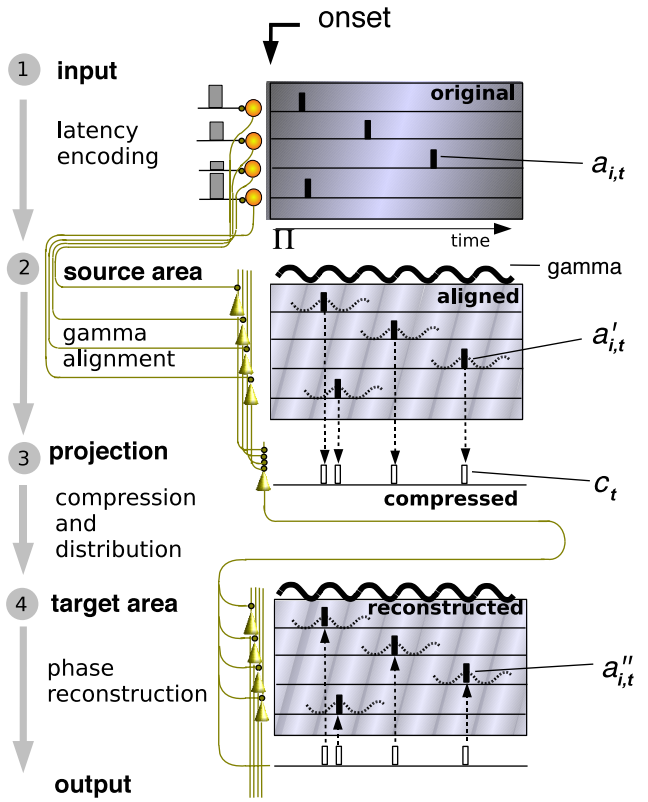

FIGURE 1 | Flow chart of information encoding and reconstruction. Stages are numbered at the left from 1 to 4. (1) Input: An intensity-modulated signal is presented to the input of the neurons and encoded as an AP latency vector ($\mathbf{a}_{i,t}$) (Gollisch and Meister, 2008). (2) Source Area: The latency encoding AP vector, when interacting with a propagating field of local oscillations, becomes aligned to the nearest SMO peaks ($\mathbf{a}'_{i,t}$). (3) Projection: The SMO-aligned AP vector is collapsed into a single AP stream via convergent connections. At the same stage, the AP vector is distributed via divergent connections (not shown), and identical AP trains are transferred to the next stage ($\mathbf{c}_t$) (Dan et al., 1998). (4) Target Area: this area receives identical copies of the AP vector through parallel pathways. When APs interfere with the local waves of SMO, a single input AP evokes a single output AP only in neurons where the input AP coincides with the peak of the local SMO. Provided that the SMOs have the same voltage gradient at the input and target areas, it is guaranteed that the coincidence pattern will reconstruct the original spatio-temporal pattern of the input ($\mathbf{a}''_{i,t}$). Output: As a result, the output AP vector reliably reproduces the phase aligned input vector.

A "1" in position $\mathbf{a}'_{i,\tau_i}$ represents an AP for neuron i at time t while a "0" represents the lack of AP (**Figure 1** stage 3).

(3) Transfer (layer 2–3): Then $\mathbf{A}'$ is collapsed into an array $\mathbf{C}$ by summing across all neurons for each time bin.

$$\mathbf{c}_t = \sum_{i=1}^{n} \mathbf{a}'_{i,\tau_i} \tag{6}$$

Since the sum is a binary function, $\mathbf{C}$ contains the APs derived from all neurons with their original time stamps. Although the neuronal specificity is lost in the sum, the precise timestamps of APs unambiguously relate the individual APs to specific locations through their phases. Thus, the spatial information is retained by the relative phases of APs (**Figure 1** stage 3).

At the same step, $\mathbf{C}$ was "cloned" to n copies and fed into the next layer of n neurons.

$$\mathbf{c}_j = \mathbf{C}, \tag{7}$$

where $j = \{1,\ldots,n\}$. The information in $\mathbf{C}$ is transferred from the input layer to the target layer. Since all the information from the input layer neurons is collapsed into a single channel (stage 3), this information is vulnerable to errors deriving from different conductivity delays. Therefore, a redistribution of $\mathbf{C}$ over multiple channels is necessary to increase redundancy for error correction.

(4) Reconstruction (layer 3): The final step is reconstruction. Here the task is to create a matrix $\mathbf{A}''$ by assigning each individual AP in $\mathbf{C}$ to a neuron such that there is a topographic mapping between $\mathbf{A}$ and $\mathbf{A}''$, consequently recovering the original spatio-temporal structure of APs from the compressed code. To do so, we simultaneously broadcast the $\mathbf{c}_j$ copies to each k-th neuron ($k = \{1,\ldots,n\}$) in the target layer. Neurons in the target layer will only generate APs if the input $\boldsymbol{c}_{jt}$ coincides with a peak of their membrane oscillation $\varphi_k(t)$ within a precision of $\Delta\tau$ (**Figure 1** stage 4 and Movie 1 in Supplementary Material). Given that the gamma phase gradients are identical between the source and the target (but see Figure 1 in Supplementary Material), these coincidences must occur in neurons at the same grid position within the target layer as the grid position of neurons stimulated in the input layer. Consequently, the topography and timing of the coincidences between the $\mathbf{C}$ and the SMO, which generates the APs at the target layer, will reproduce the topography and timing of the input APs. To implement this, we define a matrix $\mathbf{B}$ with $n \times T/\Delta\tau$ binary elements, where 1-s represent the positive peaks of SMO and 0-s represent all other voltage values, with a $\Delta\tau$ precision:

$$\mathbf{b}_{i,\tau} = \begin{cases} 1, & \text{if mod}\,(t + d_i\Delta\Phi, \gamma) = 0 \\ 0, & \text{otherwise,} \end{cases} \tag{8}$$

where $\mathbf{b}_{i,\tau}$ represents the binary state of the i-th the neuron at τ time. Since the input layer SMO is identical to the target layer SMO, it is necessary that the intersection $\mathbf{A}''$ of $\mathbf{B}$ and $\mathbf{C}$:

$$\mathbf{A}'' = \mathbf{B} \cap \mathbf{C} \tag{9}$$

will reproduce the original matrix $\mathbf{A}'$ (**Figure 1** stage 4). The output pattern $\mathbf{A}''$ can be transferred as input to other target areas. Equation 9 will be referred to as the "interference operator", and Equations 8 and 9 as the "interference principle".

SELECTIVE RECONSTRUCTION FROM COMBINED PHASE CODES

Let us define input images $\mathbf{S}^A$ and $\mathbf{S}^B$ and encode them separately as $\mathbf{A}^\alpha$ and $\mathbf{A}^\beta$. Next, align $\mathbf{A}^\alpha$ and $\mathbf{A}^\beta$ to field gradients $\Delta\Phi_\alpha$ and $\Delta\Phi_\beta$, respectively, and compress the aligned $\mathbf{A}''^\alpha$ and $\mathbf{A}''^\beta$ matrices into corresponding $\mathbf{C}^\alpha$ and $\mathbf{C}^\beta$ representations. Next, we combine the two compressed representations as $\mathbf{C}^\gamma$ by simply merging and sorting the AP times in ascending order:

$$\mathbf{C}^\gamma = \mathbf{C}^\alpha \cup \mathbf{C}^\beta. \tag{10}$$

Given that $\varphi^{\alpha}(t)$ has a phase gradient $\Delta\Phi_{\alpha}$ and $\varphi^{\beta}(t)$ has a phase gradient $\Delta\Phi_{\beta}$, the two different SMO fields must be able to selectively reconstruct the two AP patterns, $\mathbf{A''}^{\alpha}$ and $\mathbf{A''}^{\beta}$, both retaining the main features of $\mathbf{A'}^{\alpha}$ and $\mathbf{A'}^{\beta}$, respectively:

$$\mathbf{A''}^{\alpha} = \mathbf{B}^{\alpha} \cap \mathbf{C}^{\gamma} \tag{11}$$

and

$$\mathbf{A''}^{\beta} = \mathbf{B}^{\beta} \cap \mathbf{C}^{\gamma}. \tag{12}$$

With simulations (**Figure 5**) we demonstrated that given $\Delta\Phi_{\alpha} \neq \Delta\Phi_{\beta}$, $\mathbf{A'}^{\alpha}$ can be recovered from the interference of $\mathbf{B}^{\alpha}$ and $\mathbf{C}^{\gamma}$ without confusion with $\mathbf{A'}^{\beta}$. Likewise, matrix $\mathbf{A'}^{\beta}$ can be recovered from the interference of $\mathbf{B}^{\beta}$ and $\mathbf{C}^{\gamma}$ without confusion with $\mathbf{A'}^{\alpha}$.

This mechanism provides the capacity to combine information from different sources within the same target layer and selectively recall them by different SMOs.

NUMERICAL IMPLEMENTATION OF THE MODEL

Numerical simulations were implemented using Matlab (Mathworks Inc., Natick, MA, USA). For the numerical implementation, instead of simulating spiking neurons with incremental time, we computed the state of all neurons in time at once using matrix operations. We remark that it was unnecessary to introduce a spiking neuron model since all the state transitions were deterministic and the interactions were linear. Thus, the state changes of neurons, i.e., the AP times, at a given layer as a function of the state changes at the subordinate layer were analytically solvable. Therefore, numerical simulations were performed by computing the complete AP time vectors as a function of the AP time vectors in the previous layer instead of deriving the membrane voltage V_t at every time step recursively from V_{t-1}.

Architecturally, the neuronal network consisted of three layers: input-layer, projection-layer and output-layer. The input layer contained n or $n \times n$ neurons, individually assigned to each pixel of the input image. We implemented the algorithm on feed-forward networks using three types of projections between layers: (i) A 1-D vector of n values (input vector) was projecting to a 1-D array of n input-layer neurons, which were connected through projection neurons to the same number of output-layer neurons. The connectivity between the values of the input vector and input-layer neurons was one-to-one; between the input-layer and projection-layer was n-to-one; between the projection-layer and output-layer was one-to-n. (ii) A 2-D input image, digitized as $n \times n$ pixels, projecting on a 1-D array of n^2 input-layer neurons. The architecture from the input-layer to the output-layer was similar as in (i), however, the output was visualized in 2-D to compare the reconstructed pattern with the input image. (iii) A 2-D ($n \times n$) input matrix was projecting on a 2-D grid of $n \times n$ input-layer neurons by emulating "receptive fields". For this, the input matrix was partitioned into n subfields and the input-layer neurons were arranged into n non-overlapping groups that processed the n input subfields separately. Likewise, the output-layer neurons were arranged into n number of groups, emulating a topographical projection from the sensory organ to a primary sensory cortical area. The precise connectivity pattern between the input matrix and input-layer group was repeating across the groups but it was varied from simulation to simulation (see next paragraph). All neurons from a given group were converging on a single projection neuron, which in turn, terminated on all the neurons of a given output-layer group. Thus, each input-layer group was interfacing with the corresponding output-layer group through a single projection neuron.

Operatively, the input was either a 1-D (n) or a 2-D ($n \times n$) matrix mapped to the input-layer neurons. The correspondence between the input matrix elements and the input-layer neurons was one-to-one. The 1-D simulations always used random vectors as input with the range of values from 0 to 2π and transferred to n neurons. As input to the 2-D simulations, we used a set of digitized images, including photos of people, animals, complex structures of rubber bands and grid patterns. They were selected to test the accuracy and geometric preservation of the reconstruction. Images were digitized with 256×256 pixel resolution and converted to grayscale. We down-sampled them to fit to the neuronal grid with a square geometry (16×16, 18×18, 32×32, 36×36, 60×60) and input them to the neurons. The input layer contained n or $n \times n$ neurons, individually assigned to each pixel of the input image. As described earlier, the projection-layer was different for the 1-D and 2-D network. For a 1-D solution, the projection-layer contained only one neuron (one channel). All the APs from the n input layer neurons were collapsed into a single channel, serving as a projection neuron. For the $n \times n$ solution, the projection layer contained n neurons (channels), thus the $n \times n$ grid of input layer was broken down into m subfields (receptive fields) and the APs from all the input neuron of a given subfield were collapsed into a single channel. The combined m channels served as a projection pathway. All the neurons at a given subfield of the output layer received a common input from a single projection neuron, containing the combined activity from the input subfield. Different mappings between the input and input-layer neurons were implemented by connection patterns, emulating different receptive field geometries (for details on modeling different receptive field architectures, see Supplementary Material).

The SMO was modeled by sinusoids. The phase gradient was either linear, emulating a propagating wave with a constant time lag of SMO between neighbor neurons, or non-linear, emulating oscillations deriving from randomly dispersed sources (for details on constructing non-linear SMO fields, see Supplementary Material below). APs were modeled as binary events. The duration of these events was the smallest time unit of the simulation ($\Delta\tau$), defined as a constant fraction of π, the half period of the SMO. Alignment to the nearest SMO peak was implemented by reassigning each AP to the nearest subsequent peak of SMO. Combining before transferring APs via the projection neurons was done by concatenating the AP time series. Coincidences at the output layer were detected when the latency difference between the incoming AP pulse and the peak of local SMO is $< \Delta\tau$. APs were assigned to neurons of the network where coincidences occurred. The output was the temporal pattern of APs on the grid of $n \times n$ neurons, converted to an image by an inverse of the image conversion applied to the image when it was converted to a temporal pattern. To quantify the efficiency reconstruction, we computed Pearson's correlation coefficients on the AP times between the input patterns and output patterns, neuron-to-neuron, as well as between the SMO-aligned input patterns and the output patterns. The implementation

of the algorithm for numerical simulations is described in the Supplemental Computational Methods. Demo codes written in Matlab are available at the following URL: http://www.vis.caltech.edu/~zoltan/mcodes/phasecode.tgz

ALGORITHM AND BIOLOGICAL MOTIVATIONS

The model that we introduce explains how oscillations might be used in the brain to coordinate APs to encode and reconstruct information between distant cortical areas. First, we distinguish four information processing stages and corresponding neuronal layers representing the results of each stage (**Figure 1**): (1) Input layer: latency encoding; (2) Source layer: gamma alignment; (3) Projection: compression and distribution, (4) Target area: reconstruction. The output of the target area may serve as an input to a connected area. The input layer may represent a group of sensory neurons or a group of cortical pyramidal cells. Postsynaptic to these neurons are neurons that encode the input and exhibit intrinsic SMO. Postsynaptic to encoding neurons are the projection neurons, such as sensory ganglia or long-range cortico-cortical connections. Postsynaptic to projection neurons are the target neurons, such as cortical layer-4 granule cells or layer 2–3 pyramidal neurons, which are the ultimate targets of sensory or cortico-cortical projections.

Each neuron was described by its grid location and layer, its connections, and its state. The state was defined by three variables: a continuous oscillating membrane potential implementing the SMO of the soma, a binary input, and a binary output, corresponding to AP or no AP. The probability of generating an AP was dependent on the input state and the actual SMO, which determined how close the membrane potential was to the threshold. In the absence of input, the membrane potential remained subthreshold, by definition. The SMO for each neuron was modeled by a sinusoid, and the grid of neuronal SMOs formed a 2-D field (SMO field) with a common frequency and a uniform phase gradient between adjacent neurons. Thus, the SMOs of neighboring neurons were near-synchronized, with a distance dependent phase delay, mimicking a spreading wave (Benucci et al., 2007; Bringuier et al., 1999; Grinvald et al., 1994; Prechtl et al., 2000). Each neuron generated an AP when the input, received from a presynaptic neuron (i.e., from an earlier stage), coincided with the neuron's own local SMO maximum, where the neuron's membrane potential is nearest threshold. We implemented a task in which these neurons encode and reconstruct an image using exclusively a feed-forward architecture in four steps corresponding to the four stages. For the sake of simplicity, we first illustrate these steps on a 1-D example, after which we extend it to 2-D examples using real images (see Section "Results").

Encoding

First we generate a 1-D input pattern **S** that represents intensity values of an image (**Figures 2 and 3A**). Each element of the **S** vector is assigned to the input of a neuron. Next, we compute the neuronal responses to **S**. We employ a latency encoding scheme (Gollisch and Meister, 2008; Hopfield, 1995), which converts the intensity values to AP latencies, inversely proportional to the intensity of stimulus component, generating a spatio-temporal activity vector **A** (Eqs. 2 and 3).

Gamma alignment

The latency-encoded pattern **A** is transferred to the next layer of neurons exhibiting a coherent field of SMOs. The SMO field consists of local oscillations spreading through the grid of neurons as a linear or radial wave with a neuron-specific phase gradient (Eq. 1). A neuron of this layer generates APs only when the sustained input from a neuron at the previous layer coincides with its own next SMO maximum. As a result, the temporal pattern of **A** is transformed in an SMO aligned pattern **A′** (Eqs. 4 and 5). Since we considered gamma oscillation as one of the main frequency components of local SMOs, we refer to this operation as "gamma alignment" (**Figures 1 and 2B**), though phase coding does not depend on the frequency of SMO. Note, that with gamma alignment this model is critically different from synfire chain (Abeles, 1991) and AP-latency encoding (Hopfield, 1995). Gamma alignment is possible through rapid spike-time-dependent-plasticity (Bi and Poo, 1998; Cassenaer and Laurent, 2007; Markram et al., 1997).

Compression

A′ is then collapsed across all neurons into one AP sequence **C** by eliminating the neuronal identity (**Figures 1 and 2C**, and Eq. 6). This AP sequence represents all the APs pooled across all of the neurons. Pooling can be implemented by convergent feed-forward synaptic connections on a single neuron. Although neuronal identities are seemingly lost by collapsing APs over neurons, the spatial origin of the AP is still referenced by the timing, which associates the AP with the original location of the neuron through the gamma alignment. A phase difference of the local SMO, to which the AP is aligned, is preserved by the small latency differences between APs after collapsing them. The resulting new sequence is "compressed" because information from all neurons were collapsed into a single sequence of APs of the same duration, and "compact" because it contains all the information about **A′**, including time and location.

Distribution

At the same stage, the collapsed AP vector is copied over the same number of projection neurons as in **A** (Eq. 7). Compression and distribution are accomplished in a single step within a feed-forward network by convergent and divergent synaptic connections, respectively. As a result, all APs from the original **A′** pattern are represented in all the projection neurons by pattern **C**, with a redundancy (**Figures 1 and 2C**). These packets of **C** patterns can be broadcasted to many neurons simultaneously or exchanged between distant cortical areas. Since all projection neurons carry the same AP sequence, any of them is able to broadcast the complete information indiscriminately to any brain area. Notably, after compression the information content is no longer sensitive to different conduction delays. Errors deriving from differential conduction delays are self-corrected by synchronization of APs in crossed-over feed-forward pathways, typical in thalamo-cortical, callosal and long-range associational projection systems.

Reconstruction

This is the final stage where the original information **A′** (the gamma-aligned representation of **A**) is reconstructed from the pattern **C** as input to this layer. The parallel pathway of projection neurons

broadcasts the complete **C** input to each neuron at the target layer, such as layer 4 of the cerebral cortex. The target layer neurons also express an SMO field similar to the one at the input layer. Here, we apply a principle similar to the input layer, except a neuron only generates APs if the input coincides with the neuron's SMO maxima within a $\Delta\tau$ time window (**Figures 1 and 2D**). Such coincidences between the input and the local SMO occur only in selected neurons, which are located at the same grid positions as the active input-layer neurons (Movie 1 in Supplementary Material). Since the relative timing of AP is preserved, the coincidences reproduce the original **A′** pattern due to the "interference principle" (Eqs. 8 and 9). Therefore, to achieve a near perfect reconstruction, it is assumed that the SMOs at the input layer and the target layer share similar spatial and spectral properties, including the frequency and phase gradient topography (but see isomorphic reconstruction and Figure 1 in Supplementary Material). Since the interference occurs at selected neurons, the input pattern **C** will activate a sparse set of neurons, with topographic positions similar to the original neurons. Therefore, it is necessary that the reconstructed pattern **A″** resemble closely to the gamma-aligned original pattern **A′** and consequently, the original pattern **A** as well. The reconstructed pattern can be combined with patterns deriving from other input structures and a new cycle of encoding, gamma-alignment, compression and reconstruction is initiated that propagates the now combined representation to a different brain area (**Figure 5**).

RESULTS

For the sake of simplicity and algorithmic clarity, we first used a 1-D encoding and reconstruction example. A vector containing 16 random real numbers from 0 to 1 was used as the input to the network. Next, this input was converted to latencies within the range of eight SMO cycles (**Figure 2A**). This pattern was aligned to the neurons' own SMO which slightly altered the precise temporal pattern of APs relative to the original latency code (**Figure 2B**). This spatio-temporal pattern was collapsed into a single AP train by removal of the spatial dimension. At the same time the resulting AP string was distributed over 16 neurons which transferred the code from one brain structure to another with redundancy (**Figure 2C**). One of these AP strings was applied as input to a target network, consisting of 16 neurons. In addition to the input, we rendered each neuron with an SMO that shared the same phase gradient and frequency as the SMO field at the input layer. Although each individual neuron received the same AP sequence as input, due to the interference principle (Eqs. 8 and 9) only those APs that "precisely" coincided with the neuron's own SMO were effective in generating output APs (**Figure 2D**). We quantify the precision of coincidence later. As a result the ouput-layer neurons reproduced the spatio-temporal pattern of the original gamma-aligned input with high fidelity.

To demonstrate the algorithm in 2-D we used a set of grayscale images sampled at neuron resolution and projected them on the input-layer neurons so that each neuron processed one pixel, allowing no interactions between neurons of the same layer (**Figure 3**). By varying the precise projection between the image pixels and neurons we were able to test different receptive field configurations (see Supplementary Material on modeling different receptive field architectures). Each set of input-layer neuron processed the receptive field independently throughout the four stages, and at the end, the reconstructed patterns were combined from each set. Finally, AP latencies were converted to grayscale values (**Figures 3A,E**). The close resemblance of the output image to the original implies that most of the information encoded from the input were correctly recovered from the phase of APs alone, thus phase coding is efficient.

BIOLOGICAL SIGNIFICANCE OF MODEL PARAMETERS

The efficiency of reconstruction was sensitive to a number of parameters, including the connectivity, the input size, the density of neurons, the SMO oscillation, and the time window of coincidence. The operative range of these parameters must be consistent with that measured in the living brain in order for the model to be biologically relevant. To understand how these parameters influence the reconstruction efficiency, we performed simulations. The independent variables were the number of neurons, the number of gamma cycles (i.e., the duration of reconstruction), the temporal resolution $\Delta\tau$ (equivalent to the time window of coincidence), the phase gradient $\Delta\Phi$ of gamma oscillation, the connectivity pattern, and the complexity of receptive fields (the number of pixels covered). The dependent variable was the reconstruction efficiency, quantified as the pixel-to-pixel Pearson's correlation coefficients either between the original image **A** and the reconstructed image **A″** ($r = r_{\mathbf{A},\mathbf{A''}}$) or between the gamma-aligned image **A′ A″** ($r' = r_{\mathbf{A'},\mathbf{A''}}$).

First, r and r' were tested against combinations of number of neurons and number of gamma cycles. The reconstruction efficiency is expected to inversely scale with the number of neurons since the more neurons' APs are combined in a single projection neuron, the more confusion occurs due to spurious interferences (aliasing errors). A few gamma cycles were expected to be sufficient to reconstruct the most of the information and certainly less gamma cycles than neurons are necessary. The steep exponential function [$f(x) = 22.45 \times x^{0.3} - 13.83$; $R^2 = 0.99$; root mean square = 0.78] of the significant correlations (six cycles over the increase of 800 neurons) suggests that as few as 64 neurons and three to four gamma cycles (75~100 ms) were sufficient to retain the information with $r > 0.9$ (**Figure 4A**); consistent with the reaction time across species.

Second, we systematically varied the temporal resolution $\Delta\tau$ between 0.1 and 2.5 ms and the phase gradient $\Delta\Phi$ between adjacent neurons from 0.012 to 5 ms. Since the reconstruction efficiency relies on the neuronal specificity recovered from the AP phases, the temporal resolution of phase, i.e., the precision of APs, is critical. This resolution determines whether neurons at the target area are able to discern the close succession of input APs and detect coincidences between APs and gamma peaks selectively. Likewise, the gamma phase gradient between adjacent neurons determines the specificity of AP-gamma coincidences with respect to the neuron's position and with respect to the wavelength of the spreading oscillation. Since $\Delta\tau$ and $\Delta\Phi$ are independent parameters of the model while both contributing to the precision of coincidences, we expected a tight relationship between them. Our simulations confirmed a monotonic relationship between temporal resolution and reconstruction efficiency from 0.1 to 1.5 ms and uncovered a surprising non-linear relationship between the gamma phase gradient and coding efficacy. At $\Delta\tau > 1.5$ ms no precise

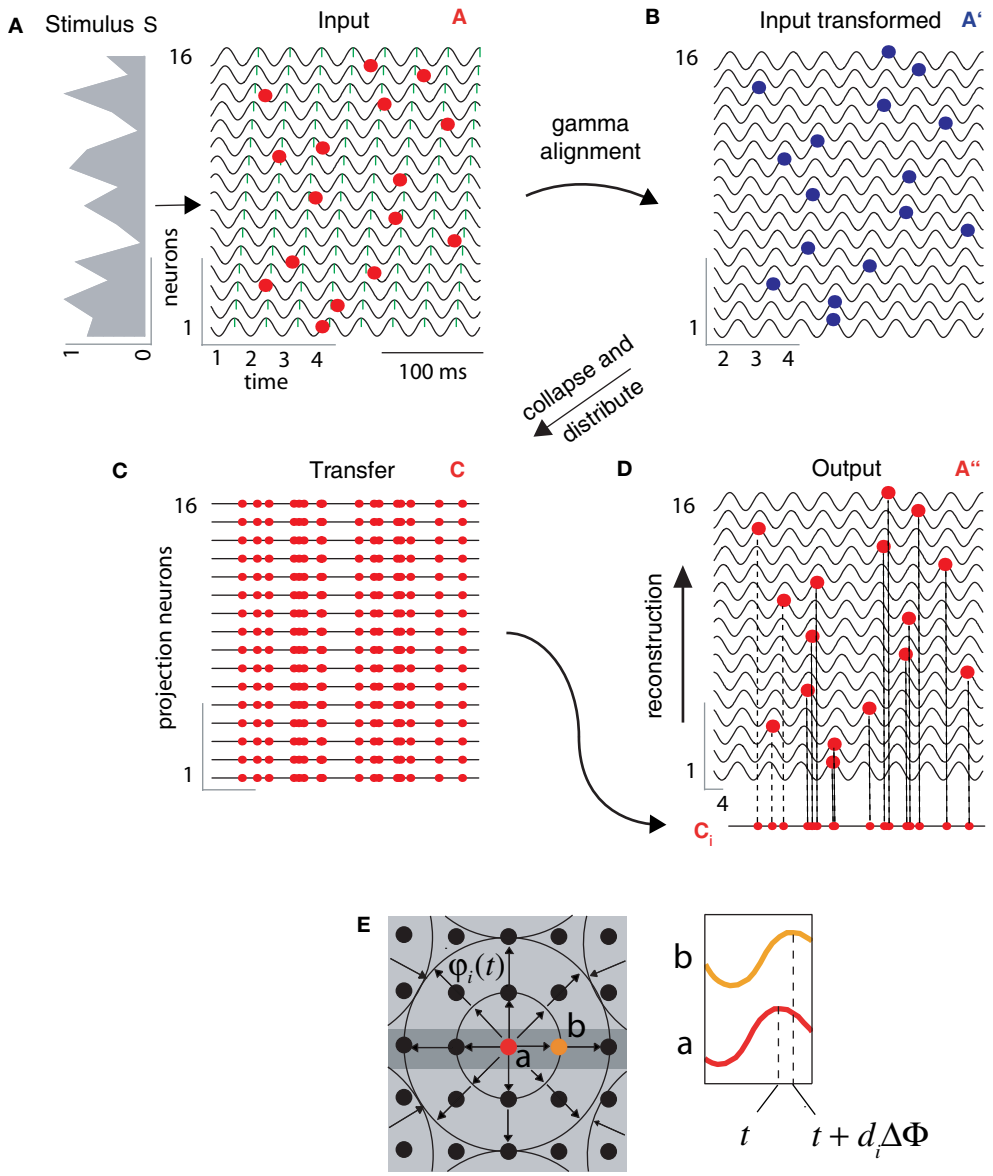

FIGURE 2 | Stages of information encoding, transfer, and reconstruction illustrated on a 16-neuron simulation. (A) INPUT: Neurons at the input layer convert the stimulus, represented by an analog intensity vector (left), to a latency vector where the delay of AP (red markers) is inversely proportional to the intensity of input. Oscillations in adjacent neurons are phase shifted by a constant 0.1 π relative to each other (green ticks mark oscillation peaks). **(B)** GAMMA ALIGNMENT: AP generation is most likely when the input pattern coincides with the maxima of the ongoing SMO (blue markers). Time is shifted one period at each stage. **(C)** TRANSFER: All APs from all neurons are collapsed into a single sequence of APs, and this sequence is distributed over an array of projection neurons (red markers). **(D)** OUTPUT: When one of the AP sequences is transferred to the target layer, it provides the same input to each neuron (dashed lines). However, only those APs that coincide with at least one neuron's membrane oscillation maximum are effective in generating AP (red markers). Given that the membrane oscillations at the output layer share the same spatial gradient as that of the input layer, the topography and timing of the output layer interferences will reproduce the topography and timing of input layer APs **(B)**. **(E)** The scheme of the spatio-temporal distribution of SMOs in a grid of neurons (filled circles). Each neuron's membrane potential is affected by a radial spread of SMO $\phi_i(t)$ that has a constant spatial voltage gradient, causing a $\Delta\Phi$ phase lag between the SMO peaks of adjacent neurons (red and orange neurons and corresponding traces of SMO). Examples in **(A–D)** related to a linear array of neurons (within the dark gray rectangle) sorted according to phase, but the same algorithm can be generalized to a 2-D grid (light gray area).

reconstruction was possible, thus setting a boundary for precise information processing consistent with empirical data (Shmiel et al., 2005). The lowest temporal resolution, or the largest time window of coincidence, which allowed a near perfect reconstruction ($r > 0.9$) was <0.72 ms, as precise as the duration of an AP. The first peak of the corresponding gamma phase gradient was $\Delta\Phi = 0.4 \pm 0.1$ ms, followed by a series of subharmonics from 0.6 to 1.59 ms (**Figures 4B,C**). Given that the average pyramidal cell density in layer 4 of the cerebral cortex is near 2.4×10^4 (Holmgren et al., 2003) and 2.5×10^4 cells/mm^3 (Peters and Yilmaz, 1993),

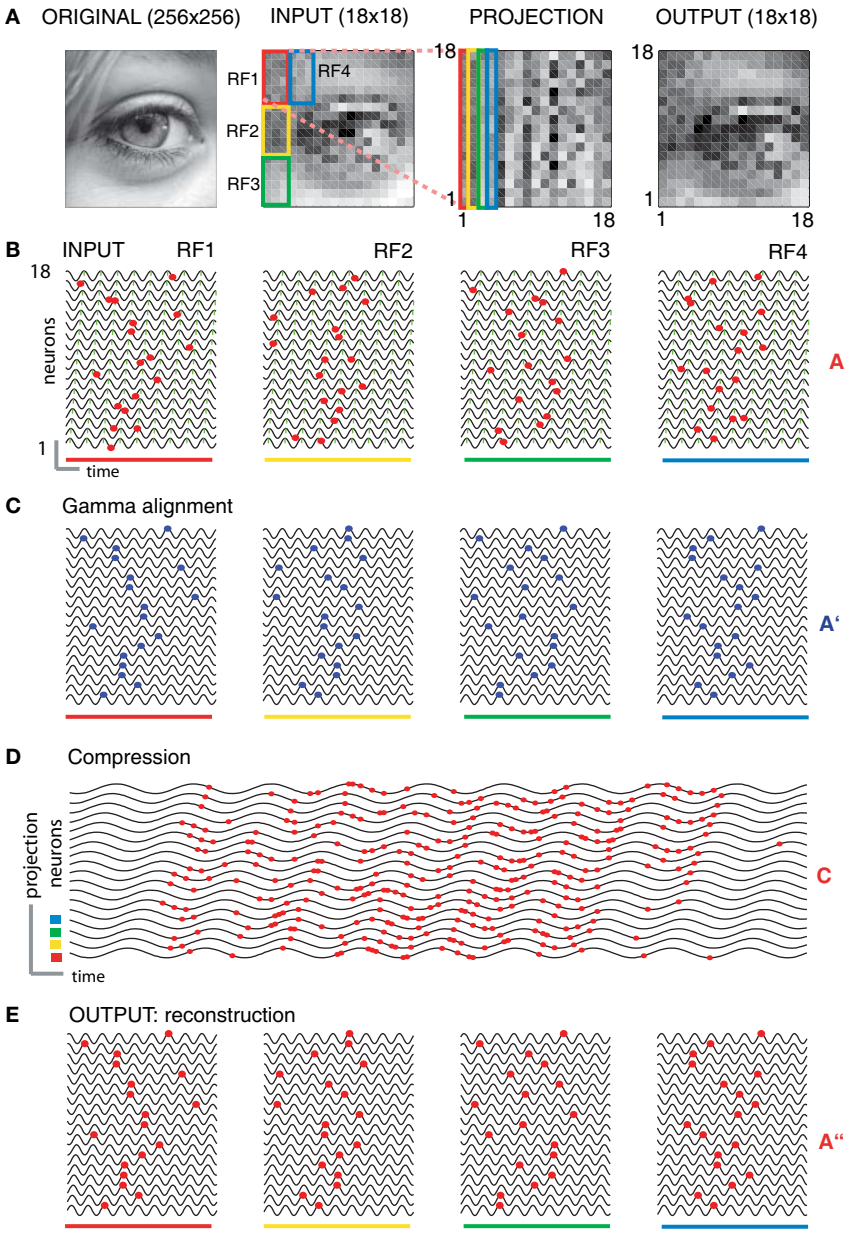

FIGURE 3 | Topographic preservation of reconstruction. (A) The original digital grayscale image (left panel) was downsampled to an 18 × 18 matrix and partitioned into 18 sub-regions mimicking receptive fields (RFs) (second panel, only four receptive fields are shown). The total of 18 RFs were projecting on 18 groups of neurons of the input layer, each consisting of 18 neurons. The inputs from the RFs (covering 3 × 6 pixels; color coded on the second panel) were vectorized and mapped on separate arrays of neurons (color coded rectangles on the third panel). The reconstruction using the "interference operator" (Eq. 9) retained most of the information from the input (forth panel). **(B)** Examples of encoding the input by four RFs [color bars relate the codes to corresponding RFs on **(A)**]. The gray levels within RFs were converted to AP latency vectors in the corresponding neurons (red markers). **(C)** APs were aligned to the nearest subsequent maxima of the local SMO oscillation (blue markers). **(D)** The spatiotemporal pattern of APs from each group was collapsed into a single sequence and combined in 18 AP sequences (red markers) to transfer through projection neurons. The sinusoid traces correspond to the first neuron's SMO of a given receptive field in **(C)**. The first four traces correspond to the RFs on **(A)**. **(E)** Reconstruction of the information from the compressed code in **(D)**. The interference between the input and the neuron's intrinsic SMO peaks generated patterns (red markers) that reproduced the original gamma-aligned patterns. To compare the reconstruction with the original input, we converted the AP latencies from all the neurons to gray level pixels (**A**; fourth panel). Note that the reconstruction of the original phase relationship between the APs and local SMO is near perfect (**C,E** and **A** fourth panel).

the average nearest cell-to-cell distance derived by Monte Carlo simulations was $\Delta x = 42$ μm (for details on computing neuron-to-neuron distance, see Supplementary Material), and that the optimal phase gradient was 0.4 ± 0.1 ms between adjacent neurons, we estimated the speed of SMO propagation ($\boldsymbol{v}$) and the diameter ($\boldsymbol{d}$) of the cortical cylinder that would be covered by a radial wave of a single SMO cycle of $\boldsymbol{f}$ frequency and $\boldsymbol{v}$ speed. Assuming that $f_{\text{gamma}} \approx 40$ Hz and $T_{\pi} \approx 12.5$ ms, and applying $\boldsymbol{v} = \Delta x/\Delta\Phi$ we

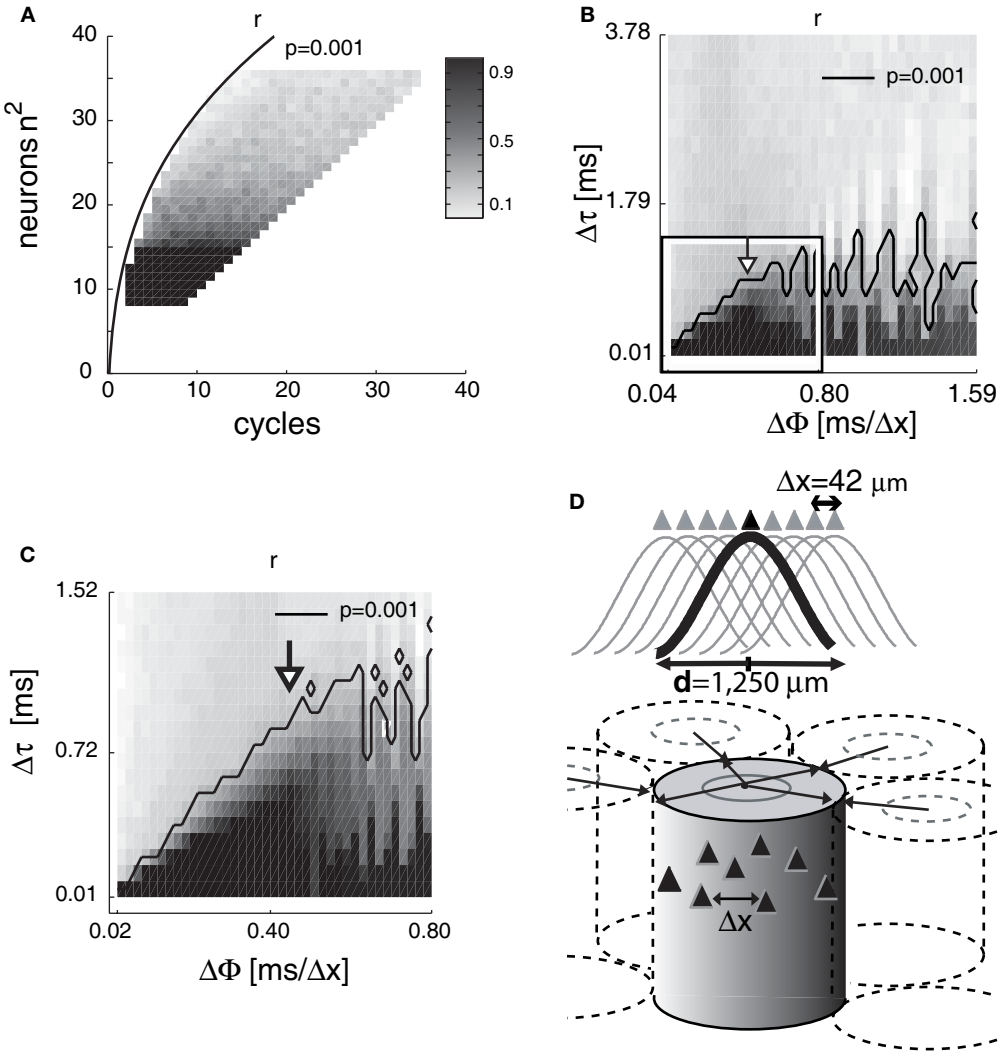

FIGURE 4 | The efficiency of reconstruction depends on the number of neurons, gamma cycles, temporal resolution and phase gradient. **(A)** Average correlation coefficients (**r**) between original and reconstructed images (grayscale) as a function of number of gamma cycles (abscissa) and number of neurons (ordinate). The right side of the exponential curve represents combinations of number of neurons and gamma cycles that enabled precise reconstructions ($P < 0.001$). **(B-C)** Average **r** as a function of temporal resolution (DT) and gamma phase gradient between adjacent neurons ($\Delta\Phi$). Unit is [ms/Δx] where Δx is the average nearest neighbor distance between pyramidal cells **(D)**. **(C)** A higher resolution simulation within parameter ranges of $\Delta\Phi$ = 0–0.8 and $\Delta\tau$ = 0.01–1.52 ms [the rectangular area in **(B)**] revealed the optimum phase gradient $\Delta\Phi$ = 0.4. The contour line represents the P = 0.001 confidence limit. **(D)** Estimating the cortical area of precise reconstruction. Given $\Delta x \approx 42$ μm average nearest-neuron distance and $\Delta\Phi \approx 0.4$ ms at gamma frequency (from **B–C**), we extrapolate $\boldsymbol{d} \approx 1{,}250$ μm as the diameter of a cylindrical cortical volume comprising a neuron population necessary and sufficient to reconstruct the complete information transferred within a single gamma cycle. Filled triangles represent neurons, cosine functions represent phases of a spreading gamma wave and arrows represent radial propagation of gamma waves.

calculated $\boldsymbol{v} = 0.1$ mm/ms as the speed of propagation, which is consistent with the 0.09–0.4 mm/ms expansion speeds of SMO measured from various species, cortical and allocortical areas (Benucci et al., 2007; Bringuier et al., 1999; Grinvald et al., 1994; Prechtl et al., 2000). To estimate $\boldsymbol{d}$, we extrapolated how far a single radial oscillation period ($\boldsymbol{T}$) would propagate as $\lambda = \boldsymbol{T} \times \boldsymbol{v}$. Given that $\boldsymbol{T} = \boldsymbol{f}^{-1} \approx 25$ ms and $\boldsymbol{v} \approx 0.1$ mm/ms the estimated diameter range of integrative cortical units are $\boldsymbol{d} = \lambda/2 \approx 1{,}250$ μm (**Figure 4D**), consistent with the 900–1,000 μm center-to-center distance of iso-orientation columns in the cat V1 (Lowel et al., 1988; Peters and Payne, 1993). Considering that the reconstruction efficiency is near perfect at as low as $\Delta\Phi = 0.1$ ms and does not improve beyond $\Delta\Phi = 0.8$ ms, a broader range of spatial domains (578 μm < $\boldsymbol{d}$ < 4.6 mm) could satisfy gamma frequency integration. This range is consistent with the 590 μm center-to-center distance of cytochrome oxidase blobs (Murphy et al., 1998), the 430 ± 139 μm center-to-center distance of cortical biocytin patches in primate V1 and 600 μm in cat V1 (Lund et al., 1993) and 1.5–2.7 mm, the space constant ($\boldsymbol{d}$ = 2 × space constant) of the radial spread of stimulus induced transmembrane voltage change (Grinvald et al., 1994). The estimated $\boldsymbol{d}$ was also consistent with the reported range of cortical columns 600–900 μm (Jones, 2000) and

350–400 μm (Favorov et al., 1987), and the 400–500 μm projection field of layer 2/3 and layer 4 neurons in the rat barrel cortex (Lubke et al., 2003). Notably, the relationship between oscillation λ and column diameter is further supported by the observation that the dominant LFP in the primate motor cortex (area 4) is 20–25 Hz (Rubino et al., 2006), half of that of V1, while the center-to-center distance of cortical biocytin patches is twice of that of V1 (Lund et al., 1993). In summary, the operative ranges of model parameters satisfy the dynamic and structural constraints of the brain.

INFORMATION RECONSTRUCTION FROM COMBINED CODES

We thought it would substantially increase the performance of phase coding if neuronal architectures were able to combine codes of independent inputs into one compressed stream of APs and selectively reconstruct these representations at the target location by the same pool of neurons. Therefore, we asked whether the interference operator (Eq. 9) is able to recover multiple representations from a superimposed phase code of different input patterns. We used two different images, image $\mathbf{S}^{\alpha}$ and image $\mathbf{S}^{\beta}$ and two slightly

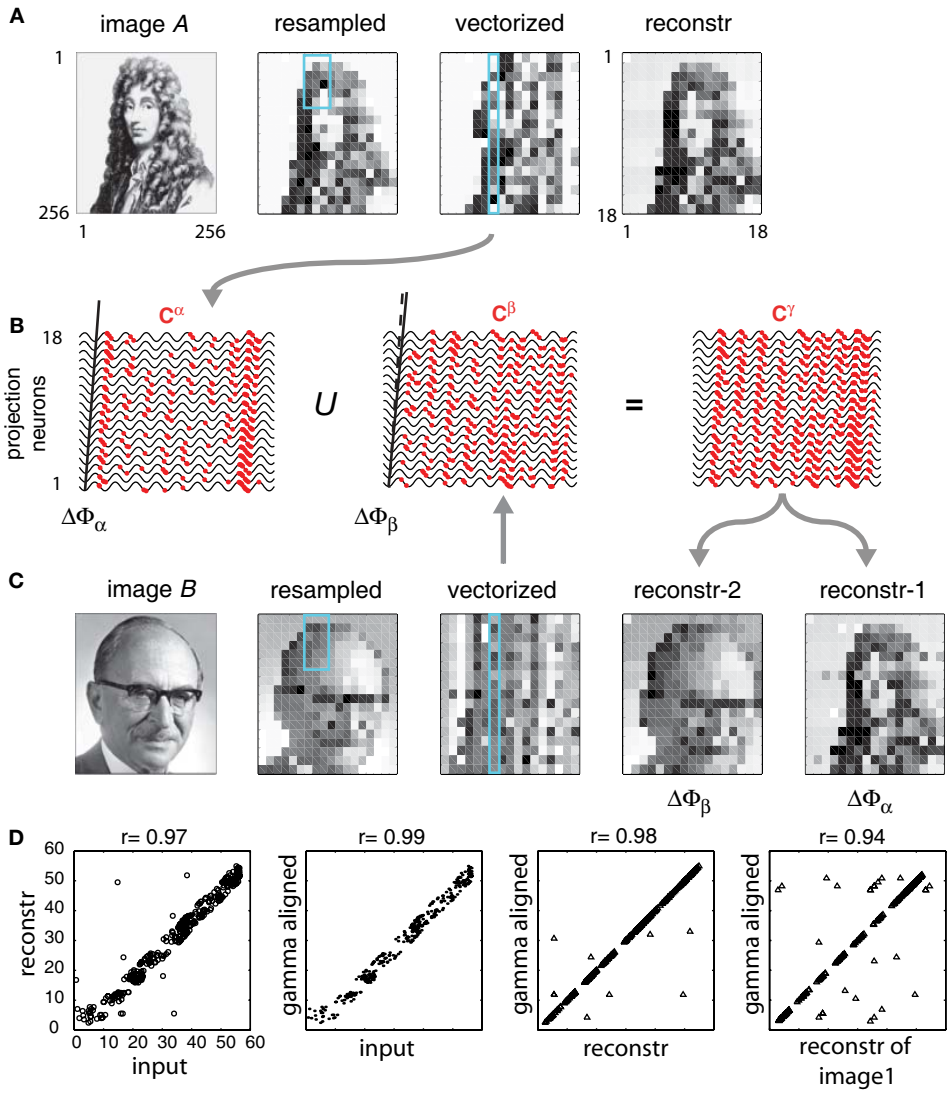

FIGURE 5 | Reconstruction of individual images from combined representations. (A,C) Two different images were digitally sampled at 18 × 18 pixel resolution and grayscales were encoded by AP phases relative to SMO field by using slightly different phase gradients $\Delta\Phi_A$ for image *A* and $\Delta\Phi_B$ for image *B*. The third panel represents the projection of input on a non-topographically organized array of neurons. The fourth panel is the reconstruction when only image *A* was applied. The receptive field was a 3 × 6 rectangle. Turquoise rectangles highlight the projection of a receptive field on the neurons. **(B)** APs collected from a single receptive field were collapsed into a single stream and processed by one of the 18 projection neurons. The left panel represents the phase code of APs derived from image *A* projected on the SMO field. The middle panel represents the same, derived from image *B*. The right panel represents the result after combining the two codes into one. This compressed AP sequence is transferred to the site of reconstruction. The last two images on **(C)** represent the reconstruction from the combined code with using $\Delta\Phi_A$ vs. $\Delta\Phi_B$. **(D)** Correlations between: input image *B* and its reconstruction from the combined code; input image *B* and SMO aligned pattern **B′**; the SMO aligned pattern **B′** and reconstruction of image *B* from the combined code; and the SMO aligned pattern **A′** and reconstruction of image *A* from the combined code.

different field gradients, $\Delta\Phi_\alpha$ and $\Delta\Phi_\beta$ (**Figures 5A–C**). First, processing image $\mathbf{S}^\alpha$ generated the $\mathbf{A}^\alpha$ latency code, transformed into $\mathbf{A'}^\alpha$ by gamma alignment to a field with gradient $\Delta\Phi_\alpha$. The pattern $\mathbf{A'}^\alpha$ was collapsed into $\mathbf{C}^\alpha$ and reconstructed $\mathbf{S'}^\alpha$ at the target using $\Delta\Phi_\alpha$ (**Figure 5A**). Likewise, we processed image $\mathbf{S}^\beta$ with the field gradient $\Delta\Phi_\beta$ and computed $\mathbf{A'}^\beta$ and $\mathbf{C}^\beta$ (**Figures 5B,C**). Next, before the reconstruction, we combined the two compressed codes $\mathbf{C}^\alpha \cup \mathbf{C}^\beta = \mathbf{C}^\gamma$, so that APs encoding image $\mathbf{S}^\beta$ were interleaved with APs encoding image $\mathbf{S}^\alpha$ (Eq. 10). The combined code included both sequences of APs, derived from two different input images, without labeling them according to the neuron of origin (**Figure 5B**). Next, we transferred the combined code $\mathbf{C}^\gamma$ to the target, where the postsynaptic neurons successfully recovered image $\mathbf{S'}^\alpha$ and image $\mathbf{S'}^\beta$ from the mixed code by applying field gradients $\Delta\Phi_\alpha$ and $\Delta\Phi_\beta$, respectively (Eqs. 11 and 12, **Figure 5C**). The reconstruction efficiency, quantified as the correlation between the gamma-aligned input and the recovered image, was near perfect ($r' > 0.9$, $P < 0.001$) when compared with the original input (**Figure 5D**). Since the variance of the correlation between the original and the gamma-aligned input was the same as the variance of the correlation between the original and reconstructed image, most of the differences between the original and reconstructed images were attributed to the gamma alignment rather than to the reconstruction.

The reconstruction from the combined phase code has intrinsic limitations. If the difference between the oscillation field gradients is small, the delay by which the two oscillation peaks reach adjacent neurons may be smaller than $\Delta\tau$, causing the neurons to confuse the input APs originating from different images. Spurious phase coincidences of the two fields may also occur if the two field gradients are very different. In order to avoid this, for a given phase gradients $\Delta\Phi_\alpha$ the second phase gradient $\Delta\Phi_\beta$ should be less than $\Delta\Phi_\alpha/(n \times \Delta\tau)$. Since n is relatively small (<9), especially when the architecture is partitioned into small receptive fields, this condition is easy to meet and does not compromise reconstruction.

Storing and retrieving multiple representations from the same pool of neurons by cueing them with slightly different SMO oscillations can be utilized as a very efficient mechanism for storing long-term memories. For the sake of algorithmic clarity, we postulated the independence of APs and SMO. However, in living tissue, large synchronized EPSPs and IPSPs may reset the field of SMOs, thus allowing selective cueing of information.

REAL-TIME MOTION PROCESSING WITH PHASE

Under natural conditions, images on the retina change rapidly either due to objects and the observer moving relative to each other or due to the observer's eye movements. A sequence of images, when presented with a frame rate ≥16 frame × s^{-1}, is perceived as motion, (Wertheimer, 1912) and motion percept does not improve beyond 48 frame × s^{-1}. This implies that under specific condition, single gamma cycles should be sufficient to process information from individual frames to generate a motion percept. It also implies that the human visual system does not benefit from a frame rate of higher than one frame per gamma cycle. We asked how phase coding would implement compression and reconstruction of a complete frame within a single gamma period with a rate of 40 frame × s^{-1}, in order to remain consistent with human motion perception. According to our simulations, a single SMO cycle is capable of capturing and retaining significant quality of the original image ($r = 0.87$ $P < 0.01$) and nearly complete representation of the gamma-aligned image ($r = 0.92$, **Figure 6**). In this simulation we used a 36×36 neuron architecture with 6×6 receptive fields converging to 36 projection neurons and reconstructed on a 36×36 neuron layer at the destination. For the SMO field we used a predefined set of 24 phase gradients. The SMO field gradients were generated by three randomly dispersed gamma sources slowly drifting frame-by-frame with Brownian motion. The input was a 24-frame segment extracted from an Eadweard Muybridge movie clip. Input frames were presented iteratively and each reconstruction was computed independently from the previous frame. The $\Delta\tau$ was 0.001, and a single gamma oscillation period was used for encoding. Because a faithful reconstruction of grayscale image requires $n > 4$ oscillation periods (**Figure 4A**), phase coding within a single oscillation period allowed to retain only the binary values per pixel (black-and-white) with no grayscale qualities processed (**Figure 6A**). Despite the black-and-white representation, the spatial reconstruction of the original frames was relatively good ($r = 0.874$, **Figure 6C**), which confirmed that sampling continuous motion by single SMO cycles is necessary and sufficient to encode a motion sequence. Notably, most differences between the original and the reconstructed image frames derived from the AP alignment (**Figure 6C**). The limited capacity to process textural details and motion at the same time is consistent with the anatomical and functional segregation of fast achromatic magno-cellular motion pathway and slow chromatic parvo-cellular pathway (Conley and Fitzpatrick, 1989; Fitzpatrick et al., 1985; Michael, 1988; Perry et al., 1984).

PHASE CODE GENERATES GRID REPRESENTATIONS

Since the discrimination time window is limited to one SMO cycle, the largest discriminative power is comprised in an area corresponding to λ (the distance that SMO travels in one oscillation). Beyond that diameter, representations likely repeat because spurious interferences will activate neurons that share the same SMO phase as they are multiples of λ apart. If the same input pixel is reconstructed by multiple neurons, separated by λ distances, as our model predicts, then it is necessary that different inputs are reconstructed by the same neuron, assuming finite input and neuron spaces. Consequently, individual neurons must endow multiple receptive fields, just like grid cells do in the medial entorhinal cortex (MEC) of rodents (Hafting et al., 2005). To provoke multiple cortical representations by spurious interferences, we performed pattern reconstructions on an image, tracking a prolonged interval of 144 gamma cycles with increased phase gradient ($\Delta\Phi = 0.1$) (**Figure 7**). The reconstruction, as predicted, yielded multiple representations of the original image (**Figure 7E**). This was due to systematic reconstruction errors caused by spurious interferences that occurred at neurons near λ distances apart within the neuronal matrix. The confusion of AP times across neurons of the output layer is clearly seen as clusters offset of the identity line of the input–output AP latency correlogram (**Figure 7F**). The consequence of these errors is twofold: (i) they generate multiple cortical representations of the same spatial location, as seen in **Figure 7E**; and (ii) these errors must make a given output layer neuron active not only when the input image is at the original position, but also a number of other positions that are multiple

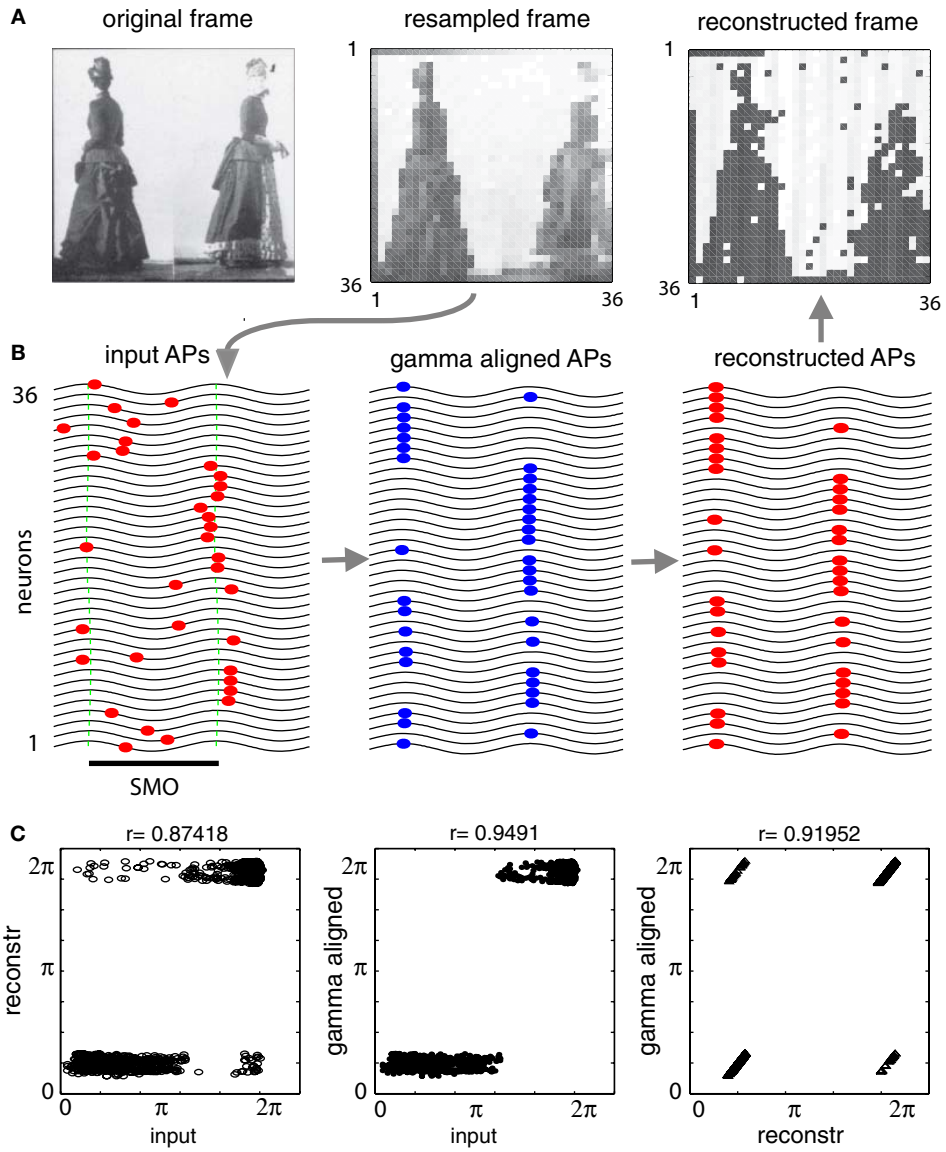

FIGURE 6 | Motion processing by successive SMO cycles. (A) An example frame of a 24-frame original movie segment by Muybridge capturing the motion of two women (left), a 36 × 36 pixel down-sampled input (middle) and the reconstruction of the frame (right). **(B)** APs evoked by image at the input layer (left), after alignment to SMO (middle) and the reconstructed APs (right). Only one row of neurons is shown. Red markers represent the APs, and waves represent the ongoing SMO per neuron. Scale bar indicates one SMO period. **(C)** Correlations between the latency-encoded input and the reconstructed AP times (left); between the latency-encoded input and the aligned APs (middle); and between the aligned APs and reconstructed APs (right). Correlation values are shown on the top. Note that most of the variances derive from the alignment to SMO. Time units are relative to the length of an SMO cycle.

of a constant distance away from the original position. In order to test this hypothesis, we kept track of the activity of an arbitrarily selected output-layer neuron (red arrow in **Figure 7E**) while circular shifting the original image matrix in 36×36 different positions. If the image on **Figure 7A** represents a square-shaped spatial environment from the rat's point of view, then shifting the image emulates an exhaustive exploration of this environment in a rat-centered coordinate system. For example, moving the image by 5 pixels north and 6 pixels east is equivalent to the rat moving 5 units south and 6 units west, where the unit is proportional to the rat's size. Next we plotted the firing probability of this neuron according to the positions of the rat in the environment (**Figure 7G**). Confirming the prediction (ii), the firing probability revealed a multifold periodic receptive-field architecture, where receptive fields were constant distance apart, reproducing false-colored copies of the original image, evenly tessellating the space. This architecture is consistent with the periodic architecture of the spatial firing fields of MEC neurons (Hafting et al., 2005). Moreover, the model provides a physiological meaning to the constant spatial separation of the observed firing fields by relating it to the λ of SMO within the MEC. In addition to grid cells, according to (i), the model predicts that the actual spatial location

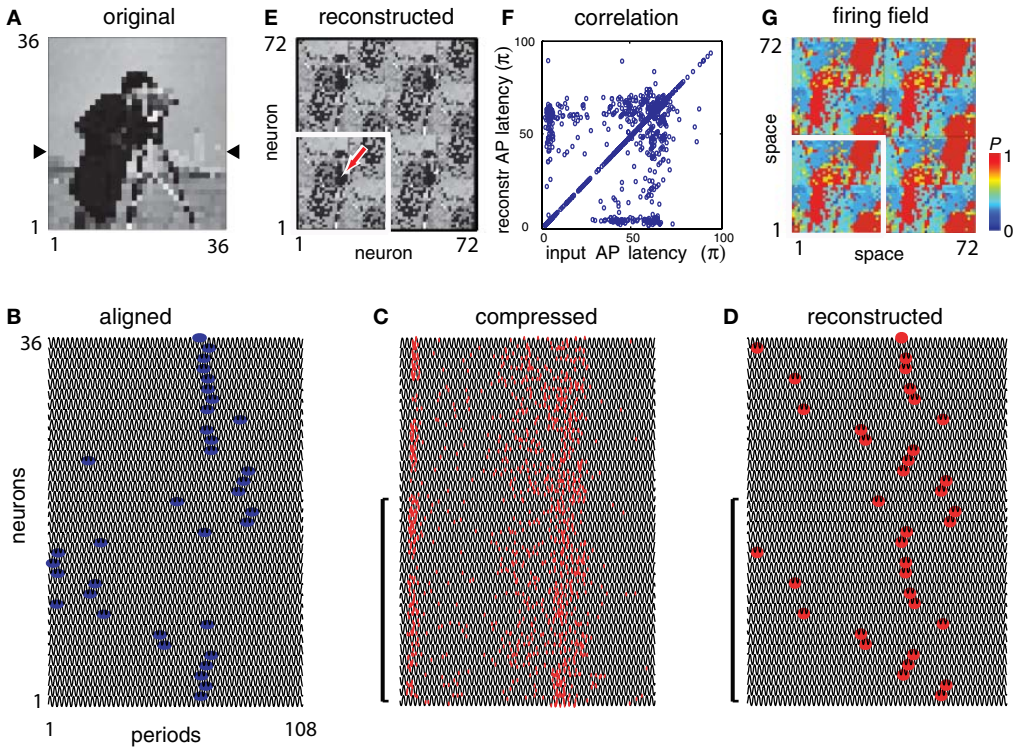

FIGURE 7 | Construction of multiple cortical representations by spurious interferences. (A) A 36 × 36 grayscale image was used as input and partitioned into 36 non-overlapping receptive fields, which were mapped on a 36 × 36 input neuron matrix. **(B)** The activity pattern of a row of neurons [between arrowheads in **(A)**] that receives input from a single receptive field. Blue-filled circles represent the APs by neurons (ordinate) after the gamma alignment, spreading through 108 cycles (abscissa). Applying a relatively steep SMO gradient ($\Delta\Phi = 0.1\pi$) ensured that multiple neurons shared identical ($<\Delta\tau$ SMO phases, thus facilitating interferences of individual APs of the compressed code with multiple target neurons. **(C)** The activity of 1,296 neurons total was compressed into 36 channels (one receptive field per neuron). APs are represented by red dots. **(D)** The spatio-temporal pattern of APs (red-filled circles) after the reconstruction. Note the spatially periodic structure of the APs (a complete period is shown within the vertical bracket). **(E)** As a result of multiple interferences, the reconstructed image retains multiple representations of the original input. The original 36 × 36 reconstruction (within the white square) was expanded to a 72 × 72 neuron architecture to make the multiple representations more apparent. **(F)** The interference that led to multiple reconstructions is evident from the correlation plot between the original input AP times and the reconstructed AP times. The dot clusters different from the diagonal are the results of spurious reconstructions, which led to the multiple representations on **(E)**. The abscissa represents input AP times, the ordinate represents reconstructed AP times in SMO cycles. **(G)** Firing field of a neuron (marked by a red arrow on **E**) in spatial coordinates. Colors represent the probability of APs generated while the neuron is exposed to a given image displacement. Construction of the plot is explained in the text. Note the grid-cell like periodic receptive field architecture.

of the rat activates not one but multiple grid cells with shared firing fields, and these neurons must be anatomically arranged in a grid-like periodic architecture over the entorhinal cortical sheet (**Figure 7E**) that mirrors the periodic receptive field architecture of individual grid cells. Consistent with the proposed relationship between the grid cell geometry and phase coding, the frequency of SMO in MEC neurons, and thus λ, has been reported to scale with grid cell field spacing (Giocomo et al., 2007). We remark that the periodic structure of reconstruction necessarily occurs in 1-D but that the exact geometry in 2-D depends on the location of neurons where spurious interferences occur. Most likely, the spurious interferences generate confusions of different degrees. Neurons that are integer cycles apart share nearly identical SMO phases. Consequently, when APs are reconstructed from phases, these neurons generate confusions, which manifest in reproduction of the original image in nearly perfect copies. These neurons represent the main-grid points of the output representation (seen as the multiple images of the photographer in **Figures 7E,G**). Other neurons generate only partial confusion. These neurons are usually half the distance of the main-grid points and they partially reproduce the original input (seen as phantom images of the photographer in the upper right and lower right corners of the area within the white frame in **Figure 7E**). Because the partial and complete confusion grids have the same period but with a half-period offset between them in both X and Y coordinates, the superposition of the two grid structures constitutes an elongated hexagonal grid topography (**Figures 7E,G**). Since there are also other ways of achieving a hexagonal structure, this may or may not be the mechanism by which the stereotypical grid cells in the MEC acquire precisely such geometry.

PHASE CODE EXHIBITS AP PHASE PRECESSION

Among the most prevalent evidence for the behavioral significance of systematic phase variation is the phase precession of hippocampal pyramidal cell firing relative to the local theta oscillation while a rat traverses through the place field of the neuron

(O'Keefe and Recce, 1993). These pyramidal neurons also exhibit theta frequency SMO (Leung and Yim, 1986). Since our model requires nothing more than that AP timing be dependent on a coherent oscillatory drive (SMO) that propagates in space, we investigated whether phase precession can occur without further assumptions. We implemented the spatial navigation condition by defining a 16×16 matrix of topographically arranged place cells where neuron a_{ij} at the ith column and jth row was driven by the input corresponding to the rat being at the location defined by its X_i and Y_j coordinates. Thus, the place field of the rat when moving through X_iY_j was modeled by neuron a_{ij} being exposed to a transient stimulus. Theoretically, this is equivalent to a transient stimulus, defined as a 2-D Gaussian, moving through the receptive field of a neuron (**Figure 8A**). This is similar to the real-time motion processing example in **Figure 6**, except that the SMO here represents theta instead of gamma. The complete path of the rat was modeled by a series of 20 frames consisting of 16×16-pixel-resolution snapshots, in which the 2-D Gaussian advanced one pixel per frame. Since the diameter of the Gaussian was larger than the place field of a neuron, the rat's position evoked activity in adjacent place cells proportional to the amplitude of the Gaussian intersecting with their place fields. The square area outlined in **Figure 8A** covers the place fields of nine neurons. Multiple neurons were activated when the rat was crossing this area. The phase-coded APs of these neurons were combined into a compressed code and shared among the nine neurons before reconstruction. When we tracked the activity of these neurons while the location of the rat changed across frames, the compressed AP sequences displayed a systematic phase precession as a function of the distance from the center of the Gaussian, consistent with the empirical phase precession of hippocampal end entorhinal cortical neurons (Hafting et al., 2008; O'Keefe and Recce, 1993). We controlled only one parameter in these simulations, the phase gradient of the SMO field. **Figures 8B–E** shows that the direction of phase precession depended on the geometry of the SMO field applied to both input encoding and reconstruction. When unidirectional propagating waves (traveling waves) were applied, depending on the direction of propagation relative to the activation sequence of place cells, we observed different monotonic phase precession effects. Wave propagation in the direction opposite of the place cell activation sequence enabled progressive phase advancement, while wave propagation in the direction of place cell activation sequence enabled progressive phase delay (**Figures 8B,D**, respectively). By reducing the SMO phase gradient ten times decreased the slope of phase precession 10 times from 280° to 28° (**Figures 8B,C**). Furthermore, when a radial propagation of SMO field was applied (from a single or from multiple sources) the precession started with increasing phase advancement until the animal, i.e., the center of the Gaussian, reached the center of the neuron's place field, followed by a progressive phase delay as the animal was leaving the center of place field (**Figure 8E**). The dependency of phase precession angle on the SMO gradient relative to the activation sequence of the place cells suggests that hippocampal pyramidal neurons may be able to "read out" the rat's heading direction from the phase precession, assuming that the local SMO field gradient does not change rapidly over time (Huxter et al., 2008). In summary, phase precession derives naturally from phase coding, without making any additional assumptions, such as asymmetric synaptic potentiation (Mehta et al., 2000) or dual-oscillator drive (Blair et al., 2008; Burgess, 2008; Lengyel et al., 2003). Phase precession is controlled by a single parameter, the SMO field gradient. Furthermore, consistent with experimental data, phase precession in our model does not require multiple trials to develop but it does require SMO (Hafting et al., 2008). Since object locations in the environment, according to this model, are originally encoded by phase, we propose that phase precession (phase advancement and phase delay) is expressed in all cortical and limbic structures, including the MEC (Hafting et al., 2008) and primary sensory areas of the neocortex where the spatial representations are continuously updated due to behavior.

MODELING STIMULUS INVARIANTS

In order to represent stable objects in a dynamic world, neurons must encode object features invariantly with respect to a few common transformations such as position, rotation and time. In order to address whether or not phase coding is able to retain some of these features in spite of spatial or temporal discontinuities, we modeled four different types of invariant stimulus conditions: (i) space-time invariant 1-D stimulus, (ii) 2-D stimulus embedded in random background noise, (iii) 2-D transposition-invariant stimulus and (iv) character recognition. We classified these invariants with respect to either temporal or spatial transformations. Among the invariants we tested, (i) and (ii) were time invariant, while (iii) and (iv) were invariant to spatial transformations. (Implementations of the ii, iii and iv types of invariant preservations are described in the Supplementary Material.)

For (i) we constructed a 1-D random vector $\mathbf{R}$ containing 32 values $[\mathbf{r}_1,\ldots,\mathbf{r}_{32}]$. Next we defined "frames" as the possible subsets of this vector containing 16 adjacent values. We then began an iterative cycle, where first we inputted the first frame $[\mathbf{r}_1,\ldots,\mathbf{r}_{16}]$ to a network of 16 neurons $[\mathbf{s}_1,\ldots,\mathbf{s}_{16}]$ and performed all four phases of information processing from encoding to reconstruction. During each of the next 16 cycles, we incremented the frame position by one step $[\mathbf{s}_1,\ldots,\mathbf{s}_{16}] = [\mathbf{r}_i,\ldots,\mathbf{r}_{i+15}]$, where $i = \{2,\ldots,17\}$, and performed all four phases of information processing. Thus in each iteration, 15 out of 16 frame values remained identical to the values in the previous frame, but each of the 15 values was projected onto a different neuron at each exposure (**Figure 9A**). Presenting the neurons with only part of the complete pattern in each cycle, such that each neuron's input value changes every cycle, allowed us to address how a constant (time-invariant) spatial pattern is represented by the phase code in the array of neurons over time (**Figures 9B–E**). When we superimposed the temporal patterns of APs of the compressed codes (transfer stage) from all of the 17 successive trials, we observed a marked conservation of AP latencies along with sudden transitions of gamma re-alignments (**Figure 9D**). The conservation of time-invariant patterns is reflected by the temporal consistency of APs over time. This consistency was quantified by correlating the AP times (wrapped around 3π) from one frame with the AP times of the next frame and comparing it to the correlation obtained when the stimulus frames were uncorrelated random patterns (i.e., when there was no overlap between successive frames). The return plots in **Figure 9F** summarize these correlations. As seen on the left return plot,

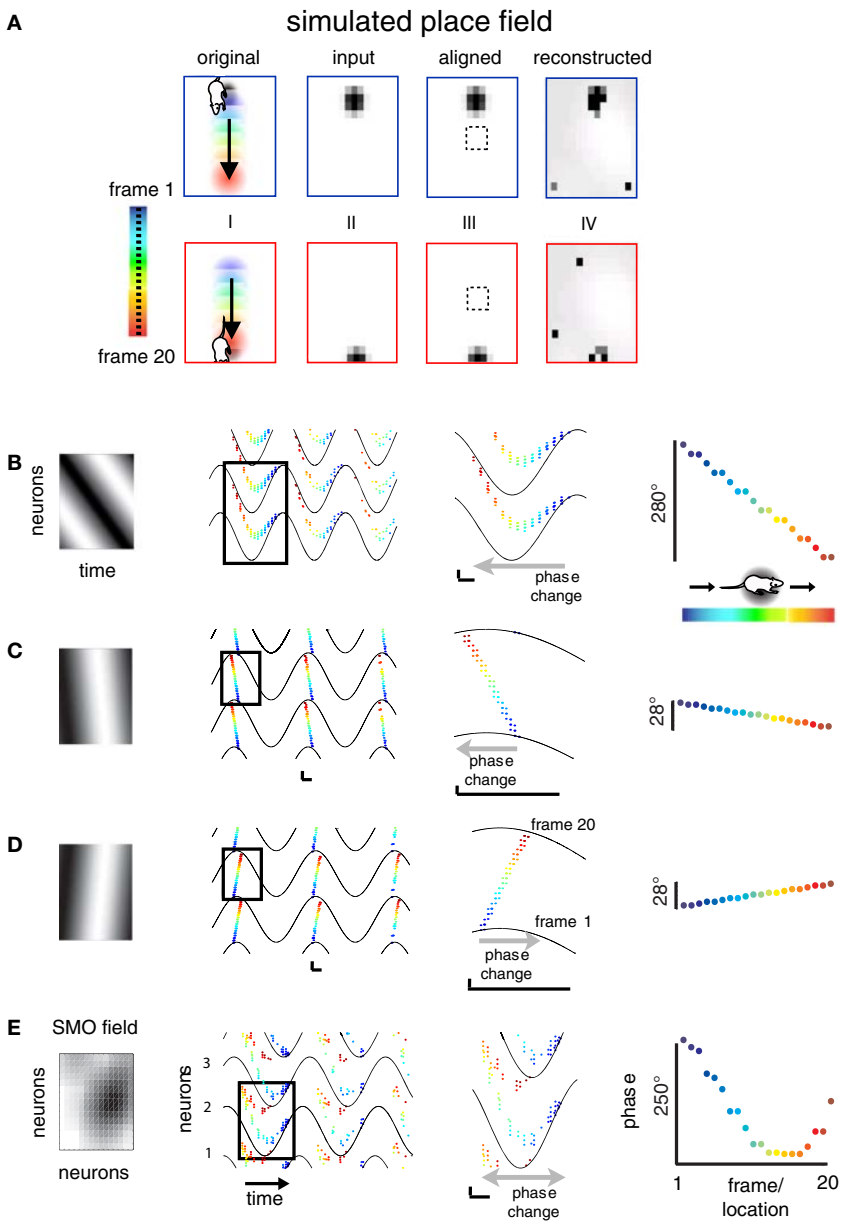

FIGURE 8 | Phase code exhibits phase precession. (A) The input to hippocampal place cells was modeled by generating a 20-frame translation of a 2-D Gaussian representing the rat's position (rendered with colors) relative to the environment (rectangle). The area was evenly tiled with place fields individually mapped on a 16 × 16 grid of input layer neurons. The size of the Gaussian was chosen such that 9–12 neurons were simultaneously exposed to the rat's location, but the composition of neurons driven by a given input frame changed with the rat's location. The four blue and red framed panels represent the four processing stages of the initial and terminal frames, respectively: (I) the rat's location, represented by a 2-D Gaussian, (II) the discrete sampling of the input by the grid of neurons (input), (III) the input phases in grayscale after APs are aligned to the SMO, and (IV) the reconstructed activity pattern of neurons encoding the rat's own location. The outlier pixels in both frames are reconstruction errors. **(B–E)** Effects of SMO field topography on phase precession. Left panels represent the SMO (**(B–D)** in time-neuron and **(E)** in neuron space). Second and third panels represent snapshots of the activity of three projection neurons at different magnifications. These neurons in the model represent hippocampal pyramidal cells with adjacent place fields within the outlined area [dashed rectangle on **(A)**]. The APs evoked by consecutive frames are projected between the SMO waves of adjacent neurons and color-coded according to the input frame in **(A)** corresponding to the rat's location. The abscissa represents the time of the APs. The forth panels represent the phase of APs during a single run as a function of the rat's location. **(B)** When a traveling wave SMO field gradient was applied the neurons expressed a monotonically advancing AP phase precession spanning 280° theta phase angle. **(C)** By reducing the phase gradient of SMO ten times the AP phase precession angle decreased proportionally to 28°. In both examples **(B,C)** the traveling direction of SMO was set to be the opposite to the place cell activation sequence. **(D)** We reversed the direction of phase precession relative to **(B,C)** from monotonically increasing advancements to monotonically increasing delays by changing the SMO phase gradient such that it traveled in the direction of the activation sequence of neurons. **(E)** A bidirectional AP phase precession was enabled by a radially propagating SMO field, where the AP phases advanced continuously until the animal reached the place field center [outlined area in **(A)**] and developed an increasing delay as the animal exited. Phase scale bars represent ¼ π. Arrows signify the directions of phase precessions.

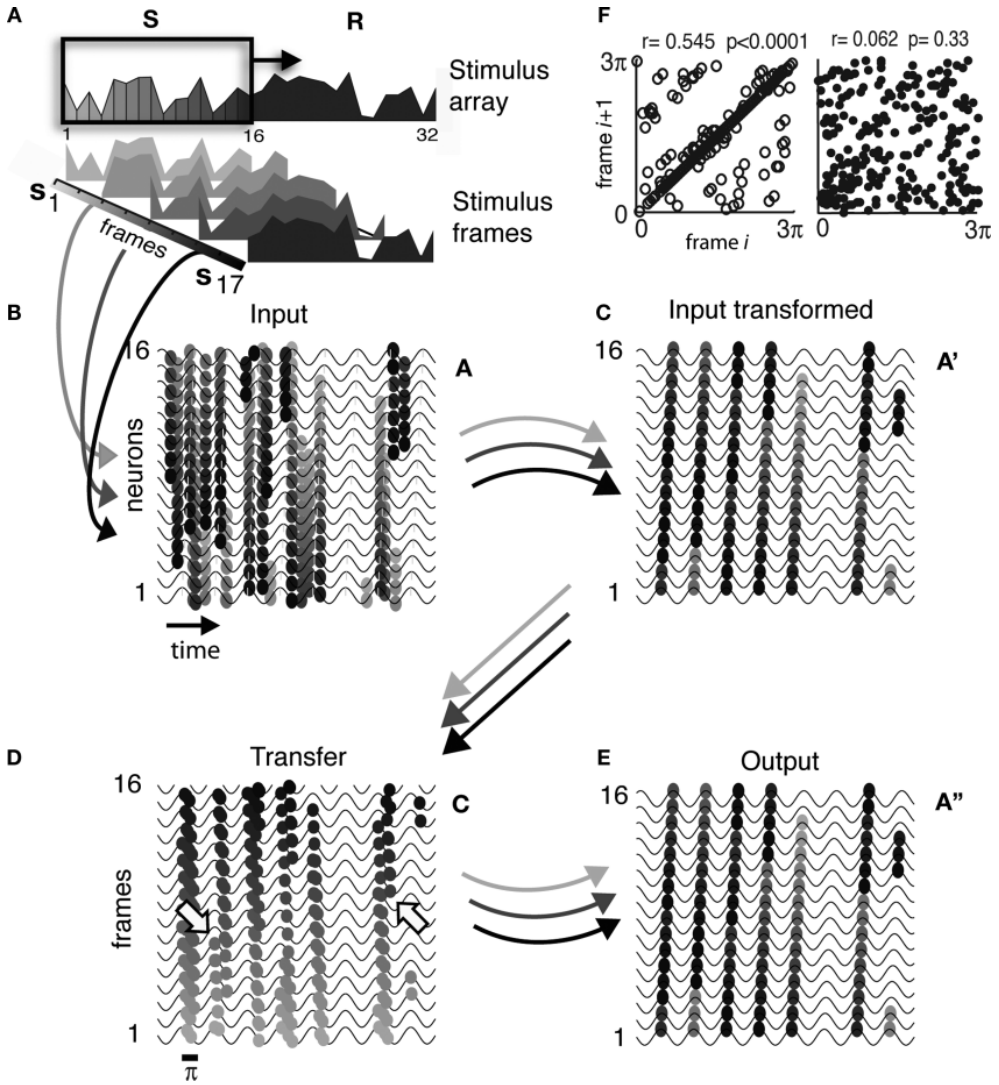

FIGURE 9 | Phase coding is sensitive to stimulus invariance. (A) A 16-sample-wide window **(S)** was applied to a stimulus vector (**R**) containing 32 intensity values and the result inputted to 16 neurons of the input layer. The window was slid across R, one sample at a time, to generate 17 successive frames. In this figure we illustrate only 5 of the 17 frames using different grayscales. The network processed each frame as an independent stimulus vector from the encoding to the reconstruction stage **(B–E)**. **(B)** Superposition of the AP patterns induced by all 16 frames. The grayscale values of filled circles correspond to the frame in **(A)**. **(C)** The temporal variability of APs is reduced after aligning them to gamma oscillations. **(D)** The compressed AP streams, superimposed across frames, show a preserved temporal pattern with sudden phase transitions (open arrows) at points where APs from a new frame are assigned to the next gamma cycle. **(E)** Superimposed traces of the reconstructed patterns. **(F)** Return plots represent the recurrence of AP-times from frame *i* to frame *i* + 1. The left return plot was calculated from the AP pattern in **(D)** when stimulus **(A)** was presented. The right return plot was calculated from an example where consecutive frames were uncorrelated. Although each neuron processed different input from every frame, the temporal patterns of APs across successive frames were highly correlated (left). In contrast, when input frames were random and independent from one another the AP patterns became uncorrelated (right). Both plots contain the same number of data points. AP latencies were wrapped around 3π. (The *r* and *P* values are shown above the plots.)

invariant stimulus frames evoke AP patterns in the compressed code that are highly correlated across frames, despite phase transitions and despite the fact that each neuron receives a different input from each frame. In contrast, uncorrelated frames evoke APs that are uncorrelated across successive frames. This conservation of the AP pattern for an invariant stimulus has implications for visual information processing. For example, we predict that V1 projecting LGN neurons should generate self-similar and stimulus-dependent AP sequences for slowly moving images. These AP sequences are expected to be invariant of position shifts of the whole image on the retina within a certain range of eye movements.

DISCUSSION

We presented theoretical support for phase coding in the CNS with the following two questions in focus: How can the precise spatio-temporal structure of a stimulus be encoded by the phase of APs, and how then can it be recovered from the phase of APs? The model outlined above interprets phase locking as a mechanism by which

the phase of APs encodes the precise spatiotemporal structure of the visual input using gamma oscillations as a reference. Utilizing the phase the brain is able to keep different stimulus features separated within the same code (impossible with rate coding) until these features are separated by individual neurons upstream, consistent with sparse coding (**Figure 5**). At the same time the phase code allows simultaneous information to be bound together by referencing them to the same gamma cycle, which allows a smooth tracking of sensory input, such as that illustrated on the example of motion processing at a physiological rate (**Figure 6**). Aside from the capability of modeling thalamo-cortical and cortico-cortical information processing, phase coding demonstrates a remarkable flexibility in reproducing known functional features of the allocortex, such as the grid cells of the entorhinal cortex and the phase precession of hippocampal pyramidal cells (**Figures 8 and 9**, respectively). Moreover, phase coding allows the extraction of stimulus features that are invariant with respect to spatial and temporal transformations (**Figure 9** and Figure 2 in Supplementary Material).

Remarkably, phase coding does not contradict with rate coding. The two encoding schemes are compatible (Ahissar et al., 2000), they may coexist (O'Keefe and Burgess, 2005) and/or may complement each other (Gollisch and Meister, 2008; Kayser et al., 2009) simply because the likelihood of coincidences between the presynaptic AP and postsynaptic SMO scales with the frequency of APs. Moreover, modulation of firing rate is concomitant with changing the phase structure of APs (Margrie and Schaefer, 2003). Immediate predictions made based on phase coding are summarized in **Table 1**.

Nevertheless, the robustness of the model depends on a number of limiting factors, which remain to be investigated. One is the dependency of phase coding on the need for compression before transmission. A key assumption we made for the sake of theoretical clarity in the 1-D model was the n-to-1 dimensionality reduction from the n input layer neurons to a single channel and a 1-to-n dimensionality expansion by information reconstruction at the target layer. This extreme information compression was feasible within the parameter space specified in **Figure 4** (Section "Biological Significance of Model Parameters"). However, considering parameters closer to the physiological condition, such as a large n with intrinsic noise in membrane potential affecting AP generation, combined with certain variance of oscillations, and heterogeneous axonal composition within the projection pathways, the n-to-1 reduction is neither necessary nor feasible. This has two consequences. First, a substantial saving in axonal volume can still be achieved with an n-to-m mapping, where $n > m \geq 1$, which would not be possible without phase coding. Second, by clustering neurons into m groups, where instead of n a smaller $n' = n/m$ neurons converges on a single channel, the need for m projection neurons would still substantially improve the reconstruction efficacy, consistent with the known convergence of sensory input on single neurons that constitutes for receptive fields (**Figure 3**).

Another limiting factor is the precision of neural code. The phase coding model requires neurons to resolve ~1.5 ms coincidences between input and intrinsic SMO under the assumption that SMO is 40 Hz. Whether or not the CNS is able to maintain this high precision has been argued (Shadlen and Newsome, 1998; Shmiel et al., 2005). Since the ~1.5 ms precision would guarantee that neighboring neurons do not confuse the origin of two input APs coinciding with their slightly different SMO, this precision is most likely to be verified in the cross-correlograms of nearby neurons. Another factor of precision is the frequency of SMO. In structures where the predominant SMO has a less than 40 Hz frequency, such as the 5–7 Hz in the entorhinal cortex (Giocomo et al., 2007), the required precision is proportionally less, only $\Delta t < 12$ ms. Thus ~1.5 ms precision is the most extreme requirement for precision.

Table 1 | Predictions based on the phase coding model. Phase coding, a common oscillatory reference with a field gradient, and the AP-SMO coincidence are the three cornerstones of the model. They are also highly interdependent, which enables to make these predictions.

#	Predictions
1	Gamma LFP must show a phase gradient (v = ~0.1 mm/ms) between adjacent neurons within a cortical column. This can be conceived as propagating waves or radial spread of gamma activity from multiple generator foci.
2	The phase gradient is dependent on the wavelength of characteristic LFP at a given region, and this wavelength is proportional to the average columnar center-to-center distance (Giocomo et al., 2007; Lund et al., 1993). Thus, the radius of cortical columns must scale with the wavelength of dominant LFP oscillations. A supportive evidence is that grid cell spacing has been reported to scale with the theta frequency SMO in layer-II entorhinal cortical neurons (Giocomo et al., 2007).
3	Among simultaneously recorded neurons, those that are exposed to their preferred stimulus should exhibit a more precise phase lock of APs with the local gamma recorded from the same electrode than neurons exposed to a suboptimal stimulus.
4	The precision of AP to AP cross-correlation between excitatory neurons in the superficial cortical layers should be an order of magnitude higher (~1.5 ms) than the precision of the autocorrelations (15–25 ms).
5	High magnitude of zero time-lag cross-correlations should be most expressed between layer-4 granule cells of the neocortex because they are the recipients of the compressed code. In contrast, supra granular layer pyramidal neurons should generate much smaller (but more precise; see Section "Discussion") cross-correlations because their outputs represent the reconstructed sparse code. The average firing rate of these neurons is expected to be also lower than that of granule cells in layer-4.
6	Intervention of SMO propagation is expected to disrupt information reconstruction, thus altering perception. Similarly, disruption of spike timing relative to the gamma oscillation must perturb perception.
7	According to our simulations, an interval of four gamma cycles is sufficient to retain more than 90% of the information, thus 100 ms processing time after the first APs reaching V1 (~60 ms) should be sufficient to make complex perceptual decisions (Thorpe et al., 1996).

The third limiting factor is the coherency of oscillations between the source and target area. Phase coding is extremely sensitive for the degree of coherence between source and target. A number of physiological mechanisms have been suggested to maintain high cross-structural coherence, such as the thalamo-cortical loop (Llinas and Ribary, 1993; Steriade et al., 1996), entrainment of cortical gamma rhythms by hippocampal theta (Sirota et al., 2008), cortical theta reset (Rizzuto et al., 2003), and gap-junctions (Traub et al., 1996), but direct evidence for an overall synchronizing mechanism that would ensure precise coherence between sensory structures and corresponding cortical areas is lacking.

The fourth limiting factor is the noise tolerance of phase coding. We argued that the compression of the phase code before transference through the projection pathways improves the noise tolerance, and we suggested that compression combined with a feed-forward parallel distribution would improve reliability by implementing an error correction mechanism.

The last limiting factor is the lack of direct evidence for phase-shifted fields of SMO. This pre-assumption was made based on combining two sources of evidence. One is the direct observation of propagating membrane potential changes by intrinsic optical signal and voltage-dependent Ca^{2+} imaging (Benucci et al., 2007; Bringuier et al., 1999; Grinvald et al., 1994; Prechtl et al., 2000) and propagating LFP waves (Prechtl et al., 2000; Rubino et al., 2006). The other source of evidence derives from direct intracellular observations of single neuronal oscillations, such as subthreshold membrane oscillations (Giocomo et al., 2007; Hutcheon and Yarom, 2000; Llinas et al., 1991). Based on the high correlation between LFP and SMO of individual neurons, the conjecture of phase-shifted field of SMO is plausible.

In conclusion, we demonstrated through various examples that the benefit of encoding information by the phase of APs relative to the intrinsic neuronal oscillations is multifold:

(i) Allows different types of sensory data to be converted to a common coding scheme in which information is referenced by the field of local oscillations and decoded independent of the neuronal distance from the original location and time in the brain, given that the reference oscillation field has the same spectral properties as at the source.
(ii) Protects the code against potential distortions due to the variance of conductivity during transmission in long projection pathways.
(iii) Enables deployment of the same compressed information over large areas of the cerebral cortex and selective "reading-out" of the local information (**Figure 5**) without point-to-point mapping between the neurons of the input and target areas.
(iv) Effectively compresses the spatio-temporal pattern of APs before transmission (n-to-1 and 1-to-n).
(v) Enables invariant temporal relations to be encoded independent of the delay and duration of sensory information processing. Similarly, it enables invariant spatial relations to be encoded independent of the absolute spatial location of the agent (**Figure 9** and Figure 2B in Supplementary Material).
(vi) It provides an intrinsic biological mechanism for stimulus segmentation.
(vii) It enables information reconstruction at single-neuronal precision (sparse coding) without confusion of information between neighboring neurons.
(viii) It implements spatial and temporal transformations between cortical representations (spatio-temporal receptive fields), which cannot otherwise be achieved by simply changing the topographic mapping between interconnected cortical areas (Figure 1 in Supplementary Material).

ACKNOWLEDGEMENTS

This work was supported by the National Eye Institute. I thank R. A. Andersen for support, reviewing and providing feedback on the manuscript. I further thank S. Gibson, C. Ustun, G. Mulliken, M. Brozovic, H. Cui, C. Stetson and C. Montz for valuable comments; and V. Shcherbatyuk for technical assistance.

SUPPLEMENTARY MATERIAL

The Supplementary Material for this article can be found online at http://www.frontiersin.org/systemsneuroscience/paper/10.3389/neuro.06/006.2009/

REFERENCES

Abeles, M. (1982). Role of the cortical neuron: integrator or coincidence detector? *Isr. J. Med. Sci.* 18, 83–92.
Abeles, M. (1991). Corticonics: Neural Circuits of the Cerebral Cortex. (Cambridge, Cambridge University Press).
Ahissar, E., Sosnik, R., and Haidarliu, S. (2000). Transformation from temporal to rate coding in a somatosensory thalamocortical pathway. *Nature* 406, 302–306.
Benucci, A., Frazor, R. A., and Carandini, M. (2007). Standing waves and traveling waves distinguish two circuits in visual cortex. *Neuron* 55, 103–117.
Bi, G. Q., and Poo, M. M. (1998). Synaptic modifications in cultured hippocampal neurons: dependence on spike timing, synaptic strength, and postsynaptic cell type. *J. Neurosci.* 18, 10464–10472.
Blair, H. T., Gupta, K., and Zhang, K. (2008). Conversion of a phase- to a rate-coded position signal by a three-stage model of theta cells, grid cells, and place cells. *Hippocampus* 18, 1239–1255.
Bragin, A., Jando, G., Nadasdy, Z., Hetke, J., Wise, K., and Buzsaki, G. (1995). Gamma (40–100 Hz) oscillation in the hippocampus of the behaving rat. *J. Neurosci.* 15, 47–60.
Bringuier, V., Chavane, F., Glaeser, L., and Fregnac, Y. (1999). Horizontal propagation of visual activity in the synaptic integration field of area 17 neurons. *Science* 283, 695–699.
Burgess, N. (2008). Grid cells and theta as oscillatory interference: theory and predictions. *Hippocampus* 18, 1157–1174.
Burgess, N., Barry, C., and O'Keefe, J. (2007). An oscillatory interference model of grid cell firing. *Hippocampus* 17, 801–812.
Buzsaki, G., Horvath, Z., Urioste, R., Hetke, J., and Wise, K. (1992). High-frequency network oscillation in the hippocampus. *Science* 256, 1025–1027.
Buzsáki, G., Traub, R. D., and Pedley, T. (2003). The cellular synaptic generation of EEG. In Current Practice of Clinical Encephalography, J. S. Ebersole and T. A. Pedley, eds (Philadelphia, Lippincott-Williams and Wilkins), pp 1–11.
Cassenaer, S., and Laurent, G. (2007). Hebbian STDP in mushroom bodies facilitates the synchronous flow of olfactory information in locusts. *Nature* 448, 709–713.
Chrobak, J. J., and Buzsaki, G. (1996). High-frequency oscillations in the output networks of the hippocampal-entorhinal axis of the freely behaving rat. *J. Neurosci.* 16, 3056–3066.

Chrobak, J. J., and Buzsaki, G. (1998). Gamma oscillations in the entorhinal cortex of the freely behaving rat. *J. Neurosci.* 18, 388–398.

Cisse, Y., Nita, D. A., Steriade, M., and Timofeev, I. (2007). Callosal responses of fast-rhythmic-bursting neurons during slow oscillation in cats. *Neuroscience* 147, 272–276.

Conley, M., and Fitzpatrick, D. (1989). Morphology of retinogeniculate axons in the macaque. *Vis. Neurosci.* 2, 287–296.

Dan, Y., Alonso, J.-M., Usrey, W. M., and Reid, R. C. (1998). Coding of visual information by precisely correlated spikes in the lateral geniculate nucleus. *Nat. Neurosci.* 1, 501–507.

de la Rocha, J., Doiron, B., Shea-Brown, E., Josic, K., and Reyes, A. (2007). Correlation between neural spike trains increases with firing rate. *Nature* 448, 802–806.

Favorov, O. V., Diamond, M. E., and Whitsel, B. L. (1987). Evidence for a mosaic representation of the body surface in area 3b of the somatic cortex of cat. *Proc. Natl. Acad. Sci. USA* 84, 6606–6610.

Fitzpatrick, D., Lund, J. S., and Blasdel, G. G. (1985). Intrinsic connections of macaque striate cortex: afferent and efferent connections of lamina 4C. *J. Neurosci.* 5, 3329–3349.

Fries, P., Womelsdorf, T., Oostenveld, R., and Desimone, R. (2008). The effects of visual stimulation and selective visual attention on rhythmic neuronal synchronization in macaque area V4. *J. Neurosci.* 28, 4823–4835.

Giocomo, L. M., Zilli, E. A., Fransen, E., and Hasselmo, M. E. (2007). Temporal frequency of subthreshold oscillations scales with entorhinal grid cell field spacing. *Science* 315, 1719–1722.

Gollisch, T., and Meister, M. (2008). Rapid neural coding in the retina with relative spike latencies. *Science* 319, 1108–1111.

Gray, C. M., and Singer, W. (1989). Stimulus-specific neuronal oscillations in orientation columns of cat visual cortex. *Proc. Natl. Acad. Sci. USA* 86, 1698–1702.

Grinvald, A., Lieke, E. E., Frostig, R. D., and Hildesheim, R. (1994). Cortical point-spread function and long-range lateral interactions revealed by real-time optical imaging of macaque monkey primary visual cortex. *J. Neurosci.* 14, 2545–2568.

Hafting, T., Fyhn, M., Bonnevie, T., Moser, M. B., and Moser, E. I. (2008). Hippocampus-independent phase precession in entorhinal grid cells. *Nature* 453, 1248–1252.

Hafting, T., Fyhn, M., Molden, S., Moser M.-B., and Moser, E. I. (2005). Microstructure of a spatial map in the entorhinal cortex. *Nature* 436, 801–806.

Holmgren, C., Harkany, T., Svennenfors, B., and Zilberter, Y. (2003). Pyramidal cell communication within local networks in layer 2/3 of rat neocortex. *J. Physiol.* 551, 139–153.

Hopfield, J. J. (1995). Pattern recognition computation using action potential timing for stimulus representation. *Nature* 376, 33–36.

Hutcheon, B., and Yarom, Y. (2000). Resonance, oscillation and the intrinsic frequency preferences of neurons. *Trends Neurosci.* 23, 216–222.

Huxter, J. R., Senior, T. J., Allen, K., and Csicsvari, J. (2008). Theta phase-specific codes for two-dimensional position, trajectory and heading in the hippocampus. *Nat. Neurosci.* 11, 587–594.

Jones, E. G. (2000). Microcolumns in the cerebral cortex. *Proc. Natl. Acad. Sci. USA* 97, 5019–5021.

Kamondi, A., Acsady, L., Wang, X. J., and Buzsaki, G. (1998). Theta oscillations in somata and dendrites of hippocampal pyramidal cells in vivo: activity-dependent phase-precession of action potentials. *Hippocampus* 8, 244–261.

Kayser, C., Montemurro, M. A., Logothetis, N. K., and Panzeri, S. (2009). Spike-phase coding boosts and stabilizes information carried by spatial and temporal spike patterns. *Neuron* 61, 597–608.

Lagier, S., Carleton, A., and Lledo, P. M. (2004). Interplay between local GABAergic interneurons and relay neurons generates gamma oscillations in the rat olfactory bulb. *J. Neurosci.* 24, 4382–4392.

Lengyel, M., Szatmary, Z., and Erdi, P. (2003). Dynamically detuned oscillations account for the coupled rate and temporal code of place cell firing. *Hippocampus* 13, 700–714.

Leung, L. S., and Yim, C. Y. (1986). Intracellular records of theta rhythm in hippocampal CA1 cells of the rat. *Brain Res.* 367, 323–327.

Llinas, R., and Ribary, U. (1993). Coherent 40-Hz oscillation characterizes dream state in humans. *Proc. Natl. Acad. Sci. USA* 90, 2078–2081.

Llinas, R. R., Grace, A. A., and Yarom, Y. (1991). In vitro neurons in mammalian cortical layer 4 exhibit intrinsic oscillatory activity in the 10- to 50-Hz frequency range. *Proc. Natl. Acad. Sci. USA* 88, 897–901.

Lowel, S., Bischof, H. J., Leutenecker, B., and Singer, W. (1988). Topographic relations between ocular dominance and orientation columns in the cat striate cortex. *Exp. Brain Res.* 71, 33–46.

Lubke, J., Roth, A., Feldmeyer, D., and Sakmann, B. (2003). Morphometric analysis of the columnar innervation domain of neurons connecting layer 4 and layer 2/3 of juvenile rat barrel cortex. *Cereb. Cortex* 13, 1051–1063.

Lund, J. S., Yoshioka, T., and Levitt, J. B. (1993). Comparison of intrinsic connectivity in different areas of macaque monkey cerebral cortex. *Cereb. Cortex* 3, 148–162.

Margrie, T. W., and Schaefer, A. T. (2003). Theta oscillation coupled spike latencies yield computational vigour in a mammalian sensory system. *J. Physiol.* 546, 363–374.

Markram, H., Lubke, J., Frotscher, M., and Sakmann, B. (1997). Regulation of synaptic efficacy by coincidence of postsynaptic APs and EPSPs. *Science* 275, 213–215.

Mehring, C., Rickert, J., Vaadia, E., Cardosa de Oliveira, S., Aertsen, A., and Rotter, S. (2003). Inference of hand movements from local field potentials in monkey motor cortex. *Nat. Neurosci.* 6, 1253–1254.

Mehta, M. R., Quirk, M. C., and Wilson, M. A. (2000). Experience-dependent asymmetric shape of hippocampal receptive fields. *Neuron* 25, 707–715.

Michael, C. R. (1988). Retinal afferent arborization patterns, dendritic field orientations, and the segregation of function in the lateral geniculate nucleus of the monkey. *Proc. Natl. Acad. Sci. USA* 85, 4914–4918.

Montemurro, M. A., Rasch, M. J., Murayama, Y., Logothetis, N. K., and Panzeri, S. (2008). Phase-of-firing coding of natural visual stimuli in primary visual cortex. *Curr. Biol.* 18, 375–380.

Murphy, K. M., Jones, D. G., Fenstemaker, S. B., Pegado, V. D., Kiorpes, L., and Movshon, J. A. (1998). Spacing of cytochrome oxidase blobs in visual cortex of normal and strabismic monkeys. *Cereb. Cortex* 8, 237–244.

Murthy, V. N., and Fetz, E. E. (1996). Oscillatory activity in sensorimotor cortex of awake monkeys: synchronization of local field potentials and relation to behavior. *J. Neurophysiol.* 76, 3949–3967.

O'Keefe, J., and Burgess, N. (2005). Dual phase and rate coding in hippocampal place cells: theoretical significance and relationship to entorhinal grid cells. *Hippocampus* 15, 853–866.

O'Keefe, J., and Recce, M. L. (1993). Phase relationship between hippocampal place units and the EEG theta rhythm. *Hippocampus* 3, 317–330.

Perry, V. H., Oehler, R., and Cowey, A. (1984). Retinal ganglion cells that project to the dorsal lateral geniculate nucleus in the macaque monkey. *Neuroscience* 12, 1101–1123.

Pesaran, B., Nelson, M. J., and Andersen, R. A. (2008). Free choice activates a decision circuit between frontal and parietal cortex. *Nature* 453, 406–409.

Pesaran, B., Pezaris, J. S., Sahani, M., Mitra, P. P., and Andersen, R. A. (2002). Temporal structure in neuronal activity during working memory in macaque parietal cortex. *Nat. Neurosci.* 5, 805–811.

Peters, A., and Payne, B. R. (1993). Numerical relationships between geniculocortical afferents and pyramidal cell modules in cat primary visual cortex. *Cereb. Cortex* 3, 69–78.

Peters, A., and Yilmaz, E. (1993). Neuronal organization in area 17 of cat visual cortex. *Cereb. Cortex* 3, 49–68.

Prechtl, J. C., Bullock, T. H., and Kleinfeld, D. (2000). Direct evidence for local oscillatory current sources and intracortical phase gradients in turtle visual cortex. *Proc. Natl. Acad. Sci. USA* 97, 877–882.

Quiroga, R. Q., Reddy, L., Kreiman, G., Koch, C., and Fried, I. (2005). Invariant visual representation by single neurons in the human brain. *Nature* 435, 1102–1107.

Rizzuto, D. S., Madsen, J. R., Bromfield, E. B., Schulze-Bonhage, A., Seelig, D., Aschenbrenner-Scheibe, R., and Kahana, M. J. (2003). Reset of human neocortical oscillations during a working memory task. *Proc. Natl. Acad. Sci USA* 100, 7931–7936.

Robbe, D., Montgomery, S. M., Thome, A., Rueda-Orozco, P. E., McNaughton, B. L., and Buzsaki, G. (2006). Cannabinoids reveal importance of spike timing coordination in hippocampal function. *Nat. Neurosci.* 9, 1526–1533.

Rockland, K. S., Jones, E. G., Kaas, J. H., and Peters, A. (1997). Cerebral Cortex: Extrastriate Cortex in Primates. New York, Plenum Press.

Rubino, D., Robbins, K. A., and Hatsopoulos, N. G. (2006). Propagating waves mediate information transfer in the motor cortex. *Nat. Neurosci.* 9, 1549–1557.

Shadlen, M. N., and Newsome, W. T. (1998). The variable discharge of cortical neurons: implications for connectivity, computation, and information coding. *J. Neurosci.* 18, 3870–3896.

Shmiel, T., Drori, R., Shmiel, O., Ben-Shaul, Y., Nadasdy, Z., Shemesh, M., Teicher, M., and Abeles, M. (2005). Neurons of the cerebral cortex exhibit precise interspike timing in correspondence to behavior. *Proc. Natl. Acad. Sci. USA* 102, 18655–18657.

Sirota, A., Montgomery, S., Fujisawa, S., Isomura, Y., Zugaro, M., and Buzsaki, G. (2008). Entrainment of neocortical neurons and gamma oscillations by the hippocampal theta rhythm. *Neuron* 60, 683–697.

Skaggs, W. E., McNaughton, B. L., Wilson, M. A., and Barnes, C. A. (1996). Theta phase precession in hippocampal neuronal populations and the compression of temporal sequences. *Hippocampus* 6, 149–172.

Soltesz, I., and Deschenes, M. (1993). Low- and high-frequency membrane potential oscillations during theta activity in CA1 and CA3 pyramidal neurons of the rat hippocampus under ketamine–xylazine anesthesia. *J. Neurophysiol.* 70, 97–116.

Steriade, M., Contreras, D., Amzica, F., and Timofeev, I. (1996). Synchronization of fast (30–40 Hz) spontaneous oscillations in intrathalamic and thalamocortical networks. *J. Neurosci.* 16, 2788–2808.

Thorpe, S., Fize, D., and Marlot, C. (1996). Speed of processing in the human visual system. *Nature* 381, 520–522.

Traub, R. D., Whittington, M. A., Colling, S. B., Buzsaki, G., and Jefferys, J. G. (1996). Analysis of gamma rhythms in the rat hippocampus in vitro and in vivo. *J. Physiol.* 493(Pt 2), 471–484.

Tukker, J. J., Fuentealba, P., Hartwich, K., Somogyi, P., and Klausberger, T. (2007). Cell type-specific tuning of hippocampal interneuron firing during gamma oscillations in vivo. *J. Neurosci.* 27, 8184–8189.

Wertheimer, M. (1912). Experimentelle Studien über das Sehen von Bewegung. *Z. Psychol. Physiol. Sinnesorgane* 61, 161–265.

Womelsdorf, T., Schoffelen J. M., Oostenveld, R., Singer, W., Desimone, R., Engel, A. K., and Fries, P. (2007). Modulation of neuronal interactions through neuronal synchronization. *Science* 316, 1609–1612.

Conflict of Interest Statement: The authors declare that the research was conducted in the absence of any commercial or financial relationships that could be construed as a potential conflict of interest.

Received: 02 February 2009; paper pending published: 19 March 2009; accepted: 05 July 2009; published online: 28 July 2009.
Citation: Nadasdy Z (2009) Information encoding and reconstruction from the phase of action potentials. Front. Syst. Neurosci. (2009) **3**:6. *doi: 10.3389/neuro.06.006.2009*

frontiers in NEUROSCIENCE

FOCUSED REVIEW
published: 15 September 2010
doi: 10.3389/fnins.2010.00051

Binding by asynchrony: the neuronal phase code

Zoltan Nadasdy*[1,2]

[1] *Seton Brain and Spine Institute, University Medical Center at Brackenridge, Austin, TX, USA*
[2] *Department of Psychology, The University of Texas at Austin, Austin, TX, USA.*

Neurons display continuous subthreshold oscillations and discrete action potentials (APs). When APs are phase-locked to the subthreshold oscillation, we hypothesize they represent two types of information: the presence/absence of a sensory feature and the phase of subthreshold oscillation. If subthreshold oscillation phases are neuron-specific, then the sources of APs can be recovered based on the AP times. If the spatial information about the stimulus is converted to AP phases, then APs from multiple neurons can be combined into a single axon and the spatial configuration reconstructed elsewhere. For the reconstruction to be successful, we introduce two assumptions: that a subthreshold oscillation field has a constant phase gradient and that coincidences between APs and intracellular subthreshold oscillations are neuron-specific as defined by the "interference principle." Under these assumptions, a phase-coding model enables information transfer between structures and reproduces experimental phenomenons such as phase precession, grid cell architecture, and phase modulation of cortical spikes. This article reviews a recently proposed neuronal algorithm for information encoding and decoding from the phase of APs (Nadasdy, 2009). The focus is given to the principles common across different systems instead of emphasizing system specific differences.

Keywords: neural code, oscillations, gamma, LFP, spike

Edited by:
Michael E. Hasselmo, Boston University, USA

Reviewed by:
Paul Miller, Brandeis University, USA
Michael E. Hasselmo, Boston University, USA

**** Correspondence:***

***Zoltan Nadasdy** is a research scientist whose main interest is to understand the fundamental mechanisms of neural coding, in particular the relationship between intrinsic oscillations and spike patterns. He developed these ideas over the years of studying Neuroscience at the Rutgers University (Ph.D.) and during his post-doctoral trainings in electrophysiology at the Hebrew University of Jerusalem and at the California Institute of Technology. His research areas are spike sequences, neural coding and neural correlates of visual perception. Currently he is working in the field of human electrophysiology.*
zoltan@vis.caltech.edu

PHASE CODING IN DIFFERENT SYSTEMS OF THE BRAIN

Ever since the correlation between the theta phases of pyramidal cell firing in the hippocampus and the position of the rat in a linear track was observed (O'Keefe and Recce, 1993), the question has lingered whether the phase of action potentials (APs) relative to local field potentials (LFPs) encode information or if this correlation is a mere epiphenomenon. Encoding implies that information available from the phase is decoded by neurons downstream, as their AP generation depends on this information. Numerous mechanisms have been proposed that could potentially generate phase precession relative to the theta oscillation. One class of models includes the dual oscillator interference model (O'Keefe and Recce, 1993; O'Keefe and Burgess, 2005; Blair et al., 2008) and the somato-dendritic dual oscillator model (Kamondi et al., 1998; Harris et al., 2002; Lengyel et al., 2003; Huhn et al., 2005). The key assumption in both models is that phase precession is generated by the interaction between two theta oscillations with slightly different frequencies. Another class of models focuses on the dendritic mechanisms (Magee, 2001), assumes a depolarization ramp (Mehta et al., 2002), or proposes network-level mechanisms (Jensen and Lisman, 1996; Tsodyks et al., 1996; Wallenstein and Hasselmo, 1997). Nevertheless, all of these models share the key assumption that the cause of phase precession is localized within the hippocampus. In contrast, we proposed an alternative model, which considers phase coding as originating

Subthreshold membrane potential oscillations
The fluctuation of neuronal membrane potential around the mean, while the neuron does not fire any action potentials.

from sensory processing, after which the code is transferred to the cortex where it is decoded and re-encoded before it is further propagated to the associated systems, including the entorhinal cortex (EC) and hippocampus (Nadasdy, 2009). Recent studies reporting AP phase modulation in the prefrontal (Montemurro et al., 2008; Kayser et al., 2009; Siegel et al., 2009), auditory (Kayser et al., 2009), visual (Montemurro et al., 2008), and EC (Hafting et al., 2008) are consistent with this view. Despite the differences in physiological characteristics, cell types, the input–output connectivity and predominant oscillation frequencies across these systems, we argue that the sensory, thalamo-cortical and limbic systems are sharing the common language of phase coding. In this review without the capacity of describing system specific implementations we overview the common mechanism of AP phase coding.

ACTION POTENTIALS AND SMO

When we record a neuron intracellularly while injecting different levels of current pulses, the current will drive the **subthreshold membrane potential oscillations** (SMOs) toward the threshold potential, evoking APs upon threshold crossing (Llinas et al., 1991). The larger the depolarizing current is, the more likely the membrane potential is to cross the threshold and generate APs. This is the mechanism by which the intensity of a sensory signal is converted to a firing rate code. Intriguingly, the level of input current in these experiments will not only affect the firing rate but also the phase of APs, as phases advance systematically with increasing depolarization, even after the firing rate has been saturated (**Figure 1**).

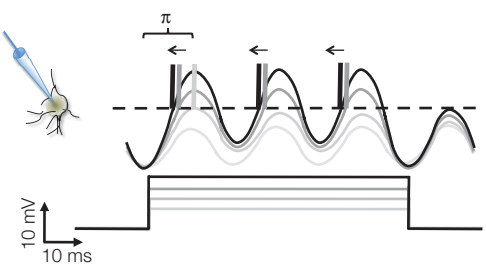

FIGURE 1 | The scheme of intracellular current clamp recordings from a neuron being depolarized by different levels of current injection. As the level of depolarizing current increases (gray levels), the amplitude of subthreshold membrane potential oscillation increases with it. At the moments when the oscillations reach the threshold (dashed line), the neuron generates action potentials (vertical lines represent truncated action potentials). Near the threshold the action potential generation is probabilistic. The number of action potentials (0, 1, 3, 3) increases with the level of depolarization. At the same time, with the increasing current, the phases of action potentials relative to the membrane oscillations advance (left pointing arrows). The range of the phase change is bound to π. Note that while the number of action potentials saturates at 3, the phase still advances. (Scale bar is at bottom left.)

Using the phase, neurons are endowed with a broader dynamic range for encoding information than they are with the firing rate. A similar sensory encoding scheme has been proposed and experimentally observed in the salamander retina (Gollisch and Meister, 2008). If neurons encode information using the phase of APs, how will that information be read out?

OSCILLATIONS: TEMPORAL AND SPATIAL COHERENCE OF NEURONAL OSCILLATIONS

The fluctuation of neuronal membrane potential around the mean without generating APs is known as SMO. This oscillation has a power spectrum with peaks at regionally specific resonant frequency bands, for instance olivary neurons ~5 Hz (Devor and Yarom, 2002a), entorhinal cortical neurons 4–7 Hz (Giocomo et al., 2007), and cortical neurons ~40 Hz (Llinas et al., 1991; Silva et al., 1991). The most likely sources of such oscillations are specific intrinsic conductances (White et al., 1998; Dickson et al., 2000; Fransen et al., 2004). However, the coherency of SMOs across neurons depends on electrotonic interactions between neurons (Devor and Yarom, 2002b). A number of mechanisms, including gap junctions, electrotonic synapses, ephaptic conductivity, and glial transfer (Yeh et al., 1996), have been proposed to mediate SMOs between neurons. These mechanisms allow the SMO to propagate in a radial spread or traveling waves, depending on the network architecture. Moreover, near-synchronized activity of interneurons impinging on different parts of principal cells may also sculpt such oscillations (Buzsaki and Chrobak, 1995).

Regardless of whether they are imposed or exchanged, we assume that these oscillations are *not independent* between neurons. Instead, oscillations of adjacent neurons stabilize themselves into a *near-synchronized* state. A number of studies confirmed the propagation of membrane oscillations and LFPs as either radial or traveling waves (Bringuier et al., 1999; Prechtl et al., 2000; Benucci et al., 2007; Lubenov and Siapas, 2009).

Based on the prevalence of SMOs, we further assume that the extracellular sum of such population-wide, near-synchronized rhythms contributes to the LFP. Although LFPs are considered to be derived from the sum of synaptic activity at the dendritic regions of neurons (Mitzdorf, 1985; Logothetis et al., 2001), a significant oscillatory component of LFP may also be derived from the sum of SMOs within a 250-μm (Katzner et al., 2009). This is supported by the shared theta frequency oscillation between intracellular SMOs and LFPs within the EC and in the frontal lobe (Alonso and

Reconstruction
When the original spatial information encoded at the source (sensory neurons/cortex), is transferred in a compressed fashion and reproduced at the target area (cortex) by principal neurons.

Llinas, 1989; Llinas et al., 1991), as well as by the high correlation between LFP and intracellular SMO (Tanaka et al., 2009). The high correlation between LFP and SMO accomplishes a conceptual link between LFP and SMO and enables an important experimental shortcut of estimating the SMO based on the LFP.

The following two sections outline the principles of the phase-coding model.

INTERFERENCE PRINCIPLE

Subthreshold membrane potential oscillations play critical roles in phase coding during both encoding and decoding. The periodic amplification of the excitatory postsynaptic potentials (EPSP) by the SMO, which causes sensory neurons to convert input to AP phases during encoding, also makes the decoding-neurons highly selective for the timing of EPSPs. A presynaptically evoked EPSP that coincides with the depolarizing phase of the SMO is more potent in evoking APs than EPSPs outside of that time window. Due to the electrotonic propagation of SMO, there is a distance-dependent phase difference in membrane oscillations between most neurons, which, in a sufficiently large network, covers the entire 180° phase range. Thus, coincidences between input APs and SMO peaks are spatially restricted and neuron-specific. Conversely, for any input AP time there will be a neuron that is most activated by the AP–SMO coincidence. We call this the *interference principle* (**Figure 2**).

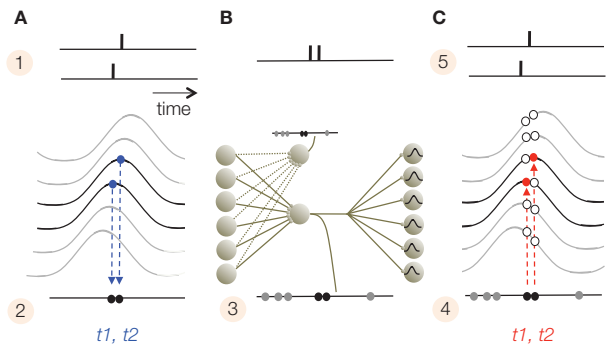

FIGURE 2 | Interference principle. (A) The top panel illustrates the times of two APs generated by two adjacent neurons (1) after their alignments to the intracellular SMO (2). Because the only APs that survive are the ones that coincide with the peak of SMO, the propagating oscillation will convert the spatial distance between the two neurons into a slight delay (*t1*, *t2*) between the two APs (2). **(B)** At the transfer stage, due to convergent and divergent synaptic connections, APs from a subset of neurons will merge on a set of projection neurons with low thresholds. Projection neurons sharing input from the same pool will replicate the same compressed AP train (3). **(C)** The compressed code projects to a large pool of target neurons. Since target neurons have a similar propagating SMO, the projected APs will generate a new AP only on neurons where the AP precisely coincides with the SMO peak (4). This is the interference principle. The red circles represent these coincidences, while open circles are the mismatches. As a result, the APs pattern (*t1*, *t2*) recovered the original input pattern from (2).

The interference principle guarantees a consistent mapping of an input AP pattern on a spatial layout of neurons, which reproduces the original temporal pattern of APs (Nadasdy, 2009). For a faithful spatial **reconstruction**, we must furthermore assume an isomorphism between the sensory and target SMO fields. We remark that the interference principle should not be confused with the "oscillatory interference model" (O'Keefe and Burgess, 2005; Burgess et al., 2007).

The interference principle is applied twice, first when the sensory input is converted to the phase code (stage 1) and second at the target area (the cerebral cortex in mammals) where information is reconstructed from the phase code (stage 4). However, neurons that convert the input to phase may operate at a lower threshold than neurons that detect coincidences. The next section will summarize a four-stage model of information encoding and reconstruction. Then we will discuss possible realizations of the interference principle in sensory and limbic information processing that are consistent with a number of empirical data.

FOUR STAGES OF INFORMATION ENCODING AND RECONSTRUCTION

We propose that in all sensory systems, phase encoding and decoding takes place by a four-stage transformation. Stages 3 and 4 are also applicable to cortico-cortical information transfer. We will illustrate the four stages on the mammalian visual system, but the same principles can be generalized to other sensory systems.

(1) Latency encoding: sensory neurons sample the physical environment by converting energy to APs, which represent the intensity and the time of a receptor-specific feature. A third dimension is indirectly provided by the position of the sensory receptor relative to the entire array of sensory receptors, although the meaning of the position varies from one sensory modality to another. While, in the visual system, stimulus times are coarsely sampled due to the relatively slow adaptation of sensory receptors (>20 ms on vertebrates and ~100 ms on primates; Glantz, 1991; Torre et al., 1995; Yeh et al., 1996; Rebrik et al., 2000; Holcman and Korenbrot, 2005), stimulus intensity is accurately represented by the frequency and latency of APs with a precision of <40 ms (Gollisch and Meister, 2008). Thus, the retinal ganglia use low (>25 ms) temporal resolution to encode sensory event times but high (<25 ms) temporal resolution to

Gamma alignment
The phase-lock of the action potentials to the neuron's own subthreshold membrane potential oscillation. The main frequency of oscillation is not necessarily gamma, but instead, often theta, alpha, or beta.

encode intensities (Koepsell et al., 2009). The important fact is that retinal ganglion cells register local luminance with a burst of one to six APs, where the burst frequency is proportional and latency is inversely proportional to the stimulus luminance (**Figure 3A**).

(2) **Gamma alignment** (alignment of APs to the SMO, however the frequency of SMO may not necessarily be gamma): Conversion of the latency code to a phase code involves aligning the APs to the local intracellular SMO. This conversion is naturally accomplished by the interference principle because, in response to the input AP burst, the first postsynaptic neuron will generate an AP only when the input AP coincides with the neuron's SMO peak (**Figure 3B**). This will reduce the input burst to a single AP output. As a result of this "gamma alignment," APs will be synchroni-

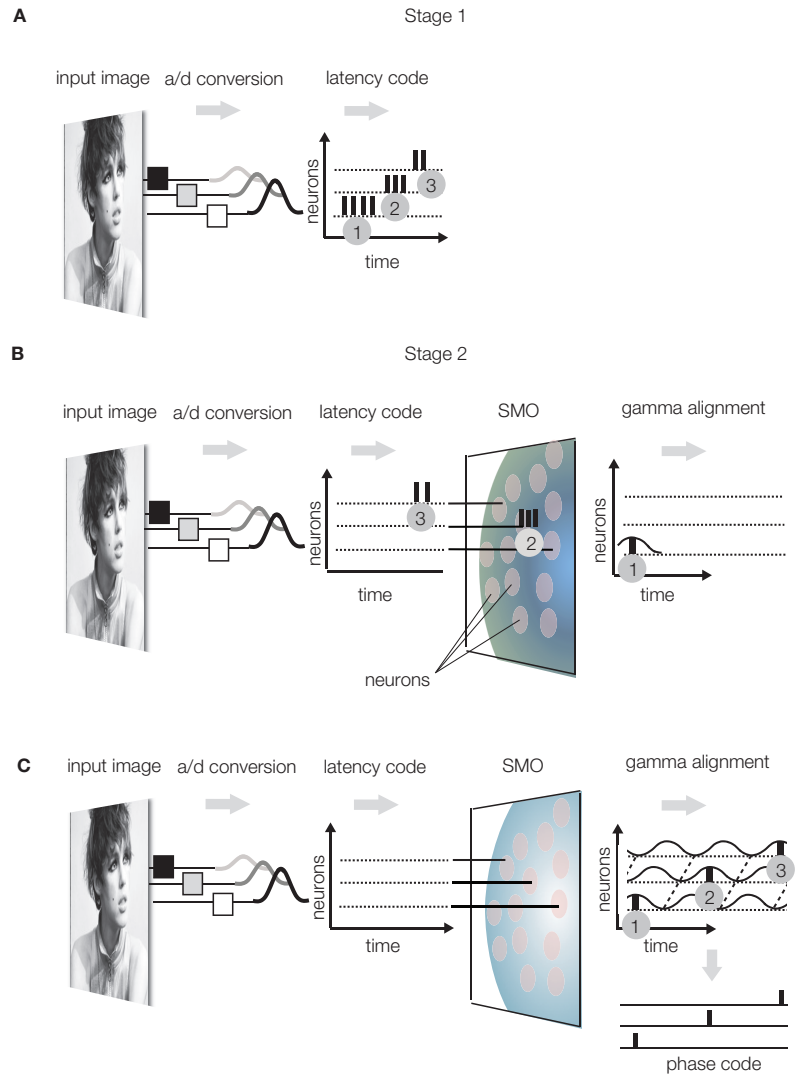

FIGURE 3 | Sensory encoding. (A) Stage 1: Luminance changes in the visual input evoke bursts of APs in the retina, where the burst frequency is proportional and burst latency is inversely proportional to the luminance. Bursts are numbered in the order of generation time. **(B)** Stage 2: bursts are filtered by the SMOs of a layer of neurons. The SMOs propagate within the transversal plane with a radial spread and depolarize the neurons in a specific order. Only single AP components of bursts will pass the layer, specifically those APs that coincide with the SMO peaks of the given neuron. Gray patches represent neurons with SMOs. As a result, APs will be aligned to the intrinsic SMO of these neurons. **(C)** The complete burst sequence is converted to a sparse AP phase code, with the topography preserved. The latency of the action potential in SMO cycles is inversely proportional to the luminance and the spatial coordinate of the action potential generating neuron is encoded by the phase relative to any single instance of SMOs (phase code).

Compression
A dimensionality reduction of the neural code when action potentials from multiple presynaptic neurons, dispersed in time, converge on a neuron and the merged action potential sequence is transmitted to the next postsynaptic neuron on a single axon as a single spike train.

zed with the intracellular SMOs (Koepsell et al., 2009). With this simple operation, the originally independent stimulus dimensions of *space*, and *quality* will be converted to *anatomical distances of neurons* and AP *time* dimensions, where the time encodes not only quality but also the anatomical distance. To keep stimulus quality and space separated in time, APs will encode information on two different time scales: *quality* will be encoded by an integer number of gamma cycles preceding the AP ($n \times 25$ ms), and the anatomical distance will be encoded by the phase within the gamma cycles ($2\ \pi \approx 25$ ms). Since the gamma alignment makes the phase of an AP specific to the neuron that generates it, the phase will associate the AP with the location of the neuron relative to the field of SMOs. Hence, phase will represent anatomical distance. Evidence supports that the spatial distance between ON and OFF ganglia generates a temporal difference between their burst firing during the early development of the retina that is controlled by propagating waves (Kerschensteiner and Wong, 2008). This space-time conversion in the visual system may generate temporary redundancy because space is represented twice, first by the anatomical distance between neurons and second by the phase. Therefore, the target topography of axonal projections is free to disperse because the phase unambiguously identifies the original location of the AP generating neuron. This saves the projection neurons from isomorphic projection of fine details and frees capacity to be utilized in the next stage to improve the reliability of transmission. (For motion processing, stimulus time replaces stimulus quality; Nadasdy, 2009).

(3) **Compression**: The major advantage of gamma alignment is that it allows all APs to be lossless compressed into a single or small number of channels/axons. By reducing the number of channels transferring different codes, the projection neurons are able to utilize the rest of the channels for transferring redundant codes, which in turn, enhances reliability. The redundant transfer is necessary for preserving the integrity of the code during long-range transmission to the cortex or between cortical areas. The compression of APs from multiple channels is accomplished by the massively divergent/convergent connections between presynaptic and postsynaptic neurons in the sensory nuclei of the thalamus (**Figure 4**). While synaptic convergence forces all APs from all projecting neurons to collapse onto a single/few channels/neurons, synaptic divergence distributes the same compressed AP code to multiple axons terminating in V1. Thus, the target area (V1) will receive a compressed code from each individual axon, while the parallel projection of the same APs via multiple axons will provide high redundancy. (For details on modeling the receptive field projections on V1 see Nadasdy, 2009). The next stage, reconstruction, is devoted to the decoding of the spatial information using the combined AP series with neuron-level specificity.

(4) Reconstruction: This is the final stage where information is decoded from AP phases. The decoding, again, relies on the *interference principle*. The compressed code reaches cortical neurons, such as granule cells in a V1 column, through multiple parallel axons, each terminating on individual neurons. We assume that cortical neurons, like sensory neurons, generate spatially and temporally coherent SMOs that propagate in a radial fashion. For the sake of simplicity, we further assume that the frequency and spatial phase gradient of this SMO field are the same as the SMO field at the sensory organ. Although each layer-4 neuron receives the same AP sequence, individual APs within the sequence may originate from different sensory neurons. The task of the cortical network is to sort these APs according to their origin and route them to specific supragranular layer neurons that will reproduce the input activity pattern. This may seem like an extremely complicated task considering the combinatorial complexity, but it is easily accomplished using the interference principle. By projecting the input APs on the SMO field and letting their coincidences select the neurons capable of firing an AP, the network will generate a coherent spatio-temporal pattern (**Figure 2**). Provided there is topographical isomorphism between the input SMO field and the target SMO field, any given AP from the input sequence will precisely coincide with the SMO peak of a neuron that represents the same anatomical distance as the input neuron to which it was originally aligned in Stage 2 (**Figure 5**). As a result, the output of these neurons in the supragranular layer of the cortex will reproduce the original sensory input and form a sparse representation (high spatial specificity and low firing rate; Sakata and Harris, 2009).

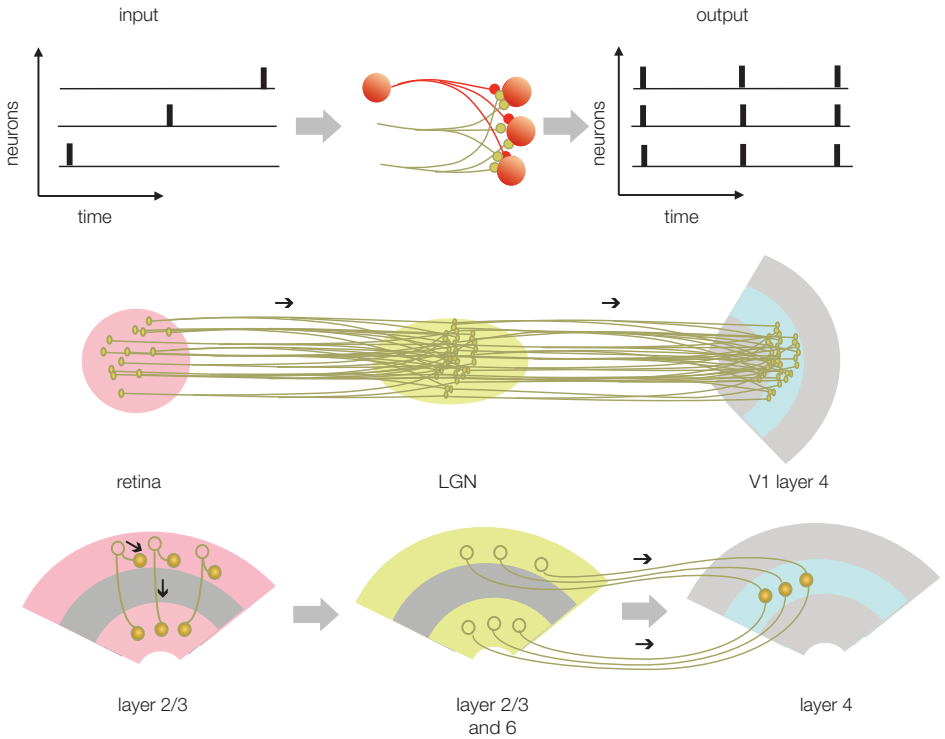

FIGURE 4 | Transferring the phase code (from Figure 3) between structures. The upper left is the phase-encoded AP pattern from **Figure 3C**. In this code AP time represents the luminance of the image in the receptive field and the position of neuron represents geometry. When the phase code enters a structure that relays the information (middle), the divergent and convergent connections will cause the APs to be dispersed and projected on a set of output neurons. As a result of the dispersion, all of the APs from each connected neurons will be combined with all other APs. The output AP trains will represent the combined APs from all the neurons. On the one hand, this code is compressed at the cellular level because it contains all the APs from all the neurons. On the other hand, the code is redundant across neurons. Underneath, middle row is the potential correspondence with the retina, LGN, and V1. Bottom, potential correspondence of the compression and transfer scheme with the cortico-cortical information transfer.

We emphasize that perfect reconstruction is neither the goal nor the final stage of information processing. When the sensory-cortical neurons reconstruct information from the phase code, they also add information to it. Reconstruction in the real brain is not an exact reproduction of the sensory information, since the input coming from the sensory thalamic nuclei is combined with inputs from a number of associated cortical areas. Rather, reconstruction is the stage at which important transformations, such as topographical and coordinate transformations and the combination of information from other cortical areas, take place. The reconstruction stage is also the starting point for cortico-cortical information transfer.

COMPUTATIONS WITH PHASE CODE

Above we described a conceptual model for neural encoding, information transmission, and decoding (for numerical simulations, see Nadasdy, 2009). For the sake of simplicity, we proved that information reconstruction from the phase code is nearly perfect within as few as four gamma cycles and 100 neurons, given the isomorphism of the SMO phase gradients at the sensory input and the target area (Nadasdy, 2009). Although this latter assumption may seem difficult to maintain under physiological conditions, there is substantial morphological and functional evidence in support of it. For example, multiple loops of the thalamo-cortical projection pathway through the thalamic reticular nucleus provide low- and high-frequency (gamma) links between the thalamus and cortex (Jones, 2002). Visual cortical areas 17 and 18 also synchronize to LGN with a 2.6-ms delay on anesthetized cats (Castelo-Branco et al., 1998). Moreover, a global retina-LGN-cortex synchronization is evident in the high gamma band (Castelo-Branco et al., 1998). On the one hand, incoherency between the encoding and decoding SMO fields would compromise phase coding. On the other hand, a systematic topographic (but not temporal) incoherency of SMO phase gradients

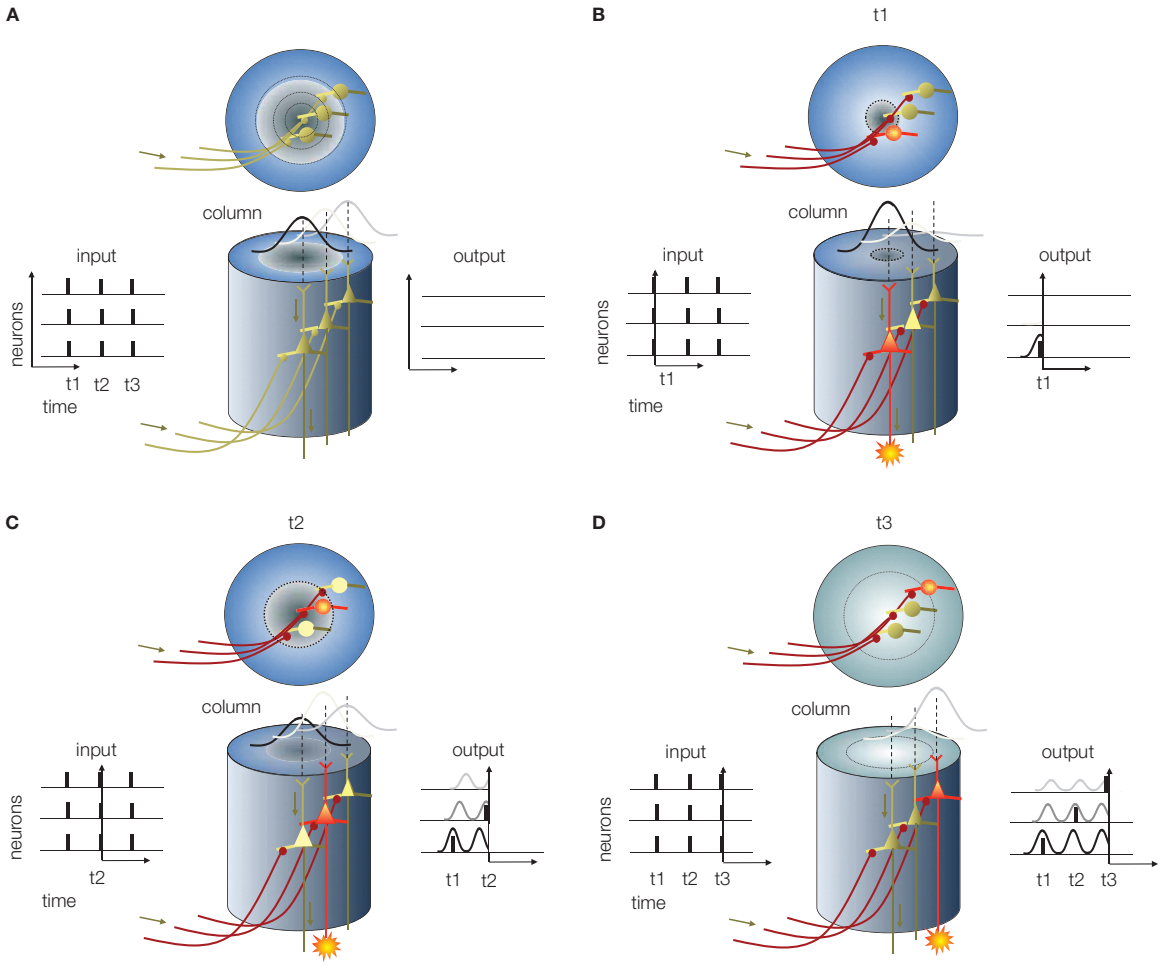

FIGURE 5 | Information reconstruction from phase of APs in the cortical column, predicted based on the "interference principle." (A) Cortical column (center). The *x*–*y* plot at the left represents the input APs entering the column, and the *x*–*y* plot at the right represents the expected activity of cortical neurons. In all *x*–*y* plots *x* is time and *y* is neuron number. The column in this example, for the sake of simplicity, contains only three neurons – without layer specificity. Above the columns are top views. Circular rings represent the radial propagation of SMO. **(B)** The first volley of APs arrives at *t1* (the output in **Figure 4**). Although the input depolarizes all receiving neurons (red axons), the only neuron in which the excitatory postsynaptic potential is able to generate an AP is the one at the center where the SMO is near a peak (red cell body). The AP generated by this neuron appears on the right *x*–*y* plot. **(C)** As time progresses, the first radial SMO wave reaches the periphery and the second wave starts while the second AP volley arrives (*t2*). Again, the input APs depolarize all the neurons. However, the only neuron capable of generating an AP is the one near peak SMO. Since the only neuron at peak SMO is the second neuron, located farther from the center, this neuron will generate an AP while the first is in the refractory period and the third's membrane potential is still approaching SMO peak. As a result, a second AP appears in the diagram at *t2*. **(D)** When the third volley arrives at *t3* and depolarizes all the postsynaptic neurons, the depolarization will coincide with the peak SMO in the third neuron, located at the periphery of the column. When this neuron fires an AP, it will be the third AP generated by the third neuron at *t3*. This sequence of events implements the "interference principle" by which the output of the neurons in the column reproduces the original input from the phase code as [$AP1_{t1}^{n1}$, $AP2_{t2}^{n2}$, $AP3_{t3}^{n3}$], where *t* is time and *n* is the neuron ID.

between the encoding and decoding structures is where transformations and computations can be implemented. For example, transformations between retinal and head-centered and between head- and body-centered coordinates can be performed by gain fields (Zipser and Andersen, 1988) or by tuning the SMO field, which transforms the map of interferences. According to the phase-coding model, the location of AP–SMO coincidences, i.e., the interference pattern smoothly shifts depending on the relative phases of APs from concurrent inputs reaching the neuron. Moreover, an arsenal of interneurons is deployed to provide fine tuning of the SMO, not unlike to the hippocampus, where each interneuron type specifically calibrates the location and frequency of membrane resonance, thus tuning the SMO in individual neurons to the gradient of the larger SMO field (Cobb et al., 1995).

DIFFERENT SOLUTIONS FOR PHASE CODING

One of the critical features of phase coding is that it allocates different frequency bands for different types of information by utilizing the

spatially and temporally coherent SMOs shared between coupled networks. One such frequency band is the range of phases within each oscillation period. The other frequency band is the frequency of SMO itself. It has been demonstrated that information can effectively be encoded and decoded by multiplexing the code in these two frequency bands (Nadasdy, 2009). The assignment of frequencies to features may vary across brain structures. Likewise, at the stage of sensory encoding and gamma alignment different scenarios are possible. The scenario we described earlier was that the spatial/anatomical location is encoded by phase and luminance is encoded by period cycles. However, these two features are interchangeable and phase can represent luminance and period cycles can represent the spatial/anatomical location. Within the visual system the magno, parvo, and konio cellular pathways represent the heterogeneity of these coding solutions. For instance, it is conceivable that since the magno cellular pathway is specialized to effectively transfer motion and orientation while the parvo cellular pathway transfers luminance and color with high spatial acuity, the former one encodes motion in phase, while the latter one encodes the spatial position or spatial frequency in phase. Thus, qualitative and spatial stimulus features are given different priorities in the different pathways of the visual system.

Another remarkable feature of phase coding is that with only a few parameter adjustments we can obtain different solutions to represent space and time. For example, if the cortical cytoarchitecture is homogeneous, such as in the EC, and if it allows an unconstrained propagation of SMO waves over multiple spatial SMO wavelengths, then multiple representations of the same input develop because of the spatial aliasing inherent to the interference principle (Nadasdy, 2009; also see a different solution by Burgess, 2008). Conversely, the same EC neuron exhibits spatial tuning to multiple, equidistant spatial locations, consistent with the definition of grid cells. The missing link between the spatial maps and network architecture could be the spatially and temporally periodic SMO field. Based on our simulations, the phase-coding model predicts that the phase-gradient map in the EC is coalescent with the topography of the grid cell map, i.e., with the matrix of grid cells that share space fields (Nadasdy, 2009).

The third important feature of phase coding becomes evident when we track the activity of a neuron relative to the SMO cycles under a dynamic input condition while also varying the propagation direction of the SMO field. This emulates the condition of recording place in a freely moving animal's hippocampus and computing the phase of spikes relative to ongoing theta LFP oscillations. In similar experiments, the AP phase systematically advances relative to the theta cycles, defined as phase precession (O'Keefe and Recce, 1993; Skaggs et al., 1996; Harris et al., 2002). However, recording theta not only from a single electrode but also from a larger volume around the place cell should reproduce what we found by modeling. Namely, APs should always phase-lock to the intracellular SMO (Harvey et al., 2009), but the direction of phase precession (advancement vs. lagging) will depend on the propagation direction of global SMO/LFP field around the neuron (Nadasdy, 2009). The assumption of SMO field propagation is consistent with the observation of traveling waves in the hippocampus on freely moving rats (Lubenov and Siapas, 2009). The phase-lock between the APs and the intracellular SMO has been confirmed during behavior (Harvey et al., 2009). Combining SMO, LFP, and AP measurements from multiple neurons separated by different distances would elucidate the underlying network dynamics and test the interference principle.

Among the predictions that can be derived from the phase-coding model is the phase modulation of spikes in the cortex in relationship to stimulus or behavioral manipulations. We earlier argued that reconstruction takes place in the supragranular layer of the neocortex. According to our model, layers 2–3 and 4b pyramidal cells vigorously respond to the granule cell input only if the time of input APs coincides with the cell's intracellular SMO peaks. In our simulations the optimal coincidence time window was ~1 ms (Nadasdy, 2009). Empirically, however, this time window is a probability function, rather than a binary function, allowing neurons to fire less frequently when the input is away from the peak but still reaches threshold. When the stimulus is optimal for the neuron, the AP will be generated reliably near the intracellular SMO peak (LFP trough). The same neuron may also respond, although less likely, to a suboptimal stimulus. If the suboptimal stimulus is optimal for another neuron, it will drive that neuron at the exact intracellular SMO peak. However, due to the slight phase difference between the two intracellular SMO processes, the same depolarization that drives the other neuron at exact SMO peak will drive the first neuron at a slightly different SMO phase than would its own optimal stimulus. As a result we shall observe a modest phase difference between spikes of the same neuron when we vary the stimulus parameters within the receptive field. Studies are in progress to test this prediction.

Prefrontal cortical neurons in a working memory task exhibit memory item dependent phase offset relative to the slow oscillations (Siegel et al., 2009). Other studies investigating the auditory and visual cortex found feature-dependent phase differences relative to theta in auditory (Kayser et al., 2009) and relative to alpha in primary visual cortex (Montemurro et al., 2008) and to gamma (Nadasdy and Andersen, 2009) also in primary visual cortex. It is also conceivable that the phases of local SMOs shift relative to the LFP, which integrates oscillations over a larger cell population (Harvey et al., 2009). We anticipate an increasing amount of data to arise in support of these so-far isolated examples in cortical recordings.

CONCERNS ABOUT THE GENERAL THEORY OF PHASE CODING

For phase coding and decoding to work, the subsystems of brain have to meet with specific dynamic conditions. One such condition is the high coherency between the SMOs at the encoding and decoding stages. For instance, the efficacy of visual information reconstruction in the cortex is highly dependent on the phase coherence between the LGN and V1. We postulated based on simulations that this coherency must approach a precision of 1 ms (Nadasdy, 2009), which is consistent with the coherency provided by the thalamo-cortical loop (Jones, 2002). The empirical precision of synchrony between cortical and LGN SMOs is yet to be determined. We also showed that the precise topographic mapping between the input and output is where the system can implement coordinate transformations between representations (Nadasdy, 2009).

The second condition is the compatibility of SMO frequencies across and within structures. While the hippocampal LFP is dominated by coherent theta and gamma oscillations, the hippocampal pyramidal cells express mainly theta frequency SMOs. If phase coding in the hippocampus relies on theta, it is not clear what role gamma oscillations may play. Likewise, entorhinal cortical neurons express theta frequency SMOs. In contrast, sensory organs and primary sensory areas are dominated by gamma oscillations. Notably, we observed visual feature-dependent spike phase modulation relative to the gamma band LFP and not to alpha, while other studies reported phase modulation relative to alpha band LFP (Belitski et al., 2008).

Although the correlation between SMO and LFP is high, they are not identical. The extent at which LFP is a good approximation of SMO is still unknown. The correlation between LFP and SMO is critical for the empirical testing of the phase-coding model and cries for defining the transfer function between population SMO and LFP.

Last, the noise tolerance of phase coding is unknown. Different types of noise need to be considered. One is the noise generated by the movement of sensory organs themselves, which affects the sensory sampling. Second is the noise level of intrinsic SMO oscillations. Third is the temporal incoherency between source and target structures. Fourth is the spatial incoherency between the neuronal source and target. While spatial incoherency can implement useful transformations in the reconstruction, the temporal incoherency is highly detrimental for the reconstruction. The effects of these concerns need to be investigated by simulations and tested empirically.

QUESTIONS LEFT OPEN

Because our understanding of the relationship between SMO and LFP is still incomplete, it leaves the question open: what is the timescale of phase modulation in the brain? The frequency of SMO and LFP consistently varies along the fronto-temporo-occipital axis, dominated by gamma in the occipital regions of the cortex, alpha in the frontal areas, and theta in the EC, hippocampal, and parahippocampal regions. In addition, gamma power is high and oscillations are phase-locked to hippocampal theta. Although hippocampal phase precession is defined relative to theta, we anticipate phase precession relative to gamma oscillations as well, while APs should be phase-locked to the intracellular gamma SMO. We also anticipate a similar relationship between EC theta and gamma. The phase modulation of spikes relative to alpha/theta LFP (Montemurro et al., 2008; Kayser et al., 2009) and relative to gamma LFP (Nadasdy and Andersen, 2009) in the visual cortex is still unclear. One of the most important questions is whether or not the interference principle would work at multiple timescales to allow information to be encoded relative to multiple frequency bands of ongoing oscillations and whether or not these frequency bands carry content-specific information. There is much to learn about the collective resonant property of the nervous system in the next few years that will complete our understanding of how the activity of millions of neurons is orchestrated, and this orchestration may happen in a much more deterministic fashion than the "noisy" brain models suggest.

Finally, as stated in the title, the phase-coding model suggests a critical revision of the concept of binding by synchrony. Accordingly, the key

of preserving the integrity of the code across multiple stages of information transfer in the brain is the precise asynchrony of APs between neighbor neurons, as opposed to the zero-phase lag synchrony proposed earlier (Gray and Singer, 1989). We argued that a subtle but constant phase gradient of the propagating SMOs is critical for encoding and reconstructing the sensory information as well as to for performing different coordinate transformations on the sensory input to achieve context invariant object representations in the brain.

ACKNOWLEDGMENTS

We acknowledge Richard A. Andersen, Neil Burgess, and Paul Miller for invaluable comments on the original manuscript (Nadasdy, 2009) and the support from the National Eye Institute. We thank Sarah Gibson, Jason Ettlinger, and Hollie S. Thomas for proofreading.

REFERENCES

Alonso, A., and Llinas, R. R. (1989). Subthreshold Na^+-dependent theta-like rhythmicity in stellate cells of entorhinal cortex layer II. *Nature* 342, 175–177.

Belitski, A., Gretton, A., Magri, C., Murayama, Y., Montemurro, M. A., Logothetis, N. K., and Panzeri, S. (2008). Low-frequency local field potentials and spikes in primary visual cortex convey independent visual information. *J. Neurosci.* 28, 5696–5709.

Benucci, A., Frazor, R. A., and Carandini, M. (2007). Standing waves and traveling waves distinguish two circuits in visual cortex. *Neuron* 55, 103–117.

Blair, H. T., Gupta, K., and Zhang, K. (2008). Conversion of a phase- to a rate-coded position signal by a three-stage model of theta cells, grid cells, and place cells. *Hippocampus* 18, 1239–1255.

Bringuier, V., Chavane, F., Glaeser, L., and Fregnac, Y. (1999). Horizontal propagation of visual activity in the synaptic integration field of area 17 neurons. *Science* 283, 695–699.

Burgess, N. (2008). Grid cells and theta as oscillatory interference: theory and predictions. *Hippocampus* 18, 1157–1174.

Burgess, N., Barry, C., and O'Keefe, J. (2007). An oscillatory interference model of grid cell firing. *Hippocampus* 17, 801–812.

Buzsaki, G., and Chrobak, J. J. (1995). Temporal structure in spatially organized neuronal ensembles: a role for interneuronal networks. *Curr. Opin. Neurobiol.* 5, 504–510.

Castelo-Branco, M., Neuenschwander, S., and Singer, W. (1998). Synchronization of visual responses between the cortex, lateral geniculate nucleus, and retina in the anesthetized cat. *J. Neurosci.* 18, 6395–6410.

Cobb, S. R., Buhl, E. H., Halasy, K., Paulsen, O., and Somogyi, P. (1995). Synchronization of neuronal activity in hippocampus by individual GABAergic interneurons. *Nature* 378, 75–78.

Devor, A., and Yarom, Y. (2002a). Coherence of subthreshold activity in coupled inferior olivary neurons. *Ann. N. Y. Acad. Sci.* 978, 508.

Devor, A., and Yarom, Y. (2002b). Electrotonic coupling in the inferior olivary nucleus revealed by simultaneous double patch recordings. *J. Neurophysiol.* 87, 3048–3058.

Dickson, C. T., Magistretti, J., Shalinsky, M. H., Fransen, E., Hasselmo, M. E., and Alonso, A. (2000). Properties and role of I(h) in the pacing of subthreshold oscillations in entorhinal cortex layer II neurons. *J. Neurophysiol.* 83, 2562–2579.

Fransen, E., Alonso, A. A., Dickson, C. T., Magistretti, J., and Hasselmo, M. E. (2004). Ionic mechanisms in the generation of subthreshold oscillations and action potential clustering in entorhinal layer II stellate neurons. *Hippocampus* 14, 368–384.

Giocomo, L. M., Zilli, E. A., Fransen, E., and Hasselmo, M. E. (2007). Temporal frequency of subthreshold oscillations scales with entorhinal grid cell field spacing. *Science* 315, 1719–1722.

Glantz, R. M. (1991). Motion detection and adaptation in crayfish photoreceptors. A spatiotemporal analysis of linear movement sensitivity. *J. Gen. Physiol.* 97, 777–797.

Gollisch, T., and Meister, M. (2008). Rapid neural coding in the retina with relative spike latencies. *Science* 319, 1108–1111.

Gray, C. M., and Singer, W. (1989). Stimulus-specific neuronal oscillations in orientation columns of cat visual cortex. *Proc. Natl. Acad. Sci. U.S.A.* 86, 1698–1702.

Hafting, T., Fyhn, M., Bonnevie, T., Moser, M. B., and Moser, E. I. (2008). Hippocampus-independent phase precession in entorhinal grid cells. *Nature* 453, 1248–1252.

Harris, K. D., Henze, D. A., Hirase, H., Leinekugel, X., Dragoi, G., Czurko, A., and Buzsaki, G. (2002). Spike train dynamics predicts theta-related phase precession in hippocampal pyramidal cells. *Nature* 417, 738–741.

Harvey, C. D., Collman, F., Dombeck, D. A., and Tank, D. W. (2009). Intracellular dynamics of hippocampal place cells during virtual navigation. *Nature* 461, 941–946.

Holcman, D., and Korenbrot, J. I. (2005). The limit of photoreceptor sensitivity: molecular mechanisms of dark noise in retinal cones. *J. Gen. Physiol.* 125, 641–660.

Huhn, Z., Orban, G., Erdi, P., and Lengyel, M. (2005). Theta oscillation-coupled dendritic spiking integrates inputs on a long time scale. *Hippocampus* 15, 950–962.

Jensen, O., and Lisman, J. E. (1996). Hippocampal CA3 region predicts memory sequences: accounting for the phase precession of place cells. *Learn. Mem.* 3, 279–287.

Jones, E. G. (2002). Thalamic circuitry and thalamocortical synchrony. *Philos. Trans. R. Soc. Lond., B, Biol. Sci.* 357, 1659–1673.

Kamondi, A., Acsady, L., Wang, X. J., and Buzsaki, G. (1998). Theta oscillations in somata and dendrites of hippocampal pyramidal cells in vivo: activity-dependent phase-precession of action potentials. *Hippocampus* 8, 244–261.

Katzner, S., Nauhaus, I., Benucci, A., Bonin, V., Ringach, D. L., and Carandini, M. (2009). Local origin of field potentials in visual cortex. *Neuron* 61, 35–41.

Kayser, C., Montemurro, M. A., Logothetis, N. K., and Panzeri, S. (2009). Spike-phase coding boosts and stabilizes information carried by spatial and temporal spike patterns. *Neuron* 61, 597–608.

Kerschensteiner, D., and Wong, R. O. (2008). A precisely timed asynchronous pattern of ON and OFF retinal ganglion cell activity during propagation of retinal waves. *Neuron* 58, 851–858.

Koepsell, K., Wang, X., Vaingankar, V., Wei, Y., Wang, Q., Rathbun, D. L., Usrey, W. M., Hirsch, J. A., and Sommer, F. T. (2009). Retinal oscillations carry visual information to cortex. *Front. Syst. Neurosci.* 3:4. doi:10.3389/neuro.06.004.2009.

Lengyel, M., Szatmary, Z., and Erdi, P. (2003). Dynamically detuned oscillations account for the coupled rate and temporal code of place cell firing. *Hippocampus* 13, 700–714.

Llinas, R. R., Grace, A. A., and Yarom, Y. (1991). In vitro neurons in mammalian cortical layer 4 exhibit intrinsic oscillatory activity in the 10- to 50-Hz frequency range. *Proc. Natl. Acad. Sci. U.S.A.* 88, 897–901.

Logothetis, N. K., Pauls, J., Augath, M., Trinath, T., and Oeltermann, A. (2001). Neurophysiological investigation of the basis of the fMRI signal. *Nature* 412, 150–157.

Lubenov, E. V., and Siapas, A. G. (2009). Hippocampal theta oscillations are travelling waves. *Nature* 459, 534–539.

Magee, J. C. (2001). Dendritic mechanisms of phase precession in hippocampal CA1 pyramidal neurons. *J. Neurophysiol.* 86, 528–532.

Mehta, M. R., Lee, A. K., and Wilson, M. A. (2002). Role of experience and oscillations in transforming a rate code into a temporal code. *Nature* 417, 741–746.

Mitzdorf, U. (1985). Current source-density method and application in cat cerebral cortex: investigation of evoked potentials and EEG phenomena. *Physiol. Rev.* 65, 37–100.

Montemurro, M. A., Rasch, M. J., Murayama, Y., Logothetis, N. K., and Panzeri, S. (2008). Phase-of-firing coding of natural visual stimuli in primary visual cortex. *Curr. Biol.* 18, 375–380.

Nadasdy, Z. (2009). Information encoding and reconstruction from the phase of action potentials. *Front. Syst. Neurosci.* 3:6. doi:10.3389/neuro.06.006.2009.

Nadasdy, Z., and Andersen, R. A. (2009). "Spike phase tuning in primary visual cortex," in *Society for Neuroscience Annual Meeting*, Chicago, IL.

O'Keefe, J., and Burgess, N. (2005). Dual phase and rate coding in hippocampal place cells: theoretical significance and relationship to entorhinal grid cells. *Hippocampus* 15, 853–866.

O'Keefe, J., and Recce, M. L. (1993). Phase relationship between hippocampal place units and the EEG theta rhythm. *Hippocampus* 3, 317–330.

Prechtl, J. C., Bullock, T. H., and Kleinfeld, D. (2000). Direct evidence for local

oscillatory current sources and intracortical phase gradients in turtle visual cortex. *Proc. Natl. Acad. Sci. U.S.A.* 97, 877–882.

Rebrik, T. I., Kotelnikova, E. A., and Korenbrot, J. I. (2000). Time course and Ca^{2+} dependence of sensitivity modulation in cyclic GMP-gated currents of intact cone photoreceptors. *J. Gen. Physiol.* 116, 521–534.

Sakata, S., and Harris, K. D. (2009). Laminar structure of spontaneous and sensory-evoked population activity in auditory cortex. *Neuron* 64, 404–418.

Siegel, M., Warden, M. R., and Miller, E. K. (2009). Phase-dependent neuronal coding of objects in short-term memory. *Proc. Natl. Acad. Sci. U.S.A.* 106, 21341–21346.

Silva, L. R., Amitai, Y., and Connors, B. W. (1991). Intrinsic oscillations of neocortex generated by layer 5 pyramidal neurons. *Science* 251, 432–435.

Skaggs, W. E., McNaughton, B. L., Wilson, M. A., and Barnes, C. A. (1996). Theta phase precession in hippocampal neuronal populations and the compression of temporal sequences. *Hippocampus* 6, 149–172.

Tanaka, N. K., Ito, K., and Stopfer, M. (2009). Odor-evoked neural oscillations in *Drosophila* are mediated by widely branching interneurons. *J. Neurosci.* 29, 8595–8603.

Torre, V., Ashmore, J. F., Lamb, T. D., and Menini, A. (1995). Transduction and adaptation in sensory receptor cells. *J. Neurosci.* 15, 7757–7768.

Tsodyks, M. V., Skaggs, W. E., Sejnowski, T. J., and McNaughton, B. L. (1996). Population dynamics and theta rhythm phase precession of hippocampal place cell firing: a spiking neuron model. *Hippocampus* 6, 271–280.

Wallenstein, G. V., and Hasselmo, M. E. (1997). GABAergic modulation of hippocampal population activity: sequence learning, place field development, and the phase precession effect. *J. Neurophysiol.* 78, 393–408.

White, J. A., Klink, R., Alonso, A., and Kay, A. R. (1998). Noise from voltage-gated ion channels may influence neuronal dynamics in the entorhinal cortex. *J. Neurophysiol.* 80, 262–269.

Yeh, T., Lee, B. B., and Kremers, J. (1996). The time course of adaptation in macaque retinal ganglion cells. *Vision Res.* 36, 913–931.

Zipser, D., and Andersen, R. A. (1988). A back-propagation programmed network that simulates response properties of a subset of posterior parietal neurons. *Nature* 331, 679–684.

Conflict of Interest Statement: The author declares that the research was conducted in the absence of any commercial or financial relationships that could be construed as a potential conflict of interest.

Received: 15 February 2010; paper pending published: 01 May 2010; accepted: 18 June 2010; published online: 15 September 2010.

Citation: Nadasdy Z (2010) Binding by asynchrony: the neuronal phase code. Front. Neurosci. ***4****:51. doi: 10.3389/fnins.2010.00051*

Chapter 4

9. Grid cells

"As already pointed out (Szentagothai & Arbib 1974 p. 386) the parallel shift in discrete steps (i.e. in those of the columns) against another of apparently irregular but repetitive arborization patterns may create a new regularity in the sense seen in the so-called 'Moire patterns'."

(Szentágothai, 1978)

Arguably, one of the most thrilling discoveries in post-millennium age neuroscience was the discovery of grid cells. Grid cells revealed a complementary aspect of spatial specificity defined by place cells and head direction cells. In contrast with place cells, grid cells express multiple firing fields, where the firing fields are defined in allocentric coordinates aligned with the environment; the firing fields register with the vertices of a hexagonal tessellation pattern; and the grid distance is invariant to the size of the environment, but grid distance varies systematically along the septo-temporal axis of the dorsomedial entorhinal cortex. While the discovery triggered a rapid frenzy to posit the causal mechanism of grid cell generation, it also marked the beginning of an insatiable search for new cell types. As a result, grid cells were soon followed by border cells, object vector cells, conjunctive head direction cells, and time cells. Among all these cell types, grid cells stand out with a combination of very attractive properties that inspired a whole generation of computational neuroscientists, mathematicians, and physicists alike. Namely, it had been reported to express a set of abstract features, such as hexagonal geometry, scale invariance, and allocentric reference frame (Hafting et al., 2005). These features were widely replicated by numerous labs with certain refinements and qualifying parameters (Barry et al., 2009; Hafting et al., 2005; Jacobs et al., 2013; Krupic et al., 2015; Nadasdy et al., 2017a; Yartsev et al., 2011), but no major challenges or contradictions were found. Importantly, grid cells were discovered in the lateral aspect of the dorsomedial entorhinal cortex first and later were inferred from fMRI in the ventromedial prefrontal cortex and orbitofrontal cortex (Doeller et al., 2010a; Kaplan et al., 2017; Raithel & Gottfried, 2021).

Despite its vague conceptual grounding, the hexadirectional modulation of activity has been interpreted by many researchers as an unmistakable signature of grid cells and it was ready to be generalized further as a fundamental principle of neuronal representations in the human brain. While, besides rodents, it was found also in bats and in monkeys (Barry et al., 2009;

Hafting et al., 2005; Jacobs et al., 2013; Krupic et al., 2015; Zoltan Nadasdy et al., 2017a; Yartsev et al., 2011) the validation by human electrophysiology was lagging despite the fierce competition. The stake was so high, that the paper explicitly reporting human grid cells for the first time provided only very circumstantial evidence by fMRI (Doeller et al., 2010a). Doeler et al., found that the mesial temporal lobe in human subjects performing a spatial memory task expressed a hexadirectional modulation of blood-oxigene-level-difference (BOLD) depending on the heading direction of the avatar on a plateau of a virtual 3D terrain. Obviously, a cellular-level resolution is unattainable by fMRI therefore a remarkable conceptual leap was made in the absence of a physiological link to relate BOLD data to grid cells. The conceptual leap made was that spatial navigation along radial directions involves across-grids passing in 0, 60, 120, 180, 240, and 300-degree directions and between grids passing in 30, 90, 150, 210, 270, and 330-degree directions. Let's call the former set of directions the A series and the latter set of directions as B series. According to the authors of the article, the high BOLD response to the directions defined by the A series was due to the activation of most frequent grid nodes encountered along the pathways running in 0, 60, 120, and 180 degrees, etc., while the troughs of BOLD were due to the lack of grid nodes in the B direction series. However, this model incorrectly assumed that the minimum number of grids were crossed along the B direction. Instead, it is easy to see that the directions in the B series are crossing a secondary set of grid points, which is evident when we draw the nodes in a hexagonal grid (Fig. D5). The directions where we would not cross grid nodes would be the 15, 45, 75, 105, …, 345 degrees. Therefore, the grid cell geometry did not explain the hexadirectional sine-wave-like modulation of BOLD. Nevertheless, the study inspired a whole new generation of experiments including local field potential proofs of the hexadirectional modulation (Maidenbaum et al., 2018). Over the last 5 years, the hexadirectional modulation has been extended beyond spatial navigation and the hexagonal grid-geometry became a putative underpinning of any conceptual classification, including category formation and semantics (Constantinescu et al., 2016).

Three years later a direct electrophysiology validation was done by Josh Jacobs in UCLA and my group at UT. A short report by the UCLA group demonstrated grid cell activity evident

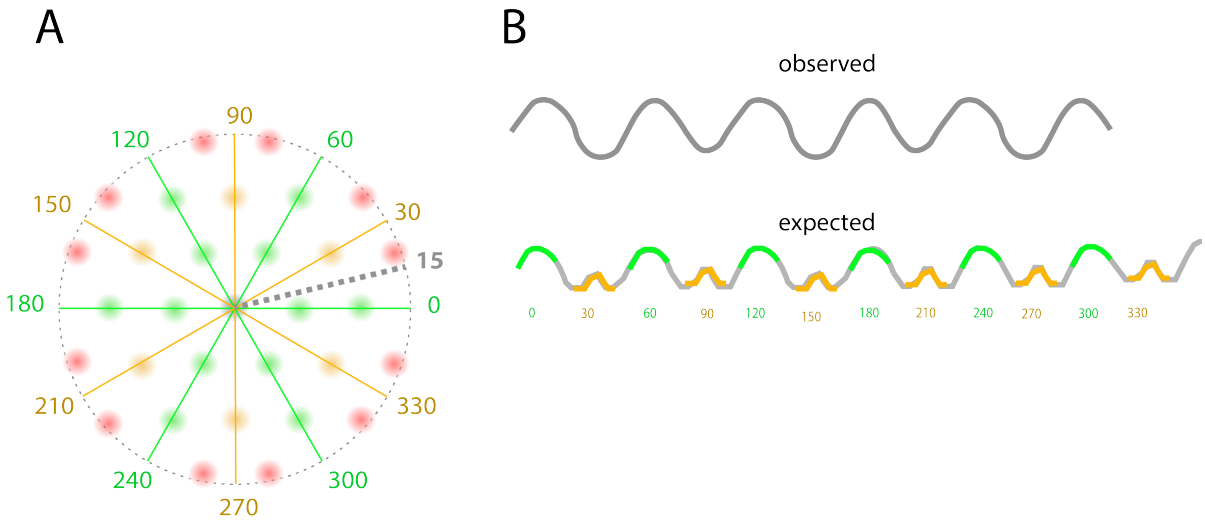

Figure D5: The model of hexadirectional modulation of BOLD. (A) A virtual surface of navigation with a hexagonally arranged grid nodes. The grid nodes are colorcoded according to primary (0º ,60º ,120º, 180º, 240º, 300º), secondary (30º ,90º, 150º, 210º, 270º, 330º) and tertial grid nodes as green, orange and pink, respectively. (B) The observed and expected hexadirectinal modulation of BOLD. An accurate model of activation of grids along any straight navigation path should generate a pattern with large bumps of BOLD for the primary directions and smaller bumps between the large ones for the secondary directions. Instead, all studies reported hexadirectional modulation patterns (observed) and none reported the expected.

from from human entorhinal cortical single unit data recorded during the patients playing a videogame (Jacobs et al., 2013). While the UCLA group published the result first, we carried out a more elaborated study that, beyond validation, unraveled the fundamental differences between rodent and human grid cell activity. Our experiment also using a virtual reality spatial navigation task, but in contrast with the Jacobs' study, we tested the key findings reported from rodents by recording the unit activity of same cells across 4 different virtual environments. The four VR environments were varied in size, aspect ratios, coverage of the spaces, and interior of the space. The results were summarized by our 2017 paper (Nadasdy et al., 2017b). Our key findings were:

1. Neurons in the medial entorhinal cortex (mEC) of the human brain display similar spatially periodic activity characteristic of grid cells in the rodent mEC.
2. The grid distances exhibited by human grid cells scale with the size of the environment, in contrast with grids produced by rat entorhinal cortical neurons.
3. Human grid orientation aligns with the corners of the environment, as opposed to being anchored to distant or local cues.

4. Human grid cells display Cartesian (orthogonal grids) as often as hexagonal geometry.

We concluded that in contrast with rodents where grid cells are context-independent (Hafting et al., 2005; Moser et al., 2014; Rowland et al., 2016), human grid cells are context-dependent as they express remarkable flexibility in scaling, anchoring, and geometry. All makes sense if we consider the differences in the spatial behavioral strategies between rodent and primate orders. Primates (including humans) live in environments where motor coordination and locomotion happen at vastly different timescales. Humans skillfully handle sewing needles and walk miles or drive cars and traverse large distances in a short period of time. The variance of spatial scales that human behavior spans through is enormous. Hence, a mechanism that renders scalable neuronal representations of space in entorhinal cortical neurons must be in place. Secondly, we humans predominantly rely on vision. We collect survey data from our surroundings by making saccadic eye movements and foveating on landmarks and targets of the environment. The sequence of saccadic eye movements is a surrogate of the exploratory process rodents perform by locomotion. The rat constructs the cognitive map step-by-step exploration of the area around its body, largely relying on somatosensory input from whiskers, olfactory input identifying smells, eventually acoustic, and lastly visual information. In contrast, a human observer does not need to locomote in space to capture the cognitive map of the environment. A few saccadic eye movements can efficiently complete that task. Hence, when the human subjects in our experiment started the navigation in a virtual environment, they looked around first with their avatar, then started walking toward the target while their entorhinal cortex produced spikes at precisely spaced often equidistant or square-grid-like locations. There was no dispersion of spikes or gradual building up of the distributions typically observed in rats. The first few spikes generated by grid cells in the rat entorhinal cortex are quite random. It takes 20 minutes for the grid pattern to manifest. In contrast, grid cells in the human brain produce spikes at locations during the first 5 minutes that are already defined by grids. Eye movements and active vision supported by a flexible oculomotor system in primates replaced the incremental construction of cognitive maps typical in rodents.

The visual strategy also explained the orientation relative to corners. Corners define the geometry of space. This framework also makes Elizabeth Buffalo's results self-evident, that primates express grid cell activity in the entorhinal cortex by mapping the spikes to eye movements during passive observation of photos of scenes (Killian et al., 2012, 2015). If we assume that eye movements became the surrogate of locomotion, the fact that tracking eye

movements instead of locomotion could reveal the same types of grids of spikes as grid cells in rodents is less surprising.

It is quite remarkable that 18 years after the discovery of grid cells we still do not have a satisfactory model of the mechanism generating grid cell activity. Eighteen years is way beyond the honeymoon when researchers can only see grid cells and they see them everywhere (Constantinescu et al., 2016; Doeller et al., 2010b; Kaplan et al., 2017; Kunz et al., 2015). This distance should provide us with the perspective, clarity, and context to better understand. Despite the abundance of models and the lack of a general mechanism, by considering the diversity of grid cell types and their spatial behavior across species I arrived at the following conclusion.

(1) The only common feature between the dorsomedial entorhinal cortical neurons in the rat and the MEC neurons in the human brain is the spatially periodic activity. Hexagonal rotation symmetry is not an identifying attribute of grid cells.
(2) The method of spatial autocorrelation that was used by the original Hafting study became a gold standard is biased and is not an adequate method to define grid cells. It is prone to generate false positives because the spatial autocorrelation of any three firing fields will generate a hexagonal tessellation pattern. Spatial periodicity should be characterized by spectral methods.
(3) Stochastic aggregation of grid cell activity is not necessary. After the cognitive map is formed a single running path will activate grid cell activity with precisely defined firing locations.
(4) Grid cell activity may adapt to culturally defined structural features such as the predominantly Cartesian coordinate systems of our cities and buildings and we also learn to organize our thoughts in Cartesian tables school.

Models of grid cells activity can be classified according to the following five models:

- The continuous attractor model (Burak & Fiete, 2009; Welinder et al., 2008).
- The oscillatory interference model (Burgess et al., 2007; Burgess & O'Keefe, 2011)
- Combined oscillatory and attractor model (Hasselmo & Brandon, 2012)
- Moiré interference (Blair et al., 2007)

- Phase coding model (Nadasdy, 2009, 2010a):

According to the last model in the list, grid cells are the byproducts of interferences that occur in multiple neurons and multiple locations in space due to an aliasing error deriving from the course temporal resolution that maps spatial information on phase. Neurons in the entorhinal cortex that are one gamma cycle apart spuriously recover the same location from the phase. Therefore, different neurons in one gamma period apart will represent the same spatial location. Due to the one-to-many and many-to-one mapping between neurons and space, the same neuron will also represent multiple spatial locations, at exactly integer multiples of gamma cycles apart. This is what we can observe as grid cells. According to this model, grid cells provide a local spatial coordinate system that covers the grid node and its immediate surrounding. The information grid cells can store from one grid field is useless in the adjacent grid field (Figure 7 in (Z Nadasdy, 2009). For a deeper understanding of the relationship between grid cells and phase coding, see Nadasdy et al 2022 in this volume (Nadasdy et al., 2022).

Context-dependent spatially periodic activity in the human entorhinal cortex

Zoltan Nadasdy[a,b,c,1], T. Peter Nguyen[d], Ágoston Török[c,e,f], Jason Y. Shen[g,h], Deborah E. Briggs[g,h], Pradeep N. Modur[g,h], and Robert J. Buchanan[b,g,i,j]

[a]Sarah Cannon, St. David's Medical Center, Austin, TX 78705; [b]Department of Psychology, The University of Texas at Austin, Austin, TX 78712; [c]Department of Cognitive Psychology, Eötvös Loránd University, 1064 Budapest, Hungary; [d]School of Medicine, Baylor College of Medicine, Houston, TX 77030; [e]Systems and Control Laboratory, Institute for Computer Science and Control, Hungarian Academy of Sciences, 1111 Budapest, Hungary; [f]Brain Imaging Centre, Research Centre for Natural Sciences, Hungarian Academy of Sciences, 1117 Budapest; [g]Seton Brain & Spine Institute, Austin, TX 78701; [h]Department of Neurology, Dell Medical School, The University of Texas at Austin, Austin, TX 78712; [i]Department of Surgery, Dell Medical School, The University of Texas at Austin, Austin, TX 78712; and [j]Department of Psychiatry, Dell Medical School, The University of Texas at Austin, Austin, TX 78712

Edited by Larry R. Squire, Veterans Affairs San Diego Healthcare System, San Diego, CA, and approved March 17, 2017 (received for review January 29, 2017)

The spatially periodic activity of grid cells in the entorhinal cortex (EC) of the rodent, primate, and human provides a coordinate system that, together with the hippocampus, informs an individual of its location relative to the environment and encodes the memory of that location. Among the most defining features of grid-cell activity are the 60° rotational symmetry of grids and preservation of grid scale across environments. Grid cells, however, do display a limited degree of adaptation to environments. It remains unclear if this level of environment invariance generalizes to human grid-cell analogs, where the relative contribution of visual input to the multimodal sensory input of the EC is significantly larger than in rodents. Patients diagnosed with nontractable epilepsy who were implanted with entorhinal cortical electrodes performing virtual navigation tasks to memorized locations enabled us to investigate associations between grid-like patterns and environment. Here, we report that the activity of human entorhinal cortical neurons exhibits adaptive scaling in grid period, grid orientation, and rotational symmetry in close association with changes in environment size, shape, and visual cues, suggesting scale invariance of the frequency, rather than the wavelength, of spatially periodic activity. Our results demonstrate that neurons in the human EC represent space with an enhanced flexibility relative to neurons in rodents because they are endowed with adaptive scalability and context dependency.

grid cell | spatial memory | entorhinal cortex | single unit | human

Neurons in the hippocampus and entorhinal cortex (EC) exhibiting spatially modulated activity are highly relevant in research and medicine because they construct an agent-independent (allocentric) metric of space for localizing and remembering places, often referred to as the cognitive map (1–4). Beyond their scientific relevance, the hippocampus and EC are clinically implicated in Alzheimer's disease (5, 6), where these structures show the earliest expression of plaques and tangles and concomitant progressive cell death, causing spatial disorientation and spatial memory loss. Coincidentally, the two structures, as part of the mesial temporal lobe, are highly susceptible to epileptic seizure (7). These cells offer a glimpse into how the brain integrates multimodal and movement-dependent sensory inputs and converts them into a coherent environment-referenced neuronal representation. Among the neurons with the greatest spatial specificity are the place cells of the hippocampus (2), head direction cells of the pre- and postsubiculum (8), border cells in the subiculum and EC (9), and grid cells in the medial EC (10). Although a place cell is only activated when the animal traverses through a unique location in its environment (2), grid-cell activity is elicited in multiple locations that the animal visits (11), and these locations span the environment periodically as vertices of a hexagonal grid formation (10). The two neuroanatomical subsystems are thought to complement each other such that individual place cells represent specific spatial locations and grid cells provide an environment-invariant metric upon which to reference the agent's (animal or human) location (12). Although the adaptive flexibility of spatial tuning of neurons in the rodent hippocampus is evident from remapping their receptive fields when switching between environments (13–17), the association between grid patterns of cells in the EC and the environment is less clear (13, 18–20). Here, we focus on three main features of grid-cell patterns: scale invariance, orientation, and rotational symmetry.

The robust grid scale invariance across differently sized (10) and shaped (20) environments is one of the key characteristics of grid cells in the rodent EC. It has repeatedly been shown that the distance between grid nodes remains constant when the animal is transferred between environments of different size (10) and shape (20). However, past studies have demonstrated that although grid distances are rigid, they are not completely inflexible. Barry et al. (19) showed that manipulations to the width and length of a familiar enclosure resulted in similar transformations of the rodents' grids: When the familiar environment was elongated, the grid patterns elongated similarly. Also in rats, grids have been shown to display expansion upon introduction to a novel environment and then relax back to the original scale when the environment becomes familiar (18). Combined, these results suggest that grid cells might have a default scale but that the default scale could be influenced by experience in the given environment.

Another key characteristic of grid cells is the alignment of grids with environmental cues. For a given environment, an animal's

Significance

In the mammalian brain, neurons in the hippocampus represent unique places and neurons in the entorhinal cortex, so-called grid cells, provide an internal coordinate system of the environment. Dysfunction in this circuit causes memory problems and disorientation, which are early symptoms of Alzheimer's disease. Much of what we have learned from this circuit is based on rodent studies. Here, we report that grid cells in the human brain represent space in a more environmentally adaptive manner than in rodents. Human grids show an increased scalability with the environment relative to rodents. The enhanced context dependency of spatial representations is probably a late development of evolution.

Author contributions: Z.N., Á.T., and R.J.B. designed research; Z.N., T.P.N., and R.J.B. performed research; Z.N., T.P.N., Á.T., J.Y.S., D.E.B., and P.N.M. contributed new reagents/analytic tools; Z.N. and T.P.N. analyzed data; Z.N. and T.P.N. wrote the paper; Z.N. and R.J.B. wrote the institutional review board (IRB) protocol; J.Y.S., D.E.B., and P.N.M. enrolled patients in the study, supervised the clinical procedures, provided neurological expertise, and followed up with the patients; and R.J.B. obtained consent from the patients, performed the electrode implantation/explantation surgery, served as the principal investigator on the IRB protocol, and provided clinical supervision.

The authors declare no conflict of interest.

This article is a PNAS Direct Submission.

Freely available online through the PNAS open access option.

[1]To whom correspondence should be addressed. Email: zoltan@utexas.edu.

This article contains supporting information online at www.pnas.org/lookup/suppl/doi:10.1073/pnas.1701352114/-/DCSupplemental.

grid-cell population shares the same grid orientation, seemingly aligned and "anchored" to a particular landmark. Rotation of a distal visual cue, serving as a landmark, resulted in similar rotations of the rodents' grids in a feature-poor circular enclosure (10). Meanwhile, if proximal cues, such as the edges and boundaries of noncircular environments, are available, they may also function as anchors to which the grids become aligned (20). Consistent with the reliance on local cues, the orientation of grids in square-shaped environments tends to align with the walls at an angle that minimizes symmetry with respect to boundaries (21). Hence, the orientation of grids seems to rely primarily on local cues, but it can be based on distant cues when local cues are ambiguous or absent.

A third key characteristic of grids in the medial EC is their 60° rotational symmetry (10). Accordingly, grids recorded in circular or symmetrical enclosures tend to exhibit a narrow range of 60 ± 5° rotational symmetry quantified from autocorrelograms (ACs) (18). However, a comprehensive analysis of spatial periodicity evident from cells in the presubiculum and medial EC of rats revealed that only about 35–50% of medial EC cells exhibited canonical 60° rotational symmetry (12% and 28% in the presubiculum and parasubiculum, respectively) (11, 22), whereas a significant fraction of medial EC neurons (43%) displayed spatially periodic activity different from the 60° rotational symmetry (11). Nonhexagonal grid structures were most prevalent in enclosures with polarized geometry (20). The modulation of rotational symmetry was also evident in the two other studies that manipulated the size and geometry of the environment (19, 20). The control of grid rotational symmetry remains a subject of active research in rodents, although it is unexplored in the human brain.

The task of informed spatial navigation is an evolutionary problem posed to all animals. The study of human grid cells is especially interesting because it might reveal specific evolutionary adaptations beyond those adaptive features seen in lower level animals. For one thing, humans' visual faculties are far more advanced than rodents' visual faculties. If grid-cell activity depends on the predominant sensory input to the EC, we would expect this fact to be reflected in the nature of grid formation, perhaps with increased variability in grids according to an individual's visual appraisal of the environment. For instance, the rat's reliance on active exploration for the formation of place fields in the hippocampus indicates that kinesthetic and proximal cues are more crucial for this process in rats than visual cues are (23, 24). Consistent with this finding, rat exploration in virtual environments, where kinesthetic and proximal cues are absent, compromises the spatial specificity of their place cells (24). The opposite might be true in humans, where the likely predominance of visual input to the EC in the human brain might compensate for the otherwise kinesthetic-deprived sensory experience during virtual navigation. Despite the overall similarity between the anatomies of the rat and human EC, primate data suggest that the human EC receives a larger contribution from higher visual cortical areas (25). In primates, behavior as restricted as eye movements over static visual displays is sufficient to elicit spatially periodic ("grid-like") patterns of neuronal activity that correlate with saccade direction (26, 27). Interspecies differences in sensory processing make the spatial representations of place cells display marked variability. Chiropterans, for example, distinctly rely on spatioacoustic cues, developing uniquely 3D place fields as opposed to the 2D place fields seen in other animals (28, 29). In humans, then, it is plausible for a visually presented virtual environment to elicit place cell (30) and grid-like activity in the EC (31) without proprioceptive and kinesthetic cues. The predominance of visual cues in spatial navigation makes human subjects less dependent on the hippocampus and EC except when spatial memory is involved. After mesial-temporal lobectomy, patients were still able to perform path integration (32). Studying the grid scale invariance in humans in light of the differences in the sensory input organization of the EC between rodents and primates may elucidate aspects of spatial awareness that remain hidden in rodents and are specific to our species.

Here, we investigated the influence of virtual (i.e., purely visual) surroundings on the spatially periodic activity of neurons in humans by exposing the same set of EC neurons to four different virtual environments in a spatial memory task. Specifically, we addressed how parameters of the spatially periodic activity changed in response to independent variables of environment size, environment length-to-width ratio, and availability of spatial environmental cues. To understand these effects, we analyzed how these independent variables correlated with dependent variables: grid quality ("gridness"), grid scale, grid orientation, and grid rotational symmetry. If the dependent variables (i.e., the parameters of spatially periodic activity) show dependence on environmental features, that would suggest that the increased reliance on visual cues in the human EC allows for quick adaptation (or rescaling) of the neuronal coordinate system to the environment, a behavior that expands models developed based on animal studies. To ascertain the scalability of neuronal representations of space in the human brain, our goal was to quantify the environmental dependency of the spatially periodic activity of EC cells and to test for the consistency of environment-dependent changes of grid-like activity over time and their consistency between subjects. To attain a relatively unbiased estimate of spatially periodic activity, we constructed three main neuronal datasets and two subsets within each dataset, resulting in a total of six datasets. The largest dataset included neurons classified as displaying significant spatially periodic activity based on spatial spectral analysis of the single units. The other two smaller datasets were both classified as "putative grid cells" (PGCs) based on their conformity of gridness scores to the definition used in studies and referred to herein as the Barry–Krupic (BK) method (11, 18). The difference between the second and third datasets was that the third dataset, in addition to being defined based on the BK method, was subjected to a thorough validation against theta modulation and directional tuning. In addition, we constructed two subsets of each of the three main datasets that included cells maintaining significant spatial periodicity or gridness scores in at least three of the four environments. Because we analyzed these datasets separately and the results were highly concordant among them, we posit that the spatially periodic and grid cell-like activity in the human EC is analogous to the grid cells described in rodents but with markedly increased variations.

Results

Two male epilepsy patients, H and K (aged 33 y and 40 y, respectively; *SI Appendix*, Table S1.2), who previously consented to participate in the experiment and to allow publication of data and MRI images, were implanted with microelectrode arrays in layer 2/3 of their medial EC (Fig. 1*A*) in preparation for surgical resection of epileptic foci. During their days of clinical recording in the hospital epilepsy monitoring unit, participants H and K were asked to perform a virtual, memory-aided navigation task on a tablet computer in four environments each day and for 7 or 8 consecutive days, respectively. Accordingly, the dataset was organized by day (days 1–8) and environment (environments 1–4). Electrophysiology was recorded from the EC and spike-sorted offline. All four environment trials were recorded in single file with maintained electrode stability, allowing us to monitor how individual cells behaved with progression through each environment (*SI Appendix*, *SI Experimental Procedures*). In the following sections, we compare the environmental dependency of neuronal activity (*i*) within each day across game environments (/environments) (*ii*) and across games played in the same environment but on different days (/days). Each game's objective was to locate randomly placed space aliens and return them to their spaceship waiting at remembered locations (*SI Appendix*, *SI Experimental Procedures* and Movie S1). We constructed realistic 3D models of four different environments with accurate sizes relative to the average adult eye height and modeled the first-person visual experience of walking in these environments with an average step

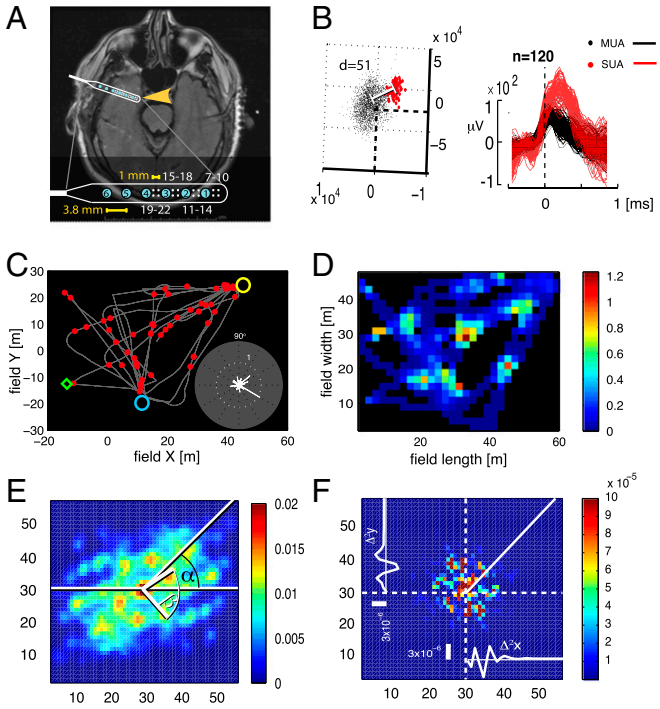

Fig. 1. Grid-cell expression in the human EC. (*A*) Position of EC electrode strip (yellow arrow) revealed on an axial MRI section. (*Inset*) Electrode location in the brain. The electrode design is magnified at the lower part of the image. Blue circles numbered from 1 to 6 are macroelectrode contacts. Dots grouped in square quartets and numbered from 7 to 22 are the microelectrodes. (*B*) Single-unit clusters (*Left*) and corresponding spike waveforms (*Right*). The separation of single-unit activity (SUA; red markers) from multiunit activity (MUA; black markers) is indicated by the Mahalanobis distance (d). (*C*) Trajectory of the subject's navigation in an environment overlaid with the SUA (red circles; same neuron as in *B*). Yellow and blue circles indicate the positions of spaceship targets, and the green diamond indicates an example target location (*SI Appendix, SI Experimental Procedures*). (*Inset*) Neuron's firing rate at different heading directions. (*D*) Average firing rate map. Color scale (spike * s^{-1}). (*E*) Spatial AC of SUA computed from *D*. (*F*) Two-dimensional autoperiodogram of the AC from *E*. The *X* and *Y* axes represent frequency.

size and constant walking speed. The environments consisted of a large open space (OS) with a boundless horizon and minimal external cues, a small open-air backyard (BY), a medium-sized area modeled after the Louvre's courtyard (LV), and a medium-sized covered space modeled after the main hall of the Temple of Luxor in Egypt (LX) (Fig. 2 *A* and *B* and *SI Appendix, SI Experimental Procedures, Properties of Environments* and Fig. S1). These environments were designed to differ in several salient features, including but not limited to size (area), aspect ratio (shape), boundaries, obstacles, and external landmarks (cues) (*SI Appendix*, Table S1.1).

From these two patients, we recorded single-unit activity over successive days. We isolated 397 single units (neurons) over 7 and 8 consecutive days from patients H and K, respectively (average overall firing rates between 0.02 Hz and 1 Hz). By keeping track of these cells' activity across four environments, a database of 1,588 single-unit spike trains (trials) was created, with each trial representing a single-unit activity in one environment. Because we sampled a different subset of electrodes each day, we treated single units recorded from different days as independent. Only single units obtained within the same day were treated as being produced by the same cells in different environments (*SI Appendix, SI Experimental Procedures*). Each of the 1,588 trials associated with a navigation pathway was converted to a firing rate map and AC using the BK method (11, 18).

Despite the aperiodic patterns of movement trajectories (Fig. 1*C*), as much as 52% of total trials (824 trials from 206 neurons) resulted in significant spatially periodic activity patterns based on a 2D spectral analysis (11) after validation of their spectral periodicity scores against ACs of a randomly displaced collection of 2D Gaussian firing rate clusters (*SI Appendix, Experimental Procedures* and Fig. S3*H*). We could rule out the possibility that spatial periodicity was a result of spike-sorting artifact (33, 34) by including only single units, which produced nonoverlapping waveform clusters with an average Mahalanobis intercluster distance of >20 (mean_{Mahal_d} = 230; *SI Appendix*, Figs. S2 and S10–S28). We refer to these 824 trials from 206 neurons as spatially periodic cells (SPCs; *SI Appendix*, Fig. S35 and Table S2). Among SPCs, 92 (45%) exhibited spatial periodicity in all three environments with architectural landmarks (BY, LX, and LV). We refer to this subclass of cells as persistent spatially

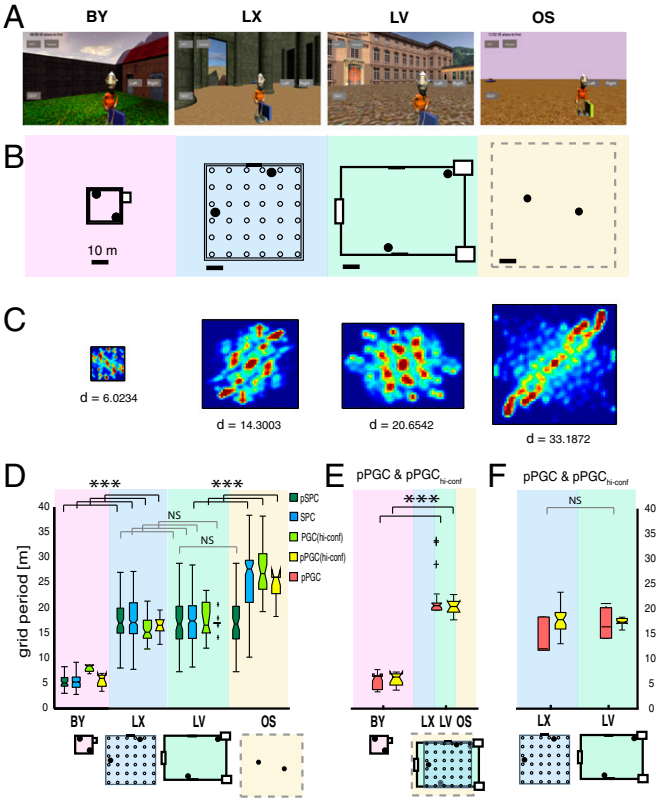

Fig. 2. Adaptive rescaling of grids in different virtual environments. Screenshots (*A*), with space alien target objects and scale layouts (*B*) of the four different environments. Filled circles are space ships. Empty circles in LX are columns. (*C*) Spatial ACs from the same cell across all four environments capture the spatial periodicity of spikes generated by the same cell across the four environments. (*D–F*) Boxes represent the distribution of grid periods from four datasets. (*D*) Environment-associated differences in grid distances derived from four datasets: SPCs (all cells), $n_{(\text{trials,cells})}$ = 824,206 (blue boxes); PGC$_{hi\text{-}conf}$s, $n_{(\text{trials,cells})}$ = 262,65 (light-green boxes), pSPCs and pPGC$_{hi\text{-}conf}$s active in all three confined environments, $n_{(\text{trials,cells})}$ = 276,92 (dark-green boxes) and $n_{(\text{trials,cells})}$ = 260,65 (yellow boxes), respectively. (*E*) Grid distances produced by pPGCs and pPGC$_{hi\text{-}conf}$s that were active in the BY and at least one of the large environments (LX, LV, and OS) (n = 20) (red and yellow boxes, respectively). (*F*) Comparing grid distances of pPGCs and pPGC$_{hi\text{-}conf}$s between LX and LV environments (n = 5) when the cells were active in both environments. The horizontal lines in boxes are medians, and boxes contain the 25th through 75th percentiles. Whiskers cover the most extreme data points and + signs are outliers. Grid periods were combined from both subjects during navigation in all four environments. The daily sequence of environments was randomized. ***P < 0.001. NS, not significant.

periodic cells (pSPCs). Among those pSPCs, 47 displayed 60 ± 10° rotation symmetry. Moreover, to classify grid cell-like activity, we further subjected the 206 SPCs to a quantification of their gridness relative to their own time-shuffled spike ACs strictly following the BK method (11, 18). To meet the definition of grid cells, we constrained this analysis by selecting cells that displayed 60 ± 10° rotation symmetry (10). This analysis resulted in 73 neurons from the two subjects ($n^{\text{subj-H}} = 40$ and $n^{\text{subj-K}} = 33$) with significant grid-like quality, 35% of the total 206 spatially periodic neurons. We further refer to this dataset as PGCs because they shared all attributes with grid cells classified in the rodent medial EC. All PGCs were a subset of SPCs. Although none of the PGCs exhibited significant gridness in all four environments (and very few in three environments), 39 of the 73 PGCs (53%) exhibited significant gridness in at least two environments. We refer to these cells as persistent putative grid cells (pPGCs) (*SI Appendix*, Fig. S3*I*, Table S2, and Movie S1).

Additionally, to reduce the chance of detecting false-positive results brought about by nonlocal covariates in our sample, such as theta modulation, spiking bursts, or direction tuning, we isolated a subset of PGC activity that was tested against a combination of theta and alpha modulations, bursting firing pattern, and directional tuning (*SI Appendix*, *SI Experimental Procedures*). Although directional tuning did not covary with the environments (*SI Appendix*, Fig. S33 and Tables S9.1–S9.3), to ensure the immunity of grids to direction tuning, we isolated a subset of spatially modulated single units that passed the BK test against direction-tuned and theta-modulated surrogate spike trains.

Single units with significant gridness relative to the temporally and directionally modulated null yielded a population denoted as high-confidence putative grid cells ($\text{PGC}_{\text{hi-conf}}$s; $n = 262$, $n^{\text{subj-H}} = 118$, $n^{\text{subj-K}} = 144$). Similar to the pPGC dataset, we separated a subset of PGC neurons, including only those PGC neurons that displayed significant spatial modulation in at least two differently sized environments (BY-LV or BY-LX), and denoted them as persistent high-confidence putative grid cells ($\text{pPGC}_{\text{hi-conf}}$s). This set included $n = 65$ single units active in at least two nonequally sized environments and $n = 28$ single units active in all three environments with spatial cues (BY, LV, and LX).

The purpose of the pSPC, pPGC, and $\text{pPGC}_{\text{hi-conf}}$ datasets was to enable us to compare grid parameters between environments using a repeated measures design. To enhance robustness, all statistical analyses were performed separately on six datasets: SPC, pSPC, PGC, pPGC, $\text{PGC}_{\text{hi-conf}}$, and $\text{pPGC}_{\text{hi-conf}}$. Although all six datasets exhibited significant spatial periodicity of firing patterns, by definition, as quantified based on a spectral method (11), only the PGC and pPGC subsets qualified as "canonical" grid cells defined by traditional methods (10, 11, 18). $\text{PGC}_{\text{hi-conf}}$ and $\text{pPGC}_{\text{hi-conf}}$ datasets further extended the BK method by applying a more stringent null for computing gridness.

Because the clinical time constraints limited the test times to 5 min per environment, there was a concern that the stability of grid patterns might be compromised. Therefore, the temporal stability and stationarity of periodic patterns and grid patterns were tested by applying a twofold cross-validation and stationarity analysis for all of the cells in the SPC and $\text{PGC}_{\text{hi-conf}}$ datasets, and both tests confirmed at the population level the stability and stationarity of grid patterns [Wilcoxon test on twofold cross-validation: for the SPC dataset, $P_{(n\,=\,879)} = 4.726\text{e}^{-49}$ and for the pSPC dataset, $P_{(n\,=\,285)} = 1.4887\text{e}^{-19}$; *SI Appendix*, Figs. S5 *F* and *G*, S36, and S37 and Table S10].

Dependence of Grid Period on Environment. Grid period is the distance between adjacent grid nodes as determined based on the spatial AC (*SI Appendix*, *SI Experimental Procedures*). Although grid periods were uniform across all electrode positions and neurons, they varied by environment (three-way ANOVA: $P^{\text{subj-H}} < 0.001$, $P^{\text{subj-K}} < 0.001$; Fig. 2 and *SI Appendix*, Tables S3.1 and S3.2). Studies in rodents using environmental manipulations, such as partitioning and transformation (10, 13, 19), suggest that the grid period produced by a particular grid cell is conserved across environments and only changes after transformation of a familiar environment (18, 19). To investigate what specific feature of the environment could best explain the observed variation (Fig. 2*C* and *SI Appendix*, Fig. S29), we sought to determine whether any of the varying spatial features of the four environments had a strong correlation with grid periods displayed by individual neurons. To do so, we quantified the grid's spatial frequency from the 2D spectral density of the AC (Fig. 1*F*). In contrast to rodent data (10), we observed a significant difference in average grid periods between environments in all of our six datasets (Fig. 2 *D* and *E*), including the spatial periods of the complete SPC dataset (Kruskal–Wallis test, $P = 2.498\text{e}^{-134}$; Fig. 2*D* and *SI Appendix*, Table S3.5). The grid scale difference was also significant when we compared the spatial behavior of the same neurons across the four environments within the pSPC dataset [Friedmann test, $P_{(n\,=\,73)} = 8.4344\text{e}^{-32}$; Fig. 2*D* and *SI Appendix*, Table S3.8]. The difference in average grid distance in the pSPC dataset was significant when the smallest environment was contrasted against any of the three larger environments or all three combined [Friedman's test, $P_{(n\,=\,115)} = 2.1748\text{e}^{-26}$; Fig. 2*D* and *SI Appendix*, Table S3.9], but grid distance was no different between large environments (*SI Appendix*, Table S3.11). The PGC dataset reflected the same pattern (*SI Appendix*, Fig. S7). Additionally, we compared the average grid periods of pPGCs between the small and large environments. Because not all PGCs were active in both the small and large environments, we compared a subset of PGCs, including only those PGCs that were active in both. To achieve sufficient statistical power, we selected neurons that were active in both the smallest environment (BY) and in at least one of the two larger environments with well-defined spatial landmarks (LV and LX) and compared their grid periods ($n = 19$). The average grid period of PGCs determined in the small environment showed a significant expansion when probed in the larger environments [Wilcoxon signed rank test, $P_{(n\,=\,19)} = 1.2937\text{e}^{-04}$; Fig. 2*E* and *SI Appendix*, Table S3.10]. No significant difference in grid periods between the large environments (LV and LX) was found owing to the similarity of their dimensions [Wilcoxon signed rank test, $P_{(n\,=\,5)} = 0.3125$; Fig. 2*F* and *SI Appendix*, Table S3.11]. To verify the validity of grid scale dependence on environment size, we repeated the test in our $\text{PGC}_{\text{hi-conf}}$ dataset (*SI Appendix*, Fig. S8). Both $\text{PGC}_{\text{hi-conf}}$ and $\text{pPGC}_{\text{hi-conf}}$ datasets accurately reproduced the significant grid rescaling between small and large environments seen in the other four datasets [Kruskal–Wallis test on $\text{PGC}_{\text{hi-conf}}$: $P^{\text{subj-H}}{}_{(n\,=\,113)} = 1.0719\text{e}^{-14}$, $P^{\text{subj-K}}{}_{(n\,=\,85)} = 3.7179\text{e}^{-15}$; Friedmann's test on $\text{pPGC}_{\text{hi-conf}}$: compared across three environments, interpolated, and combined between subjects, $P_{(n\,=\,10)} = 5.5560\text{e}^{-06}$; compared between the small and any of the larger environments, $P_{(n\,=\,10)} = 0.0016$; *SI Appendix*, Tables S3.9.1–S3.9.3]. Conversely, no grid rescaling was observed between the two similarly sized (LX and LV) environments [Wilcoxon signed rank test $P_{(n\,=\,32)} = 0.5475$; *SI Appendix*, Table S3.9.4]. Hence, the neurons in our sample tested against spike trains endowed with theta modulation and directional tuning retained a significant environment-dependent rescaling of grid distance, no less than those neurons tested against Poisson spike time shuffling (Fig. 2 *D*–*F*).

The described grid-scale differences were consistent between the two subjects (Fig. 3*A* and *SI Appendix*, Fig. S8 *A* and *B* and Table S3.15) and remarkably stable over successive days (Fig. 3*B*). Grid distances within a specific environment displayed substantially less variation across different days than across environments (Kruskal–Wallis one-way ANOVA, $P^{\text{subj-H}} > 0.05$ and $P^{\text{subj-K}} > 0.05$; Friedman's test, the exact P values are listed in *SI Appendix*, Tables S3.6 and S3.7, respectively). Because the grid periods did not differ between the two subjects with respect to any of the three datasets

($P > 0.05$, Wilcoxon rank-sum test), we combined the same type of datasets from the two subjects for statistical evaluation. The effect of the environment was consistent over all three datasets (Kruskal–Wallis test with independent samples on the SPC dataset, $P < 0.001$, *SI Appendix*, Table S3.5; Friedman's test with repeated measures on the same cells' pSPC dataset, $P < 0.001$, *SI Appendix*, Table 3.8; and Wilcoxon signed rank tests on the pPGC dataset, $P < 0.001$, *SI Appendix*, Tables S3.10 and S3.11). The grids transformed in a fashion similar to what is found when rodents are presented with a transformed version of a familiar environment (19); the rescaling was proportional to the edge length of the environment because it was smallest in BY, larger in LX and LV, and largest in OS (Fig. 3*B* and *SI Appendix*, Figs. S6*A* and S7*C* and Table S3.10). LX and LV were not different (*SI Appendix*, Table S3.11). We reasoned that if grid periods linearly scale with the size of environment (Fig. 3*A* and *SI Appendix*, Figs. S5*A*, S6*A*, and S7*A*), then normalizing them to the size of the environment should reduce the grid period differences across environments (*SI Appendix*, Figs. S6*B* and S7*B*). This hypothesis was confirmed because the environment size-normalized average grid period difference either disappeared, as it did in the SPC, pSPC, and PGC datasets [two-way ANOVA, $P_{(df\ =\ 3,6)} > 0.3$, and Kruskal–Wallis test, $P_{(df\ =\ 3,6)} = 0.0509$, compare *SI Appendix*, Tables S3.1 and 3.2 with *SI Appendix*, Tables S3.3 and S3.4; PGC dataset: two-way ANOVA, $P^{subj\text{-}K} = 0.4547$ and $P^{subj\text{-}H} = 0.3819$, *SI Appendix*, Table S3.14] or was greatly reduced in the pPGC dataset between small and large environments when comparing the difference between before [Friedman's test, $P_{(BY\text{-}LV,\ LX,\ OS)} = 1.2937e^{-04}$; *SI Appendix*, Table S3.10] and after [$P_{(BY\text{-}LV,\ LX,\ OS)} = 0.011$; *SI Appendix*, Figs. S6*B* and S7*B* and Table S3.12] normalization. Normalization of grid periods did not affect the similarity of grid distances between large environments [Friedman's test, $P_{(n\ =\ 5)} = 0.91$; *SI Appendix*, Table S3.13]. For both subjects, correlations between grid periods and environment sizes in both types of datasets, SPC and pPGC, were high (SPC: Pearson's $r^{subj\text{-}H} = 0.877$, $P < 0.0001$; pPGC: Pearson's $r^{subj\text{-}K} = 0.879$, $P < 0.0001$, Fig. 3*A*; pPGC combined: Pearson's $r = 0.5139$, $P < 0.0001$, *SI Appendix*, Figs. S6*A* and S7*A*) and displayed an average grid period-to-environment dimension ratio of 0.3954 [$f(x)^{subj\text{-}H} = 0.4047x\text{-}2.81$] and 0.3509 [$f(x)^{subj\text{-}K} = 0.3509x\text{-}0.6187$] and 0.4108 [$f(x)^{subj\text{-}H} = 0.4108x\text{-}0.241$] and 0.4153 [$f(x)^{subj\text{-}K} = 0.4153x\text{-}4.218$) in the SPC (Fig. 3*A*) and pPGC datasets (*SI Appendix*, Fig. S7*A*), respectively.

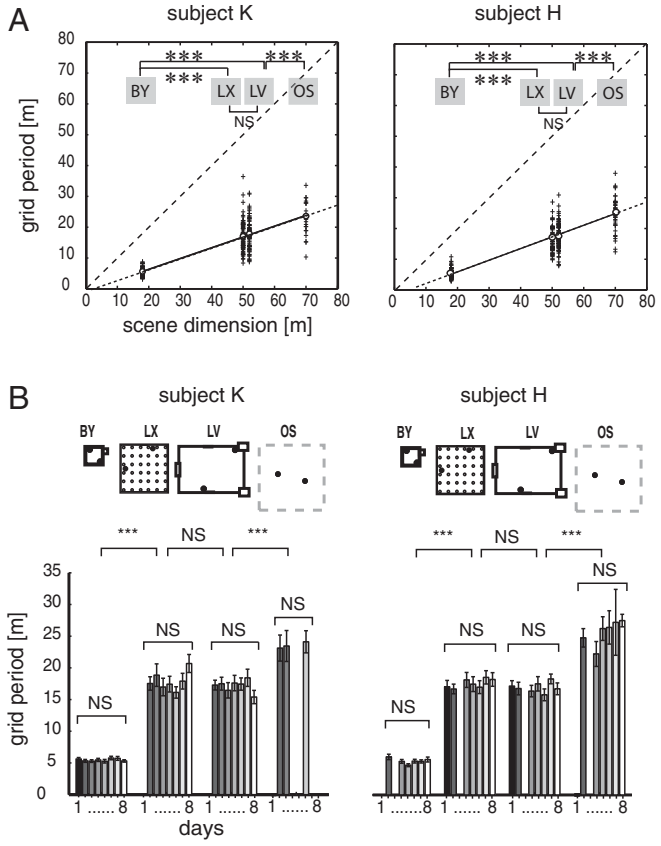

Fig. 3. Grid period is environment-dependent and stable over days. (*A*) Grid periods are shown as a function of the size of the environment. Data were combined over multiple days from navigation trials in the same four environments and are displayed according to environments (BY, LX, LV, and OS) and subjects (patients K and H) ($n = 436$ and $n = 388$ segments, respectively). The length of the shorter axes of given environments (X) is plotted against the grid period (Y). The sparse-dashed lines represent identity lines. The fine-dashed lines are extrapolations of slopes. (*B*) Average grid periods from the two subjects grouped according to the environments (layouts on top) and consecutive days (days 1–8). The variation of grid periods over days was insignificant relative to the variation across environments. Error bars represent SEM. ***$P < 0.001$. NS, not significant.

The variation in grid period might have also been affected by factors such as covariance with the cells' gridness, the firing rate difference between environments, and the unequal coverage of environments by exploration. However, no consistent covariations of gridness scores and environments were observed across datasets. Although the general spatial periodicity (*gsp* score; *Materials and Methods* and *SI Appendix*, *Experimental Procedures*) decreased with increasing environment sizes in the large SPC dataset ($P < 0.001$, ANOVA with independent measures; *SI Appendix*, Fig. S30 *A* and *B* and Table S4.1), other datasets (pSPC and PGC) did not confirm any environmental dependency of the magnitude of spatial periodicity [pSPC: one-way ANOVA, $P_{(n\ =\ 26)}{}^{subj\text{-}H} = 0.4248$ and $P_{(n\ =\ 24)}{}^{subj\text{-}K} = 0.2575$; *SI Appendix*, Fig. S31 *A* and *B* and Table S4.2], not even when gridness scores were determined based on the BK method [$P_{(n\ =\ 12)}{}^{subj\text{-}K} = 0.1258$ and $P_{(n\ =\ 16)}{}^{subj\text{-}H} = 0.1330$; *SI Appendix*, Table S4.3]. The firing rate was also uniform across environments for all datasets (SPC, pSPC, and pPGC; *SI Appendix*, Tables S5.1–S5.3, respectively) across different environments (*SI Appendix*, Fig. S30*C*).

Differences in environment coverage was inherent in the task design because the areas of modeled environments varied between 324 m^2 and 4,900 m^2. This variation naturally affected the coverage (*SI Appendix*, Tables S6.1–S6.3) because the large environments received an average of 60% of the coverage of the smallest. To compensate for the effect of uneven coverage across environments, in a separate analysis, we shortened the navigation trajectories in the BY environment by 50% of their original length (hence, the duration of navigation as well) and recomputed the grid distances of all 1,588 segments (397 neurons). This manipulation reduced the difference in path density across all environments (*SI Appendix*, Fig. S9*A*), whereas it left the average gridness scores, $\langle \hat{g} \rangle = \frac{1}{n} \sum_{i=1}^{n} gsp$, and environmental grid scale differences unaffected relative to the complete datasets [gridness scores: two-sample t test, $\hat{g}^{subj\text{-}K}{}_{halfpath} = -0.1000$, $\hat{g}^{subj\text{-}K} = -0.1454$, $P_{(n\ =\ 59,8)} = 0.2594$; $\hat{g}^{subj\text{-}H}{}_{halfpath} = -0.2064$, $\hat{g}^{subj\text{-}H} = -0.2817$, $P_{(n\ =\ 58,33)} = 0.2165$; grid distances: Kruskal–Wallis test, $P^{subj\text{-}H}{}_{(n\ =\ 79)} = 5.8221e^{-14}$, $P^{subj\text{-}K}{}_{(n\ =\ 164)} = 4.2568e^{-26}$; *SI Appendix*, Fig. S9 *B–D* and Table S6.4]. The average slope and y-intercept of the regression line [$f(x) = 0.4130x\text{-}3.7295$] reproduced the $f(x) = 0.3954$ regression line observed in datasets, including the complete navigation path. Hence, the increased coverage in the smallest environment did not account for the smaller grid distances consistently observed across all six datasets.

Altogether, the consistency of the environment-specific magnitude of grid rescaling across datasets and between the two subjects, the independence of grid scale from the variations of firing rate and gridness scores, and the invariance of the effect of

environmental coverage speaks strongly to the overall environment dependency of grid scaling in the human EC.

Grid Orientation. Rodent grids normally orient themselves relative to distant or local landmarks, whichever provides the most consistent spatial cue in repeated visits to an environment. Because grid orientation was a stable feature of grid cells in rodents (10, 21), we sought to determine if this grid orientation was preserved in humans. Aside from OS, all of our environments had two types of spatial landmarks available: initial orientation and architectural cues. Because each navigation session in the same environment always started from the same location and facing the same direction, thus providing unambiguous initial visual orientation cues (*SI Appendix*, Fig. S1), our subjects could orient themselves in each environment based on the initial orientation cues, except in the OS, where those cues were lacking. The consistency of spatial references at the start of each trial had the theoretical possibility of providing sufficient input to the neurons in the EC to anchor their grid orientation. Therefore, we calculated the principal orientation of ACs for all recorded single units with significant spatial periodicity, including the SPC and PGC datasets. Due to the poor orientation cues available in the OS environment (*SI Appendix*, Fig. S1) and lower gridness scores (*SI Appendix*, Fig. S30*A*), we excluded the OS environment from this analysis. In the remaining three environments with rich visual cues, where grid orientation could be determined more accurately, we found that neurons in all datasets tended to adopt environment-specific orientations (Fig. 4 *A* and *B*). Grid orientations in the SPC dataset displayed a predominantly 45° alignment in the two square-shaped environments relative to the main axes defined by the architecture ($BY^{Subj\text{-}H}$: 45.24°, $LX^{Subj\text{-}H}$: 46.84°, n = 311; $BY^{Subj\text{-}K}$: 44.21°, $LX^{Subj\text{-}K}$: 47.47°; n = 376; *SI Appendix*, Fig. S32). In contrast, the only rectangular environment (LV) generated grid orientations close to 33° ($LV^{Subj\text{-}H}$: 38.28°, $LV^{Subj\text{-}K}$: 33.92°). Neither of these orientations were aligned with 60°, the initial orientation of the avatar (*SI Appendix*, Fig. S1). Instead, the average grid orientations reflected the 45° direction of corners in both square-shaped environments (BY and LX). If grid orientation aligns with the corners, then we expect a deviation from the 45° angle in the rectangular environment (LV). Consistent with this hypothesis, we observed an average 34.89° grid orientation that closely matches the 33° direction of corners in the LV environment relative to the center and the east–west cardinal axis of the environment (Fig. 4*B* and *SI Appendix*, Figs. S1*A* and S32), which also served as the axis of the ACs. Cells maintained these orientation differences across days of recording [two-way circular ANOVA on the SPC dataset, $P_{(df = 2,5)}^{subj\text{-}H} < 0.0001$ and $P_{(df = 2,6)}^{subj\text{-}k} < 0.0001$, Fig. 4*C*; two-way circular ANOVA in the pSPC dataset, $P_{(df = 2,4)}^{subj\text{-}H} < 0.02$ and $P_{(df = 2,4)}^{subj\text{-}K} < 0.02$, *SI Appendix*, Figs. S12–S28 and Tables S7.1 and S7.2, respectively]. Closer examination of the polar histograms revealed that the distribution of grid orientations in the rectangular environment (LV) was bimodal and divided between 30° and 45° (*SI Appendix*, Fig. S32).

Furthermore, the grids seemed to adopt very similar grid orientations between the patients [Watson–Williams test, $P_{(n = 49)} > 0.05$; *SI Appendix*, Tables S7.3 and S7.6 for the pSPC dataset], a possible indication that both patients used the same landmark in each environment to anchor grids. This finding allowed us to combine both subjects' data and gain the necessary statistical power for the analysis of grid orientation in the pPGC dataset as well. With the grouped data, the average grid orientations displayed by the same cells (pPGC dataset; *SI Appendix*, Table S7.5) inside the two square-shaped environments, BY and LX, were 56° and 61°, respectively; neither was significantly different from 60° or from one another (*SI Appendix*, Table S7.7). Note that a hexagonal grid with a 60° orientation is in perfect alignment with the east–west axis of both environments and reflects the avatar's initial orientation. However, both of those average grid orientations were significantly different from the 36.22° mean grid orientation displayed by the same cells in the rectangular environment (LV) (circular ANOVA and circular test for mean grid orientation, $P < 0.05$; *SI Appendix*, Tables S7.7, S7.8, and S7.13 for pPGC, pSPC, and $pPGC_{hi\text{-}conf}$ datasets, respectively). These grid orientation-related differences between square-shaped and rectangular environments were significant in all datasets (SPC, pSPC, PGC, pPGC, $PGC_{hi\text{-}conf}$, and $pPGC_{hi\text{-}conf}$) and stable over days when comparing them by circular ANOVA using independent and repeated samples, respectively (days effect: $P_{(pSPC)} > 0.05$; environment effects: $P_{(SPC)} < 0.001$, $P_{(pSPC)} < 0.05$, and $P_{(pPGC)} < 0.05$, *SI Appendix*, Tables S7.1, S7.2, and S7.4; $P_{(PGChi\text{-}conf)} < 0.01$, *SI Appendix*, Tables S7.9 and S7.10; and $P_{(pPGChi\text{-}conf)} < 0.05$, *SI Appendix*, Tables S7.11–S7.13). The specificity of grid orientation to the aspect ratio of the environment and consistency of adopted grid orientations over days,

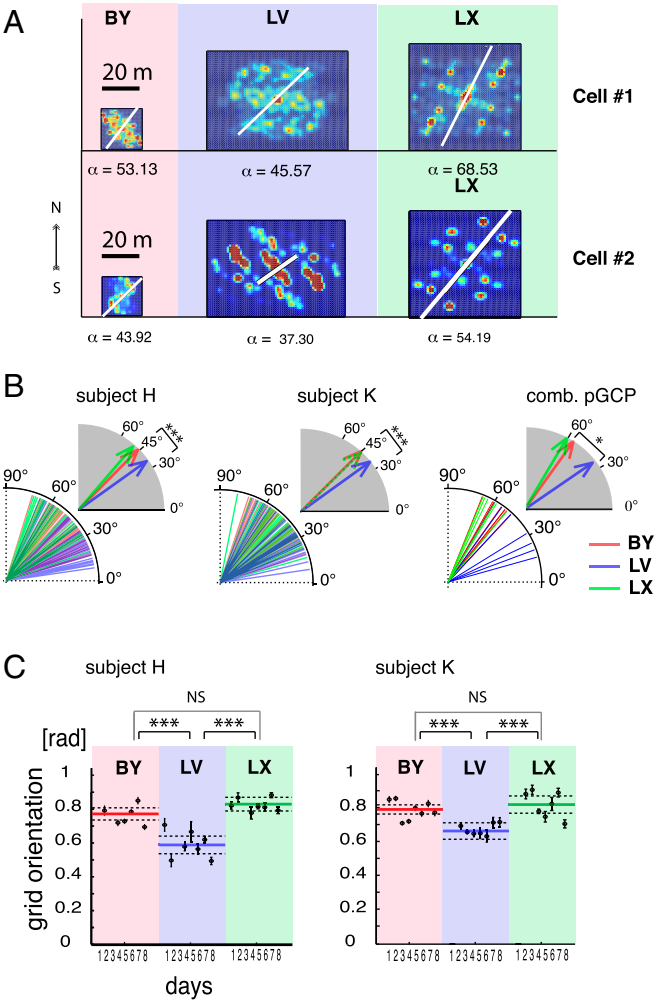

Fig. 4. Environment-dependent grid orientation. (*A*) ACs of two example neurons (cells 1 and 2) with their grid orientations in each environment within the same day of recording. The white line and corresponding α-values (in angular degrees) indicate grid orientation. (*B*) Population plots of grid orientations from all cells of the SPC dataset color-coded according to environments from the two subjects (*Left* and *Center*) and the same for the pPGC dataset (*Right*). comb., combined. Vectors in gray-shaded quadrants represent angular averages of the corresponding population of grid orientations, according to environments. (*C*) Grid orientations from the SPC dataset grouped according to environments (large groups) and consecutive recording days (individual filled symbols) from the two subjects (*Left* and *Right*, n = 311 and n = 376 segments, respectively). Error bars indicate angular dispersion. Colored lines represent grand averages of grid orientation associated with the three environments. Dashed lines are confidence intervals. Asterisks represent statistical significance of differences (*$P < 0.05$, ***$P < 0.001$). [rad], radian.

as well as between the two subjects, strongly suggest that grid orientation is dependent on the geometry of the environment (Fig. 4*C*). We could rule out that the consistency of grid orientation with environment geometry depended on the neurons' directional tuning, because we did not observe any difference in directional tuning between neurons active in multiple environments [repeated measures ANOVA on resultant vectors with the factors of /days and /environments, $F_{(4,2)}$ =1.2264, $P_{(n\ =\ 74)}$ = 0.758; *SI Appendix*, Fig. S32 and Tables S9.1–S9.3]. This result further corroborates the result that grid cells align their orientation to the virtual environment as opposed to the patient's actual orientation in the hospital or respond uniformly to different environments.

The Rotation Symmetry of Grid Patterns. Despite the consistent coordination of the grid orientation with the geometry of the environment, grid angles in the square-shaped environments differed between the two datasets, pSPC and pPGC, with a notable 12.73° (mean $\beta_{\mathrm{pSPC}} = 45.85°$ and $\beta_{\mathrm{pPGC}} = 58.59°$). Because grid geometry (i.e., square, hexagon, pentagon) may affect grid orientation, the variation of rotational symmetry of spatially periodic activity patterns in different environments was investigated next. We focused this analysis on the SPC dataset (Fig. 5*A*), because the *gsp* scores [*SI Appendix*, *SI Experimental Procedures*, *Quantifying "General Spatial Periodicity"* (gsp *Score*) and Fig. S3*G*] were agnostic to rotational symmetry, thus allowing for quantification of a broader range of 15–90° rotation symmetries, and not only 60° (±10°).

We were surprised to observe that a substantial fraction of spatially periodic activity deviated from the hexagonal geometry (11). In addition to a number of data segments with predominantly 60° rotational symmetry, characteristic of grid cells in the rodent brain, we observed a significant number of non-hexagonal grid-like patterns (Fig. 5 *B* and *C*). We classified these cells as SPCs to discriminate them from the PGCs of our PGC population. Many of the SPCs displayed variants of rectangular or octagonal grid geometry with a 90° or 45° rotational symmetry, respectively (*SI Appendix*, Figs. S13, S15–S20, S22, S23, and S25–S28), which is undocumented in rodents and primates to date. The fraction of SPCs deviating from the 60° rotational symmetry accounted for 65% of neurons with significant spatially periodic activity (*SI Appendix*, Fig. S3*I*). Overall, the population mean of rotational symmetries for the complete dataset did not conform to 60° [circular one-sample test for specified mean direction, subject H: $P_{(n\ =\ 435)} > 0.05$, subject K: $P_{(n\ =\ 387)} > 0.05$], and the distribution was asymmetrical around the median [circular symmetry test, subject H: $P_{(n\ =\ 435)} = 0.0078$, subject K: $P_{(n\ =\ 387)} = 0.0412$].

Next, we investigated whether or not an environmental dependency of the rotational symmetry of the ACs may underlie the heterogeneity of grid geometry displayed by the same or a mixed population of neurons (pSPCs and SPCs) during navigation in different environments (Fig. 5*B*). We focused the analysis on the rotational symmetry of the ACs computed from the SPC dataset. The comparison of rotational symmetry across environments revealed a predominant 60° angle of rotational symmetry in the BY, our smallest virtual environment. In contrast, a significant decrease in the proportion of hexagonal grids was evident in the other environments, consistent between both subjects [Fig. 5*B*; one-way circular ANOVA, $P_{(n\ =\ 213)}^{\mathrm{subj\text{-}H}} < 0.001$ and $P_{(n\ =\ 214)}^{\mathrm{subj\text{-}K}} < 0.001$; *SI Appendix*, Tables S8.1 and S8.3]. No significant difference between the circular means of rotational symmetry between the two similarly sized larger environments (LV and LX) was found [circular ANOVA, $P_{(1,132)}^{\mathrm{subj\text{-}H}} = 0.8875$, $P_{(1,136)}^{\mathrm{subj\text{-}K}} = 0.1640$; *SI Appendix*, Table S8.2]. However, differences in rotational symmetry between environments of much different sizes were significant in both subjects' datasets [circular ANOVA, BY and LV: $P_{(1,102)}^{\mathrm{subj\text{-}H}} < 0.005$ and $P_{(1,160)}^{\mathrm{subj\text{-}K}} < 0.005$; circular ANOVA, LX and OS: $P_{(1,106)}^{\mathrm{subj\text{-}H}} < 0.001$ and $P_{(1,92)}^{\mathrm{subj\text{-}K}} < 0.001$]. In general, the proportion of cells expressing the canonical 60° angle of rotational symmetry negatively correlated with the dimensions of the environment (Pearson's $r^{\mathrm{subj\text{-}H}} = -0.4293$, $P < 0.0001$ and Pearson's $r^{\mathrm{subj\text{-}K}} = -0.3915$, $P < 0.0001$; Fig. 5*D* and *SI Appendix*, Table S8.3). The dependency of grid rotation symmetry on environments was confirmed within the pSPC dataset containing neurons that displayed persistently significant spatial periodicity in all three environments (with well-defined external cues) during the same session (BY, LX, and LV; *SI Appendix*, Table S8.4). Although the negative correlation was consistent over days and subjects [two-factor circular ANOVA: environment effect, $P_{(n\ =\ 74)}^{\mathrm{subj\text{-}H}} < 0.01$ and $P_{(n\ =\ 71)}^{\mathrm{subj\text{-}K}} < 0.001$; days effect: $P_{(n\ =\ 74)}^{\mathrm{subj\text{-}H}} = 0.4871$ and $P_{(n\ =\ 71)}^{\mathrm{subj\text{-}K}} = 0.1571$; *SI Appendix*, Table S8.5], factors such as the differing complexity of environments, the relative position invariance of external cues in larger environments, or the decreasing reliance on external cues and lack of boundaries in the OS environment, might have also played a role separately or in combination. Other factors, such as the partial

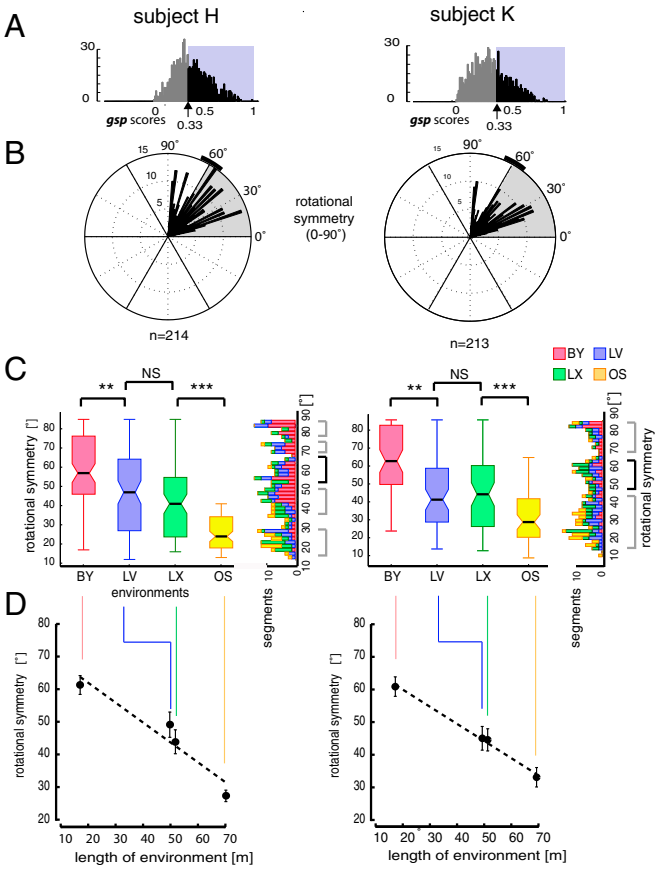

Fig. 5. Rotational symmetry of spatial periodicity. (*A*) Distribution of *gsp* score per subject determined based on the spectral method. We selected neurons with *gsp* scores >0.33, the 5% confidence interval of the randomized spatial ACs (*SI Appendix, SI Experimental Procedures* and Fig. S3*H*). (*B*) Distributions of angles of rotational symmetry from the two subjects over all environments using a 2° bin size. The *n* values indicate the number of data segments. (*C*, *Left*) Box and whisker plots for grid rotational symmetries observed in each environment color-coded according to environments. (*C*, *Right*) Rotated histograms show the composition of rotation symmetries according to the environment. Note that in addition to data segments displaying ~60° rotational symmetries (black bracket), comparable numbers of data segments exhibited rotational symmetry at other angles (gray brackets). $^{**}P < 0.01$, $^{***}P < 0.001$. (*D*) Angle of rotational symmetry negatively correlated with environment size. Significant differences in angles of rotational symmetry were found across environments, except between LV and LX, consistent between both subjects (*SI Appendix*, Tables S8.1–S8.5). Error bars represent angular variance (Subjects H and K, $n = 214$ and $n = 213$ segments, respectively).

coverage of larger environments, could have also contributed to incomplete grid formations. Therefore, we also tested the rotational symmetry of grids under a balanced coverage condition. Even after a 50% reduction of navigation paths in the BY environment, the 60° rotational symmetry of cells prevailed, whereas other rotation symmetries predominated in the larger environments [circular ANOVA: $F_{(3,75)} = 9.034$ $P_{(n = 78)} < 0.001$; $F_{(3,134)} = 23.7839$, $P_{(n = 140)} < 0.001$; *SI Appendix*, Tables S8.6 and S8.7]. Hence, among other factors, we can rule out that the significant deviation from 60° rotational symmetry in the larger environments was a result of incomplete spatial coverage of these environments.

Discussion

Context-dependent spatial representations in the hippocampus of various species have been widely documented. Neurons in CA1 and CA3 remap their place fields upon changes made in the environment, as demonstrated in rodents (13–17), Chiroptera (35), and primates (36). Because the adaptive remapping of hippocampal place fields is a relatively fast and EC-dependent process (13, 37), it is plausible to assume that neurons in the EC are endowed with some degree of flexibility. Contrary to this hypothesis, initial reports on grid cells based on rodent experiments suggested a universal metric for path integration-type navigation (10, 12). This metric appeared to be scale-invariant with respect to the geometry and size of the environment, despite having been challenged by a number of rodent studies (18–20). One such challenge involved moving the walls of the enclosure, which induced temporary elastic changes of the grid geometry (19). In a more common scenario, mere environment novelty elicited expanded grids (18), while neither novelty nor stretching affected border cell activity (9). Likewise, grid cells in rats exploring polarized asymmetrically shaped (trapezoidal) enclosures develop heterogeneous gridness of activity between different parts of the enclosure in contrast to the homogeneous gridness typical in symmetrical enclosures (e.g., square, rectangle). Nevertheless, grid distances in trapezoid enclosures remained uniform (20). Although the grid scale invariance might be robust across species of the rodent order, comparing it with the human analog might reveal aspects of neuronal representation of space that are specific to the human brain.

We obtained stable recordings of different neurons in the human EC across spatial navigation trials in multiple virtual environments (Fig. 2) over successive days. More than half of the neurons displayed spatially periodic activity (a fraction of those neurons specifically displayed grid-like activity), and they did so consistently and specifically for given environmental features, independent of the order of presentation of the environments and day of recording (*SI Appendix*, Figs. S2 and S5). Convincingly, these effects of the environment were consistent between the two subjects.

The observed proportion of neurons with spatial tuning is consistent with data from the rat EC (11), but larger than observed in the primate EC during visual tasks (35) and in the human EC during other virtual navigation tasks (31). Because our electrodes were nonmoveable, selective sampling could not bias this ratio. The relatively high ratio of neurons displaying spatially periodic activity has two implications. First, consistent with earlier results (31), neurons in the human EC are able to form neural representations of space in a virtual reality environment induced by a small, handheld display (25.6 cm diagonal and ∼23° horizontal visual field) in the absence of proprioceptive and kinesthetic cues. Second, these neural representations, relying mainly on visual cues, showed adaptive scaling.

The spatial periodicity of neuronal activity was not uniform across all four studied environments. Instead, spatial periodicity systematically decreased with the increasing size of the environments (*SI Appendix*, Fig. S30 *A* and *B*). However, this finding was not confirmed by the gridness of PGCs (*SI Appendix*, Fig. S31 *A* and *B*). Although we could rule out partial coverage as a potentially confounding factor contributing to cells in the OS environment showing less spatial periodicity than in any other environment, other factors, such as the lack of orienting spatial cues or the lack of polarity of the environment (20), might have played a role. We remark that in the absence of orienting distal cues, the grids were less consistently aligned.

Besides gridness, a key factor regarding the effect of the environments on grids is the parameter of grid scale. Although the original report of grid cells in rodents documented scale independence of grids (10), other studies have found an experience-dependent rescaling of grid cells under special conditions, such as in response to distortion of the aspect ratio of a familiar environment (19, 20) and transient rescaling during exposure to a novel environment (18). Similar to the grid transformations brought about by adjusting environments, we observed elastic transformations of grids across environments (Figs. 2 and 3). The EC neurons in both patients investigated over multiple days showed a consistent environment-dependent preservation of grid geometry and orientation over days with small variance, suggesting that each grid type was optimal for the environment it was applied to. We can rule out both effects: the distortion effect, because our subjects were fully aware of the switch between the environments, and the novelty effect, because none of the investigated grid parameters changed over time. However, we cannot rule out the contribution of proprioceptive cues to the scale invariance of grids observed in rodents and the effect of eliminating those cues in the virtual navigation condition.

The second key feature of the observed grids was the preserved orientation of the main grid axis across repeated trials in an environment. These data suggest that, as in rats, human grids utilize cues, such as environment geometry, to anchor grid orientation (20). However, in our virtual navigation task, there were three independent but consistent orienting cues available. The first was the starting orientation of the avatar relative to the walls (*SI Appendix*, Fig. S1*A*), the second was the constant presence of architectural cues (except in the OS environment), and the third was the memory of the environment. The starting orientation of the avatar was the same relative to the *X*–*Y* axes in all environments (*SI Appendix*, Fig. S1*A*), which may have predisposed the grids toward assuming a similar orientation within each environment. In contrast, comparisons between the three enclosed environments showed that average grid orientation in LV differed significantly from average grid orientation in BY and LX (Fig. 4 and *SI Appendix*, Fig. S32). Although grids of SPCs in square-shaped environments aligned with the angle of a 45° orientation, they tended to align at an angle of 33° in a rectangular environment relative to the same cardinal axes (*SI Appendix*, Fig. S1*A*). Because both angles represent the direction toward the corner of the actual environment from the starting position, the difference suggests that the geometry of the environment determines grid orientation rather than the avatar's starting orientation or architectural cues. The environmental dependency of grid orientation is in agreement with studies on rodents showing that grid orientation is aligned with the boundaries of the enclosure (20, 21); however, in contrast to the findings of rodent EC, which minimizes the symmetry of grid angles relative to the walls (21), human EC grids tend to align with the corners of environments.

The third key grid feature we investigated was the rotational symmetry of grids. Studies in rodent EC have described neurons with firing fields organized in periodic bands (11), in addition to cells with canonical hexagonal grids. We quantified the distribution of grid rotational symmetry for neurons from human EC and observed a wide range of symmetries (Fig. 5 *B* and *C*), with a strong negative correlation between the angle of symmetry and environment size (Fig. 5*D*). With a post hoc analysis of balanced environmental coverage, we were able to rule out that the higher prevalence of hexagonal grids in the smallest environment (BY) was only due to the more complete coverage relative to the larger areas of the other environments. Nevertheless, the incomplete coverage might have compromised the interpretation of these factors. Whether the relatively large proportion of noncanonical symmetry observed in our human grid cells compared with the

rodent's grid cells reflects an adaptation to a predominantly Cartesian organization of our human-made environments, or if it is constrained by other physiological mechanisms, is beyond the scope of this study.

On several occasions, we omitted one trial to double the time spent in another environment, which helped to affirm that none of the rescaling effect was due to the limited sampling time and poor spatial coverage. To compensate for the poor spatial coverage and increase our confidence in the sparse sampling of grid-cell activity, one can combine spikes of neurons from the same electrode (*SI Appendix*, Fig. S10) and confirm the hexagonal tessellation on the firing rate maps consistent with rodent, primate, and human studies (10, 26, 31, 38).

Contrary to rats, in which grid fields initially expanded in novel environments (18), all three monitored grid features were stable across 7–8 d and showed no systematic variation over time (Fig. 3 and 4 and *SI Appendix*, Figs. S7*C* and S8*B*). Nodes of spatial periodicity (putative grid vertices) were also stable over time within the same environment during the same session, as illustrated by individual examples of spatial mapping of single-unit activity between the first and fourth segments of a 20-min recording session (*SI Appendix*, Fig. S5 *A–E*). Moreover, the stability and stationarity of grids in the firing rate maps were confirmed at a population level by cross-validation and stationarity analysis that included both SPC and $PGC_{hi\text{-}conf}$ datasets (*SI Appendix*, Fig. S5 *F* and *G*). Consistent with the stability of grid nodes, the environment-dependent scaling and rescaling in our human datasets were instantaneous. We observed no gradual adaptation within each day (*SI Appendix*, Fig. S5) or across days of recordings (Fig. 3*B* and *SI Appendix*, Tables S3.6 and S3.7). The rapid adaptation to environmental parameters suggests a dynamic reconfiguration of neuronal activity consistent with attractor switching (39–41) or oscillatory interference (42–44) models.

The advantage of a visual system in spatial navigation is multifold. First, endowed with a larger visual information-processing capacity with which to assess an environment, humans are able to form a cognitive map or a "survey representation" of their environment without the need for visiting all parts, and adapt grids based on visual spatial cues accordingly. Second, the dimensions of the environments can be ascertained by a few saccadic eye movements prior to physical exploration. Third, considering the complexity and scalability of human environments, humans might rely on extracting information from optic flow more efficiently than rats do, given that there is theoretically sufficient information available from optic flow for grid formation (45). The predominance of visual input in the human brain allows detection and mapping of spatial cues more quickly and may influence grid parameters to a greater degree than is possible in the rat brain (35–37). It might also allow the human hippocampus and EC to perform more naturally in virtual navigation tasks, where proprioceptive and kinesthetic cues are absent (30, 31, 46, 47).

Nevertheless, our results corroborate evidence that a visually cued, active navigation task in a virtual reality environment provides sufficient input to the human EC to elicit spatially coherent localized activity, similar to the spatially coherent localized activity found before in humans (31) and rodents (10, 38, 48). This discovery is intriguing because it occurs despite the conflict between the patient's simulated self-motion and natural vestibular and proprioceptive signals, as well as an awareness of the patient's true location relative to the hospital. As initial evidence of sufficient stimulation, we observed that the baseline activity of EC neurons substantially increased when the patients began playing the game.

Despite the common cellular mechanisms in rodent and human brains, spatial navigation and spatial memory may involve slightly different networks in the human brain. For instance, human subjects are able to perform path integration without the hippocampus and EC (32), except when the navigation involves memory recall of places like in our task. The human EC may also contribute to the formation of declarative/semantic memories or abstract conceptual representations (49) as a part of the mesial temporal lobe that cannot be studied adequately in the rodent brain. With the help of virtual reality (30, 46), our experimental paradigm establishes a common ground to compare neural mechanisms of representing space across different species and to study the evolution of spatial navigation in the mesial temporal lobe in relation to memory and perception of locations and more abstract visual spaces (26). Furthermore, with instructed navigation in virtual reality environments, we will be able to investigate the relationship between memory and anticipation experimentally (50), which is currently unattainable by neuroimaging techniques. We argue that with these experiments, the virtual reality paradigm is not only well-suited for investigating the complex environmental determinants of neuronal representations, including grid formation, but that these complex environmental determinants may also help us to understand the neural representation of spatial, episodic, and semantic memory, which are fundamental aspects of our internal model of reality.

Materials and Methods

Subjects. One female and three male patients with epilepsy (ages: 33–41 y, average age of 38.5 y; *SI Appendix*, Table S1.2), who had previously provided informed consent, were implanted with microelectrode arrays in their EC (Fig. 1*A*) in preparation for surgical resection of epileptic foci. All surgical and experimental procedures were approved by the Seton Institutional Review Board. From two patients (subjects H and K), we could record well-isolated single-unit activity throughout a 7-d period and an 8-d period in the hospital's epilepsy monitoring unit while they performed a virtual navigation task on a tablet computer.

Tasks. The subjects' task was to play a computer game on a tablet they held on their lap. The game's objective was to locate space aliens and return them to their spaceship parking at memorized locations (*SI Appendix, SI Experimental Procedures*). Four different virtual environments were modeled: BY, LV, LX, and OS (Fig. 2 *A* and *B* and *SI Appendix*, Fig. S1). These environments differed in several features, including scenery, size, aspect ratio, and presence of obstacles or boundaries (*SI Appendix, SI Experimental Procedures*, Table S1.1, and Movie S1).

Recordings. Single-unit activity was obtained from five microelectrodes implanted in layers II and III of the medial EC in the right hemisphere. Microelectrodes were integrated or plug-in components of a macroelectrode strip made by Ad-Tech Medical and PMT. The electrode strip was placed and secured by the neurosurgeon at the surface of the EC such that only the blunt tip of microelectrodes penetrated the pia. The wide-band signal was recorded at a sampling frequency of 24 kHz and bandpass-filtered between 300 and 6,000 Hz. Spike sorting was done off-line on the continuous recording (including all environments) using WaveClus software (51) on MATLAB (MathWorks), and spike trains were segmented according to environments later. Only single units with Mahalanobis distances of >20 separations were included.

Analysis of Grid Parameters. Firing rate maps, spatial ACs, and autoperiodograms were computed using standard methods (11). We quantified the gridness scores, grid orientation, and grid rotational symmetry (52, 53) by precisely following the method outlined by Barry et al. (18), Sargolini et al. (54), and Krupic et al. (11) (*SI Appendix, SI Experimental Procedures* and Fig. S3 *A–F*). Grid distance was determined based on the autoperidogram and manually cross-validated with the ACs. To compute confidence intervals for statistical significance of gridness scores, we applied a standard Poisson bootstrap method and shuffled spike times 1,000 times (*SI Appendix*, Fig. S3*G*), as well as theta, alpha, and direction-modulated surrogate spike trains. Validation of spatial periodicity against the by-chance was done using a Monte Carlo method by comparing the spectral modulation depth (*gsp* scores; *SI Appendix, SI Experimental Procedures*) of each AC against the distribution of *gsp* scores of 1,000 randomized ACs generated from mixtures of 2D Gaussians.

If X and Y are the coordinates of the largest peak near the center in the autoperiodogram, the grid distance is defined as the Euclidean distance of the peak from the center: $\lambda = \sqrt{X^2 + Y^2}$. After λ was computed, it was and manually cross-validated with the ACs.

Grid orientations were computed from the autoperiodograms (*SI Appendix, SI Experimental Procedures* and Fig. 1*F*). Given X and Y as the coordinates of

the largest peak on the 2D autoperidogram, the principal orientation (β) is defined as $\beta = \arctan(\frac{X}{Y})$.

The angle of rotational symmetry was defined by the angle (γ) of rotation that maximized the Pearson's correlation between the original and rotated AC [*SI Appendix, SI Experimental Procedures, Quantifying "Gridness" (Gridness Score)*].

Datasets and Statistical Methods. Based on the spatial spectral analysis, gridness scores, and persistence of single-unit activity in different environments, we constructed six datasets: SPC, pSPC, PGC, pPGC, $PGC_{hi\text{-}conf}$, and $pPGC_{hi\text{-}conf}$ (*SI Appendix*, Table S2). To compare gridness scores and grid periods across environments for the SPC, PGC, and $PGC_{hi\text{-}conf}$ datasets, the general linear model ANOVA and its nonparametric version, the Kruskal–Wallis test (MATLAB), were applied. The main factor was the environment (BY, LV, LX, and OS), and the dependent variables were gridness and grid period. For the pSPC, pPGC, and $pPGC_{hi\text{-}conf}$ datasets, ANOVA with repeated measures or its nonparametric version, the Friedman test, was used. To compare grid orientations and grid symmetry between environments, we applied circular ANOVA (Watson–Williams test) on von Mises distributions (53) or the Wheeler–Watson test as an alternative when von Mises distributions did not qualify (55). We performed Rayleigh tests for testing nonuniformity of circular data and Watson's goodness-of-fit test for testing conformity with the von Mises distribution (MATLAB Circular Statistics Toolbox) (53) (*SI Appendix, SI Experimental Procedures*).

ACKNOWLEDGMENTS. We thank Dr. David Darrow for his advice. The study was funded by the Seton Research Award.

1. Tolman EC (1948) Cognitive maps in rats and men. *Psychol Rev* 55:189–208.
2. O'Keefe J, Dostrovsky J (1971) The hippocampus as a spatial map. Preliminary evidence from unit activity in the freely-moving rat. *Brain Res* 34:171–175.
3. Suthana NA, Ekstrom AD, Moshirvaziri S, Knowlton B, Bookheimer SY (2009) Human hippocampal CA1 involvement during allocentric encoding of spatial information. *J Neurosci* 29:10512–10519.
4. Burgess N (2006) Spatial memory: How egocentric and allocentric combine. *Trends Cogn Sci* 10:551–557.
5. Braak H, Braak E (1985) On areas of transition between entorhinal allocortex and temporal isocortex in the human brain. Normal morphology and lamina-specific pathology in Alzheimer's disease. *Acta Neuropathol* 68:325–332.
6. Kunz L, et al. (2015) Reduced grid-cell-like representations in adults at genetic risk for Alzheimer's disease. *Science* 350:430–433.
7. Curia G, et al. (2014) Pathophysiogenesis of mesial temporal lobe epilepsy: Is prevention of damage antiepileptogenic? *Curr Med Chem* 21:663–688.
8. Taube JS, Muller RU, Ranck JB, Jr (1990) Head-direction cells recorded from the postsubiculum in freely moving rats. II. Effects of environmental manipulations. *J Neurosci* 10:436–447.
9. Solstad T, Boccara CN, Kropff E, Moser M-B, Moser EI (2008) Representation of geometric borders in the entorhinal cortex. *Science* 322(5909):1865–1868.
10. Hafting T, Fyhn M, Molden S, Moser M-B, Moser EI (2005) Microstructure of a spatial map in the entorhinal cortex. *Nature* 436:801–806.
11. Krupic J, Burgess N, O'Keefe J (2012) Neural representations of location composed of spatially periodic bands. *Science* 337:853–857.
12. McNaughton BL, Battaglia FP, Jensen O, Moser EI, Moser M-B (2006) Path integration and the neural basis of the 'cognitive map'. *Nat Rev Neurosci* 7:663–678.
13. Fyhn M, Hafting T, Treves A, Moser M-B, Moser EI (2007) Hippocampal remapping and grid realignment in entorhinal cortex. *Nature* 446:190–194.
14. Bostock E, Muller RU, Kubie JL (1991) Experience-dependent modifications of hippocampal place cell firing. *Hippocampus* 1:193–205.
15. Kentros C, et al. (1998) Abolition of long-term stability of new hippocampal place cell maps by NMDA receptor blockade. *Science* 280:2121–2126.
16. Wills TJ, Lever C, Cacucci F, Burgess N, O'Keefe J (2005) Attractor dynamics in the hippocampal representation of the local environment. *Science* 308:873–876.
17. Anderson MI, Jeffery KJ (2003) Heterogeneous modulation of place cell firing by changes in context. *J Neurosci* 23:8827–8835.
18. Barry C, Ginzberg LL, O'Keefe J, Burgess N (2012) Grid cell firing patterns signal environmental novelty by expansion. *Proc Natl Acad Sci USA* 109:17687–17692.
19. Barry C, Hayman R, Burgess N, Jeffery KJ (2007) Experience-dependent rescaling of entorhinal grids. *Nat Neurosci* 10:682–684.
20. Krupic J, Bauza M, Burton S, Barry C, O'Keefe J (2015) Grid cell symmetry is shaped by environmental geometry. *Nature* 518:232–235.
21. Stensola T, Stensola H, Moser M-B, Moser EI (2015) Shearing-induced asymmetry in entorhinal grid cells. *Nature* 518:207–212.
22. Boccara CN, et al. (2010) Grid cells in pre- and parasubiculum. *Nat Neurosci* 13:987–994.
23. Song EY, Kim YB, Kim YH, Jung MW (2005) Role of active movement in place-specific firing of hippocampal neurons. *Hippocampus* 15:8–17.
24. Aghajan ZM, et al. (2014) Impaired spatial selectivity and intact phase precession in two-dimensional virtual reality. *Nat Neurosci* 18:121–128.
25. Suzuki WA, Amaral DG (1994) Perirhinal and parahippocampal cortices of the macaque monkey: cortical afferents. *J Comp Neurol* 350:497–533.
26. Killian NJ, Jutras MJ, Buffalo EA (2012) A map of visual space in the primate entorhinal cortex. *Nature* 491:761–764.
27. Killian NJ, Potter SM, Buffalo EA (2015) Saccade direction encoding in the primate entorhinal cortex during visual exploration. *Proc Natl Acad Sci USA* 112:15743–15748.
28. Hayman R, Verriotis MA, Jovalekic A, Fenton AA, Jeffery KJ (2011) Anisotropic encoding of three-dimensional space by place cells and grid cells. *Nat Neurosci* 14:1182–1188.
29. Las L, Ulanovsky N (2014) *Hippocampal Neurophysiology Across Species–Bookmetrix Analysis* (Springer, Vienna), pp 431–461.
30. Ekstrom AD, et al. (2003) Cellular networks underlying human spatial navigation. *Nature* 425:184–188.
31. Jacobs J, et al. (2013) Direct recordings of grid-like neuronal activity in human spatial navigation. *Nat Neurosci* 16:1188–1190.
32. Shrager Y, Kirwan CB, Squire LR (2008) Neural basis of the cognitive map: Path integration does not require hippocampus or entorhinal cortex. *Proc Natl Acad Sci USA* 105:12034–12038.
33. Navratilova Z, Godfrey KB, McNaughton BL (2016) Grids from bands, or bands from grids? An examination of the effects of single unit contamination on grid cell firing fields. *J Neurophysiol* 115:992–1002.
34. Krupic J, Burgess N, O'Keefe J (2015) Spatially periodic cells are neither formed from grids nor poor isolation. arXiv: 1512.06248. Available at https://arxiv.org/abs/1512.06248. Accessed July 17, 2016.
35. Geva-Sagiv M, Romani S, Las L, Ulanovsky N (2016) Hippocampal global remapping for different sensory modalities in flying bats. *Nat Neurosci* 19:952–958.
36. Hori E, et al. (2005) Place-related neural responses in the monkey hippocampal formation in a virtual space. *Hippocampus* 15:991–996.
37. Miao C, et al. (2015) Hippocampal remapping after partial inactivation of the medial entorhinal cortex. *Neuron* 88:590–603.
38. Fyhn M, Hafting T, Witter MP, Moser EI, Moser M-B (2008) Grid cells in mice. *Hippocampus* 18:1230–1238.
39. Burak Y, Fiete IR (2009) Accurate path integration in continuous attractor network models of grid cells. *PLOS Comput Biol* 5:e1000291.
40. Fuhs MC, Touretzky DS (2006) A spin glass model of path integration in rat medial entorhinal cortex. *J Neurosci* 26:4266–4276.
41. Samsonovich A, McNaughton BL (1997) Path integration and cognitive mapping in a continuous attractor neural network model. *J Neurosci* 17:5900–5920.
42. Burgess N (2008) Grid cells and theta as oscillatory interference: Theory and predictions. *Hippocampus* 18:1157–1174.
43. Nadasdy Z (2009) Information encoding and reconstruction from the phase of action potentials. *Front Syst Neurosci* 3:6.
44. Hasselmo ME, Giocomo LM, Zilli EA (2007) Grid cell firing may arise from interference of theta frequency membrane potential oscillations in single neurons. *Hippocampus* 17:1252–1271.
45. Raudies F, Mingolla E, Hasselmo ME (2012) Modeling the influence of optic flow on grid cell firing in the absence of other cues1. *J Comput Neurosci* 33:475–493.
46. Doeller CF, Barry C, Burgess N (2010) Evidence for grid cells in a human memory network. *Nature* 463:657–661.
47. Török A, Nguyen TP, Kolozsvári O, Buchanan RJ, Nadasdy Z (2014) Reference frames in virtual spatial navigation are viewpoint dependent. *Front Hum Neurosci* 8:646.
48. Moser EI, et al. (2014) Grid cells and cortical representation. *Nat Rev Neurosci* 15:466–481.
49. Constantinescu AO, O'Reilly JX, Behrens TEJ (2016) Organizing conceptual knowledge in humans with a gridlike code. *Science* 352:1464–8.
50. Lisman J, Redish AD (2009) Prediction, sequences and the hippocampus. *Philos Trans R Soc Lond B Biol Sci* 364:1193–1201.
51. Quiroga RQ, Nadasdy Z, Ben-Shaul Y (2004) Unsupervised spike detection and sorting with wavelets and superparamagnetic clustering. *Neural Comput* 16:1661–1687.
52. Hines ML, Morse T, Migliore M, Carnevale NT, Shepherd GM (2004) ModelDB: A database to support computational neuroscience. *J Comput Neurosci* 17:7–11.
53. Berens P (2009) CircStat: A MATLAB toolbox for circular statistics. *J Stat Softw* 31:1–21.
54. Sargolini F, et al. (2006) Conjunctive representation of position, direction, and velocity in entorhinal cortex. *Science* 312:758–762.
55. Mardia KV (1969) On Wheeler and Watson's two-sample test on a circle. *Sankhya Ser A* 31:177–190.

Chapter 5

5. Phase coding and grids

> *"Whatever the case, these diffuse connections may participate in the emergence of dynamic patterns of largely sub-threshold activities, which may modify the supra-threshold functions of the network, by adding some neurons here or subtracting (through inhibition) some other neurons there, to or from the active population. This system of initially sub-threshold patterns, superimposed upon or underlying the conventional operations of the neural connections and networks, might be what makes the difference between the nervous system and even our most sophisticated electronic hardware systems."*
>
> *(Szentágothai, 1978)*

Szentágothai's vision was far ahead of its time. Those words could have been written today as neuroscientists still struggle to make sense of sub-threshold activity.

The premise of the previous two chapters was that the very same property that enables neurons to encode information by the phase of action potentials is the same that endows them with the self-organizing capability to form grid-like spatial representations. If information is encoded by the phase, then we should be able to decode that information from the phase. Hence, if neurons in the medial entorhinal cortex (MEC) encode location, then we should be able to decode the location from the phase. This was the tenet of my 2018 and 2022 papers (Nadasdy et al., 2018, 2022). The experiment involved only two subjects, but those subjects devoted their time to run the experiment in seven and eight sessions on different days to generate sufficiently large datasets.

First, we had to establish a firm methodological ground for recording grid cell activity. That was accomplished by our 2017 PNAS paper (Nadasdy et al, 2017). Second, we had to define the frequency bands that could serve as references for defining the phase of firing. We had two candidates, theta and gamma, based on previous literature (Bragin et al., 1995; Chrobak & Buzsaki, 1998; Colgin et al., 2009; Colgin & Moser, 2010; Fernández-Ruiz et al., 2021; Harris et al., 2003; Hinman et al., 2016; Jensen & Lisman, 2000; Lenck-Santini & Holmes, 2008; Penttonen et al., 1998; Qasim et al., 2021; Senior et al., 2008; Tingley & Buzsáki, 2018; Umbach et al., 2020; Yartsev & Ulanovsky, 2013). Most of the prior research in this field implicated theta because theta provides reproducible correlations with behavior in rodents. However, theta in primates (including humans) is intermittent in contrast with the continuous

theta observed in rodents. It forms bouts rather than a sustained oscillation, and these bouts of theta often align with eye and body movements (Killian et al., 2012; M. Aghajan et al., 2017).

In contrast to theta, the gamma rhythm is continuous, and the gamma phase does not reset on any behavioral events, such as starting or stopping motion (Tallon-Baudry & Bertrand, 1999). We computed spike phases relative to both the theta (2-8 Hz) and slow-gamma (25-45 Hz) LFPs separately and worked with both. It was striking from the beginning that gamma provided a significantly narrower phase tuning of the same action potentials than theta recorded from the same cell. Gamma phases of spikes expressed sharp von Mises distributions with often discrete arms (Zoltan Nadasdy et al., 2022). A methodological innovation key to this project was to color-code the phase of spikes in the 2D plane of navigation. This is a non-trivial task because the trajectory of navigation could be relatively sparse, and it does not cover large parts of the navigable area. We had to partition the area into square shape bins to compute the average phase and variance of spike phases per bin and show both features plus the 2D map in the same figure. Altogether 4 dimensions. Each tile was color-coded according to the mean phase of the spikes relative to theta or gamma. In addition, the inverse variance of phase was represented by the hue of the color. The larger the variance, the darker the color of that tile was. Hence, the bright colors represented phases where the phase was reliably defined across multiple crosses of the same bin. This new type of “phase map” representation revealed the hidden topography of the firing phase structure beyond what can be ascertained from firing rates (Zoltan Nadasdy et al., 2022).

An unanticipated outcome of converting the two-dimensional neuronal activity to phase maps was that a larger proportion of entorhinal cortical neurons exhibited grids with respect to the *phase* than to the firing rate. Could phase be a more reliable feature of the neuronal code than the firing rate? That is an empirical question for future research to address.

Let's take a broader and more distant perspective to understand how neurons encode space by the phase of spikes. Millions of neurons are tracking our position while we move. The three main types of spatially tuned neurons are place cells, head direction cells, and grid cells. While place cells fire at specific spatial locations and head direction cells fire when the head turns in a certain direction (hence the name), grid cells fire at the vertices of a spatially oriented periodic grid, where each class is defined in allocentric coordinates. Let’s focus on the grid cells. Although several theories have been proposed, we do not have a coherent narrative of how this

grid-like coordinate system contributes to encoding our actual location. We addressed this question by recording grid cells from the medial entorhinal cortex of human subjects during navigation in virtual environments. The participants were patients diagnosed with epilepsy performing spatial memory tasks while they were implanted with microelectrodes in the entorhinal cortex to determine the sources of seizures for surgical intervention.

To understand the spatial encoding of grid cells, we correlated the avatar's position with the phase of neuronal activity. Cells in the MEC, in addition to firing at grid positions, temporally align their firing to intrinsic ongoing neuronal oscillations, such as theta (2-8 Hz), and slow gamma (25-45 Hz) oscillations, the two most prevalent oscillations of the LFP spectrum. The phase alignment of spikes with slow gamma is surprisingly precise, as cells tend to fire at specific phases of the oscillation while the subject's avatar traverses between locations. Conspicuously, each cell represents the closed space with ~7 locations on average. We observed that every time the avatar crossed any of those locations, neurons fired action potentials at the same phase relative to the ongoing gamma as they did the last time at the same place. Considering that the paths we take when we navigate are not entirely deterministic as we don't cross the same place at precisely determined times, we don't assume to traverse a specific place in sync with any hypothetical internal neuronal clock either. Rather the opposite: instead of aligning our path with an internal clock, our brain aligns the speed of the internal clock to our location. Assuming that gamma is that clock, the alignment of that clock can be achieved by the modulation of frequency, i.e., by speeding up or slowing down gamma. As a result, the phase of gamma oscillations changes as a function of location. To utilize the information built in the gamma oscillations for self-localization, the gamma phase should topographically be anchored to the environment. Therefore, we must assume a 3D landscape of the gamma field where the X and Y axes represent the two orthogonal directions in the horizontal plane referenced to the environment (virtual or real), and the Z axis represents the phase of gamma (Fig. D6). When we (or the avatar) move across a familiar room, gamma rhythm climbs the phase landscape and makes the neuron fire at the peak positions of the membrane depolarization.

The scenario is a bit different when we record single-unit activity from the brain. We do not have direct access to individual neurons' subthreshold oscillation. However, we can approximate that with the LFP that we typically record from a different electrode. While according to the model, action potentials are aligned with the neuron's subthreshold membrane

oscillation, empirically, they are offset relative to the oscillatory component of the LFP, which is the average of a population of neurons' SMO sampled from a separate electrode. This was also the scenario during our recording of entorhinal cortical neurons in the human brain. Because the single-unit activity and gamma LFP were recorded from separate electrodes, the spikes from other electrodes appeared to coincide with various gamma phases. Despite the spread of phases, the average phases were consistent with the locations the avatar visited. They were expected to be consistent because the phases of local gamma waves were locked to the environment; hence phase was specific to that location, as predicted by the phase coding model (Z Nadasdy, 2009).

That was just a model, but it took years to test it empirically. The testbed was our experiment described in Chapter 4 (Nadasdy et al., 2017b). In these experiments, we recorded entorhinal cortical neuronal activity from the human brain in patients undergoing surgical resection of brain tissue to control seizures. Among the more than 100 macroelectrodes, we implanted a small array of 4 x 4 microelectrodes in the medial entorhinal cortex (MEC) and asked the patients to play a computer game that involved spatial navigation in virtual environments using a tablet computer. One of the 16 microelectrodes was dedicated to recording the LFP, and we used that to extract theta and gamma oscillations. The other 15 electrodes were used to record single-unit activity. By tracking the avatar's trajectory during virtual navigation, we could map the neuronal activity in space, not only in one but across multiple environments. This provided unmatched flexibility in studying the behavior of grid cells under transformations of the environment unattainable in rodent experiments or in real life. We used this paradigm to validate the existence of grid cells in the human brain. This was the second direct electrophysiological evidence for grid cells in the human brain and the first to show that grid cells in the human brain are fundamentally different from those of rodents. These experiments leveraged the unparalleled potential of VR that we also used in our later experiments. For analyzing the contribution of phase coding to the grid cell activity, we returned to the data from our 2017 experiment (Nadasdy et al., 2017b). We showed (1) a precise phase locking between gamma oscillations and spikes and (2) by converting the spike times to the instantaneous phases of ongoing gamma and theta oscillations, we arrived at stable phase maps (Nadasdy et al., 2022). The plots we published (Fig. 1-4) show the topography of phases combined with the variance, hence providing a measure of confidence associated with these phase maps. These phase maps revealed that phase-encoded positions in an allocentric coordinate system and phases were locked to the environment, just like our model predicted.

We took this result one step further and asked: If the coupling between the avatar's location and the grid cell's firing phase is as strong as observed, can we predict the avatar's location based on the phase of firing relative to the gamma oscillation? The gamma reference can be selected arbitrarily because only the relative phase differences matter when changing location. This is exactly what we found. Using a Bayesian decoding model, we could predict the position of the avatar at the upcoming spike with +/- 1 virtual m precision based on the phase probability map (as prior probability). Considering that these cells were not place cells from the hippocampus but grid cells supposedly providing an internal coordinate system, it was surprising that they also contribute to self-localization. Or perhaps that is their primary job, and providing the coordinate system is just a byproduct of encoding location. Let's leave that question open for future research.

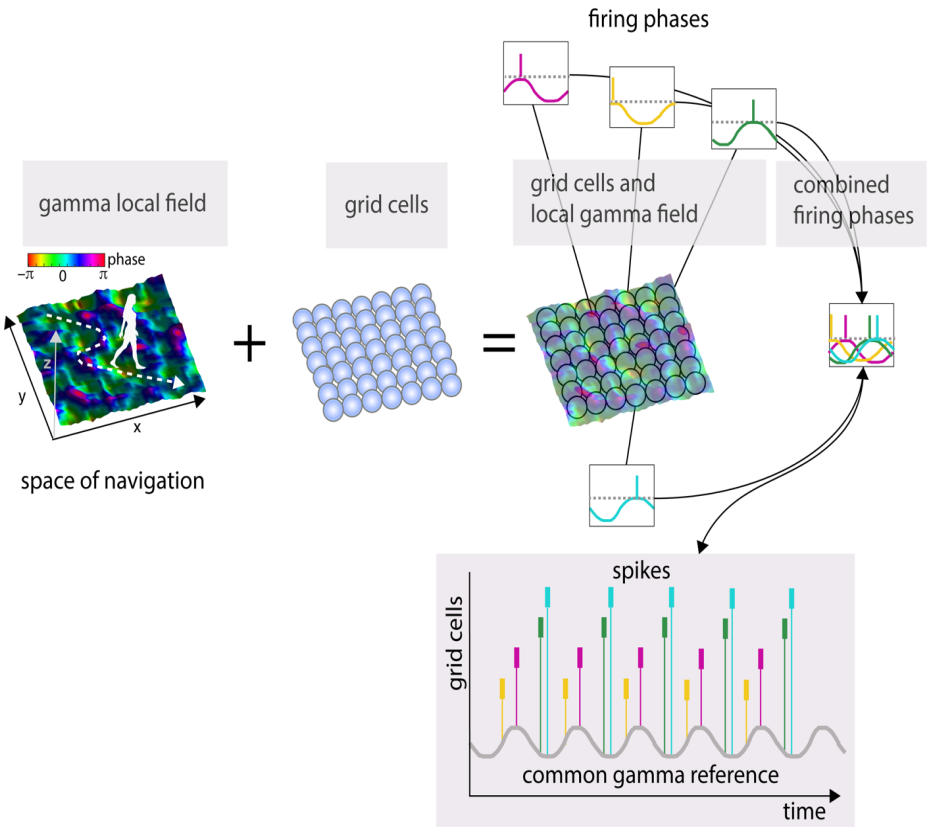

Figure D6. Schematic of the model behind phase of spike encoding location of the avatar in the environment. From left to right: gamma oscillations form a dynamically changing local field in the human EC, which updates the phase as the avatar walks across the field. This field renders the phase of SMO of the grid cells, including those that are activated by the avatar moving across the area. While each grid cell fires at the peak of its SMO, that peak is different from the peaks of LFP recorded from a distant electrode ("common gamma reference"). Hence, relative to the common gamma reference, the phase modulation of cells representing the avatar's position (different colors) enable neurons downstream to decode the position of the avatar solely from the relative phase (not shown).

SCIENCE ADVANCES | RESEARCH ARTICLE

NEUROSCIENCE

Phase coding of spatial representations in the human entorhinal cortex

Zoltan Nadasdy[1,2,3]*, Daniel H. P. Howell[2,4], Ágoston Török[5], T. Peter Nguyen[6], Jason Y. Shen[7,8], Deborah E. Briggs[7,8], Pradeep N. Modur[7,8], Robert J. Buchanan[2,7,9,10]

The grid-like activity pattern of cells in the mammalian entorhinal cortex provides an internal reference frame for allocentric self-localization. The same neurons maintain robust phase couplings with local field oscillations. We found that neurons of the human entorhinal cortex display consistent spatial and temporal phase locking between spikes and slow gamma band local field potentials (LFPs) during virtual navigation. The phase locking maintained an environment-specific map over time. The phase tuning of spikes to the slow gamma band LFP revealed spatially periodic phase grids with environment-dependent scaling and consistent alignment with the environment. Using a Bayesian decoding model, we could predict the avatar's position with near perfect accuracy and, to a lesser extent, that of heading direction as well. These results imply that the phase of spikes relative to spatially modulated gamma oscillations encode allocentric spatial positions. We posit that a joint spatiotemporal phase code can implement the combined neural representation of space and time in the human entorhinal cortex.

INTRODUCTION

The entorhinal cortex (EC) is an integral part of the medial temporal lobe of the mammalian brain and plays a critical role in memory-guided spatial navigation in rodents (*1*, *2*) and in humans (*3*–*6*). Grid cells, border cells, and conjunctive head direction cells in the medial EC (mEC), along with place cells and head direction cells in associated areas of the hippocampus and subiculum, are key cellular constituents of the functional network underlying allocentric spatial navigation and enable individuals to localize themselves relative to the environment (*7*–*9*). However, grid cells, defined on the basis of the grid-like pattern of their firing rate (FR), account for less than 30% of cells in the rodent dorsomedial EC (*2*) and less than 25% in the human EC (*4*, *6*). Those cells in the rodent also include conjunctive cells (*10*). The rest of the neurons (>70%) include head direction cells (58%) (*11*) and time cells (20%) (*10*, *12*). The network of functionally heterogeneous classes of neurons implies a combined spatial-directional-temporal coding scheme to be prevalent at a cellular level in the EC, yet no such unified code has been identified (*13*).

Beside their spatial modulation of FR, mEC neurons also exhibit a robust phase tuning relative to intracellular subthreshold oscillations (*14*, *15*) and local field potentials (LFPs) primarily within two harmonic bands: theta and gamma (*16*). Theta (2 to 12 Hz) and gamma (25 to 60 Hz) oscillations were found to be most prominent during active exploratory behavior and rapid eye movement sleep in rodents (*17*) and intermittent but still prevalent in the human medial temporal lobe during both real and virtual navigation (*3*, *18*–*22*). The spatial periodicity of grid cell activity is also critically dependent on theta band oscillatory drive by the medial septum (*23*, *24*), and inactivation of the septal input was shown to reduce the theta frequency coding of running speed (*25*). On the other hand, gamma frequency communication between the EC and dentate gyrus underlies spatial and object learning (*26*). In addition, theta and gamma tend to phase couple in the rodent and human medial temporal lobe (*27*–*30*), and both gamma-to-theta and spike-to-theta phase coherence are instrumental for encoding and recall (*31*–*33*). Despite the indisputable role of grid cells in the allocentric spatial navigation across the range of mammalian species (*2*, *4*, *6*, *34*, *35*) and the dependency of spatial behavior on theta rhythm, our understanding of the relationship between spatially modulated spike rate, spike phase, and ongoing LFP oscillations during unconstrained two-dimensional (2D) spatial navigation is incomplete, especially in the human brain (*15*, *36*–*40*).

Efforts to model grid cell properties from the combination of spatial and oscillatory features led to the oscillatory interference model, which explained the emergence of equidistant FR nodes, and a further extension of the model hypothesized that the phase of velocity-controlled oscillations relative to the baseline theta rhythm encodes the distance traveled along a specific direction (*41*). Elegantly, the same model explained phase precession (*42*–*44*). Other models posited that spatial information encoded by the spike phase naturally generates spatially distributed periodic activity patterns as a by-product of the inherent ambiguity of decoding locations from phases (*45*). However, neither the predicted phase patterns nor allocentric interference patterns have been observed. The challenge was to integrate the phases of spikes over spatial locations and recover the map of phase modulation in two dimensions over the area of the environment. The 1D approach by mapping the phase of spikes relative to theta component of the LFP while the rat is running in a linear track revealed systematic phase precession in the hippocampus (*46*–*48*) and in the mediolateral EC (*49*, *50*). However, because the neuronal mechanism of phase precession and the role it plays in encoding space are still debated (*51*–*56*), the questions of whether phase coding contributes to the construction of cognitive maps and

[1]Zeto Inc., Santa Clara, CA 95054, USA. [2]Department of Psychology, The University of Texas at Austin at Austin, Austin, TX 78712, USA. [3]Department of Cognitive Psychology, Eötvös Loránd University, 1064 Budapest, Hungary. [4]Department of Neuroscience, The University of Texas at Austin, Austin, TX 78712, USA. [5]Systems and Control Laboratory, Institute for Computer Science and Control, Hungarian Academy of Sciences, 1111 Budapest, Hungary. [6]School of Medicine, Baylor College of Medicine, Houston, TX 77030, USA. [7]Seton Brain and Spine Institute, Austin, TX 78701, USA. [8]Department of Neurology, Dell Medical School, The University of Texas at Austin, Austin, TX 78712, USA. [9]Department of Surgery, Dell Medical School, The University of Texas at Austin, Austin, TX 78712, USA. [10]Department of Psychiatry, Dell Medical School, The University of Texas at Austin, Austin, TX 78712, USA.
*Corresponding author. Email: zoltan@utexas.edu

the specific frequency band of intrinsic oscillation involved in this coding are still open. Despite various reports of decoding the animal's position and heading direction from theta phase precession of hippocampal place cells (*57*, *58*) or the animal's position from the activity of mEC grid cells (*43*, *44*) during unconstrained 2D navigation, the concept of 2D phase maps (i.e., the spatial distribution of phases) across the entire environment previously only existed in simulations (*42*–*44*). Nevertheless, leveraging the theta phase precession using a Bayesian maximum likelihood method afforded moderate decoding performance of the animal's position relative to the center of the place field (*57*) or the head direction of the animal (*58*). The common features of these approaches were, regardless of predicting location or direction of the animal, to hinge the decoding on theta phase precession and place cell activity (*44*, *57*–*59*). On the other hand, previous studies that concerned phase precession in grid cell activity were unable to detect directional or field-specific phase coding (*43*, *44*). A complete empirical 2D reconstruction of phase maps has not been accomplished, neither with respect to theta nor to gamma band LFP.

Since these earlier studies limited the analysis of motion trajectories either by using a linear track (*49*) or by extracting omnidirectional trajectory segments from the 2D navigation (*43*), the location-invariant nature of phase coding remained hypothetical (*45*). Conservation of phase upon unconstrained reentry to a location from different directions, the ultimate proof of phase coding, has not been shown. In addition, earlier experiments did not validate the decoding performance against randomized spike phases dispersed along the actual trajectories to provide an unbiased estimate of decoding. Moreover, although it has long been suggested (*46*), an allocentric 2D spike phase code across a full environment has never been demonstrated, neither in animals nor in humans. Last, none of the previous studies investigated gamma band LFP as a potential reference for phase coding.

Therefore, we investigated the cellular-level phase coding relative to theta and gamma LFP during unconstrained spatial navigation in 2D environments from the human EC. We were able to derive phase maps to decode the avatar's movement from the phase of spikes, validated the phase decoding against randomized phases, and, lastly, compared the decoding performance between spike phases and FR.

Since spikes of mEC neurons maintain high temporal coherence with local theta and gamma oscillations during locomotion (*60*), for the same cells to express grid-like spatial periodicity in the environment, a 2D map of the spike to LFP phase coherence must conform with the spatially periodic topography, similar to the FR grids. Given that single-unit activity of the human mEC expresses grid-like firing patterns (*4*, *6*) and the human EC shows intermittent but robust oscillatory LFP both at theta (*18*, *19*, *32*) and gamma frequency bands (*29*, *30*), we sought evidence of spatially organized phase maps in data recorded from two patients (subjects 1 and 2) performing spatial navigation tasks in four different virtual environments. These environments were a backyard (BY), a courtyard of the Louvre (LV), a model reconstruction of the main hall of the Luxor (LX) Temple in Egypt, and a large open space (OS) with a boundless horizon and minimal external cues. Both patients in our study underwent intracranial monitoring of epileptiform activity in their medial temporal lobe before the surgical resection of the seizure focus. Because theta frequency modulations correlate with running speed in the rodent and the human (*61*–*63*), the walking speed of the avatar in our virtual navigation experiment was set to be constant to eliminate the potential confound of speed affecting the phase of LFP.

RESULTS

Definition of phase maps

Grids of 16 microelectrodes (Fig. 1, A and B) were implanted in the right EC of two previously consented subjects along with different configurations of macroelectrode strips (Table 1). The locations of electrodes were verified by postsurgical magnetic resonance imaging (MRI) and computed tomography (Fig. 1A). We analyzed the single-unit activity (Fig. 1C) from 525 putative neurons isolated with 99% confidence based on their intercluster Mahalanobis distances (*64*) and verified by >5-ms refractoriness of spike times. LFPs were recorded simultaneously from a separate electrode to rule out contamination of LFP by spike waveforms (Fig. 1B). The two subjects performed spatial navigation tasks in four virtual environments for 30 min each day over seven to eight consecutive days, resulting in a total of 2100 data segments (Table 2). Each data segment was associated with 30 min of navigation in four different virtual environments, spending 5 or 10 min in each. The spike phase analysis was focused on the two most prominent frequency bands of the LFP that significantly deviated from the 1/*f* spectral function: 2 to 2 Hz and 25 to 35 Hz (slow gamma). We identified the former as theta and the latter frequency range as slow gamma or gamma for short (Fig. 1D and fig. S1) (*13*). Building on previous findings (*4*, *6*, *13*) of grid cells expressing allocentric spatially periodic firing patterns in humans (Fig. 1, F and G) while maintaining firing phase coherence with LFP [including phase precession (*65*)], we hypothesized that average aggregate spike phases should unravel spatially periodic patterns when resolved in the 2D space of navigation (Fig. 1H). Although our analysis was agnostic to the frequency band of the LFP, the theta and gamma frequency band LFP references generated different maps from the same spike train. To determine the optimal frequency band to serve as reference, we compared the temporal stability of the resulting phase maps between theta and gamma band LFP. Furthermore, we were also aware that spike trains may not reveal consistent phase maps beyond the by-chance joint probability of spatial and temporal patterns.

To determine the phase of spikes, we first bandpass-filtered the wide-band LFP at theta (2 to 12 Hz) and gamma (25 to 35 Hz) frequency bands and then computed the Hilbert transforms of the filtered signals separately (Fig. 1E). The Hilbert transforms of LFP defined the instantaneous phases of spikes relative to theta and gamma band LFP with less than 1° resolution at 1-ms sampling frequency. The 1-ms precise intersections of spike times with the two phase transforms defined two phase vectors converting the spike times to spike phases (ϕ), one vector relative to theta and the other vector relative to gamma, referred herein as gamma phases and theta phases, respectively (Fig. 1E) (*13*). While the distributions of spike phases for most cells were nonuniform, three times as many (19%) neurons expressed deviation from uniform phase distribution relative to gamma as to theta (6.21%) [Fig. 1I and figs. S3 and S6E; $\text{Rayleigh}_{(\text{gamma})} P < 0.05$: 94 of 478 cells or 376 of 1914 epochs; binomial test, $P = 2.3066 \times 10^{-43}$ and $\text{Rayleigh}_{(\text{theta})} P < 0.05$: 23 of 370 cells or 92 of 1480 epochs; binomial test, $P = 0.0274$] and 10 times as many ϕ with $\text{Rayleigh}_{(\text{gamma})} P < 0.01$. Moreover, the average single-unit ϕ, examined individually or combined across electrodes 1 to 4, displayed notable polarization relative to gamma [Figs. 2B, 3 (A to E), and 4 (A to D, third column) and figs. S3 and S9J] but distributed uniformly relative to theta (Figs. 3F and 4E, third column; Rayleigh *P* values are indicated above the circular histograms).

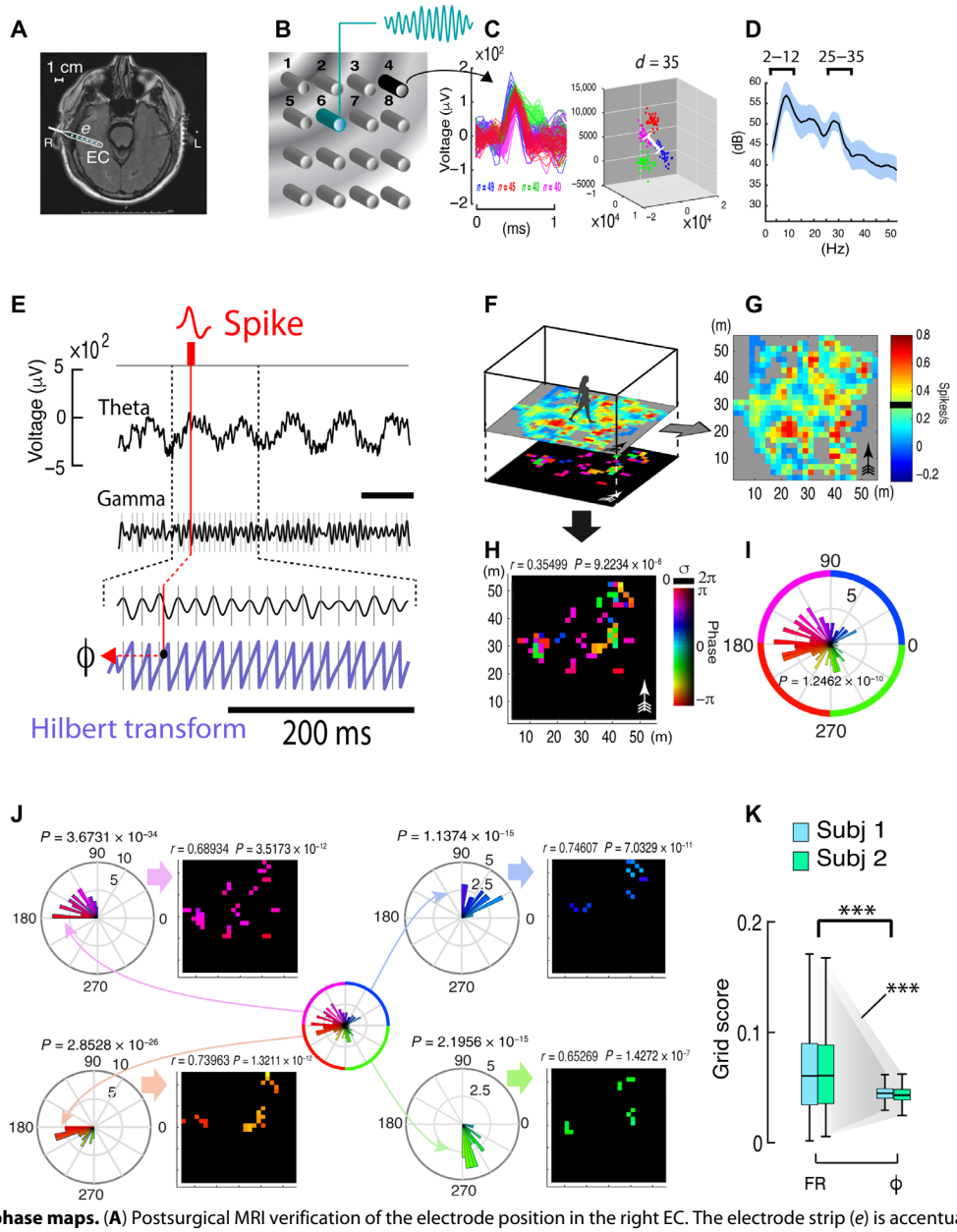

Fig. 1. Construction of phase maps. (**A**) Postsurgical MRI verification of the electrode position in the right EC. The electrode strip (*e*) is accentuated. (**B**) Schematic of the 4 by 4 microelectrode grid (interelectrode spacing is 1 mm). A designated electrode (#6) served as the source of LFP, while other electrodes recorded single-unit activity. Circular waves illustrate propagating gamma waves. (**C**) Spike waveforms and clusters extracted from 20 min of data with the shortest intercluster Mahalanobis distance indicated. (**D**) Average spectral density of LFP sampled at 2 to 50 Hz during a 10-min spatial memory task. The two most prominent frequency components at theta (2 to 12 Hz) and slow gamma (25 to 35 Hz) are labeled (shaded area represents SEM). (**E**) Computation of phase of spikes relative to LFP (1-s data). From the top: spike event, broad-band LFP (bandpass filtered, 0.1 to 300 Hz) displaying theta-modulated gamma oscillations, and gamma LFP (bandpass filtered, 25 to 35 Hz) and its Hilbert transform (purple trace). The phase of a spike is defined by the intersection of spike time (red line) with the Hilbert transform (red arrow) of the bandpass-filtered LFP. (**F**) A 3D representation of the mean FR map overlaid on the mean phase map (bin size = 4 virtual $m̄^2$) and their respective orthogonal views (**G** and **H**). For phase maps, the hue and luminance correspond with mean phase and variance of phase, respectively. (**I**) Radial histogram of spike phases (ϕ) relative to gamma LFP combined and (**J**) separated according the four quadrants of the phase spectrum. The *r* and *P* values correspond to Pearson's correlation coefficients between phase and avatar's trajectory and their significance. (F and J) Plots are based on recording of one cell in one environment. (**K**) Comparisons of grid scores between FRs and gamma phases (ϕ) by combining all data from two subjects (blue and green represent subjects 1 and 2, respectively). ***$P < 0.001$.

To elucidate the spatial distribution of ϕ, we binned the area of each virtual environment into uniform size proportionate square units (.7 by .7, 2 by 2, and 3 by 3 m̄, where m̄ is virtual meter) and computed the circular mean and circular variance of ϕ over the visited units [equivalent of computing the resultant vector of ϕ (*48*)]. By integrating ϕ over the visited areas, we computed a variance-weighted spatial distribution of phases ("phase map" hereinafter) denoted by Φ (Figs. 1H and 2C) (*13*). Moreover, we computed traditional FR maps (Figs. 1G and 2A), phase tuning histograms (Figs. 1I and 2B), maps of mean heading direction denoted by ρ

Table 1. Patients' data, diagnoses, and recording information.

Patient no.	Diagnosis	Symptoms	Hemisphere of seizure origin	Dominant Hemisphere	Electrode implantation	Number of recording days
Subject 1	Multifocal epilepsy due to cavernous angiomas in the right mesial temporal lobe and in the inferior aspect of the right frontal lobe.	Intractable seizures	Right	Left	An array of subdural electrodes over the right convexity temporal lobe and EC. Bilateral hippocampal depth electrodes.	8
Subject 2	Multifocal epilepsy	Intractable seizures	Right	Left	An array of subdural electrodes over the right convexity temporal lobe and EC. Bilateral hippocampal depth electrodes.	7

Table 2. Dimensions and features of the virtual environments. N/A, not applicable.

Environments	Size (m)	Area (m^2)	Bin size (m)	Shape	Boundaries	Obstacle	External cues	Topology (roof)
BY	18 by 18	324	.7 by .7	Square	✓	None	✓	Open
LV	50 by 70	3500	2 by 2	Rectangle	✓	None	✓	Open
LX	52 by 52 by 10	2704	2 by 2	Square	✓	✓	✓	Closed
OS	(70 by 70)*	4900	3 by 3	N/A	None	None	Spaceships	Open

*The OS environment did not have visible boundaries, nevertheless above dimensions apply to the navigable area.

(Fig. 2D), the resultant vector length (RVL) of the heading direction, and the correlation of Φ with heading direction and with RVL from daily navigation sessions for each cell in four different environments (Fig. 2E and fig. S7, fourth column). According to these correlations, most cells expressed strongly nonuniform phase distributions, clustered heading directions to phase relationship (Fig. 2E, "BY" environment, and fig. S7) and occasional dependency of phase ϕ on heading directions ($P_{\chi 2} < 0.0001$; Fig. 2E, "LV" environment; and figs. S7, A and C, and S8, A to E).

Despite the large positional and directional variability of trajectories within and across environments, the Φ phase maps revealed environment-aligned periodic clusters of iso-phase densities with smooth phase transitions between clusters (fig. S11). The stability of iso-phase clusters was tested by cross-validation (fig. S5). The patterns of iso-phase nodes resembled those of grid cell FR maps (*2*). The spatially periodic pattern was prevalent even if the cell's Φ grids did not coregister with the FR grids (Figs. 1, G and H, and 2, A and C). The composition of iso-phase nodes in Φ was consistent with a grid-like pattern expressing a constant spatial shift between Φ nodes after decomposition of ϕ according to phase quadrants (Figs. 1J and 2C and fig. S10, C, E, and F). Moreover, phase grids displayed sharper clusters than FR grids as the variance of grid scores computed from the Φ-values of all cells was significantly smaller than those computed from FR maps [coefficient of variation $CV_{FR-gridmod} = 0.5997$ and $CV_{phase-gridmod} = 0.2623$ and two-way analysis of variance (ANOVA): $F_{subject} = 0.73$, $P_{(1,2094)} = 0.3917$ and $F_{FR,\phi} = 143.02$, $P_{(1,2094)} = 0.00097$; Fig. 1K].

Environment-dependent scaling of phase maps

To examine the environmental dependence of Φ, we calculated the average distance between iso-phase nodes (Fig. 2C) within each environment across the six to nine sessions played per subject and found a monotonic increase of iso-phase distances with the size of environments (Fig. 2, F to H; BY = 5.462 m̄, LX = 15.812 m̄, LV = 18.242 m̄, and OS = 19.119 m̄). Although the FR grids did not necessarily coregister with the iso-phase nodes of Φ, as mentioned earlier (Fig. 2, A to C), the average iso-phase distance and its scaling with the size of the environment were consistent with the FR grid scaling (Fig. 2, F and H) (*6*, *13*). The average iso-phase distance scaled linearly with the size of the environment ($\sqrt{ab}$) [Fig. 2G; subject 1: R^2 (coefficient of determination) = 0.5448, root-mean-square error (RMSE) = 4.711, $f(x) = 0.2835x + 0.669$; subject 2: $R^2 = 0.2026$, RMSE = 7.395, $f(x) = 0.1834x + 3.087$]. The slope of iso-phase grid scaling (0.2835 and 0.1834) was slightly smaller but comparable to the slope of FR grids (subject 1 = 0.4108 and subject 2 = 0.3509; Fig. 2H) (*6*, *13*).

Because of the low FRs of cells (<1 Hz for $n_{[0...1\ Hz]} \geq 80\%$ of cells), most of the EC neurons generated sparse phase maps (Figs. 3, B to E, and 4, B to D; and fig. S4). To increase the spatial coverage of these neurons and unravel the spatial pattern of Φ

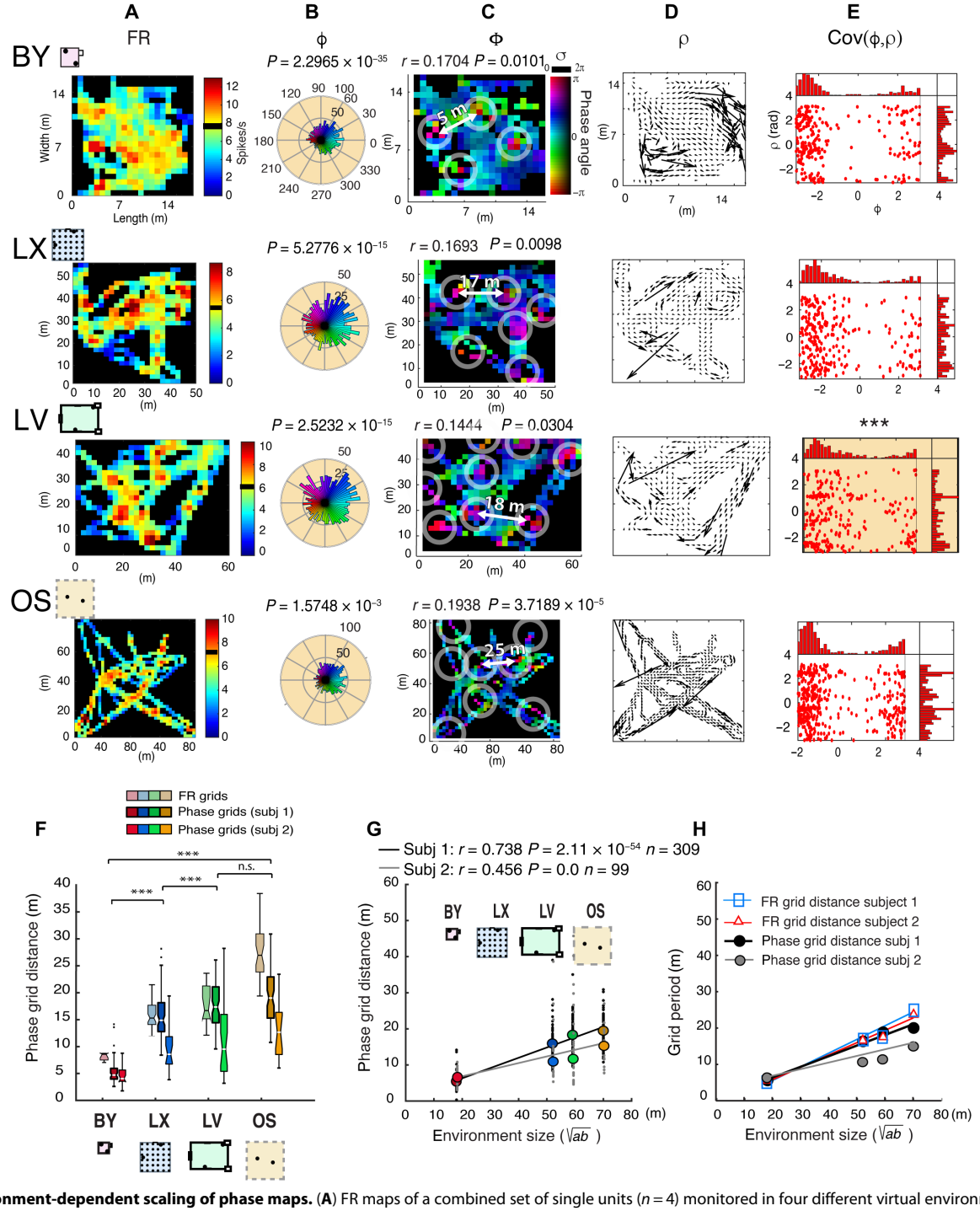

Fig. 2. Environment-dependent scaling of phase maps. (**A**) FR maps of a combined set of single units ($n = 4$) monitored in four different virtual environments (BY, LV, LX, and OS). The axis scaling in virtual meters (m̄) reflects the dimension of environments. Black horizontal lines on scale bars indicate mean FR. (**B**) Polar histograms of gamma phase tuning (ϕ) of combined unit activity per environment. *P* values represent the significances of Rayleigh tests for circular nonuniformity. (**C**) Variance-weighted gamma phase maps (Φ described in Fig. 1). The *r* values represent correlation coefficients between gamma ϕ and RVL of heading, along with the corresponding *P* values. Circles highlight near-π (purple) iso-phase nodes close. Iso-phase distances are indicated. (**D**) Local RVL and ρ of heading directions. Larger arrows represent smaller variance. (**E**) Heading direction (ρ) and gamma ϕ covariance. Red symbols depict the local heading direction ($-\pi <$ dir $< \pi$) as a function of ϕ. Histograms capture the marginal distributions. Asterisks above the plot indicate the nonindependence of phase and heading direction ($\chi^2 = 107.5121$, $P = 0.0005$). (**F**) Comparison of FR grid and Φ grid scaling across environments. The boxplot triplets from left to right represent the distribution of mean distances between FR grid centers and mean distances between iso-phase grid centers for subjects 1 and 2 (boxes represent the median, 25th, and 75th percentile of the data). Color rectangles depict scale proportional layouts of the four environments. (**G**) Phase grid scaling as a function of environment size in virtual meters (m̄) (subjects 1 and 2). Pearson's correlation coefficients between iso-phase distance and environment sizes are indicated. (**H**) Comparison of slopes of the environment-dependent scale functions of Φ relative to FR grids. (A to E) Examples from a single subject in the same day in four different environments. (F to H) Population data from both subjects over all days and environments combined.

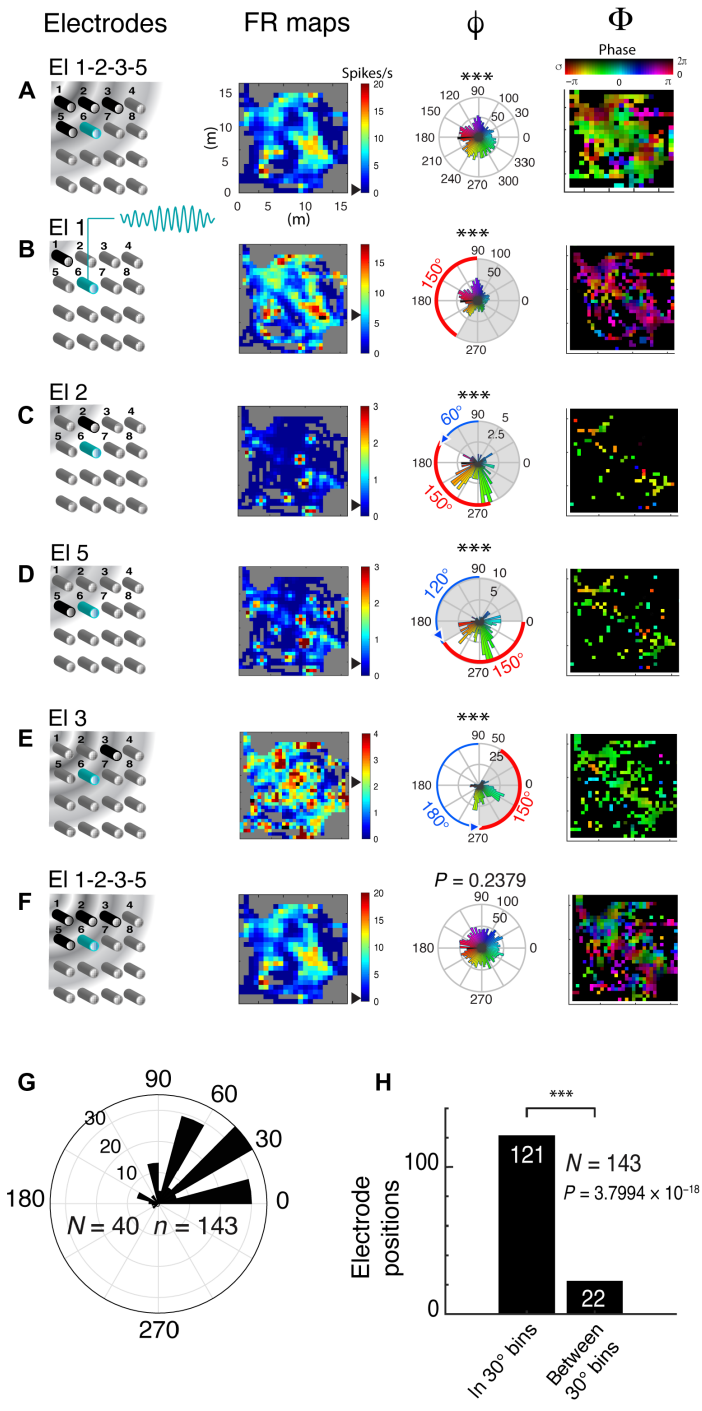

Fig. 3. Dependence of spike phase on electrode position. (**A** to **F**) FR maps and phases of single units grouped by electrodes (examples from a single environment from one subject and 1 day over multiple electrodes). Phases were computed relative to gamma (A to E) and theta (F). (A and F) Spikes combined over four electrodes ($n = 2908$ spikes). (B to E) Units combined over single electrodes. Electrode position varied. First column: Spatial configurations of the microelectrode grid. Gray shading illustrates the theoretical gamma phase difference between electrodes. Second column: FR maps. Arrowheads on scale bars represent average FRs. Third column: Polar histograms of ϕ relative to gamma LFP, except that (F) is relative to theta. Blue angles represent a constant rotation of ϕ between electrodes, and red angles signify the angular span of the phase distribution. Fourth column: Spatial phase maps (Φ) relative to gamma and theta (A to E and F, respectively). Local mean phase and phase variance are represented by colors and darkness, respectively. Asterisks above ϕ indicate the significance of the Rayleigh test of directionality; under ϕ heading represent χ^2 test of phase RVL covariance. (**G**) Summary of phase rotation. Polar histogram represents the interelectrode rotation angles combined over days and sessions from both subjects between electrode pairs. (**H**) Bar chart represents the difference between counts of rotation angles between electrode pairs when the angles fall within bins defined as integer multiples of 30° and between those. *P* value indicates the significance of the binomial test between the two counts. (A to F) Examples from one subject, 1 day, one environment, one electrode, and different units. Spatial dimension of pixels is 0.7 by 0.7 m̄. *P* values of polar histograms under ϕ represent the Rayleigh test of directionality. The polar histograms were binned by 5°, and phase maps and average velocity maps were binned by 0.7 by 0.7 m̄ bins.

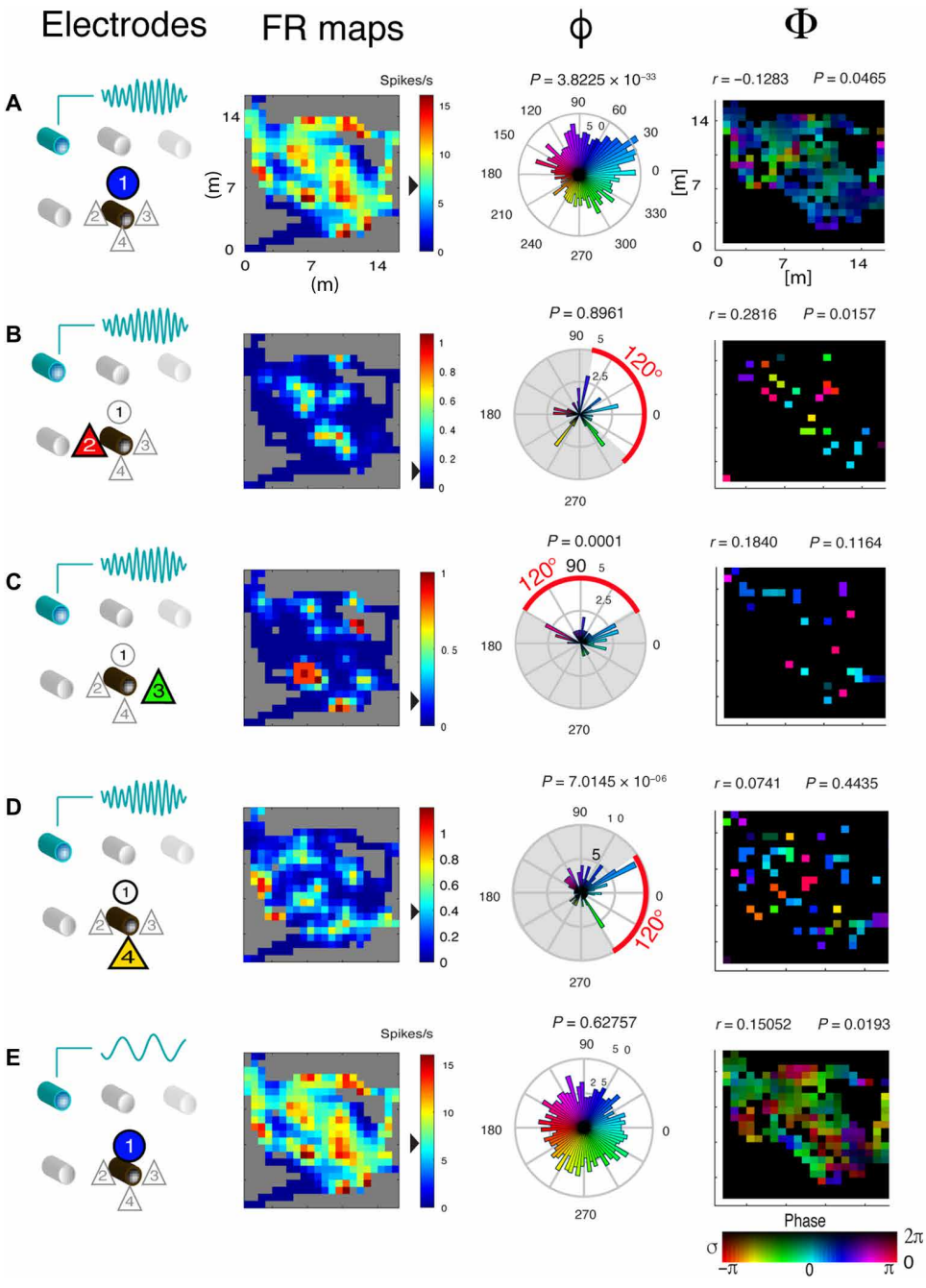

Fig. 4. Dependence of spike phase on single-unit identity. (**A** to **E**) Phase differences across single units isolated from the same electrode with respect to gamma (A to D) and theta (E). First column: Schematics of putative single neurons recorded from 1 of the 16 microwire electrodes. Second to fourth columns: Same as in Fig. 3, except that ϕ and Φ represent the activity of individual neurons isolated from the same electrode. Red angles under ϕ indicate differences in phase between discrete phase tuning modes. Color and darkness in Φ represent phase and variance, respectively, as in Figs. 1 to 3. (All examples were recorded simultaneously from one subject, 1 day, one environment, one electrode, and different units. Same subject and same environment as in Fig. 3 but different day and electrode.) Spatial dimension of pixels is 0.7 by 0.7 m̄. *P* values of polar histograms under ϕ represent the significance of Rayleigh test of directionality. The polar histograms were binned by 5°, and phase maps and average velocity maps were binned by 0.7 by 0.7 $\bar{m}$ bins.

despite low FR units, we merged the spike times of 16 putative neurons (four units from four electrodes) before computing the average phase map that evolved during each 5-min navigation session and compared that with the phase maps of individual single units. The angular distribution of gamma or theta phases ϕ across all spatial locations was typically uniform when combined across all four electrodes during 5-min navigation in a given environment (Rayleigh $P > 0.05$; Fig. 2B and fig. S4A). In contrast, the same set of neurons displayed highly polarized spatial distributions of Φ when the phases were displayed in the 2D area of virtual navigation (Fig. 2C

and fig. S4A, third column), regardless of the choice of LFP reference gamma or theta (Fig. 3, A and F). Whether the topography of the Φ is stable in the given environment or changing over time is crucial for the reliability of allocentric spatial representations. The stability of Φ maps over time and their robustness to spike sampling were tested using two independent cross-validation methods, blockwise and subsampling, each applied to a 5-min interval of game playing (fig. S5, A, B to D, and E to G). The correlations between the subsampled spikes confirmed the stability and robustness of phase maps to spike sampling [Pearson's $r = 0.403$, $P_{(1,359)} < 0.0001$ and $r = 0.239$, $P_{(1,359)} < 0.0001$ for stability and robustness, respectively].

Phase maps are different from by-chance phase coincidences

To test the statistical significance of spatial organization of Φ against by-chance pattern formation and to elucidate the feature that controls the topography of phase maps, we applied two types of surrogate tests: interspike interval (ISI) shuffling and phase permutation of the LFP (fig. S6, A to C). Both types of surrogate spike trains retained the average FR and the original ISI histograms of neurons. At the same time, both methods effectively eliminated any systematic temporal relationship between spikes and LFP. Although the 2D entropy of Φ and its correlation with navigation were immune to the ISI shuffling, entropy increased, and behavioral correlation decreased after phase permutation of LFP (Table 3). The concordance of the two results suggests that the spatial pattern of the LFP phase, as a 2D projection of the collective membrane potential oscillation dynamics, may effectively control the spike timing of grid cells.

Next, we compared the spatial organization of Φ between gamma and theta with respect to entropy, prominence of low spatial frequency components of phase autocorrelograms, and the correlation of phase maps with the avatar's movement directions in space. Although both theta and gamma Φ-values displayed equally high correlations with the avatar's movement directions [Kruskal-Wallis test, $P = 0.4528$, $r_{(\Phi, \mathrm{dir})} > 0.5$, $P_{(\Phi, \mathrm{dir})} > 0.0001$], gamma Φ displayed a significantly higher-order spatial structure (smaller entropy) and larger power in the low-frequency spatial harmonics than theta Φ (Kruskal-Wallis tests, $P_{\chi 2} < 0.0001$; fig. S6D and Table 4).

Phase relationship between distant groups of neurons

In all previous examples, we combined single-unit activity across electrodes to increase the spatial coverage of neuronal activity and elucidate the phase maps in their entirety (fig. S4). However, by doing so, the contribution of single cells to the average phase maps remained obscured by the contribution of the entire cell population. To tease apart the effects of single neurons to the average phase map, we compared Φ across different electrodes and across individual neurons isolated from the same electrode. First, we identified a recording from a single 5-min session of one environment from one subject and day where we could isolate 16 single-unit spike trains from four different electrodes (four neurons per electrode) and investigated the phase composition of ϕ-values and Φ-values by merging the spike trains at the electrode level. The phase was computed relative to gamma and theta LFP, where the LFP was always recorded from a separate electrode to ensure that the phase and frequency of LFP were uncontaminated by the harmonic components of single-unit activity (Fig. 3, A to F, and figs. S7 and S8). When electrodes and units were combined, the ϕ polar histogram displayed a highly nonuniform phase distribution (Rayleigh $P < 0.001$; Fig. 3A). Despite the moderate FR gridness scores ($g = 0.014$, $P > 0.05$), the gamma Φ expressed strong periodicity in alignment with the environment (Fig. 3A). Comparisons of phase differences (β_{ij}) between pairs of electrodes 1 and 2, 1 and 5, and 1 and 3 revealed a rotation series of 60°, 120°, and 180° rotation of phases (Fig. 3, B and C, B to D, and B to E), respectively. Hence, the phase spectrum rotates with 60° increments with every electrode position as the Euclidean distance increases between the electrodes, whereas the 150° span of the phase tuning was invariant to the electrode position (Fig. 3, B to E, and fig. S7, red angles). Notably, the observed phase tuning was specific to gamma band LFP (Rayleigh $P < 0.001$; Fig. 3, A to E). On one hand, the distance-dependent rotation of ϕ suggests a spatially nonlinear but constant interelectrode delay of gamma phases, which is consistent with a propagating gamma fields dynamics (Fig. 3, first column), also evident from the delayed correlation analysis of gamma and theta between electrode pairs (figs. S1 and S2). On the basis of the known interelectrode distance, the angle of phase rotation, and the predefined gamma frequency, the speed estimate of gamma field propagation was between 0.135 and 0.189 mm/ms. To demonstrate that the discrete and constant phase rotation between electrodes was not an isolated example, we combined the phase rotations between pairs of electrodes where the two phase distributions allowed for unambiguous identification of the corresponding peaks and histogrammed them with 15° bins (Fig. 3G). The polar histogram revealed a discrete sequence of angles that represent integer multiples of 30° phase rotations, consistent with the propagation delay between electrode pairs of the evenly spaced multielectrode grid. The interelectrode phase rotations of 30°, 60°, or 90° between electrodes were reproducible across virtual environments, days, and subjects with very few exceptions (binomial test, $P < 0.00001$; Fig. 3H). Moreover, the gamma phase of combined single-unit activity on each electrode expressed a significant dependency on the avatar's heading direction (χ^2 test, $P < 0.05$), but no similar relationship was observed between heading and theta phases (χ^2 test, $P = 0.1157$) (fig. S8F, rightmost column).

Phase relationship between nearby neurons

Next, we examined the contribution of individual neurons to the average phase composition of a group of neurons recorded from the same electrode over a 5-min duration of navigation in one environment (Fig. 4, A to E). Single units were verified by their high isolation coefficients [Mahalanobis distance between nearest clusters $d_{n>50} \geq 20$ corresponds with >99% confidence (*6*, *13*, *64*)] and >5-ms refractory period in their ISI histograms. The second column of fig. S8 represents typical examples of single-unit ϕ-values isolated from a group of neurons simultaneously recorded from the same electrode, each displaying highly polarized phase tuning. The first neuron displayed a strong 30° polarity with relatively high FR (mean = 7 spikes/s, Rayleigh $P < 0.0001$; Fig. 4A, ϕ). The second neuron with low FR (mean = 0.1 spikes/s) displayed five equiangular phases with 72° rotational symmetry (Rayleigh $P = 0.8961$; Fig. 4B, ϕ). Whereas the other two neurons displayed only two components of the pentangular phase tuning, one with 144° and another with 72° between the peaks, both of these neurons' phase tuning histograms were highly polarized (Rayleigh $P \leq 0.0001$), conformed with the fivefold symmetry (Fig. 4, C and D, ϕ and Φ), and retained a precise coregistration with firing phases of all the other cells from this electrode. The highly polarized ϕ, typical of gamma LFP, was in stark contrast with the lack of phase tuning expressed with respect to theta

Table 3. The statistics of surrogate analysis. Nos. 1 and 2 are the difference between original and ISI-permuted dataset and between original and phase-randomized LFP dataset with respect to the correlation between phase and resultant vector length (RVL) of movements. No. 3 represents the medians of data per datasets (from left to right) in the original dataset and the ISI-permuted LFP and phase-permuted LFP datasets separately for subject 1 and subject 2. Nos. 4 and 5 represent the entropy difference between the original and ISI-permuted datasets and between the original and phase-randomized LFP datasets. No. 6 contains the median entropy values of original data and ISI-permuted LFP and phase-permuted LFP datasets. Nos. 7 and 8 represent the statistical difference in the low-frequency power of the 2D spectrum between the original spatial phase and the ISI-permuted phase and between the original spatial phase and phase-randomized LFP phase patterns. No. 9 lists the median power corresponding to the low-frequency power of original and ISI-permuted LFP and phase-randomized LFP datasets.

No.	Test	Variable	*P*	Ha *P* < 0.05	*zval*	*n*	*P*	Ha *P* < 0.05	*zval*	*n*	Supplementary figure
1	Rank sum	PH-VELO-ISI	0.5348	0	−0.6207	910 910	0.8165	0	0.2321	1004 1004	fig. S6A
2	Rank sum	PH-VELO-REVLFP	0	1	10.5241	910 909	0	1	7.8262	1004 1003	fig. S6A
3	Medians		0.4982	0.5046	0.3965		0.5575	0.5586	0.4905		
4	Signed rank	PH-GRID-ENTR-PHGRID-ENTR-ISI	0.7487	0	0.3204	910	0.3619	0	0.9118	1004	fig. S6B
5	Signed rank	PH-GRID-ENTR-PHGRID-ENTR-REVLFP	0	1	−10.51	910	0.0026	1	−3.0143	1004	fig. S6B
6	Medians		0.1544	0.1525	0.1621		0.0923	0.1	0.1015		
7	Signed rank	PH-GRID-POWER-PHGRID-POWER-ISI	0.0072	1	2.6879	697	0	1	11.8777	1004	fig. S6C
8	Signed rank	PH-GRID-POWER-PHGRID-POWER-REVLFP	0.0956	0	1.6668	697	0	1	8.6097	1004	fig. S6C
9	Medians		0.0551	0.0532	0.0544		0.0821	0.0654	0.0708		

Table 4. The Kruskal-Wallis nonparametric ANOVA of theta to gamma phase map comparison. Data from the two subjects were combined. First row: Comparison of spike phase to heading direction correlations between spike phases derived from gamma versus theta oscillations showed no significant difference. Second row: Kruskal-Wallis test comparing gamma and theta phase maps with respect to entropy indicated significantly lower entropy for gamma phase maps. Third row: Kruskal-Wallis test comparing the power of low-frequency components of the 2D spectra between gamma and theta phase maps indicated significantly larger low-frequency power in the gamma phase maps.

No.	Statistics	Theta-gamma	df	*n*	χ^2 test	*P*	Sign	Supplementary figure
1	Kruskal-Wallis	Phase heading *r*	1	3396	0.5637	0.4528		fig. S6D, left
2	Kruskal-Wallis	Entropy *e*	1	3396	24.3	8.24×10^{-7}	***	fig. S6D, middle
3	Kruskal-Wallis	Low-frequency power	1	3396	41.61	1.12×10^{-10}	***	fig. S6D, right

(Fig. 4E). Despite the dispersed spatial scattering, each cell maintained the association of iso-phase nodes with spatial locations relative to the environment (Fig. 4, A to D, **Φ**). Although theta ϕ was homogeneously distributed across the phase spectrum (Rayleigh $P = 0.627$), it displayed a clear dependency on the direction of heading [χ^2 test, $P_{(n = 196)} = 7.3819 \times 10^{-6}$; Fig. 4E, ϕ heading].

In summary, distant groups of neurons show a distance-dependent rotation of their phase spectrum, while the shape of the phase spectrum does not change (Fig. 3, A to E, and fig. S12A). In contrast, individual neurons within the same local assembly display discrete equiangular phase distributions with preserved absolute angle of peaks but different prominence of certain angles (Fig. 4, A to D, and fig. S12B). These two observations suggest that while the absolute phases of the group of neurons cannot encode information, the phase difference between neurons potentially could. If gamma oscillations manifest as traveling waves through the EC, then the absolute phase of spikes has no physiological meaning because it depends on where we measure gamma, except when taking the neuron's own subthreshold gamma oscillation as a reference. However, the relative spike phase differences between neurons are maintained across the

population regardless of the actual phase of the gamma field. Therefore, the next question we address is whether we can decode the spatial information from the relative phase differences between neurons.

Decoding positional information from phase

If the phase of spikes relative to gamma encodes allocentric localization information (position and/or direction), then given that the same gamma oscillation is shared with downstream neurons, it follows that they can decode the avatar's position/direction from the phase itself as precisely as our subjects were able to localize their avatar in the virtual environment. However, because of the spatial periodicity of phase maps, multiple locations can be associated with a given gamma phase. To reduce the ambiguity of localization, our goal was to use the avatar's actual position at a time of the spike for predicting the impending spatial position at the next spike ($x_{\text{spike}i+1}$, $y_{\text{spike}i+1}$) and the heading direction ($\alpha_{\text{spike}i,\ i+1}$) within the neighborhood defined by the 20 forthcoming spikes $x_{k \in i1 \ldots 20}$, $y_{k \in i1 \ldots 20}$ (fig. S13, C to F). Although the decoding was performed relative to the previous spike, both (α) and position (x, y) estimates were computed in environment-referenced, allocentric coordinates (fig. S13, E and F). Following the Bayesian decoding framework, we used the actual position of the avatar at the time of a predicate spike (x_0, y_0), the phase of the next spike ϕ_1, the phase probability map Φ, and the probability of the avatar being at that position $p_{A(x,\ y)}$. The goal of decoding was to predict the position of the subsequent spike (x_1, y_1) from the phase ϕ_1 given Φ and $p_{A(x,\ y)}$. We captured the direction decoding errors in a circular histogram (fig. S13G) and in a form of a confusion matrix (CM) (fig. S13H), comprising the predicted positions or directions as a function of observed positions or heading directions of the avatar, respectively. To increase the spatial density of spikes for reliable spike phase estimates of Φ^{prior}, we combined the spikes across all neurons and electrodes but kept the days and navigation sessions (environments) separate. To ensure that the gamma component of the LFP was uncontaminated by the spikes, we recorded the LFP and the spikes from different electrodes separated by at least 1 mm. For decoding the avatar's position or direction from the phase of spike, we sought to determine the spike with the maximum likelihood arg max ($p(\phi_T \mid x, y)$), where (x, y) was the estimated allocentric coordinate. The tangent of the shortest Euclidean path between successive spike positions relative to the opposite and adjacent walls provided the heading direction as $\alpha = \tan^{-1}(dx/dy)$ of the avatar, where $dx = x_1 - x_0$ and $dy = y_1 - y_0$. We iterated the process for every spike in the test set per session and computed the average CM for each session and day (fig. S13H). The mean decoding error matrices of direction [$\alpha_{(\text{error})}$], positions [x, $y_{(\text{error})}$], and path lengths [$l_{(\text{error})}$] were averaged across environments and days, but the two subjects' data were kept separated (Fig. 5). Correlations between decoded and actual movement parameters including heading direction, position, and path length were all significant (circ $r_{\text{dir}} = 0.347$, $P < 0.001$ and circ $r_{\text{dir}} = 0.332$, $P < 0.001$ for subjects 1 and 2, respectively; $r_{\text{pos}} = 0.838$, $P < 0.001$ and $r_{\text{pos}} = 0.688$, $P < 0.001$ for subjects 1 and 2, respectively; $r_{\text{length}} = 0.714$, $P < 0.001$ and $r_{\text{length}} = 0.625$, $P < 0.001$ for subjects 1 and 2, respectively). Representative decoding performances are illustrated in Fig. 5 (A and B, insets) and fig. S14. Nevertheless, to compensate for the decoding bias deriving from the narrow dispersion of spikes along straight trajectories, we applied two interventions. First, we excluded straight movement trajectories from the analysis by limiting the analysis to $r < 15\ \bar{m}$, where r is the radius of path curvature. Second, we computed a CM [$M_{(\text{Null})}$] using the original spike time data and movement trajectory but shuffled the spike phases across the spikes and subtracted the shuffled phase CM M_{Null} from the observed phase CM M_{obs} for directions [$\alpha_{(\text{error})}$] and for positions x, $y_{(\text{error})}$ separately (Fig. 5, A and B). The corrected CMs retained a near-perfect decoding performance for allocentric positions (Fig. 5B; Pearson's $r_{\text{subj1}} = 0.3220$, $P = 0.005$ and $r_{\text{subj2}} = 0.1957$, $P = 0.0046$, and areas under receiver operating characteristic (ROC) curves for both subjects were above 0.99; Fig. 5D and see fig. S15 for the construction of ROC curves) but partly lost predictability for directions (Fig. 5A; $r_{\text{dir}} = 0.092$, $P = 0.0001$ and $r_{\text{dir}} = 0.037$, $P = 0.120$ for subjects 1 and 2, respectively) as also evident from the differential dispersion of the distributions of CMs. At the same time, the diagonal distribution of the true phase CM was narrower than that of the phase-shuffled Null for data from both subjects (Kolmogorov-Smirnoff test after Benjamini-Hochberg correction for multiple comparisons).

The results deriving from the corrected CMs suggest that position information encoded by phase is accurate within 2 by 2 $\bar{m}$ (Fig. 5B, diagonal histograms), and the likelihood of getting a phase readout by chance at this level of accuracy is $P_{\text{subj1}} = 0.0323$ and $P_{\text{subj2}} = 0.0417$. We conclude that in contrast with the heading direction, the position information of the avatar from the phase of spikes is available to neurons downstream, whether it is used.

Comparing position and direction decoding between phase and FR

To assert whether decoding the phase of spikes has any benefit relative to FRs, we compared the position and direction decoding performances of the gamma phase with the decoding from FR. Since the spatial FR distribution of EC grid cells is also spatially periodic, the Bayesian decoding algorithm that we applied to the gamma phase was applicable to FRs with minor modifications. Because unlike phase, FR is bounded to a frequency range between 0 and the maximum FR of the cell, it had to be z-transformed over the area of navigation before using it for decoding. If FR is just as efficient for encoding positions and directions as the phase of firing, then the decoding performance of spike phase could be accounted for by the topography of spike density as opposed to the spike phase relative to LFP. However, the CMs of FR indicated a moderate yet significant decoding power from FR as compared to the gamma phase for both features, allocentric position and allocentric direction in both subjects' data ($\chi^2_{\text{subj1,dir}} = 1.4339$, $P_{\text{subj1,dir}} = 0.2311$; $r_{\text{subj1,dir}} = 0.1356$, $P_{\text{subj1,dir}} = 2.36 \times 10^{-08}$; $\chi^2_{\text{subj1,pos}} = 8.4044$, $P_{\text{subj1,pos}} = 0.0037$; $r_{\text{subj1,pos}} = 0.0235$, $P_{\text{subj1,dir}} = 0.2399$; $t^{\text{subj1}}_{(\text{TP}-\text{FP})} = 4.2297$, df = 99, $P = 5.2276 \times 10^{-0.5}$; $\chi^2_{\text{subj2,dir}} = 0.09164$, $P_{\text{subj2,dir}} = 0.7621$; $r_{\text{subj2,dir}} = 0.01262$, $P_{subj2,dir} = 0.60496$; $\chi^2_{\text{subj2,pos}} = 23.5638$, $P_{\text{subj2,pos}} = 1.2084 \times 10^{-06}$; $r_{\text{subj2,pos}} = 0.0295$, $P_{\text{subj2,dir}} = 0.1390$; tsta $t^{\text{subj2}}_{(\text{TP}-\text{FP})} = 2.2087$, df = 99, $P = 0.0295$, where TP and FP denote true positive rate and false positive rate, respectively; fig. S16). The areas under ROC curves (AUC) of position decoding from FR for subjects 1 and 2 were $\text{AUC}_{\text{subj1}} = 0.7072$ and $\text{AUC}_{\text{subj2}} = 0.6150$, respectively, smaller than for gamma phase decoding (fig. S16). In summary, FR provided less information about direction and position of the avatar than the Φ.

DISCUSSION

Spike-LFP phase coherence has been extensively studied within (*66*–*68*) and across cortical areas (*69*). A special class of spike-LFP phase coherence, the theta phase precession, has elucidated the intricate interplay between spikes and the theta oscillation observed in the rodent hippocampus and EC during traversing a place field

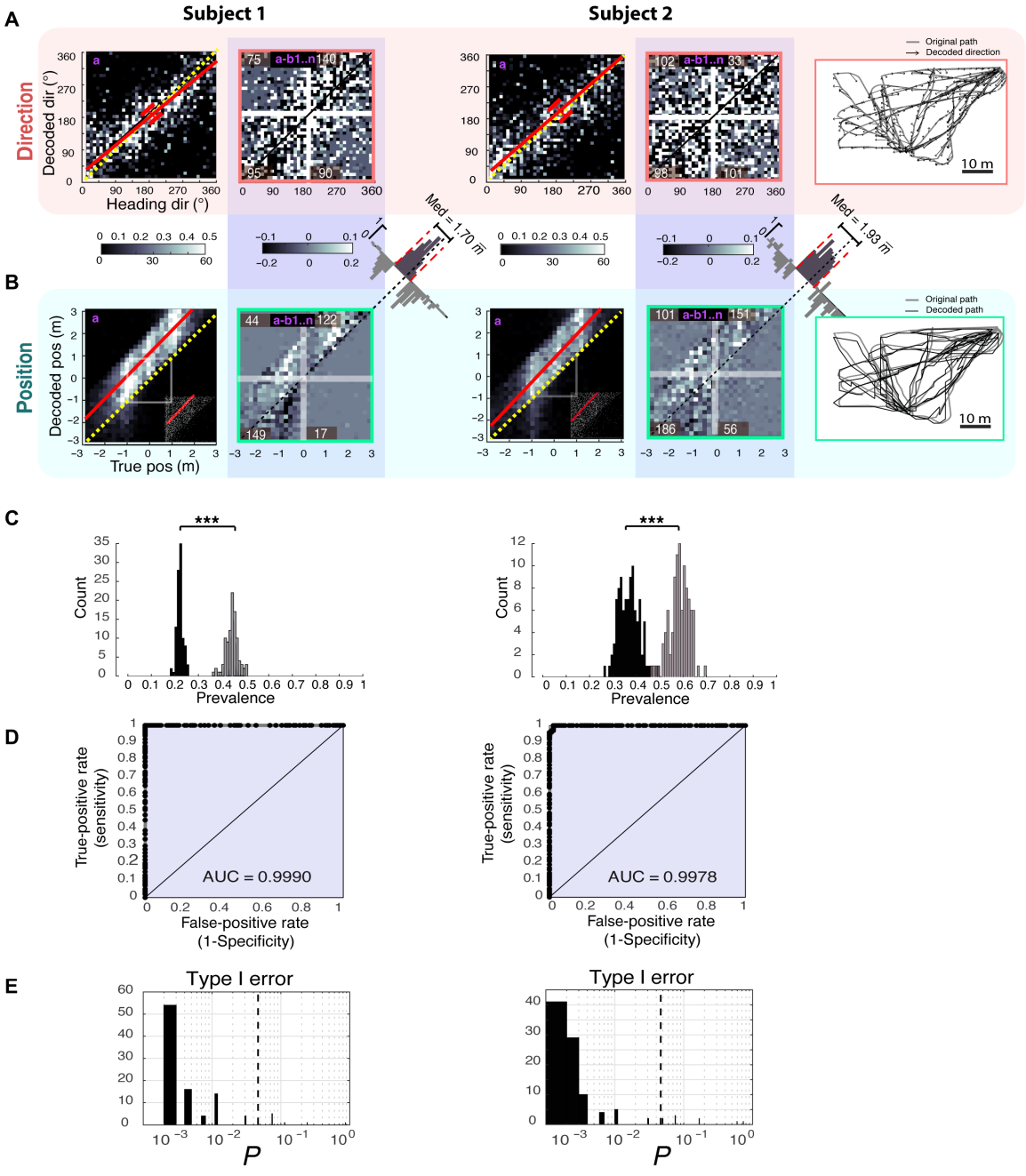

Fig. 5. Bayesian decoding of heading direction and position from the phase of spikes. (**A**) Panels from the left to right are normalized population average of CMs of the decoding of the heading direction before (a) and after trajectory bias correction (a-b), respectively. Left and right blocks represent data (combined across all days, from all environments, and cells) from subjects 1 and 2, respectively. (**B**) Same panels as in (A) except decoding the avatar's position. Possible positions were limited to a 6 by 6 m̄ space. Tilted histograms represent the distributions of position decoding errors (median errors are indicated) with respect to identity lines (dashed line). Insets in (A) represent data points magnified. White numbers are the positive bin counts per quadrant. Trajectory plots at the far right represent single-session examples of direction decoding (top plot) and position decoding (bottom plot). Gray lines are true trajectories, and black arrows and black lines represent the decoded directions and positions, respectively. Examples derived from merging all single units per session in the same environment. (**C**) Histograms show the prevalence of correct position decoding (gray bars) relative to by-chance decoding from phase-shuffled spikes (black bars) for subjects 1 and 2 separately. ***$P < 0.001$. (**D**) ROC curves capture the ratio of spikes correctly decoding the position from phase (true positive) relative to spikes decoding the correct position by chance (false positive). The curve is the aggregate of data points over all experiments grouped by subjects. AUC, area under the curve. (**E**) Distributions of P values of the Kolmogorov-Smirnov tests when comparing the cumulative probability density functions between the observed prediction errors and the errors deriving from 100 shuffled spike phase datasets relative to the identity lines of the CMs. The P values represent the false discovery rate after Benjamini-Hochberg correction. Dashed lines represent the $P = 0.05$ level of confidence.

(*46*, *49*, *70*) as well as in the human hippocampus (*65*). While previous studies have investigated the spike phase within a 1D framework by using linear mazes (*49*), constraining the analysis to omnidirectional passes in open environments (*43*, *71*), analyzing the theta phase during approaching navigational goals (*72*), or predicting trajectories of the animal from 1D theta phase precession of neurons in the CA1 area of the hippocampus and lateral septum (*47*, *48*, *58*), none of these studies extended the scope to reveal the 2D map of spike phase modulation. In contrast, by introducing three manipulations—(i) expressing the same spike phases relative to gamma and theta, (ii) computing the spatial average of phases within 2D environment-aligned bins, and (iii) allowing for 2D navigation—we were able to combine the navigation trajectories into a 2D map and observed grid-like discrete gamma–iso-phase nodes with systematic phase transitions between nodes (Figs. 1, H and J, and 2C and figs. S4 and S11).

By comparing phases of the same spikes when referencing them to gamma versus theta band LFPs, we found that 3 to 10 times as many neurons expressed significant environment-specific phase nonuniformity relative to gamma than to theta (*13*). In addition, gamma phase tuning showed an increased polarization (Figs. 3, A to E, and 4, A to D) relative to theta (Figs. 3F and 4E), and iso-phase node distances in gamma phase were smaller than those constructed from theta (figs. S3, A to D, and S9, E and K), contrary to other approaches focusing only on theta (*18*, *43*, *71*). Not only the gamma phase tuning was more articulated than theta but also the low-frequency components of spatial autocorrelograms computed from gamma phase maps had a larger power than those of theta phase maps. Moreover, the spatial distribution of gamma phase maps, as quantified by entropy, was overall more clustered than that of the theta phase maps (fig. S6, D and E). The enhanced spatial coherence of gamma phase maps relative to the theta phase maps could, at least partly, be accounted to the increased phase variance deriving from the theta phase precession, an explanation that requires further validation.

The third main observation was that the coefficient of variation of population-wide gamma phase modulation was smaller than that of the FR grids' (Fig. 1K), suggesting that the spike phase can encode information under either extremely low or high FR conditions when no grids can be extracted from FRs. This observation was supported by our result showing the immunity of phase maps to ISI shuffling, while the phase randomization of LFP was able to compromise the spike phase maps significantly (fig. S6B) (*13*).

The fourth main observation was that the interelectrode phase shift (Fig. 3, B to E) was consistent with the model of propagating gamma waves (*40*, *67*, *73*), which also can explain why the activities of cells recorded from two adjacent electrodes display a constant phase difference. Moreover, we observed that gamma phases from both multiple neurons recorded from the same electrode and single neurons resulted in discrete multimodal phase distributions (Figs. 3, B to E, and 4, A to D, respectively) (*13*).

Fifth, we demonstrated that both position and direction information can reliably be read out from the phase of spikes (Fig. 5), which raises the intriguing hypothesis that downstream neurons, including pyramidal cells in the hippocampal CA1 and CA3 areas, may be able to decode position and direction information from the phase of action potentials given a shared gamma oscillation, as predicted by the model of gamma phase coding (*45*, *74*).

Last, we showed that gamma phase coding provides a surplus of information relative to the information available from FR alone by comparing the precision by which Bayesian decoding can predict the direction and position of the avatar from FR versus gamma phase (Fig. 5 and fig. S16). We concluded that gamma phase decoding far exceeded the performance of decoding the FR; hence, there must be information contained by the phase that is not available from the FR alone.

The joint representation of direction and location observed in our experiment over the same neuron population is a defining feature of conjunctive cells in layers 3 and 5 of the mEC of the rodent (*75*) with the qualification of head-directional tuning, which should not be confused with the heading direction tuning of phase in our study. However, head direction and heading direction in our experiment were inseparable because the avatar was always facing in the heading direction. Therefore, it is conceivable that a class of grid cells in the human EC also jointly represent direction and location, consistent with reports on goal-specific spike-LFP phase coding found in the human hippocampus relative to theta oscillations (*72*). Although speed was constant in our experiment, location and direction combined with speed could provide a complete positional representation of the agent relative to the navigation space.

In summary, beyond simple phase tuning, we demonstrated a 2D modulation of spike-LFP phase relationship that is (i) periodic in space, (ii) strongest at slow gamma LFP, (iii) persistent, (vi) scales with the environments, (v) allocentric, and (vi) jointly encodes heading direction and relative location. To prove the efficacy of this code, we applied Bayesian decoding on the phases of spikes generated by EC neurons, which demonstrated a reliable readout of positions with a ±1 $\bar{m}$ precision in both x and y dimensions. Given the areas of the mid-size virtual environments (52 by 52 and 50 by 70 $\bar{m}$) and the average seven subdomains within which spike phases uniquely associated with specific locations were observed (i.e., the number of iso-phase nodes), the probability of correctly guessing the location of the impending spike based on the spike phase is less than 0.01, a likelihood worth to consider. To attain this level of confidence, spike phase coding is critically dependent on the frequency and phase of gamma oscillations. On the basis of the dynamic features shared between the human EC neurons and grid cells in the rodent mEC, we posit that the phase of spikes enables the agent to localize itself relative to an allocentric reference frame within the subspace defined by the phase grids with precision exceeding that of FR grids. Whether the two kinds of information encoded by spike phases and FRs are redundant, complementary, or represent disjunct readouts altogether remains to be determined. Regardless of the precise relationship between phase grids and FR grids, the spatial modulation of spike phases by the slow gamma rhythm suggests a new mechanism by which EC acquires stable allocentric representations via the subtle interaction between spiking neurons and the propagating field of gamma oscillation in the human brain.

MATERIALS AND METHODS

Subjects

Two male patients (ages 33 and 40; average, 36 and a half years; Table 1), diagnosed with multifocal epilepsy, were previously consented and implanted with microelectrode arrays in their EC in preparation for surgical resection of epileptic foci. From these two patients (subjects 1 and 2), we could record well-isolated single-unit activity with one channel LFP throughout a 7- and 8-day period in the hospital's epilepsy monitoring unit, while they performed a virtual navigation task that required spatial memory on a tablet computer (Table 1). All surgical and experimental procedures were approved by the Seton Institutional Review Board.

Tasks

The subjects were asked to play a computer game on a tablet they held on their lap. The game's objective was to locate randomly dispersed space aliens in four different environments and return them to preassigned spaceships parking at memorized locations. The four virtual environments included a BY, a courtyard of the LV, a model reconstruction of the main hall of the LX Temple in Egypt, and a large OS with a boundless horizon and minimal external cues (*6*). These environments differed in several features, including scenery, size, aspect ratio, and presence of obstacles or boundaries (Table 2). The virtual reality environments were designed using Unity 3D (version 3.5.6) and were compiled for Android 4.0. The game rendered the 3D environment from the player's point of view. The player was constrained to the flat ground surface of each map, and their movement speed was a constant 5 m̄/s, unless the "GO" button was released or an obstacle inhibited the movement.

Game control

The task was performed on a tablet PC (ASUS Transformer 201 running Android 4.0 at 1280 by 800–pixel resolution). Subjects maneuvered by pressing a GO button with their left thumb and controlled the direction by pressing either a "LEFT" or "RIGHT" button with their right thumb. Before experimental data were collected, subjects were allowed to practice playing the game until they were accustomed to the game controls. The subjects' virtual trajectory and heading (relative to the north-south axis in each game environment) were recorded (*6*, *13*).

Implementation of the task

Our subjects performed virtual spatial navigation tasks implemented as video games using a tablet computer, for a 5- or 10-min duration per game in four different environments (see the "Tasks" section), a total of 40 min/day. The four environments differed in size, geometry, architecture, indoor, outdoor space, and the richness of spatial landmarks (*6*). The subjects viewed these scenes from the first-person point of view (further referred to as the "avatar's view"). The avatar's movement was controlled by touch screen buttons, allowing movement controls of advancing along a straight or a curved trajectory by pressing GO and/or LEFT or RIGHT buttons at the same time, respectively. The touch screen control enabled also stopping (when not pressing GO) and turning while stopping. The avatar moved by emulating real walking with a constant step size and a constant speed of 1.4 m̄/s, where m̄ denotes for virtual meter. The objective of the game was to locate randomly placed space aliens, pick them up one by one, and deliver them to one of the two spaceships parked at constant locations within the space. The game program kept track of the avatar's movements with a 16-ms sampling rate synchronized with the display frame rate. The pickup and delivery of a space alien were displayed on the screen giving continuous feedback to the subject on his/her performance. We motivated the subjects to exceed his/her last day's performance. Our subjects were able to complete as many as 50 space alien deliveries per day, with an average of 2 space aliens/min (*6*, *13*).

Synchronizing spatial navigation with neuronal data logging

The subjects' navigation data, recorded on the tablet, was associated with the neuronal data by sending a 25-ms duration frequency-modulated waveform from the tablet's audio output port to the analog auxiliary input port of the data acquisition system each time the "START" button for the game was released and periodically afterward. The precision of data synchronization between the tablet and the neuronal data logging was <2 ms (SD, 1 ms). This resulted in a spatial localization error of less than 2.5-cm virtual distance (<0.048% of average map width) (*6*, *13*).

Surgical procedures and electrode implantation and explantation

We recorded wide-band signals from no deeper than layers 2 and 3 (given the <0.8-mm tissue penetration and the average 5-mm cortical thickness of human EC, although lacking histological verification) of the mEC. Ad-Tech macro/micro subdural electrodes (catalog code: CMMS-22PX-F478), custom made per our specifications, were surgically implanted in the right hemisphere of two patients. The macro/microelectrode assembly consisted of six macroelectrodes and 16 microelectrode wires arranged in a 4 by 4 grid between the macroelectrodes. The microelectrodes were made of 35-μm platinum-iridium wires arranged in a 4 by 4 wire grid with 1-mm spacing between nearest electrodes. Electrodes were cut to 0.8 mm in length from the electrode base and with a nominal impedance of <3 megohm. Craniotomy and electrode implantation were performed under general anesthesia. After craniotomy, the electrodes were inserted subdurally to the surface of the EC by the neurosurgeon with stereotactic control. The dura was hermetically closed in a watertight fashion, and the bone flap was reattached. The patient remained in the hospital intensive care unit under continuous epilepsy monitoring for 5 to 14 days following the surgery. After sufficient evidence for seizure origin had been collected, electrode explantation and surgical resection of the seizure foci were performed under general anesthesia (*6*, *13*).

Recording neuronal data

Simultaneous single-unit activity was obtained from 5 of 16 microelectrodes at 24-kHz sampling frequency using an FHC Guideline 4000 system, a Food and Drug Administration–approved amplifier for neuronal data acquisition in the human brain. The five electrodes varied across the days and were selected before the recording session based on the largest amplitude and most promising single-unit isolation. The 5- or 10-min traces were bandpass-filtered (300 to 6000 Hz) using a noncausal elliptic filter offline. Because we selected 5 of 16 electrodes with the highest unit activity each day before data logging, we are unable to claim the identity of single units across different days. Simultaneous LFP was sampled from all the five electrodes filtered digitally by a noncausal filter ("filtfilt" function in MATLAB) between 1 and 300 Hz (*6*, *13*).

Spike detection

We applied Wave_clus offline spike detection and spike sorting (*76*). Spike detection was followed by isolation of single-unit activity using an unsupervised spike-sorting method. For spike detection, we applied a threshold fitted to the median SD of the data (Eq. 1)

$$\mathrm{Thr} = 4\sigma_n; \sigma_n = \mathrm{median}\left\{\frac{|x|}{0.6745}\right\} \quad (1)$$

where x is the bandpass-filtered signal and σ_n is an estimate of the SD of the background noise. In cases when the amplitude threshold did not provide a clear separation between single and multiunit activity, the multiunit activity generated a large "noise

cluster" in the wavelet coefficient space at near-zero amplitude. This isolated noise cluster enabled us to separate single-unit clusters from noise with high confidence. We only included single-unit activity in our dataset if it was separated from the noise cluster by $d > 20$, where d is the Mahalanobis distance (*6*, *13*).

Spike sorting

Spikes different from noise were sorted using the WaveClus method that uses superparamagnetic clustering as a nonparametric classifying engine (*76*). WaveClus is the second most popular semisupervised method worldwide, used by more than 110 publications, and the most efficient among the bench-marked spike sorting methods (*77*). The wavelet transform is defined as the convolution between the signal $x(t)$ and a Haar wavelet functions $\psi_{a,b}(t)$

$$W\psi X(a,b) = x(t) \mid \psi_{a,b}(t) \tag{2}$$

where $\psi_{a,b}(t)$ is dilated (contracted) and shifted versions of a unique wavelet function $\psi(t)$

$$\psi_{a,b}(t) = \mid a \mid^{\frac{1}{2}} \psi\left(\frac{t-b}{a}\right) \tag{3}$$

where a and b are the scale and translation parameters, respectively. Last, we obtained 12 wavelet coefficients and reduced those to four dimensions with the highest multimodality and deviation from normal distribution. These were the dimensions best discriminating the spikes in wavelet coefficient space. Each spike was associated with a combination of these k most informative wavelet coefficients and hence represented by a point in the k-dimensional space. The data using superparamagnetic clustering resulted in clusters associated with spikes of similar waveforms, where $k = 12$ for all present datasets. The spike times of classified waveforms were tested against 4-ms refractoriness before being associated with putative neurons. We only included neurons where the Mahalanobis distance between the centroid of the noise cluster and the elements of a single-unit cluster or between the centroid of a given single-unit cluster and the elements of another cluster was $d > 20$. We refer to these single-unit clusters as the activity of putative "neurons" (Fig. 1A). Spike times were rounded to the nearest 1-ms interval and expressed in 1-ms precision (*6*, *13*).

Computational methods

Characterizing the avatar's movement in space

The subject's task in the game was to navigate the avatar to pick up randomly displaced space aliens and reach memorized targets with them. During the navigation, some areas were visited more often than others, resulting in an inhomogeneous distribution of sampling of the environment. The $\bar{v}_{(x,y)}$ expressed the distribution of direction crossing at (x,y) area of the environment. The map of directions $\bar{v}_{(x,y)}$ and the RVL ($\sigma\bar{v}_{(x,y)}$) quantified the avatar's movement in four dimensions as the X-Y location, the mean heading direction $\bar{v}_{(x,y)}$ (angle), and the RVL of heading direction $1/\sigma\bar{v}_{(x,y)}$ (the inverse of the variance of directions), given that the avatar was moving with a constant speed. The mean heading direction quantified the angular mean direction of all pathways taken by crossing a unit area regardless of the uniformity of directions, whereas the RVL quantified the unidirectionality of those crosses (*6*, *13*).

Computing heading direction and resultant vectors

The X-Y coordinates of the avatar's movements and heading directions in the environments were up-sampled to 1 kHz by cubic spline interpolation to match with the temporal resolution of neuronal data. Data synchronization was achieved through audio trigger pulses generated by the tablet and recorded through an analog auxiliary input of the data acquisition computer [for method details, see (*6*)]. From the positions and facing directions (in angular degrees), we constructed a probability density of visits over each unit area of an environment during each game. For the construction of these maps, we divided each environment uniformly by a square grid that was proportional to the size of environments (0.7 m̄ by 0.7 m̄ for the small BY, 2 m by 2 m for the large LX and LV, and 3 m by 3 m for the largest OS environments). Next, we determined the total amount of time spent in each square area, the number of crossings in that area, the circular mean direction of movement $\bar{\omega}_k$ from a set of vectors representing the avatar passing through at a given ij unit area, and the resultant vector of all passes. The length of the resultant vector served as an estimate of the consistency of heading directions over an area. Conversely, the inverse of the RVL described the variance of directions of passing. The average direction $\bar{\omega}_{ij} = 1/N\sum_{k=1}^{N}\omega_k$ was defined as the mean direction of vectors at a given unit area. The mean direction informed us how stereotypical the view was from that location, and the RVL informed us directly about the variance of the directions the avatar took by crossing the place. Given the average constant speed of the avatar, a small resultant vector m_{ij} indicated a large variance of directions, while large m_{ij} implied consistent directions. Direction and resultant vectors were all normalized by the number of vectors in the area. Four types of correlations with phase of spikes were computed: (i) circular correlation between phase angles and motion direction angles (*78*), (ii) circular to linear correlation between the spike phases and RVL, (iii) independence of spike phase and motion direction distributions vectors using χ^2 tests, and (iv) independence of spike phase and RVL distributions using χ^2 tests (*6*, *13*).

Circular to linear correlation between spike phase and movement resultant vectors

To correlate the average neuronal activity (FRs or spike phases) with movement parameters (heading direction or resultant vector) at any spatial location, we counted the spikes and trajectory segments over small areas each environment was divided into. All trajectory segments crossing a given area were aggregated, and average direction and resultant vectors were computed. Likewise, all spikes within that area were aggregated, and the mean circular phase of spikes was computed. Next, we computed the correlation between mean spike phases and the RVL as circular to linear correlation (*78*). If our data consist of n pairs of movement velocity (m_{11}, m_{12}, m_{1n}) and spike phase angle (a_{21}, a_{22}, a_{2n}), then the circular correlation is defined (*79*).

$$r_c l = \frac{\sum_{k=1}^{n}(\sin(\bar{\omega}_{1k}) - m_{1,1})(\sin(\bar{\omega}_{2k}) - m_{2,1})}{\sqrt{\sum_{k=1}^{n}(\sin^2(\bar{\omega}_{1k}) - m_{1,1})(\sin^2(\bar{\omega}_{2k}) - m_{2,1})}} \tag{4}$$

Correlation between movement direction and spike phase

Let assume our data consist of n pairs of movement angular velocity (ω_{11}, ω_{12}, ω_{1n}) and spike phase angle (ω_{21}, ω_{22}, ω_{2n}). The circular correlation is defined (*79*, *80*).

$$r_c = \frac{\sum_{k=1}^{n} \sin(\bar{\omega}_{1k} - \Omega_{1,1}) \sin(\bar{\omega}_{2k} - \Omega_{2,1})}{\sqrt{\sum_{k=1}^{n} \sin^2(\bar{\omega}_{1k} - \Omega_{1,1}) \sin^2(\bar{\omega}_{2k} - \Omega_{2,1})}} \quad (5)$$

where $\Omega_{1,1}$ and $\Omega_{2,1}$ are the grand mean direction of the movements and spike phases, respectively. The estimated P value associated with the correlation is based on the assumption that z_r is distributed as standard normal

$$z_r = r_c \sqrt{\frac{n \lambda_{20} \lambda_{02}}{\lambda_{22}}} \quad (6)$$

and

$$\lambda_{ij} = \frac{1}{n} \sum_{k=1}^{n} \sin^i(a_{1k} - T_{1,1}) \sin^j(a_{2k} - T_{2,1}) \quad (7)$$

where $T_{1,1}$ and $T_{2,1}$ denote appropriate angular sample means.

Binning the space for FR maps and phase maps

To elucidate the spatial aspect of spike phase (ϕ), the navigation arena was divided into uniformly sized (1 m by 1 m, 2 m by 2 m, or 3 m by 3 m) squares (unit areas) proportional to the total area of the environment. The size of the unit area did not influence the results within a range of 0.5 m by 0.5 m to 3 m by 3 m (*6*). For each of those areas, we determined the times of visiting and the number of spikes generated inside the area. The computation of FR maps and phase maps is described in the "Computing spike to LFP phase" and "Spatial FR maps" sections, respectively (*13*).

Computing 2D entropy

Instead of using traditional grid-score metrics (*81*, *82*), we used entropy for comparing phase maps of original spike trains with surrogate spike and LFP processes [(*13*). The advantage of entropy over gridness is that it is (i) more general than gridness; (ii) less sensitive to specific features such as rotational symmetry; (iii) agnostic to the grid distance and rotation symmetry unlike gridness, while it is still sensitive to the periodic structure of the 2D image; and (iv) easy to interpret and straightforward to compute. If $p(z_i)$ is the gray-level histogram of the phase map, then the entropy of the image is (*83*)

$$e - \sum p(z_i) \log_2 p(z_i) \quad (8)$$

Analysis of grid parameters

FR maps, spatial autocorrelograms (ACs), and autoperiodograms were computed using standard methods (*6*, *75*, *81*, *82*, *84*). We quantified grid scores by precisely following the method outlined by Barry and Bush (*81*), Sargolini *et al.* (*75*), and Krupic *et al.* (*82*). Grid distance was determined on the basis of the autoperiodogram and manually cross-validated with the ACs. To compute the confidence intervals for statistical significance of gridness scores, we applied a standard Poisson bootstrap method and shuffled spike times 1000 times (not to be confused with the method of generating surrogate spike trains for phase maps in the "Generating surrogate spike trains" section). Validation of spatial periodicity against the by-chance was done using a Monte Carlo method by comparing the spectral modulation depth of each AC against the distribution of gridness scores of 1000 randomized AC generated from mixtures of 2D Gaussian distributions (*6*, *13*).

Computing the FR grid period (grid distance)

Grid period is the wavelength of the spatially periodic single-unit activity. It is equivalent with distance between adjacent nodes of the AC. Since ACs are periodic by construction, this spatial wavelength is defined as the inverse of the predominant spatial frequency component and could also be measured by hand as the average grid distance (*2*). Grid distances were measured following the method outlined in Nadasdy *et al.* (*6*). Briefly, after the removal of the central peak from the AC (nonspecific to the spatial pattern), we computed the 2D spectral density of the ACs by taking the complex conjugate of the inverse 2D Fourier transform (*82*). We next averaged the 2D spectral distribution across the X and Y coordinates and determined the largest amplitude peak positions. The peak position corresponds to the predominant spatial frequency component of the grid. This method was chosen because it is more precise and less biased than measuring the distance between the nodes by hand. Dividing the dimensions of the AC by the spatial frequency provided the distance of the X-Y peak in spatial bins. We then computed the Euclidean distance of the peak (defined by its X and Y coordinates) from the origin, the center of the autoperiodogram. This distance was multiplied by the scalar bin size (in meters) to give the main grid period λ. Grid frequencies were computed for ACs generated by each neuron and compared between environments. Not to confuse the FR grid distance with the "grid phase node distances" (described in the "Computing grid iso-phase node distance" section) (*6*, *13*).

Computing grid iso-phase node distance

In the lack of a standard method for quantifying the spatial distribution of spike phases projected onto a 2D plane, we applied a manual method. First, we plotted the color-coded phase maps for every single unit that exceeded an average FR of 1 Hz, providing $n \geq 300$ spikes during a 5-min navigation session. The justification for the 1-Hz FR threshold was empirical, as it provided the sufficient coverage for generating continuous phase gradients and discernible iso-phase nodes, i.e., areas where the same phase repeats. We calibrated each phase map according to the size of the virtual environment and digitized the position of iso-phase nodes relative to the edges of the environment. Defining iso-phase nodes started with dividing the phase spectrum to four equal segments (1° to 90°, 91° to 180°, 181° to 270°, and 271° to 360°) corresponding roughly to blue, red, yellow, and green colors of the hue, saturation, value (HSV) color map. Next, we asked unbiased volunteers to mark the centroids of areas on the phase maps where one of the four colors is represented by at least three connected pixels and enter the coordinates into separate spreadsheets. To avoid a bias, the volunteers were blinded to the purpose of the study and the goal of measurements. Once the phase maps were digitized, we computed the Euclidean distances between each node (N) of the same color and determined the inter node distances between them. The total number of distances within an iso-phase node graph is $N = \frac{n*(n-1)}{2}$. Next, we constructed the distribution of these distances. For a periodic graph, the distribution of internode distances formed several prominent peaks with subharmonics. The first peak in the distribution provided the average nearest neighbor internode distance [$\bar{d}$; the mean of $\bar{d}$ across the four phase ranges (color) was used to express the iso-phase distance ($\bar{D}$)] (*13*).

Datasets and statistical methods

To compare grid scores and grid periods across environments, the general linear model ANOVA and its nonparametric version the Kruskal-Wallis test (MATLAB, MathWorks, Nattick, MA) were applied. The main factor was the environment (BY, LV, LX, and OS),

and the dependent variables were grid period and phase internode distance (*6*, *13*). We performed Rayleigh tests for testing nonuniformity of circular data and Watson's goodness of fit test for testing conformity with the von Mises distribution [MATLAB Circular Statistics Toolbox (*78*)].

Processing LFPs

Wide-band signals were recorded from all five electrodes, but we computed the phase of single-unit activity relative to the LFP from only a single dedicated electrode, referred to as El 5. For this electrode, we down-sampled the original wide-band recording from 24 to 1 kHz and digitally filtered the LFP between 1 and 300 Hz for broad spectrum overview using a noncausal, zero phase digital filter implemented in MATLAB as filtfilt (www.mathworks.com/help/signal/ref/filtfilt.html). LFP was then further filtered at specific frequency bands by also using filtfilt for theta (2 to 12 Hz) and gamma (25 to 35 Hz). These frequency intervals were determined on the basis of the prominent frequencies of the fast Fourier transform (FFT) (Fig. 1B). We selected epochs for the phase analysis when the spectral density function at theta or gamma band deviated by ± 2 standard deviations from the 1/*f* regression. Hence, the number of epochs included in the theta and gamma phase analysis differed (*13*).

Computing spike to LFP phase

To get a precise phase estimate of the spikes, we sampled the spike waveform at a 24-kHz sampling rate. We determined the spike time based on the largest first derivative of the positive going component of action potentials. This time point was then rounded to the nearest 1-ms scale and associated with the LFP also sampled at 1 kHz. Next, to obtain the instantaneous phase, the Hilbert transforms of both theta and gamma frequency-filtered signals were computed using the "hilbert" function of MATLAB (www.mathworks.com/help/signal/ref/hilbert.html). The Hilbert phase at spike times (both defined at 1-ms precision) served as instantaneous phase estimate of spike relative to the theta or gamma oscillation (*13*).

Spatial FR maps

The spatial tuning of single-unit activity was characterized by FR maps and their spatial autocorrelation functions. For the FR map, the game area was divided into 1 m–by–1 m, 2 m–by–2 m, or 3 m–by–3 m spatial bins, depending on the size of the virtual environment (Table 2). For each of those spatial bins, we determined the duration of time spent and the number of spikes generated during crossings. By normalizing the number of spikes by the time spent, we obtained the FR in spikes per second (in Hertz). Binning had no significant effect on the grid parameters (*6*, *13*).

Computing phase maps

Besides the local FRs, the circular average phase of spikes (ϕ) relative to the theta and gamma bandpass-filtered LFP was computed. Because the frequency of visits varied area to area, including no visit at all, the reliability of (ϕ) estimate also varied with the number of visits. Therefore, we computed the mean and variance (σ^{ϕ}) of the phase estimate for each area. By spatially integrating the local phase estimates, we constructed a global map ($\hat{\sigma}_{\phi}$), where the mean phase estimate [$\hat{\phi}_{(x,y)}$] at any given area was associated with a color of the HSV color cylinder (red = $-\pi$, green = 0, and red = π), while [$\sigma^{\phi}_{(x,y)}$] was represented by the value ($\sigma_{max} = 2\pi$= black and $\sigma_{min} = 0$ = maximum hue) (Figs. 1H and 2C). We refer to the variance-weighted spatial distribution of a phase plot as phase map denoted by (Φ) (*13*). The variance-weighted representation of phase is equivalent to the resultant vector of spike phase (*48*).

Computing autocorrelation

To compute the autocorrelation, the FR map was first smoothed with a Gaussian filter [5 by 5 bin neighborhood, ($\sigma = 0.8$)], and non-visited bins, originally assigned with NaN, were replaced by FR = 0 spikes/s. Autocorrelograms were computed as follows. Given that the original FR map is *f* and the number of overlapping bins between the original and shifted FR maps at a given τ_x, τ_y offset is *n*, the equation for the 2D discrete autocorrelation is as follows

$$r(\tau_x,\tau_y)=\frac{n\sum f(x,y)f(x-\tau_x,y-\tau_y)-\sum f(x,y)f(x-\tau_x,y-\tau_y)}{\sqrt{n\sum f(x,y)^2-(\sum f(x,y))^2}\sqrt{n\sum f(x-\tau_x,y-\tau_y)^2-(\sum f(x-\tau_x,y-\tau_y))^2}} \quad (9)$$

where $r(\tau_x, \tau_y)$ is the autocorrelation. Correlations were estimated for all values of *n*. The central peak of the autocorrelogram was removed before computing the gridness (*84*, *85*).

Computing grid scores

We quantified canonical "gridness" based on the autocorrelograms (ACs) by computing a 60° gridness score (**g**) step by step following the exact procedure outlined by Barry and Bush (*81*), Sargolini *et al.* (*75*), and Krupic *et al.* (*82*) as described in our earlier study (*6*). We first normalized the FR maps by the sizes of environments that allowed for equal spatial resolutions for the ACs of different environments, but we kept the aspect ratio differences. Next, we computed the 2D ACs by applying 2D cross-correlation to the FR maps (*6*). After centering and clipping the AC to a 100 by 100 matrix, we located the largest peak after the removal of central peak, which defined a concentric ring containing the circular or ellipsoid arrangement of the first set of autocorrelation peaks at radius *R*. The outer radius of the ring was, based on the Barry-Krupic (BK) method, chosen to be 2.5*R* (*6*, *13*, *75*, *81*, *82*). For the computation of gridness scores, we followed the method by Sargolini *et al.* (*75*). Accordingly, we filtered the AC with the above-defined ring. Then, we rotated the extracted ring from 1° to 180° and computed the Pearson's correlation coefficients $\bar{r}_{(1°\ldots180°)}$ between the original and rotated matrix with an eight-point moving average applied to it. We determined gridness **g** as the difference between the minimum of $r_{60°}$ or $r_{120°}$ and the maximum of $r_{30°}$, $r_{90°}$, or $r_{150°}$. This function of gridness assumed a 60° modulation of AC as it expresses the modulation depth relative to 60° rotation symmetry. Because *r* modulation extended between 0 and 1, therefore, **g** was also bounded between 0 and 1.

Generating surrogate spike trains

For testing the deterministic spike-LFP phase relationship against by-chance phase coincidences, we generated surrogate spike trains. To preserve the ISI statistics of the original spike train yet decouple spike times from the phase of LFP, we resampled the ISIs from the ISI histogram and distributed them randomly during the interval of the LFP. We refer to this surrogate as "ISI shuffling." The first ISI of the original spike train was considered relative to time 0. ISI shuffling provided a Null to test the topographical consistency of spike-LFP phase relationship. We reasoned that if the observed spike-LFP phase coupling is topography preserving, then randomizing the phase relationship while retaining the statistics of both ISIs and LFP should lead to a dispersion of topography. Phase topography preservation was tested by cross-validation (see the "Testing the consistency of phase topography by cross-validation" section). Even if spike trains were highly periodic (with a narrow ISI histogram) and potentially increase the by-chance phase coupling between spikes

and LFP, the ISI shuffling would retain that by-chance coupling. In addition, to test whether periodic spike processes are sufficient to model the observed spike to LFP phase relationship, we created spike trains with uniform ISIs by determining the average ISI ($1/f$) and distributed the same number of spikes evenly within the recorded interval. Because trajectories were controlled by the nondeterministic placements of navigation targets, we can rule out any systematic or periodic coupling between the avatar's positions and spike processes. Hence, the periodic spike processes alone cannot account for topography-preserving spike-LFP phase relationship (*13*).

Generating surrogate LFP

Testing the deterministic contribution of LFP to the observed spike to LFP phase relationship, we generated LFP surrogates by phase randomization of the LFP. We applied a phase decomposition of the original LFP, which preserved the original power spectral density, except that the phases of oscillatory components were randomly shifted relative to the original. If spike processes were coordinated with the phase of any LFP component, then that relationship was dissolved by phase randomization. As a result, the observed topographic structure of spike to LFP phase relationship should have been compromised in the surrogate. To remove the low-frequency coherence between spikes and LFP, we reversed the phase-randomized LFP in time. As a result, the phase-randomized and time-reversed LFP should destroy any systematic phase relationship between spikes and LFP (*13*).

Comparing phase maps of original to surrogate spike and LFP

We compared the original (Φ) with those of constructed from surrogate spike trains and surrogate LFP with respect to (i) correlation of phase $\phi_{(x,y)}$ and variance of heading direction [$\sigma\bar{v}_{(x,y)}$] (the inverse of RVL), (ii) grid entropy, and (iii) the power of the low-frequency components of the autocorrelation of (Φ). Statistics were summarized in Table 4. While random LFP phases significantly decreased the covariance of local spike phase with the RVL [$zval^{subj1} = 10.5241$, $P_{(n=910)} = 0.0$ and $zval^{subj2} = 7.8262$ $P_{(n=1004)} = 0.0$], ISI permutation did not [$zval^{subj1} = -0.6207$, $P_{(n=910)} = 0.5348$ and $zval^{subj2} = 0.2321$, $P_{(n=1004)} = 0.8165$] (fig. S5A). Similarly, random LFP phase increased the entropy of (Φ), while ISI permutation did not [$zval^{subj1}$=0.3204, $P_{(n=910)} = 0.7487$ and $zval^{subj2} = 0.9118$, $P_{(n=1004)} = 0.3619$] (fig. S5B). Moreover, the original (Φ) patterns displayed a significantly larger low-frequency power of the 2D Fourier transform of phase maps than the ISI-shuffled and phase-randomized LFP [ISI shuffling: $zval^{subj1}$=2.6879, $P_{(n=697)} = 0.0072$ and $zval^{subj2} = 11.8777$, $P_{(n=1004)} = 0.0$; phase-randomized LFP: $zval^{subj2} = 8.6097$, $P_{(n=1004)} = 0.0$], except subject 2 for LFP phase randomization [$zval^{subj1} = 1.6668$, $P_{(n=697)} = 0.0956$] (fig. S5C).

Testing the consistency of phase topography by cross-validation

To test for temporal stability, we split a 300-s spike and LFP data into two nonoverlapping 150-s duration epochs and computed an element-to-element correlation between the phase maps (fig. S4, A to D). We excluded the nonvisited areas from the correlation that would otherwise generate spurious correlation. For the 2D cross-correlation, we applied Pearson's correlation between the two vectorized maps following 2D cross-correlation formula

$$r(A,B) = \frac{1}{N-1}\sum_{i=1}^{N}\left(\frac{A_i - \mu_A}{\sigma_A}\right)\left(\frac{B_i - \mu_B}{\sigma_B}\right) \quad (10)$$

where $r(A, B)$ is the cross-correlation; A and B were matrices representing the two phase maps; μ_A and σ_A are the mean and SD of A, respectively; and μ_B and σ_B are the mean and SD of B. For circular correlation, the same formula was used as above except that (ω_{11}, ω_{12}, ω_{1n}) and (ω_{21}, ω_{22}, ω_{2n}) are the gamma phases of corresponding elements in the two matrices μ_A and μ_B representing the means and σ_A and σ_B were the variance of A and B matrices, respectively (*79*).

For testing the robustness of the spike-gamma phase association, first, we eliminated the odd numbered spikes followed by the even numbered spikes and then constructed phase maps A and B. First, we eliminated the odd numbered spikes, then the even numbered spikes second, and then constructed phase maps A and B (fig. S4, A and E to G). Next, we computed the element-wise 2D correlation coefficients between the two matrices, similar to what we did to the split-half dataset above (*13*).

Generating autocorrelograms of surrogate spike to LFP phases

The topographic maps of spike to LFP phase relationship are affected by the inhomogeneous coverage of space by the time-limited navigation, regardless of whether we were using the original spike trains and LFPs or the surrogate counterparts. All reflected the pattern of spatial coverage, hence increased the correlation between original and surrogate patterns (path correlation). To remove the path correlation confound when evaluating the difference between surrogate and original spike and LFP processes, we constructed autocorrelograms between the spike-LFP phase maps. The nonvisited areas of maps were rendered by random phase values, hence resulted in low average correlations, while visited areas reflected true correlations between original spike/LFP and surrogate spike/LFP. We constructed autocorrelograms of true spike to LFP phase maps, surrogate spike to true LFP phase maps, and true spike to surrogate LFP phase maps (*13*).

Computing the speed of propagation of gamma field

We were interested to compute the speed of gamma wave propagation between electrodes. The 4 by 4 microelectrode grid represents 120 ($n = 16 \times 15/2$) speed measurement options between any two electrodes i and j. Given the known electrode grid geometry and interelectrode distances (λ), the frequency of the gamma carrier wave (f_γ), and the time difference of nearest gamma peaks detected on the electrode pair ij, we can compute the local speed of propagation as the fraction of distance over time

$$\bar{v} = \Delta x/\Delta t \quad (11)$$

where $\Delta x = \lambda$ and $\Delta t = (\phi_i - \phi_j)/2\pi \times 10e^2/f_\gamma$. Given that the gamma spectrum was set to low gamma (between 25 and 60 Hz) and that the nearest interelectrode distance of our microelectrodes was 0.9 mm, the $\phi_i - \phi_j = 60°$, and the speed of propagation was found to be between 0.3241 mm/ms (at 60 Hz) and 0.1350 mm/ms (at 25 Hz), also consistent with the literature (*45*).

Decoding of position and heading direction from spike phase

In preparation for phase decoding, we assume that all spike time data (T) have been converted to spike phase data (ϕ)

$$T_i \Rightarrow \phi_i \quad (12)$$

It was also assumed that the navigation area was divided into spatial bins as described earlier, except that for all four environments, we used a uniform 2 by 2 m̄ binning of the area. Hence, the notation ij refers to the ith and jth position of the area of navigation. For predicting the next position of the avatar, we used the actual position

at the time of spike (x_{Ti}, y_{Ti}), the phase of the subsequent spike ϕ_{Ti+1}, and the phase probability map Φ (including the variance). To obtain a reliable estimate of the phase distribution in space (Φ) at each visited spatial bin, we combined the spikes across all units and electrodes for given navigation session per day and per environment

$$\phi_{(ij,1\ldots n)} = \frac{\sum_{k=1}^{E}\sum_{l=1}^{N}\phi_{kN+l}}{EN} \quad (13)$$

where E is the number of electrodes and N is the number of units detected from each electrode.

To ensure that the spike pool used for constructing the phase probability map (Φ) was nonoverlapping with the test set, i.e., the spike pool ϕ used for decoding, we used every even and odd numbered spike for the test set and for the phase probability map, respectively

$$\phi \notin \Phi \quad (14)$$

Next, we integrated the phases across spatial bins of ij into a phase probability map by computing the circular average of spike phases Φ

$$\Phi = \int_i^L \int_j^M \phi_{(ij,1,3,5\ldots n)} \quad (15)$$

where L and M defines the size of the environment. Next, we computed the von Mises mean of phases in the space over each spatial bin that provided the phase probability map Φ^{prior}

$$\Phi_{ij} = \frac{\sum_{k=1}^{n_{ij}}\phi_{ijk}}{n_{ij}} \quad (16)$$

The Bayesian decoding started by reading the first spike position (x_{T1}, y_{T1}) of the vector of positions and the phase of the second spike ϕ_2 of the phase vector and loading the phase vector of the next 20 ($i = 2\ldots21$) spikes from the average phase map $\Phi_{(2\ldots21)}$ based on their [$x_{(2\ldots21)}$, $y_{(2\ldots21)}$] spatial bin coordinates. The upcoming position of the avatar was predicted as the position with the largest Bayesian probability of positions among the next 20 positions. The Bayesian probability of the avatar's position at x,y given that the spike was fired at a phase of ϕ_i was defined as the product of the likelihood of that phase at that location ($\Phi_{x,y}$ and the prior probability of visiting that location divided by the marginal likelihood of that specific phase occur relative to all the phase values)

$$p(x_i, y_i \mid \phi_i) = \frac{p(\phi \mid x_i, y_i)\, p(x_i, y_i)}{p(\phi)} \quad (17)$$

Since we already computed the phase probability map Φ, the simplified Bayesian probability is the weighted product of Φ and the probability of occupying the x, y position divided by the probability of phase

$$p(x_i, y_i \mid \phi_i) = \frac{p(\Phi_{x,y})\, p(x_i, y_i)}{p(\phi)} \quad (18)$$

where ϕ_i was the observed phase of the ith spike and $\Phi_{x,y}$ was the average phase at the (x, y) spatial bin of the environment. The predicted position was the maximum of the Bayesian probabilities among the 20 upcoming spikes

$$(x_i, y_i) = \arg\max\left(p(x_{(i,\ldots i+20)}, y_{(i,..i+20)} \mid \phi_{(i,\ldots i+20)})\right) \quad (19)$$

From (x_i, y_i) and (x_{i-1}, y_{i-1}), we computed the direction of heading as

$$\alpha = \operatorname{atan}(x_i - x_{i-1}, y_i - y_{i-1}) \quad (20)$$

The reason we used only 20 as opposed to all of the spikes was that phase maps were periodic; hence, the same phase value could be mapped to multiple spatial locations. The choice of 20 spikes ensured that the Bayesian prediction will find a local solution within the proximity of the previous spike. We always predicted the upcoming position of a spike relative to the actual spike; hence, we were able to generate vectors of heading directions, which were directly compared to the actual heading direction allowing for statistical estimates of the decoding performance to be made (fig. S12, C to F).

Decoding of position and heading direction from FR

While the firing data are prepared differently, ultimate decoding of position and heading direction information from FRs followed the same procedure as from spike phase (see the "Decoding of position and heading direction from spike phase" section). Because spike density for most neurons was sparse as the pyramidal neurons' FR is less than 1 Hz, we first estimated the continuous FR function from the actual spike times by computing the instantaneous FR at the time of spike $\text{FR}_i = (t_i - t_{i-1})/1000$ in hertz and resampled the nonuniform data at 1.0 kHz by the "resample" function of MATLAB (MathWorks, Nattick, MA), which uses a polyphase anti-aliasing filter. Next, we resampled the data again in 100-ms intervals using the Savitzky-Golay filter, a generalized moving average with filter coefficients determined by an unweighted linear least squares regression and a polynomial model of second degree

$$(T_i \implies t_{\text{resampled}} \implies \text{FR}_i) \quad (21)$$

Then, we treated FR_i exactly as ϕ_i and Eqs. 15 to 20 from the "Decoding of position and heading direction from spike phase" section was applied. Note that FR is a bounded variable between 0 and max(FR), as opposed to phase, but the rest of the data analysis and the Bayesian decoding model was agnostic to this difference.

Construction of CMs of position and heading direction from spike phase

To compare predicted position with observed position, and likewise the predicted heading direction with observed heading direction, we computed the CMs. The CMs represent the observed values (position or direction) on the x axis and the predicted values (position or direction) on the y axis. The resulting 2D histograms represent the aggregate of the pairs of the observed and predicted values at the observed (x) and predicted (y) coordinates for each spike. The scale of the heading direction CM was $x = y = [1...360]°$, while the position was [0...60] m̄.

Construction of angular histograms of aggregate difference between the observed and predicted heading directions

The aggregate differences between actual heading direction vectors and predicted direction vectors constructed a von Mises distribution. The mean of the difference was close to zero if the prediction was correct. We also computed the 360° CM between the predicted and observed directions of heading.

Dependency of decoding on the curvature of trajectories

Because the avatar's movement depended on the location of programmed targets, such as the alien and the spaceships, the avatar's trajectory varied between straight lines and sharp turns. Hence, the spatial distribution of the spikes along the trajectory as potential targets of the next move (among the 20 upcoming spikes) was highly sensitive to the curvature. As a result, when the trajectory was close to a straight line, the 20 upcoming spikes, as possible targets, lined up along the trajectory with a relatively small variation in heading directions and a larger variation in position, while the effect of the large curvature trajectory segments was the opposite. Consequently, the curvature affected the prediction error for direction and for position in an opposite fashion. Small curvature made direction errors small and position errors large, owing to the small directional variance and large positional variance of spike scatter along the straight trajectory. Hence, straight trajectories introduced a direction decoding bias during navigation, while highly curved trajectories introduced a position decoding bias. To compensate for these biases without changing the trajectory, we introduced two interventions: to constrain the decoding to mid-range trajectories and to generate a surrogate spike train (Null) as a control spike dataset described below.

Computing path curvatures

Curvature was defined on every P_{i-1}, P_i, P_{i+1} triplet of trajectory as $\kappa_i = 1/R_i$; hence, $R_i = 1/\kappa_i$, where R is the radius as estimated by the circumcenter of the triangle defined by the three points on the osculating circle (by A. Mjaavatten, MathWorks File Exchange). Regarding the curvature constraints on decoding, we selected trajectory segments where the radius of curvature was larger than 0 and smaller than 15 m and performed all the decoding on these segments. This treatment of using paths with middle-range curvatures served to minimize the influence of curvature on the phase decoding.

Construction of the Null spike dataset

To compensate for any behavioral bias, including the trajectory curvature bias, we generated a dataset (Null) that contained the same number of spikes and same time stamps as in the real data except that spike phases were shuffled. The Null dataset eliminated the association between the spike phase and the avatar's location. To obtain an unbiased estimate of the decoding performance from the shuffled phase dataset, we constructed a CM from the Null. The CM depicted the density of combinations of all observed and decoded movement directions in 360° space and position differences relative to the axes of the environment. When we subtracted the Null from the observed CM (Fig. 4, A and B), the difference represented the unbiased CM. We quantified the decoding by the resultant vector of the polar distribution of angle difference between decoded and true angles. Last, we computed the Kuiper two-sample statistic of the original and Null CMs, as well as the correlation and statistical difference between the decoded true positions and positions decoded from the Null dataset.

Determine precision of position decoding

If Δ_{pos} represents the precision of location decoding from phase, A_1, A_2, A_3, and A_4 are the areas of four different environments, and n_{grids} represent the average number of grid nodes, then the $P(dx, dy \mid \phi)$ probability of the location given a specific spike phase is

$$P(dx, dy \mid \phi) = \frac{\Delta_{pos} * 1/4 * (A_1 + A_2 + A_3 + A_4)}{n_{grids}} \quad (22)$$

Because the Δ_{pos} was different for each individual subjects and the rest of the parameters were fixed, the $1/4 * (A_1 + A_2 + A_3 + A_4) = 2857$ and $n_{grids} = 8$, the formula of computing the probability of by chance, i.e., getting the correct location right from a random code is $P(dx, dy \mid \phi) = \Delta_{pos} * 357.1250$.

Statistical evaluation of CMs by χ^2 statistics

We constructed four different CMs for both subjects (a total of eight CMs), representing the direction decoding from phase, position decoding from phase, direction decoding from FR, and position decoding from FR. For a statistical evaluation of these CMs, first, we eliminated the negative values resulted from subtracting the randomized contingency matrices from the original ones

$$\mathrm{CM} = \sqrt{(M \circ M)_{ij}} \quad (23)$$

Second, we split the CM into 2 by 2 quadrants (Q_1, Q_2, Q_3, Q_4) and summed the values within each quadrant generating a 2 by 2 contingency table (n_{q1}, n_{q2}, n_{q3}, n_{q4}). Then, the test of independence boils down to a χ^2 statistics. If the decoding of position or direction as an expected variable was independent from the avatar's observed position or direction, then the observed quantities in (n_{q1}, n_{q2}, n_{q3}, n_{q4}) quadrants should be no different from the expected distribution based on the marginal sums. However, if the decoding works and the expected and observed values are concordant, then the diagonal sum (N_B, N_C) should be significantly larger than chance. With the χ^2 test, we computed the probability of rejecting H_0: the independence of true and decoded movement parameters, i.e., position or direction

$$\chi^2 = \sum_{k=1}^{n} \frac{(O_k - E_k)^2}{E_k} \quad (24)$$

where O_k is the observed and E_k is the expected value in the kth quadrant ($n = 4$). We remark, while χ^2 test quantitatively confirmed the visual observation of the CMs, the 50 by 50 CMs contain much more information than that captured by the 2 by 2 χ^2 test.

Statistical evaluation of CMs by Kolmogorov-Smirnov test

To compare the true CMs with the CMs obtained from the Null dataset, we used the Kolmogorov-Smirnov tests. The Kolmogorov-Smirnov test computes the distance between the two cumulative probability distributions of the two samples and tests the Null hypothesis that the two samples were drawn from the same distribution against the alternative that they are not

$$D^* = \max_x(|\hat{F}_1(x) - \hat{F}_2(x)|) \quad (25)$$

where $\hat{F}_1(x)$ and $\hat{F}_2(x)$ are the empirical distribution functions representing the proportion of ×1 values less than or equal to x and $\hat{F}_2(x)$ the ×2 values less than or equal to x, respectively. If the D^* statistics is larger than the critical value, then we reject the Null and accept the H_1 that the two samples were deriving from two different distributions. Our hypothesis was that if the phase of spikes is informative about the position of the avatar, then the pairs of decoded and actual positions will distribute near the unity line of the CM, while the phase randomized dataset will distribute broadly. Because we generated 100 Null dataset with randomized phases, we obtained not only one but also the statistics of 100 Kolmogorov-Smirnov tests, the distribution of which was computed as a bar chart of P values.

Statistical evaluation of CMs by ROC test

In addition to χ^2 statistics and Kolmogorov-Smirnov test, we quantified how well an ideal observer would discriminate the decoding performance of spike phase code from the decoding of random (shuffled) phases. If the difference between the two distributions is discernible, then the ROC analysis should be able to determine the specificity and sensitivity of the phase code. First, we partitioned the CM to two areas: (i) the diagonal strip defined as $x = y \pm 2\sigma$, also called the identity line; and (ii) everything else around it. If the spike phase decoder worked perfectly, then all the decoded positions or directions would have concentrated along the diagonal. All other scenarios would generate a dispersion of $x \neq y$ values. Since we subtracted the random phase CM from the true phase CM to reduce trajectory bias, if the decoder was operating by chance, then the diagonal confidence interval would have contained close to equal number of positive and negative values, i.e., values reflecting surplus correct decoding and values where the random spike phases would yield to correct position estimates, respectively. Hence, an excess number of positive values would represent a surplus of correctly decoded directions or positions (fig. S15C). In contrast, the negative values would represent correct by-chance decoding performance from random phase distributions, i.e., the false positives (fig. S15D). Likewise, positive values outside of the confidence interval would represent targets missed by the decoder, while negative values off-diagonal represent correctly undetected targets, i.e., negative surplus values from random phase decoding. To compute the ROC curves and the area under that, we plot the function of the number of $s_{x,y} < 0$ values of false positives (fig. S15D) against the number of correctly decoded direction or position parameters (fig. S15C). If the area under the curve is significantly larger than 0.5, then we have a good reason to believe an ideal observer could easily discriminate between decoding of real location or heading direction from decoding randomized spike phase data. The ROC curve enables us to quantify how an ideal observer would be able to discriminate between the two distributions.

SUPPLEMENTARY MATERIALS

Supplementary material for this article is available at https://science.org/doi/10.1126/sciadv.abm6081

View/request a protocol for this paper from *Bio-protocol*.

REFERENCES AND NOTES

1. L. R. Squire, Memory and the hippocampus: A synthesis from findings with rats, monkeys, and humans. *Psychol. Rev.* **99**, 195–231 (1992).
2. T. Hafting, M. Fyhn, S. Molden, M.-B. Moser, E. I. Moser, Microstructure of a spatial map in the entorhinal cortex. *Nature* **436**, 801–806 (2005).
3. A. D. Ekstrom, J. B. Caplan, E. Ho, K. Shattuck, I. Fried, M. J. Kahana, Human hippocampal theta activity during virtual navigation. *Hippocampus* **15**, 881–889 (2005).
4. J. Jacobs, C. T. Weidemann, J. F. Miller, A. Solway, J. F. Burke, X. X. Wei, N. Suthana, M. R. Sperling, A. D. Sharan, I. Fried, M. J. Kahana, Direct recordings of grid-like neuronal activity in human spatial navigation. *Nat. Neurosci.* **16**, 1188–1190 (2013).
5. Y. Shrager, C. B. Kirwan, L. R. Squire, Neural basis of the cognitive map: Path integration does not require hippocampus or entorhinal cortex. *Proc. Natl. Acad. Sci.* **105**, 12034–12038 (2008).
6. Z. Nadasdy, T. P. Nguyen, Á. Török, J. Y. Shen, D. E. Briggs, P. N. Modur, R. J. Buchanan, Context-dependent spatially periodic activity in the human entorhinal cortex. *Proc. Natl. Acad. Sci. U.S.A.* **114**, E3516–E3525 (2017).
7. J. O'Keefe, J. Dostrovsky, The hippocampus as a spatial map. Preliminary evidence from unit activity in the freely-moving rat. *Brain Res.* **34**, 171–175 (1971).
8. J. S. Taube, R. U. Muller, J. B. Ranck, Head-direction cells recorded from the postsubiculum in freely moving rats. II. Effects of environmental manipulations. *J. Neurosci.* **10**, 436–447 (1990).
9. T. Solstad, C. N. Boccara, E. Kropff, M.-B. Moser, E. I. Moser, Representation of geometric borders in the entorhinal cortex. *Science* **322**, 1865–1868 (2008).
10. A. Tsao, J. Sugar, L. Lu, C. Wang, J. J. Knierim, M. B. Moser, E. I. Moser, Integrating time from experience in the lateral entorhinal cortex. *Nature* **561**, 57–62 (2018).
11. L. M. Giocomo, T. Stensola, T. Bonnevie, T. van Cauter, M. B. Moser, E. I. Moser, Topography of head direction cells in medial entorhinal cortex. *Curr. Biol.* **24**, 252–262 (2014).
12. B. J. Kraus, M. P. Brandon, R. J. Robinson II, M. A. Connerney, M. E. Hasselmo, H. Eichenbaum, During running in place, grid cells integrate elapsed time and distance run. *Neuron* **88**, 578–589 (2015).
13. Z. Nadasdy, Á. Török, T. P. Nguyen, J. Y. Shen, D. E. Briggs, P. N. Modur, R. J. Buchanan, Phase of neuronal activity encodes 2-dimensional space in the human entorhinal cortex. *bioRxiv* , 352815 (2018).
14. L. M. Giocomo, E. A. Zilli, E. Fransen, M. E. Hasselmo, Temporal frequency of subthreshold oscillations scales with entorhinal grid cell field spacing. *Science* **315**, 1719–1722 (2007).
15. T. A. Engel, L. Schimansky-Geier, A. V. M. Herz, S. Schreiber, I. Erchova, Subthreshold membrane-potential resonances shape spike-train patterns in the entorhinal cortex. *J. Neurophysiol.* **100**, 1576–1589 (2008).
16. C. B. Lu, J. G. R. Jefferys, E. C. Toescu, M. Vreugdenhil, In vitro hippocampal gamma oscillation power as an index of in vivo CA3 gamma oscillation strength and spatial reference memory. *Neurobiol. Learn. Mem.* **95**, 221–230 (2011).
17. G. BuzsÁki, Theta oscillations in the hippocampus. *Neuron* **33**, 325–340 (2002).
18. J. Jacobs, Hippocampal theta oscillations are slower in humans than in rodents: Implications for models of spatial navigation and memory. *Philos. Trans. R. Soc. Lond. B Biol. Sci.* **369**, 20130304 (2014).
19. H. Zhang, J. Jacobs, Traveling theta waves in the human hippocampus. *J. Neurosci.* **35**, 12477–12487 (2015).
20. B. R. Cornwell, L. L. Johnson, T. Holroyd, F. W. Carver, C. Grillon, Human hippocampal and parahippocampal theta during goal-directed spatial navigation predicts performance on a virtual Morris water maze. *J. Neurosci.* **28**, 5983–5990 (2008).
21. Z. M. Aghajan, P. Schuette, T. A. Fields, M. E. Tran, S. M. Siddiqui, N. R. Hasulak, T. K. Tcheng, D. Eliashiv, E. A. Mankin, J. Stern, I. Fried, N. Suthana, Theta oscillations in the human medial temporal lobe during real-world ambulatory movement. *Curr. Biol.* **27**, 3743–3751.e3 (2017).
22. D. J. White, M. Congedo, J. Ciorciari, R. B. Silberstein, Brain oscillatory activity during spatial navigation:theta and gamma activity link medial temporal and parietal regions. *J. Cogn. Neurosci.* **24**, 686–697 (2012).
23. M. P. Brandon, A. R. Bogaard, C. P. Libby, M. A. Connerney, K. Gupta, M. E. Hasselmo, Reduction of theta rhythm dissociates grid cell spatial periodicity from directional tuning. *Science* **332**, 595–599 (2011).
24. J. Koenig, A. N. Linder, J. K. Leutgeb, S. Leutgeb, The spatial periodicity of grid cells is not sustained during reduced theta oscillations. *Science* **332**, 592–595 (2011).
25. J. R. Hinman, M. P. Brandon, J. R. Climer, G. W. Chapman, M. E. Hasselmo, Multiple running speed signals in medial entorhinal cortex. *Neuron* **91**, 666–679 (2016).
26. A. FernÁndez-Ruiz, A. Oliva, M. Soula, F. Rocha-Almeida, G. A. Nagy, G. Martin-Vazquez, G. BuzsÁki, Gamma rhythm communication between entorhinal cortex and dentate gyrus neuronal assemblies. *Science* **372**, eabf3119 (2021).
27. A. Bragin, G. Jando, Z. Nadasdy, J. Hetke, K. Wise, G. Buzsaki, Gamma (40-100 Hz) oscillation in the hippocampus of the behaving rat. *J. Neurosci.* **15**, 47–60 (1995).
28. L. L. Colgin, T. Denninger, M. Fyhn, T. Hafting, T. Bonnevie, O. Jensen, M. B. Moser, E. I. Moser, Frequency of gamma oscillations routes flow of information in the hippocampus. *Nature* **462**, 353–357 (2009).
29. N. Axmacher, M. M. Henseler, O. Jensen, I. Weinreich, C. E. Elger, J. Fell, Cross-frequency coupling supports multi-item working memory in the human hippocampus. *Proc. Natl. Acad. Sci. U.S.A.* **107**, 3228–3233 (2010).
30. F. Mormann, J. Fell, N. Axmacher, B. Weber, K. Lehnertz, C. E. Elger, G. FernÁndez, Phase/amplitude reset and theta-gamma interaction in the human medial temporal lobe during a continuous word recognition memory task. *Hippocampus* **15**, 890–900 (2005).
31. M. Hasselmo, C. Bodelon, B. Wyble, A proposed function for hippocampal theta rhythm: Separate phases of encoding and retrieval enhance reversal of prior learning. *Neural Comput.* **14**, 793–817 (2002).
32. U. Rutishauser, I. B. Ross, A. N. Mamelak, E. M. Schuman, Human memory strength is predicted by theta-frequency phase-locking of single neurons. *Nature* **464**, 903–907 (2010).
33. A. C. Heusser, D. Poeppel, Y. Ezzyat, L. Davachi, Episodic sequence memory is supported by a theta-gamma phase code. *Nat. Neurosci.* **19**, 1374–1380 (2016).
34. M. M. Yartsev, M. P. Witter, N. Ulanovsky, Grid cells without theta oscillations in the entorhinal cortex of bats. *Nature* **479**, 103–107 (2011).
35. N. J. Killian, M. J. Jutras, E. A. Buffalo, A map of visual space in the primate entorhinal cortex. *Nature* **491**, 761–764 (2012).

36. A. Alonso, R. R. LlinÁs, Subthreshold Na^+-dependent theta-like rhythmicity in stellate cells of entorhinal cortex layer II. *Nature* **342**, 175–177 (1989).
37. R. R. Llinas, A. A. Grace, Y. Yarom, In vitro neurons in mammalian cortical layer 4 exhibit intrinsic oscillatory activity in the 10- to 50-Hz frequency range. *Proc. Natl. Acad. Sci. U.S.A.* **88**, 897–901 (1991).
38. M. Okun, A. Naim, I. Lampl, The subthreshold relation between cortical local field potential and neuronal firing unveiled by intracellular recordings in awake rats. *J. Neurosci.* **30**, 4440–4448 (2010).
39. T. V. Ness, M. W. H. Remme, G. T. Einevoll, Active subthreshold dendritic conductances shape the local field potential. *J. Physiol.* **594**, 3809–3825 (2016).
40. B. Telenczuk, N. Dehghani, M. Le Van Quyen, S. S. Cash, E. Halgren, N. G. Hatsopoulos, A. Destexhe, Local field potentials primarily reflect inhibitory neuron activity in human and monkey cortex. *Sci. Rep.* **7**, 40211 (2017).
41. N. Burgess, C. Barry, J. O'Keefe, An oscillatory interference model of grid cell firing. *Hippocampus* **17**, 801–812 (2007).
42. N. Burgess, Grid cells and theta as oscillatory interference: Theory and predictions. *Hippocampus* **18**, 1157–1174 (2008).
43. J. R. Climer, E. L. Newman, M. E. Hasselmo, Phase coding by grid cells in unconstrained environments: Two-dimensional phase precession. *Eur. J. Neurosci.* **38**, 2526–2541 (2013).
44. A. Jeewajee, C. Barry, V. Douchamps, D. Manson, C. Lever, N. Burgess, Theta phase precession of grid and place cell firing in open environments. *Philos. Trans. R. Soc. B Biol. Sci.* **369**, 20120532 (2014).
45. Z. Nadasdy, Information encoding and reconstruction from the phase of action potentials. *Front. Syst. Neurosci.* **3**, 6 (2009).
46. J. O'Keefe, M. L. Recce, Phase relationship between hippocampal place units and the EEG theta rhythm. *Hippocampus* **3**, 317–330 (1993).
47. D. Tingley, G. BuzsÁki, Transformation of a spatial map across the hippocampal-lateral septal circuit. *Neuron* **98**, 1229–1242.e5 (2018).
48. J. D. Monaco, R. M. De Guzman, H. T. Blair, K. Zhang, Spatial synchronization codes from coupled rate-phase neurons. *PLoS Comput. Biol.* **15**, e1006741 (2019).
49. T. Hafting, M. Fyhn, T. Bonnevie, M. B. Moser, E. I. Moser, Hippocampus-independent phase precession in entorhinal grid cells. *Nature* **453**, 1248–1252 (2008).
50. E. T. Reifenstein, R. Kempter, S. Schreiber, M. B. Stemmler, A. V. M. Herz, Grid cells in rat entorhinal cortex encode physical space with independent firing fields and phase precession at the single-trial level. *Proc. Natl. Acad. Sci. U.S.A.* **109**, 6301–6306 (2012).
51. J. C. Magee, Dendritic mechanisms of phase precession in hippocampal CA1 pyramidal neurons. *J. Neurophysiol.* **86**, 528–532 (2001).
52. A. P. Maurer, B. L. McNaughton, Network and intrinsic cellular mechanisms underlying theta phase precession of hippocampal neurons. *Trends Neurosci.* **30**, 325–333 (2007).
53. N. Burgess, J. O'Keefe, Models of place and grid cell firing and theta rhythmicity. *Curr. Opin. Neurobiol.* **21**, 734–744 (2011).
54. A. Kamondi, L. AcsÁdy, X. J. Wang, G. BuzsÁki, Theta oscillations in somata and dendrites of hippocampal pyramidal cells in vivo: Activity-dependent phase-precession of action potentials. *Hippocampus* **8**, 244–261 (1998).
55. E. Pastalkova, V. Itskov, A. Amarasingham, G. BuzsÁki, Internally generated cell assembly sequences in the rat hippocampus. *Science* **321**, 1322–1327 (2008).
56. C. D. Harvey, F. Collman, D. A. Dombeck, D. W. Tank, Intracellular dynamics of hippocampal place cells during virtual navigation. *Nature* **461**, 941–946 (2009).
57. O. Jensen, J. E. Lisman, Position reconstruction from an ensemble of hippocampal place cells: Contribution of theta phase coding. *J. Neurophysiol.* **83**, 2602–2609 (2000).
58. J. R. Huxter, T. J. Senior, K. Allen, J. Csicsvari, Theta phase-specific codes for two-dimensional position, trajectory and heading in the hippocampus. *Nat. Neurosci.* **11**, 587–594 (2008).
59. C. Guger, T. Gener, C. M. A. Pennartz, J. R. Brotons-Mas, G. Edlinger, S. Bermúdez i Badia, P. Verschure, S. Schaffelhofer, M. V. Sanchez-Vives, Real-time position reconstruction with hippocampal place cells. *Front. Neurosci.* **5**, 85 (2011).
60. E. W. Schomburg, A. FernÁndez-Ruiz, K. Mizuseki, A. Berényi, C. A. Anastassiou, C. Koch, G. BuzsÁki, Theta phase segregation of input-specific gamma patterns in entorhinal-hippocampal networks. *Neuron* **84**, 470–485 (2014).
61. F. Bender, M. Gorbati, M. C. Cadavieco, N. Denisova, X. Gao, C. Holman, T. Korotkova, A. Ponomarenko, Theta oscillations regulate the speed of locomotion via a hippocampus to lateral septum pathway. *Nat. Commun.* **6**, 8521 (2015).
62. O. J. Ahmed, M. R. Mehta, Running speed alters the frequency of hippocampal gamma oscillations. *J. Neurosci.* **32**, 7373–7383 (2012).
63. A. J. Watrous, I. Fried, A. D. Ekstrom, Behavioral correlates of human hippocampal delta and theta oscillations during navigation. *J. Neurophysiol.* **105**, 1747–1755 (2011).
64. P. H. Garthwaite, F. G. Elfadaly, J. R. Crawford, Modified confidence intervals for the Mahalanobis distance. *Stat. Probab. Lett.* **127**, 131–137 (2017).
65. S. E. Qasim, I. Fried, J. Jacobs, Phase precession in the human hippocampus and entorhinal cortex. *Cell* **184**, 3242–3255.e10 (2021).
66. M. Vinck, B. Lima, T. Womelsdorf, R. Oostenveld, W. Singer, S. Neuenschwander, P. Fries, Gamma-phase shifting in awake monkey visual cortex. *J. Neurosci.* **30**, 1250–1257 (2010).
67. M. Besserve, S. C. Lowe, N. K. Logothetis, B. Schölkopf, S. Panzeri, Shifts of gamma phase across primary visual cortical sites reflect dynamic stimulus-modulated information transfer. *PLoS Biol.* **13**, e1002257 (2015).
68. M. Siegel, M. R. Warden, E. K. Miller, Phase-dependent neuronal coding of objects in short-term memory. *Proc. Natl. Acad. Sci. U.S.A.* **106**, 21341–21346 (2009).
69. B. Pesaran, J. S. Pezaris, M. Sahani, P. P. Mitra, R. A. Andersen, Temporal structure in neuronal activity during working memory in macaque parietal cortex. *Nat. Neurosci.* **5**, 805–811 (2002).
70. W. E. Skaggs, B. L. McNaughton, M. A. Wilson, C. A. Barnes, Theta phase precession in hippocampal neuronal populations and the compression of temporal sequences. *Hippocampus* **6**, 149–172 (1996).
71. E. Reifenstein, M. Stemmler, A. V. M. Herz, R. Kempter, S. Schreiber, Movement dependence and layer specificity of entorhinal phase precession in two-dimensional environments. *PLOS ONE* **9**, e100638 (2014).
72. A. J. Watrous, J. Miller, S. E. Qasim, I. Fried, J. Jacobs, Phase-tuned neuronal firing encodes human contextual representations for navigational goals. *eLife* **7**, e32554 (2018).
73. A. Bahramisharif, M. A. J. van Gerven, E. J. Aarnoutse, M. R. Mercier, T. H. Schwartz, J. J. Foxe, N. F. Ramsey, O. Jensen, Propagating neocortical gamma bursts are coordinated by traveling alpha waves. *J. Neurosci.* **33**, 18849–18854 (2013).
74. Z. Nadasdy, Binding by asynchrony: The neuronal phase code. *Front. Neurosci.* **4**, 51 (2010).
75. F. Sargolini, M. Fyhn, T. Hafting, B. L. McNaughton, M. P. Witter, M. B. Moser, E. I. Moser, Conjunctive representation of position, direction, and velocity in entorhinal cortex. *Science* **312**, 758–762 (2006).
76. R. Q. Quiroga, Z. Nadasdy, Y. Ben-Shaul, Unsupervised spike detection and sorting with wavelets and superparamagnetic clustering. *Neural Comput.* **16**, 1661–1687 (2004).
77. J. Wild, Z. Prekopcsak, T. Sieger, D. Novak, R. Jech, Performance comparison of extracellular spike sorting algorithms for single-channel recordings. *J. Neurosci. Methods* **203**, 369–376 (2012).
78. P. Berens, CircStat: A MATLAB toolbox for circular statistics. *J. Stat. Softw.* **31**, 1–21 (2009).
79. S. R. Jammalamadaka, A. SenGupta, *Topics in Circular Statistics [electronic resource]* (World Scientific, 2001).
80. N. I. Fisher, A. J. Lee, A correlation coefficient for circular data. *Biometrika* **70**, 327–332 (1983).
81. C. Barry, D. Bush, From A to Z: A potential role for grid cells in spatial navigation. *Neural Syst. Circuits* **2**, 6 (2012).
82. J. Krupic, N. Burgess, J. O'Keefe, Neural representations of location composed of spatially periodic bands. *Science* **337**, 853–857 (2012).
83. R. C. Gonzalez, R. E. Woods, S. L. Eddins, in *Digital Image Processing Using Matlab* (Gonzalez Woods & Eddins, 2004), vol. 624, pp. 609.
84. M. Migliore, T. M. Morse, A. P. Davison, L. Marenco, G. M. Shepherd, M. L. Hines, ModelDB: Making models publicly accessible to support computational neuroscience. *Neuroinformatics* **1**, 135–140 (2003).
85. M. L. Hines, T. Morse, M. Migliore, N. T. Carnevale, G. M. Shepherd, ModelDB: A database to support computational neuroscience. *J. Comput. Neurosci.* **17**, 7–11 (2004).

Acknowledgments

Funding: The study was funded by the Seton Research Award. **Author contributions**: Study design: Z.N., Á.T., and R.J.B. Institutional Review Board protocol: Z.N. and R.J.B. Stimulus presentation codes: Á.T. Data analysis codes: Z.N., D.H.P.H., Á.T., and T.P.N. Data collection: Z.N. and T.P.N. Patient selection and neurology support: J.Y.S., D.E.B., P.N.M., and R.J.B. Surgical planning: J.Y.S., D.E.B., P.N.M., and R.J.B. Neurosurgery and electrode implantations: R.J.B. Manuscript editing: Z.N. and D.H.P.H. Revisions: Z.N., Á.T., and D.H.P.H. All authors read and approved the final manuscript. **Competing interests:** The authors declare that they have no competing interests. **Data and materials availability:** All data needed to evaluate the conclusions in the paper are present in the paper and/or the Supplementary Materials. The data used for the analysis have been deposited in Zenodo and are accessible through the following link: https://doi.org/10.5281/zenodo.6326460.

Submitted 28 September 2021
Accepted 15 March 2022
Published 4 May 2022
10.1126/sciadv.abm6081

ScienceAdvances

Phase coding of spatial representations in the human entorhinal cortex

Zoltan NadasdyDaniel H. P. HowellÁgoston TörökT. Peter NguyenJason Y. ShenDeborah E. BriggsPradeep N. ModurRobert J. Buchanan

Sci. Adv., 8 (18), eabm6081. • DOI: 10.1126/sciadv.abm6081

Science Advances (ISSN) is published by the American Association for the Advancement of Science. 1200 New York Avenue NW, Washington, DC 20005. The title *Science Advances* is a registered trademark of AAAS.

Summary

This dissertation captures the central narrative of my research journey spanning 30 years in the intersection of neuroscience, cognition, and computational neuroscience, searching for "the neural code." It is not the sole narrative but a personal one that renders my key publications by a coherent story in theoretical end experimental neuroscience. The story revolved around the question: "*What is the smallest meaningful unit of information contained by the neuronal activity?* This "*unit"* must transcend single neurons and single spikes because the spikes of single neurons are identical, and they don't represent specific information without the context of the other spikes. The context can be defined by anatomy and/or behavior. We sought the *smallest* meaningful unit, which, in addition to the signal itself, contains sufficient context, to interpret the message. By rephrasing the above question, "If action potentials were the alphabet of the brain's language, what would the words be?". This question boils down to defining the simplest meaningful combinations of action potentials with cognitive functions starting with the concept of *spike sequences* (Nadasdy 1999, Nadasdy 2000) and arriving at *phase coding* (Nadasdy 2009, 2010, 2022).

In the first chapter, we discussed various model realizations of *spike sequences* and their fit with empirical data. One was Moshe Abeles' synfire chain model (Abeles, 1991; Aviel et al., 2004), which remains purely theoretical until its predictions become widely replicated (Shmiel et al., 2005). Another model realization was the hippocampal replay of place cell and non-place cell activity termed "*forward replay"* and "*reverse replay."* Both have been widely demonstrated and replicated on rodents running linear tracks and primates, including humans as well (Diba & Buzsaki, 2007; Foster & Wilson, 2006; Ji & Wilson, 2007; Nadasdy, Hirase, Czurko, et al., 1999; Skaggs & McNaughton, 1996; Vaz et al., 2020). While the association of these sequences with the intrinsic local theta rhythm was conspicuous from the beginning, recognizing their coherence with slow-gamma oscillations had to wait almost two decades (Nadasdy et al., 2022; Pfeiffer & Foster, 2015).

The next chapter (Chapter 2) addressed whether spike sequences were products of the self-organizing nature of neurons. The spontaneous formation of self-organized attractor dynamics was evident in dissociated tissue cultures by using multi-electrode array (MUA) technique. We unraveled the emergence of coherent oscillatory population activity without external drive

(Wagenaar et al., 2006). This intrinsic oscillatory activity always converged to a stereotypical and stable two-level dynamic of bursts and superbursts. Most importantly, the activity propagation in the dish was an ordered sequence consistent with the physics of traveling waves. However, the contribution of individual neurons to the repeating activity motifs was variable. We concluded that spike sequences do not recur precisely with the participation of the same set of neurons. Instead, the dynamics will unfold by taking alternate routes involving different neurons. Hence, the contribution of neurons to the sequences is variable. This observation also challenged the basic assumption of the synfire chain model that hypothesized the repetition of sequences in cortical circuitries with a cellular precision.

The third chapter, "*Can Phase be a code?"* was a theoretical journey of integrating spike sequences with neuronal oscillations. It posited that the phases of continuous subthreshold oscillations self-organize into waves (just like in tissue cultures), and these waves play a critical role in resolving (discretizing) information for encoding and associating the spikes with neurons (a spatial code) during decoding. Phase coding postulates that (1) gamma (or other sufficiently coherent) oscillations play a fundamental role in information encoding; (2) action potentials tend to cohere with the subthreshold oscillation of the neuron; (3) subthreshold oscillations combine into traveling waves; (4) the topography of those oscillations can control the information-flow within the circuitry; (5) given a sufficient match of oscillation parameters between the encoding and decoding sites, the recovery of information from phase code is near perfect. The encoding and decoding concept is quite similar to the principle of holography, where a laser beam is applied as a reference wave for scanning the surface of an object, and the same reference laser beam is used for decoding the information from the phase imprint generated by interferences (Gabor et al., 1971). If the two reference waves are identical, the recovery of the surface is possible with a small margin of error. The phase coding model made predictions that were tested in Chapter 5. Moreover, it was a pivotal prediction of the phase coding model that gamma and theta oscillations propagate in the cortex and hippocampus as traveling waves (Nadasdy, 2009). These traveling waves since then have been widely reported (Das et al., 2022; Hangya et al., 2011; Lubenov & Siapas, 2009; Muller et al., 2018; Zhang et al., 2018; Zhang & Jacobs, 2015).

Chapter 4 was devoted to the experimental validation of the human brain's grid cells and laid the foundation for recording single neuronal activity to unravel circuitry dynamics in a well-controlled virtual environment (Nadasdy et al., 2017c). We discovered that (1) about 25-30 %

of human medial entorhinal cortical cells (MEC) express grid cell properties. (2) However, these cells represent spatial relations differently from grid cells in the rodent brain because (i) grid distances in human MEC neurons scale with the size of the environment; (ii) grids orient relative to the corners; and (iii) they express Cartesian grid geometry in addition to hexagonal. (3) We also showed that these grids are formed instantly due to the reliance on scanning the environment by saccadic eye movements as opposed to by locomotion, as typical in rodents. (4) The novel Cartesian grids (iii) may represent a neuronal solution specific to humans, an interesting avenue to explore further and clarify the role of culture and education in forming cognitive maps. While this discovery was concerned mainly with establishing a firm experimental paradigm to study neural coding of space in patients during seizure monitoring, it set the stage for validating phase coding in the human brain (Chapter 5).

I consider Chapter 5 the real testbed for phase coding. Previously, I have shown by simulation that information can be recovered from phase (Chapter 3) (Nadasdy, 2009, 2010c, 2015). However, this theoretical possibility had not been proven in vivo until we showed that cognitive content, such as the allocentric spatial position of the agent, can be decoded from the phase with a precision unattainable by firing rate metric (Kayser et al., 2009; Montemurro et al., 2008). We tested the hypothesis that information about the spatial position of the agent can be recovered from the phase of the single-unit activity (Nadasdy et al., 2018, 2022). To do that, we developed a new method to visualize the information associated with the phase of spikes. By leveraging that tool, we showed that (1) the 2D phase maps unraveled a hidden allocentric topography of the firing phase that was conserved over time. (2) This allocentric topography was more prevalent in the population of MEC cells than the grid cell firing property from the firing rate. (3) The firing phase of cells was better tuned to slow-gamma LFP than theta, and phase maps of slow-gamma were more reproducible than phase maps of theta. (4) The phase maps of slow-gamma were more precisely aligned with the environment than the spatial variance of spikes. (5) The self-preserving microstructure of the gamma field is more critical for map formation than the spikes. This last finding puts the microstructure of gamma oscillations in the focus of computation as it shifts our attention from the activity of individual neurons to the field generated by a population of neurons.

Based on these findings, a new view of neural dynamics is shaping up. According to this view, neurons and spikes are interchangeable entities of the neural code. At the same time, the local field of subthreshold oscillations (LFO) are the placeholders for information by modulating the

spike probability. Information is still conveyed by action potentials, but the spatial-temporal granularity of information (i.e., which neuron fires and when) encoded by spikes (i.e., which neuron fires and when) is defined by the dynamics of the LFO.

Let me illustrate this with an example. Suppose we daisy-chain a group of neurons from ***a*** to ***h*** where ***a*** provides input to ***b***, ***b*** provides input to ***c***, …, and ***h*** provides input to ***a*** by closing the loop. Each neuron's firing pattern is denoted by zeros and ones, such as in the example below (left side). We observe the activity of these cells at times t_1 and t_2 for the duration of 8 consecutive state readouts, which generates an 8-bit binary word (such as 10000000 and 01000000 in the first row). Despite the t_2 - t_1 delay in the readouts, the two patterns sampled at t_1 and t_2 are identical as generated by the same neuron with a time shift. Because neuron ***b*** receives the input from neuron ***a*** plus a delay, the state of ***b*** at t_1 will be identical to the state of neuron ***a*** at t_2. Hence, seeing the binary code "00000010" will identify neither the neuron nor the time when the neuron's state was read. However, suppose we introduce a periodic function marked as '_', which tags the beginning of each binary word on all eight neurons simultaneously at any time. In that case, the readout of neuron ***a*** at t_2 (01000_00) will not be confused with the readout of neuron ***b*** at t_1 (0100_000) relative to the periodic marker. The periodic marker provides a reference, such as a start or stop bit. Oscillations may naturally play such a role in information segmentation.[2]

	without periodic marker		with periodic marker	
neuron	t_1	t_2	t_1	t_2
	↓	↓	↓	↓
a	10000000	01000000	1000_000	01000_00
b	01000000	00100000	0100_000	00100_00
c	00100000	00010000	0010_000	00010_00
d	00010000	00001000	0001_000	00001_00
e	00001000	00000100	0000<u>1</u>000	00000<u>1</u>00
f	00000100	00000010	0000_100	00000_10
g	00000010	00000001	0000_010	00000_01
h	00000001	10000000	0000_001	10000_00

Neuronal cooperation expresses the same principle from the dissociated neuronal cell culture to the human MEC. Using a metaphor, consider neurons musicians in a symphonic orchestra.

[2] A very similar model and explanation was put forward by Buzsáki in his "neural syntax" article (Buzsáki, 2010).

Individual musicians (together with their instruments) might be interchangeable during a performance. The violinists may exchange seats within the sting section and, likewise the trombonists. Nobody would notice the difference in sound. However, if the percussionists swap seats with the trombonists, not to mention replacing the entire string section with a brass section would make a noticeable difference. Likewise, neurons play interchangeable roles in generating recurring firing patterns because the population activity and/or the external input may coordinate the rhythm that recruits neurons on the fly. Just like how the conductor dictates the rhythm for the orchestra and makes the music piece reproducible from one performance to another every night in the concert hall. That should disappoint neither musicians nor neurons.

For a while, we believed that neurons simply sum their dendritic input and relay a sequence of action potentials if the sum exceeds a constant threshold. This meant neurons did not see beyond their synaptic inputs. This view needs to be updated. Mounting evidence, including our results, suggests that neurons are embedded in a highly structured conductive media, enabling them to propagate electric current in waves due to ephaptic or volume conductance far beyond their synaptic connections. This media, in addition to neurons, contain highly conductive passive and active elements such as glial cells and astrocytes (Ashhad & Narayanan, 2019), and they articulate the complex terrain of traveling waves at different frequencies, propagation speeds, and directions. These oscillations modulate the subthreshold membrane oscillations of neurons such that, in turn, they affect dendritic integration and modulate neurons' likelihood of firing action potentials. Hence, neurons see far beyond their synaptic neighbors and sense the larger context of the current-source landscape, unlocking a whole different level of complexity and computation we have not even considered. When neurons start talking to other neurons beyond their immediate contact is a prerequisite for self-organization and catalyzes conative functions to emerge.

REFERENCES

Abeles, M. (1982). Role of the cortical neuron: integrator or coincidence detector? *Isr J Med Sci*, *18*(1), 83–92.

Abeles, M. (1991). *Corticonics: Neural Circuits of the Cerebral Cortex*. Cambridge University Press.

Abeles, M., & Gat, I. (2001). Detecting precise firing sequences in experimental data. *J Neurosci Methods*, *107*(1–2), 141–154. https://doi.org/S0165027001003648 [pii]

Adrian, E. D. (1954). The basis of sensation; some recent studies of olfaction. *British Medical Journal*, *1*(4857), 287–290. http://www.pubmedcentral.nih.gov/articlerender.fcgi?artid=2093300&tool=pmcentrez&rendertype=abstract

Alberini, C. M., & Kandel, E. R. (2015). The regulation of transcription in memory consolidation. *Cold Spring Harbor Perspectives in Biology*, *7*(1), a021741.

Amit, D. J. (1989). *Modeling Brain Function: The World of Attractor Neural Networks*. Cambridge University Press. https://books.google.co.zw/books?id=fvLYch1yQncC

Anishchenko, V. S., & Strelkova, G. I. (1997). Attractors of dynamical systems. *1997 1st International Conference, Control of Oscillations and Chaos Proceedings (Cat. No.97TH8329)*, *3*, 498–503 vol.3. https://doi.org/10.1109/COC.1997.626654

Ashhad, S., & Narayanan, R. (2019). Stores, Channels, Glue, and Trees: Active Glial and Active Dendritic Physiology. *Molecular Neurobiology*, *56*(3), 2278–2299. https://doi.org/10.1007/s12035-018-1223-5

Aviel, Y., Horn, D., & Abeles, M. (2004). Synfire waves in small balanced networks. *Neurocomputing*, *58–60*, 123–127. https://doi.org/https://doi.org/10.1016/j.neucom.2004.01.032

Bahramisharif, A., van Gerven, M. A. J., Aarnoutse, E. J., Mercier, M. R., Schwartz, T. H., Foxe, J. J., Ramsey, N. F., & Jensen, O. (2013). Propagating Neocortical Gamma Bursts Are Coordinated by Traveling Alpha Waves. *Journal of Neuroscience*, *33*(48), 18849–18854. https://doi.org/10.1523/JNEUROSCI.2455-13.2013

Barry, C., O'Keefe, J., & Burgess, N. (2009). Effect of novelty on grid cell firing. *Proc ICCNS*, *35: 101.24*, 35.

Berger, H. (1929). Über das Elektrenkephalogramm des Menschen. *Archiv Für Psychiatrie Und Nervenkrankheiten*, *87*(1), 527–570. https://doi.org/10.1007/BF01797193

Besserve, M., Lowe, S. C., Logothetis, N. K., Schölkopf, B., & Panzeri, S. (2015). Shifts of Gamma Phase across Primary Visual Cortical Sites Reflect Dynamic Stimulus-Modulated Information Transfer. *PLOS Biology*, *13*(9), e1002257. https://doi.org/10.1371/journal.pbio.1002257

Bienenstock, E., & Malsburg, C. von der. (1987). A Neural Network for Invariant Pattern Recognition. *EPL (Europhysics Letters)*, *1*, 121. http://stacks.iop.org/0295-5075/4/121

Blair, H. T., Welday, A. C., & Zhang, K. (2007). Scale-Invariant Memory Representations Emerge from Moiré Interference between Grid Fields That Produce Theta Oscillations: A Computational Model. *Journal of Neuroscience*, *27*(12), 3211–3229. https://doi.org/10.1523/JNEUROSCI.4724-06.2007

Bragin, A., Jando, G., Nadasdy, Z., Hetke, J., Wise, K., & Buzsaki, G. (1995). Gamma (40-100 Hz) oscillation in the hippocampus of the behaving rat. *J Neurosci*, *15*(1 Pt 1), 47–60. http://www.ncbi.nlm.nih.gov/entrez/query.fcgi?cmd=Retrieve&db=PubMed&dopt=Citation&list_uids=7823151

Burak, Y., & Fiete, I. R. (2009). Accurate path integration in continuous attractor network models of grid cells. *PLoS Computational Biology*, *5*(2), e1000291. https://doi.org/10.1371/journal.pcbi.1000291

Burgess, N., Barry, C., & O'Keefe, J. (2007). An oscillatory interference model of grid cell firing. *Hippocampus*, *17*(9), 801–812. https://doi.org/10.1002/hipo.20327

Burgess, N., & O'Keefe, J. (2011). Models of place and grid cell firing and theta rhythmicity. In *Current Opinion in Neurobiology*. https://doi.org/10.1016/j.conb.2011.07.002

Buzsaki, G. (1989). Two-stage model of memory trace formation: a role for "noisy" brain states. *Neuroscience*, *31*(3), 551–570. https://doi.org/0306-4522(89)90423-5 [pii]

Buzsáki, G. (2010). Neural syntax: cell assemblies, synapsembles, and readers. *Neuron*, *68*(3), 362–385.

Chiang, C.-C., & Durand, D. M. (2023). Subthreshold Oscillating Waves in Neural Tissue Propagate by Volume Conduction and Generate Interference. *Brain Sciences*, *13*(1). https://doi.org/10.3390/brainsci13010074

Chrobak, J. J., & Buzsaki, G. (1998). Gamma oscillations in the entorhinal cortex of the freely behaving rat. *J Neurosci*, *18*(1), 388–398. http://www.hubmed.org/display.cgi?uids=9412515

Coenen, A., Fine, E., & Zayachkivska, O. (2014). Adolf beck: A forgotten pioneer in electroencephalography. In *Journal of the History of the Neurosciences*. https://doi.org/10.1080/0964704X.2013.867600

Colgin, L. L., Denninger, T., Fyhn, M., Hafting, T., Bonnevie, T., Jensen, O., Moser, M. B., & Moser, E. I. (2009). Frequency of gamma oscillations routes flow of information in the hippocampus. *Nature*, *462*(7271), 353–357. https://doi.org/nature08573 [pii] 10.1038/nature08573

Colgin, L. L., & Moser, E. I. (2010). Gamma oscillations in the hippocampus. *Physiology (Bethesda)*, *25*(5), 319–329. https://doi.org/25/5/319 [pii] 10.1152/physiol.00021.2010

Constantinescu, A. O., O'Reilly, J. X., & Behrens, T. E. J. (2016). Organizing conceptual knowledge in humans with a gridlike code. *Science*, *352*(6292).

Das, A., Myers, J., Mathura, R., Shofty, B., Metzger, B. A., Bijanki, K., Wu, C., Jacobs, J., & Sheth, S. A. (2022). Spontaneous neuronal oscillations in the human insula are hierarchically organized traveling waves. *ELife*, *11*, e76702. https://doi.org/10.7554/eLife.76702

Desmaisons, D., Vincent, J.-D., & Lledo, P.-M. (1999). Control of Action Potential Timing by Intrinsic Subthreshold Oscillations in Olfactory Bulb Output Neurons. *J. Neurosci.*, *19*(24), 10727–10737. http://www.jneurosci.org/content/19/24/10727.short

Dias, I., Levers, M. R., Lamberti, M., Hassink, G. C., van Wezel, R., & le Feber, J. (2021). Consolidation of memory traces in cultured cortical networks requires low cholinergic tone, synchronized activity and high network excitability. *Journal of Neural Engineering*, *18*(4), 046051. https://doi.org/10.1088/1741-2552/abfb3f

Diba, K., & Buzsaki, G. (2007). Forward and reverse hippocampal place-cell sequences during ripples. *Nat Neurosci*, *10*(10), 1241–1242. https://doi.org/nn1961 [pii] 10.1038/nn1961

Diesmann, M., Gewaltig, M. O., & Aertsen, A. (1999). Stable propagation of synchronous spiking in cortical neural networks. *Nature*, *402*(6761), 529–533. https://doi.org/10.1038/990101

Doeller, C. F., Barry, C., & Burgess, N. (2010a). Evidence for grid cells in a human memory network. *Nature*, *463*(7281), 657–661. http://dx.doi.org/10.1038/nature08704

Dragoi, G., & Buzsáki, G. (2006). Temporal Encoding of Place Sequences by Hippocampal Cell Assemblies. *Neuron*, *50*(1), 145–157. https://doi.org/10.1016/j.neuron.2006.02.023

Dragoi, G., & Tonegawa, S. (2011). Preplay of future place cell sequences by hippocampal cellular assemblies. *Nature*, *469*(7330), 397–401. https://doi.org/10.1038/nature09633

Dragoi, G., & Tonegawa, S. (2013). Distinct preplay of multiple novel spatial experiences in the rat. *Proceedings of the National Academy of Sciences*, *110*(22), 9100–9105. https://doi.org/10.1073/pnas.1306031110

Eccles, J. C. (1994). *How the Self Controls its Brain*. Springer.

Engel, T. A., Schimansky-Geier, L., Herz, A. V. M., Schreiber, S., & Erchova, I. (2008). Subthreshold Membrane-Potential Resonances Shape Spike-Train Patterns in the Entorhinal Cortex. *Journal of Neurophysiology*. https://doi.org/10.1152/jn.01282.2007

Eyal, G., Verhoog, M. B., Testa-Silva, G., Deitcher, Y., Benavides-Piccione, R., DeFelipe, J., de Kock, C. P. J., Mansvelder, H. D., & Segev, I. (2018). Human Cortical Pyramidal Neurons: From Spines to Spikes via Models. *Frontiers in Cellular Neuroscience*, *12*. https://doi.org/10.3389/fncel.2018.00181

Farooq, U., Sibille, J., Liu, K., & Dragoi, G. (2019). Strengthened Temporal Coordination within Pre-existing Sequential Cell Assemblies Supports Trajectory Replay. *Neuron*, *103*(4), 719-733.e7. https://doi.org/https://doi.org/10.1016/j.neuron.2019.05.040

Fernández-Ruiz, A., Oliva, A., Soula, M., Rocha-Almeida, F., Nagy, G. A., Martin-Vazquez, G., & Buzsáki, G. (2021). Gamma rhythm communication between entorhinal cortex and dentate gyrus neuronal assemblies. *Science*. https://doi.org/10.1126/science.abf3119

Fosse, M. J., Fosse, R., Hobson, J. A., & Stickgold, R. J. (2003). Dreaming and episodic memory: a functional dissociation? *Journal of Cognitive Neuroscience*, *15*(1), 1–9. https://doi.org/10.1162/089892903321107774

Foster, D. J., & Wilson, M. A. (2006). Reverse replay of behavioural sequences in hippocampal place cells during the awake state. *Nature*, *440*(7084), 680–683. https://doi.org/nature04587 [pii] 10.1038/nature04587

Fournier, J., Saleem, A. B., Diamanti, E. M., Wells, M. J., Harris, K. D., & Carandini, M. (2020). Mouse Visual Cortex Is Modulated by Distance Traveled and by Theta Oscillations. *Current Biology*, *30*(19), 3811-3817.e6. https://doi.org/https://doi.org/10.1016/j.cub.2020.07.006

Freeman, W. J. (2000). Mesoscopic neurodynamics: From neuron to brain. *Journal of Physiology Paris*. https://doi.org/10.1016/S0928-4257(00)01090-1

Frey, U., & Morris, R. G. (1997). Synaptic tagging and long-term potentiation. *Nature*, *385*(6616), 533–536. https://doi.org/10.1038/385533a0

Friston, K. (2010). The free-energy principle: A unified brain theory? In *Nature Reviews Neuroscience*. https://doi.org/10.1038/nrn2787

Gabor, D., Kock, W. E., & Stroke, G. W. (1971). Holography. *Science*, *173*(3991), 11–23. https://doi.org/10.1126/science.173.3991.11

Georgopoulos, A. P., Schwartz, A. B., & Kettner, R. E. (1986). Neuronal population coding of movement direction. *Science*, *233*(4771), 1416–1419. http://www.hubmed.org/display.cgi?uids=3749885

Gollisch, T., & Meister, M. (2008). Rapid neural coding in the retina with relative spike latencies. *Science*, *319*(5866), 1108–1111. http://www.hubmed.org/display.cgi?uids=18292344

Gray, C. M., & Singer, W. (1989). Stimulus-specific neuronal oscillations in orientation columns of cat visual cortex. *Proc Natl Acad Sci U S A*, *86*(5), 1698–1702.

Grion, N., Akrami, A., Zuo, Y., Stella, F., & Diamond, M. E. (2016). Coherence between rat sensorimotor system and hippocampus is enhanced during tactile discrimination. *PLoS Biology*, *14*(2), e1002384.

Grosmark, A. D., & Buzsáki, G. (2016). Diversity in neural firing dynamics supports both rigid and learned hippocampal sequences. *Science (New York, N.Y.)*, *351*(6280), 1440–1443. https://doi.org/10.1126/science.aad1935

Hafting, T., Fyhn, M., Molden, S., Moser, M.-B., & Moser, E. I. (2005). Microstructure of a spatial map in the entorhinal cortex. *Nature*, *436*(7052), 801–806. https://doi.org/10.1038/nature03721

Haken, H. (1983). *Introduction BT - Advanced Synergetics: Instability Hierarchies of Self-Organizing Systems and Devices* (H. Haken, Ed.; pp. 1–60). Springer Berlin Heidelberg. https://doi.org/10.1007/978-3-642-45553-7_1

Hangya, B., Tihanyi, B. T., Entz, L., Fabó, D., Eröss, L., Wittner, L., Jakus, R., Varga, V., Freund, T. F., & Ulbert, I. (2011). Complex Propagation Patterns Characterize Human Cortical Activity during Slow-Wave Sleep. *The Journal of Neuroscience*, *31*(24), 8770 LP – 8779. https://doi.org/10.1523/JNEUROSCI.1498-11.2011

Harris, K. D., Csicsvari, J., Hirase, H., Dragoi, G., & Buzsaki, G. (2003). Organization of cell assemblies in the hippocampus. *Nature*, *424*(6948), 552–556. https://doi.org/10.1038/nature01834 nature01834 [pii]

Harvey, C. D., Collman, F., Dombeck, D. A., & Tank, D. W. (2009). Intracellular dynamics of hippocampal place cells during virtual navigation. *Nature*, *461*(7266), 941–946. https://doi.org/nature08499 [pii] 10.1038/nature08499

Hasselmo, M., & Brandon, M. (2012). A Model Combining Oscillations and Attractor Dynamics for Generation of Grid Cell Firing. *Frontiers in Neural Circuits*, *6*. https://doi.org/10.3389/fncir.2012.00030

Hatsopoulos, N., Geman, S., Amarasingham, A., & Bienenstock, E. (2003). At what time scale does the nervous system operate? *Neurocomputing*, 25–54.

Hebb, D. O. (1949). *The organization of behavior*. Wiley.

Hebb, D. O. (1995). *A pszichológia alapkérdései*. Gondolat Kiadó. https://books.google.hu/books?id=3l7zsgEACAAJ

Hebb, D. O. (2005). *The Organization of Behavior: A Neuropsychological Theory*. Taylor \& Francis. https://books.google.hu/books?id=ddB4AgAAQBAJ

Hinman, J. R., Brandon, M. P., Climer, J. R., Chapman, G. W., & Hasselmo, M. E. (2016). Multiple Running Speed Signals in Medial Entorhinal Cortex. *Neuron*. https://doi.org/10.1016/j.neuron.2016.06.027

Hoffman, D. D. (2019). *The Case Against Reality: Why Evolution Hid the Truth from Our Eyes*. W.W. Norton. https://books.google.hu/books?id=EcT0uwEACAAJ

Hopfield, J. J. (1982). Neural networks and physical systems with emergent collective computational abilities. *Proceedings of the National Academy of Sciences of the United States of America*, *79*(8), 2554–2558. https://doi.org/10.1073/pnas.79.8.2554

Hopfield, J. J. (1995). Pattern recognition computation using action potential timing for stimulus representation. *Nature*, *376*(6535), 33–36.

Jacobs, J., Weidemann, C. T., Miller, J. F., Solway, A., Burke, J. F., Wei, X.-X., Suthana, N., Sperling, M. R., Sharan, A. D., Fried, I., & Kahana, M. J. (2013). Direct recordings of grid-like neuronal activity in human spatial navigation. *Nature Neuroscience*. https://doi.org/10.1038/nn.3466

Jensen, O., & Lisman, J. E. (2000). Position Reconstruction From an Ensemble of Hippocampal Place Cells: Contribution of Theta Phase Coding. *Journal of Neurophysiology*, *83*(5), 2602–2609. https://doi.org/10.1152/jn.2000.83.5.2602

Ji, D., & Wilson, M. A. (2007). Coordinated memory replay in the visual cortex and hippocampus during sleep. *Nat Neurosci*, *10*(1), 100–107. https://doi.org/nn1825 [pii] 10.1038/nn1825

Jones, M. W., & Wilson, M. A. (2005). Phase precession of medial prefrontal cortical activity relative to the hippocampal theta rhythm. *Hippocampus*, *15*(7), 867–873. https://doi.org/10.1002/hipo.20119

Josselyn, S. A., & Tonegawa, S. (2020). Memory engrams: Recalling the past and imagining the future. *Science (New York, N.Y.)*, *367*(6473). https://doi.org/10.1126/science.aaw4325

Kaplan, R., Schuck, N. W., & Doeller, C. F. (2017). The Role of Mental Maps in Decision-Making. *Trends in Neurosciences*, *40*(5), 256–259. https://doi.org/10.1016/j.tins.2017.03.002

Katlowitz, K. A., Picardo, M. A., & Long, M. A. (2018). Stable Sequential Activity Underlying the Maintenance of a Precisely Executed Skilled Behavior. *Neuron*, *98*(6), 1133-1140.e3. https://doi.org/https://doi.org/10.1016/j.neuron.2018.05.017

Kauffman, S. A., & Kauffman, M. S. F. I. P. B. S. A. (1993). *The Origins of Order: Self-organization and Selection in Evolution*. Oxford University Press. https://books.google.hu/books?id=lZcSpRJz0dgC

Kayser, C., Montemurro, M. A., Logothetis, N. K., & Panzeri, S. (2009). Spike-phase coding boosts and stabilizes information carried by spatial and temporal spike patterns. *Neuron*, *61*(4), 597–608. https://doi.org/S0896-6273(09)00075-0 [pii] 10.1016/j.neuron.2009.01.008

Killian, N. J., Jutras, M. J., & Buffalo, E. A. (2012). A map of visual space in the primate entorhinal cortex. *Nature*, *491*(7426), 761–764. https://doi.org/10.1038/nature11587

Killian, N. J., Potter, S. M., & Buffalo, E. A. (2015). Saccade direction encoding in the primate entorhinal cortex during visual exploration. *Proceedings of the National Academy of Sciences of the United States of America*. https://doi.org/10.1073/pnas.1417059112

Koepsell, K., Wang, X., Vaingankar, V., Wei, Y., Wang, Q., Rathbun, D. L., Usrey, W. M., Hirsch, J. A., & Sommer, F. T. (2009). Retinal oscillations carry visual information to cortex. *Front Syst Neurosci*, *3*, 4. https://doi.org/10.3389/neuro.06.004.2009

Krupic, J., Burgess, N., & O'Keefe, J. (2015). *Spatially Periodic Cells Are Neither Formed From Grids Nor Poor Isolation*. http://arxiv.org/abs/1512.06248

Kunz, L., Lee, H., Montag, C., Lachmann, B., Sariyska, R., Reuter, M., Messing-floeter, P. C., Fell, J., Doeller, C. F., & Axmacher, N. (2015). *430.Full*. *350*(6259).

Legéndy, C. R., & Salcman, M. (1985). Bursts and recurrences of bursts in the spike trains of spontaneously active striate cortex neurons. *Journal of Neurophysiology*, *53*, 926–939.

Lenck-Santini, P.-P., & Holmes, G. L. (2008). Altered Phase Precession and Compression of Temporal Sequences by Place Cells in Epileptic Rats. *Journal of Neuroscience*. https://doi.org/10.1523/jneurosci.5024-07.2008

Litvak, V., Sompolinsky, H., Segev, I., & Abeles, M. (2003). On the transmission of rate code in long feedforward networks with excitatory-inhibitory balance. *J Neurosci*, *23*(7), 3006–3015. https://doi.org/23/7/3006 [pii]

Logothetis, N. K. (2003). The Underpinnings of the BOLD Functional Magnetic Resonance Imaging Signal. *J. Neurosci.*, *23*(10), 3963–3971. http://www.jneurosci.org/content/23/10/3963.full

Lubenov, E. V, & Siapas, A. G. (2008). Decoupling through synchrony in neuronal circuits with propagation delays. *Neuron*, *58*(1), 118–131. https://doi.org/S0896-6273(08)00128-1 [pii] 10.1016/j.neuron.2008.01.036

Lubenov, E. V, & Siapas, A. G. (2009). Hippocampal theta oscillations are travelling waves. *Nature*. https://doi.org/nature08010 [pii] 10.1038/nature08010

M. Aghajan, Z., Schuette, P., Fields, T. A., Tran, M. E., Siddiqui, S. M., Hasulak, N. R., Tcheng, T. K., Eliashiv, D., Mankin, E. A., Stern, J., Fried, I., & Suthana, N. (2017). Theta Oscillations in the Human Medial Temporal Lobe during Real-World Ambulatory Movement. *Current Biology*. https://doi.org/10.1016/j.cub.2017.10.062

Madhavan, R., Chao, Z. C., & Potter, S. M. (2007). Plasticity of recurring spatiotemporal activity patterns in cortical networks. *Physical Biology*, *4*(3), 181. https://doi.org/10.1088/1478-3975/4/3/005

Maidenbaum, S., Miller, J., Stein, J. M., & Jacobs, J. (2018). Grid-like hexadirectional modulation of human entorhinal theta oscillations. *Proceedings of the National Academy of Sciences*, *115*(42), 10798–10803. https://doi.org/10.1073/pnas.1805007115

McCulloch, W. S., & Pitts, W. (1943). A logical calculus of the ideas immanent in nervous activity. *The Bulletin of Mathematical Biophysics*, *5*(4), 115–133. https://doi.org/10.1007/BF02478259

Mitchell-Heggs, R., Prado, S., Gava, G. P., Go, M. A., & Schultz, S. R. (2023). Neural manifold analysis of brain circuit dynamics in health and disease. *Journal of Computational Neuroscience*, *51*(1), 1–21. https://doi.org/10.1007/s10827-022-00839-3

Mitzdorf, U. (1987). Properties of the evoked potential generators: current source-density analysis of visually evoked potentials in the cat cortex. *Int J Neurosci*, *33*(1–2), 33–59. http://www.ncbi.nlm.nih.gov/entrez/query.fcgi?cmd=Retrieve&db=PubMed&dopt=Citation&list_uids=3610492

Montemurro, M. A., Rasch, M. J., Murayama, Y., Logothetis, N. K., & Panzeri, S. (2008). Phase-of-firing coding of natural visual stimuli in primary visual cortex. *Curr Biol*, *18*(5), 375–380. https://doi.org/S0960-9822(08)00168-1 [pii] 10.1016/j.cub.2008.02.023

Moore, G. P., Segundo, J. P., Perkel, D. H., & Levitan, H. (1970). Statistical signs of synaptic interaction in neurons. *Biophysical Journal*, *10*(9), 876–900. https://doi.org/10.1016/S0006-3495(70)86341-X

Moser, E. I., Roudi, Y., Witter, M. P., Kentros, C., Bonhoeffer, T., & Moser, M.-B. (2014). Grid cells and cortical representation. *Nature Reviews. Neuroscience*, *15*(7), 466–481. https://doi.org/10.1038/nrn3766

Muller, L., Chavane, F., Reynolds, J., & Sejnowski, T. J. (2018). Cortical travelling waves: Mechanisms and computational principles. In *Nature Reviews Neuroscience*. https://doi.org/10.1038/nrn.2018.20

Nadasdy, Z. (2000). Spike sequences and their consequences. *J Physiol Paris*, *94*(5–6), 505–524. https://doi.org/S0928-4257(00)01103-7 [pii]

Nadasdy, Z. (2009). Information encoding and reconstruction from the phase of action potentials. *Front Syst Neurosci*, *3*, 6. https://doi.org/10.3389/neuro.06.006.2009

Nadasdy, Z. (2010a). Binding by asynchrony: the neuronal phase code. *Front Neurosci*, *4*. https://doi.org/10.3389/fnins.2010.00051

Nadasdy, Z. (2015). *Information Encoding and Reconstruction by Phase Coding of Spikes BT - Analysis and Modeling of Coordinated Multi-neuronal Activity* (M. Tatsuno, Ed.; pp. 269–298). Springer New York. https://doi.org/10.1007/978-1-4939-1969-7_13

Nadasdy, Z., & Andersen, R. A. (2007). Modeling perceptual ambiguity resolution in V1. In *Neuroscience Meeting: Vol. 715.8/FF1*. Society for Neuroscience.

Nadasdy, Z., & Andersen, R. A. (2009). Phase coding in the primary visual cortex of wake monkeys. *(Submitted)*.

Nadasdy, Z., Csicsvari, J., Penttonen, M., Hetke, J., Wise, K., & Buzsaki, G. (1998). Extracellular recording and analysis of neuronal activity: from single cells to ensembles. In H. B. Eichenbaum & J. L. Davis (Eds.), *Neuronal Ensembles: Strategies for Recording and Decoding*. Wiley.

Nadasdy, Z., Hirase, H., Czurko, A., Csicsvari, J., & Buzsaki, G. (1999). Replay and time compression of recurring spike sequences in the hippocampus. *J Neurosci*, *19*(21), 9497–9507. http://www.ncbi.nlm.nih.gov/entrez/query.fcgi?cmd=Retrieve&db=PubMed&dopt=Citation&list_uids=10531452

Nadasdy, Z., Howell, D. H. P., Török, Á., Nguyen, T. P., Shen, J. Y., Briggs, D. E., Modur, P. N., & Buchanan, R. J. (2022). Phase coding of spatial representations in the human entorhinal cortex. *Science Advances*, *8*(18), eabm6081. https://doi.org/10.1126/sciadv.abm6081

Nadasdy, Z., Nguyen, T. P., Török, Á., Shen, J. Y., Briggs, D. E., Modur, P. N., & Buchanan, R. J. (2017a). Context-dependent spatially periodic activity in the human entorhinal cortex. *Proceedings of the National Academy of Sciences of the United States of America*, *114*(17), E3516–E3525. https://doi.org/10.1073/pnas.1701352114

Nadasdy, Z., Torok, A., Nguyen, T. P., Shen, J. Y., Brigg, D. E., Modur, P. N., & Buchanan, R. J. (2018). Phase of neuronal activity encodes 2-dimensional space in the human entorhinal cortex. *BioRxiv*. https://doi.org/10.1101/352815

Narahashi, T. (2008). Tetrodotoxin: a brief history. *Proceedings of the Japan Academy. Series B, Physical and Biological Sciences*, *84*(5), 147–154. https://doi.org/10.2183/pjab.84.147

O'Keefe, J., & Recce, M. L. (1993). Phase relationship between hippocampal place units and the EEG theta rhythm. *Hippocampus*, *3*(3), 317–330.

Pang, R., Lansdell, B. J., & Fairhall, A. L. (2016). Dimensionality reduction in neuroscience. *Current Biology*, *26*(14), R656–R660. https://doi.org/10.1016/j.cub.2016.05.029

Pasquale, V., Martinoia, S., & Chiappalone, M. (2017). Stimulation triggers endogenous activity patterns in cultured cortical networks. *Scientific Reports*, *7*(1), 9080. https://doi.org/10.1038/s41598-017-08369-0

Patel, J., Fujisawa, S., Berényi, A., Royer, S., & Buzsáki, G. (2012). Traveling theta waves along the entire septotemporal axis of the hippocampus. *Neuron*, *75*(3), 410–417. https://doi.org/10.1016/j.neuron.2012.07.015

Penttonen, M., Kamondi, A., Acsady, L., & Buzsaki, G. (1998). Gamma frequency oscillation in the hippocampus of the rat: intracellular analysis in vivo. *Eur J Neurosci*, *10*(2), 718–728. http://www.hubmed.org/display.cgi?uids=9749733

Perkel, D. H., Gerstein, G. L., & Moore, G. P. (1967a). Neuronal spike trains and stochastic point processes. I. The single spike train. *Biophysical Journal*, *7*(4), 391–418. https://doi.org/10.1016/S0006-3495(67)86596-2

Perkel, D. H., Gerstein, G. L., & Moore, G. P. (1967b). Neuronal spike trains and stochastic point processes. II. Simultaneous spike trains. *Biophysical Journal*, *7*(4), 419–440. https://doi.org/10.1016/S0006-3495(67)86597-4

Pfeiffer, B. E., & Foster, D. J. (2015). Autoassociative dynamics in the generation of sequences of hippocampal place cells. *Science*, *349*(6244), 180–183. https://doi.org/10.1126/science.aaa9633

Pinotsis, D. A., & Miller, E. K. (2022). Beyond dimension reduction: Stable electric fields emerge from and allow representational drift. *NeuroImage*, *253*, 119058. https://doi.org/https://doi.org/10.1016/j.neuroimage.2022.119058

Potter, S. M. B. T.-P. in B. R. (2001). Chapter 4 Distributed processing in cultured neuronal networks. In *Advances in Neural Population Coding* (Vol. 130, pp. 49–62). Elsevier. https://doi.org/https://doi.org/10.1016/S0079-6123(01)30005-5

Qasim, S. E., Fried, I., & Jacobs, J. (2021). Phase precession in the human hippocampus and entorhinal cortex. *Cell*, *184*(12), 3242-3255.e10. https://doi.org/10.1016/J.CELL.2021.04.017

Raithel, C. U., & Gottfried, J. A. (2021). What are grid-like responses doing in the orbitofrontal cortex? *Behavioral Neuroscience*, *135*(2), 218–225. https://doi.org/10.1037/bne0000453

Rajan, K., Harvey, C. D., & Tank, D. W. (2016). Recurrent Network Models of Sequence Generation and Memory. *Neuron*, *90*(1), 128–142. https://doi.org/10.1016/j.neuron.2016.02.009

Rao, R. P. N., & Ballard, D. H. (1999). Predictive coding in the visual cortex: a functional interpretation of some extra-classical receptive-field effects. *Nature Neuroscience*, *2*(1), 79–87. https://doi.org/10.1038/4580

Rowland, D. C., Roudi, Y., Moser, M.-B., & Moser, E. I. (2016). Ten Years of Grid Cells. *Annual Review of Neuroscience*, *39*(1), annurev-neuro-070815-013824. https://doi.org/10.1146/annurev-neuro-070815-013824

Rumelhart, D. E., Hinton, G. E., & Williams, R. J. (1986). Learning representations by back-propagating errors. *Nature*, *323*(6088), 533–536. https://doi.org/10.1038/323533a0

Saleem, A., Lien, A., Krumin, M., Haider, B., Rosón, M., Ayaz, A., Reinhold, K., Busse, L., Carandini, M., & Harris, K. (2017). Subcortical Source and Modulation of the Narrowband Gamma Oscillation in Mouse Visual Cortex. *Neuron*, *93*, 315–322. https://doi.org/10.1016/j.neuron.2016.12.028

Schneider, M., Silveira Broggini, A. C., Dann, B., Tzanou, A., Uran, C., Sheshadri, S., Scherberger, H., & Vinck, M. (2021). A mechanism for inter-areal coherence through communication based on connectivity and oscillatory power. *Neuron*, *109*. https://doi.org/10.1016/j.neuron.2021.09.037

Senior, T. J., Huxter, J. R., Allen, K., O'Neill, J., & Csicsvari, J. (2008). Gamma oscillatory firing reveals distinct populations of pyramidal cells in the CA1 region of the hippocampus. *J Neurosci*, *28*(9), 2274–2286. https://doi.org/28/9/2274 [pii] 10.1523/JNEUROSCI.4669-07.2008

Shadlen, M. N., & Movshon, J. A. (1999). Synchrony unbound: a critical evaluation of the temporal binding hypothesis. *Neuron*, *24*(1), 67-77,111-125. https://doi.org/S0896-6273(00)80822-3 [pii]

Shadlen, M. N., & Newsome, W. T. (1994). Noise, neural codes and cortical organization. *Current Opinion in Neurobiology*, *4*(4), 569–579. https://doi.org/10.1016/0959-4388(94)90059-0

Sherrington, C. S. (1906). *The integrative action of the nervous system* (Vol. 35). Yale University Press.

Shmiel, T., Drori, R., Shmiel, O., Ben-Shaul, Y., Nadasdy, Z., Shemesh, M., Teicher, M., & Abeles, M. (2005). Neurons of the cerebral cortex exhibit precise interspike timing in correspondence to behavior. *Proc Natl Acad Sci U S A*, *102*(51), 18655–18657. https://doi.org/0509346102 [pii] 10.1073/pnas.0509346102

Shmiel, T., Drori, R., Shmiel, O., Ben-Shaul, Y., Nadasdy, Z., Shemesh, M., Teicher, M., & Abeles, M. (2006). Temporally precise cortical firing patterns are associated with distinct action segments. *Journal of Neurophysiology*, *96*(5). https://doi.org/10.1152/jn.00798.2005

Skaggs, W. E., & McNaughton, B. L. (1996). Replay of neuronal firing sequences in rat hippocampus during sleep following spatial experience. *Science*, *271*(5257), 1870–1873. http://www.ncbi.nlm.nih.gov/entrez/query.fcgi?cmd=Retrieve&db=PubMed&dopt=Citation&list_uids=8596957

Sloin, H. E., Levi, A., Someck, S., Spivak, L., & Stark, E. (2022). High Fidelity Theta Phase Rolling of CA1 Neurons. *The Journal of Neuroscience : The Official Journal of the Society for Neuroscience*, *42*(15), 3184–3196. https://doi.org/10.1523/JNEUROSCI.2151-21.2022

Softky, W. R., & Koch, C. (1993). The highly irregular firing of cortical cells is inconsistent with temporal integration of random EPSPs. *The Journal of Neuroscience : The Official Journal of the Society for Neuroscience*, *13*(1), 334–350. https://doi.org/10.1523/JNEUROSCI.13-01-00334.1993

Souza, B. C., & Tort, A. B. L. (2017). Asymmetry of the temporal code for space by hippocampal place cells. *Scientific Reports*, *7*(1), 8507. https://doi.org/10.1038/s41598-017-08609-3

Szentágothai, J. (1978). The Ferrier Lecture, 1977 The neuron network of the cerebral cortex: a functional interpretation. *Proceedings of the Royal Society of London. Series B. Biological Sciences*, *201*(1144), 219–248.

Szilagyi, A., Zachar, I., Fedor, A., de Vladar, H. P., & Szathmary, E. (2017). Breeding novel solutions in the brain: A model of Darwinian neurodynamics [version 2; peer review: 3 approved]. *F1000Research*, *5*(2416). https://doi.org/10.12688/f1000research.9630.2

Tallon-Baudry, C., & Bertrand, O. (1999). Oscillatory gamma activity in humans and its role in object representation. *Trends Cogn Sci*, *3*(4), 151–162. https://doi.org/S1364-6613(99)01299-1 [pii]

Tan, A. Y. Y., Chen, Y., Scholl, B., Seidemann, E., & Priebe, N. J. (2014). Sensory stimulation shifts visual cortex from synchronous to asynchronous states. *Nature*, *509*(7499), 226–229. https://doi.org/10.1038/nature13159

Tingley, D., & Buzsáki, G. (2018). Transformation of a Spatial Map across the Hippocampal-Lateral Septal Circuit. *Neuron*, *98*(6), 1229-1242.e5. https://doi.org/10.1016/j.neuron.2018.04.028

Tonegawa, S., Liu, X., Ramirez, S., & Redondo, R. (2015). Memory Engram Cells Have Come of Age. *Neuron*, *87*(5), 918–931. https://doi.org/10.1016/j.neuron.2015.08.002

Turing, A. M. (1937). On Computable Numbers, with an Application to the Entscheidungsproblem. *Proceedings of the London Mathematical Society*, *s2-42*(1), 230–265. https://doi.org/https://doi.org/10.1112/plms/s2-42.1.230

Umbach, G., Kantak, P., Jacobs, J., Kahana, M., Pfeiffer, B. E., Sperling, M., & Lega, B. (2020). Time cells in the human hippocampus and entorhinal cortex support episodic memory. *Proceedings of the National Academy of Sciences of the United States of America*, *117*(45), 28463–28474. https://doi.org/10.1073/pnas.2013250117

van Vreeswijk, C., & Sompolinsky, H. (1996). Chaos in neuronal networks with balanced excitatory and inhibitory activity. *Science (New York, N.Y.)*, *274*(5293), 1724–1726. https://doi.org/10.1126/science.274.5293.1724

Vaz, A. P., Wittig, J. H. J., Inati, S. K., & Zaghloul, K. A. (2020). Replay of cortical spiking sequences during human memory retrieval. *Science (New York, N.Y.)*, *367*(6482), 1131–1134. https://doi.org/10.1126/science.aba0672

von der Malsburg, C. (1999). The What and Why of Binding: The Modeler's Perspective. *Neuron*, *24*(1), 95–104. https://doi.org/https://doi.org/10.1016/S0896-6273(00)80825-9

Von Neumann, J. (1958). The computer and the brain. In *Yale University. Mrs. Hepsa Ely Silliman memorial lectures*. Yale Univ. Press.

Wagenaar, D. A., Nadasdy, Z., & Potter, S. M. (2006). Persistent dynamic attractors in activity patterns of cultured neuronal networks. *Phys Rev E Stat Nonlin Soft Matter Phys*, *73*(5 Pt 1), 51907. http://www.ncbi.nlm.nih.gov/entrez/query.fcgi?cmd=Retrieve&db=PubMed&dopt=Citation&list_uids=16802967

Wamsley, E. J., & Stickgold, R. (2011). Memory, Sleep, and Dreaming: Experiencing Consolidation. *Sleep Medicine Clinics*, *6*(1), 97–108. https://doi.org/10.1016/j.jsmc.2010.12.008

Welinder, P. E., Burak, Y., & Fiete, I. R. (2008). Grid cells: the position code, neural network models of activity, and the problem of learning. *Hippocampus*, *18*(12), 1283–1300. https://doi.org/10.1002/hipo.20519

Wilson, C. J., Higgs, M. H., Simmons, D. V, & Morales, J. C. (2018). Oscillations and Spike Entrainment. *F1000Research*, *7*. https://doi.org/10.12688/f1000research.16451.1

Wilson, M. A., & McNaughton, B. L. (1994). Reactivation of hippocampal ensemble memories during sleep. *Science (New York, N.Y.)*, *265*(5172), 676–679. https://doi.org/10.1126/science.8036517

Wyler, A. R., Ojemann, G. A., & Ward, A. A. J. (1982). Neurons in human epileptic cortex: correlation between unit and EEG activity. *Annals of Neurology*, *11*(3), 301–308. https://doi.org/10.1002/ana.410110311

Yartsev, M. M., & Ulanovsky, N. (2013). Representation of three-dimensional space in the hippocampus of flying bats. *Science (New York, N.Y.)*, *340*, 367–372. https://doi.org/10.1126/science.1235338

Yartsev, M. M., Witter, M. P., & Ulanovsky, N. (2011). Grid cells without theta oscillations in the entorhinal cortex of bats. *Nature*, *479*(7371), 103–107. https://doi.org/10.1038/nature10583

Zhang, H., & Jacobs, J. (2015). Traveling Theta Waves in the Human Hippocampus. *Journal of Neuroscience*, *35*(36), 12477–12487. https://doi.org/10.1523/JNEUROSCI.5102-14.2015

Zhang, H., Watrous, A. J., Patel, A., & Jacobs, J. (2018). Theta and Alpha Oscillations Are Traveling Waves in the Human Neocortex. *Neuron*, *98*(6), 1269-1281.e4. https://doi.org/10.1016/j.neuron.2018.05.019